Phytochemical Mediated CuO, ZnO and MgO Based Mono, Bi and Trimetallic Oxide Nanomaterials for Biological Applications

Temesgen Achamo Orshiso

Ph.D. Dissertation Submitted to the Department of Applied Chemistry
School of Applied Natural Sciences

Presented in Fulfillment of the Requirement for the Degree of
Doctor of Philosophy in Chemistry (Bioinorganic Chemistry)

Office of Graduate Studies
Adama Science and Technology University

April, 2024
Adama, Ethiopia

Phytochemical Mediated CuO, ZnO and MgO Based Mono, Bi and Trimetallic Oxide Nanomaterials for Biological Applications

Temesgen Achamo Orshiso

Supervisor: Enyew Amare (PhD, Associate Professor)

Co-supervisor: H. C. Ananda Murthy (PhD, Associate Professor)

Ph.D. Dissertation Submitted to the Department of Applied Chemistry, School of Applied Natural Sciences

Presented in Fulfillment of the Requirement for the Degree of Doctor of Philosophy in Chemistry (Bioinorganic Chemistry)

Office of Graduate Studies

Adama Science and Technology University

April, 2024

Adama, Ethiopia

Declaration

I hereby declare that this dissertation entitled "**Phytochemical Mediated CuO, ZnO and MgO Based Mono, Bi and Trimetallic Oxide Nanomaterials for Biological Applications"** is my own original work conducted at the Department of Applied Chemistry under supervision of Dr. Enyew Amare, and Dr. H. C. Ananda Murthy. It has never been submitted for the award of any academic degree, diploma or certificate in any other university. All sources of materials used for this dissertation have been duly acknowledged through the appropriate list of references.

Temesgen Achamo	_____	_____
Name of Student	Signature	Date

Recommendation

We, the supervisors of this dissertation, hereby certify that we have read and revised the Dissertation entitled "**Phytochemical Mediated CuO, ZnO and MgO Based Mono, Bi and Trimetallic Oxide Nanomaterials for Biological Applications"** prepared under our guidance by **Temesgen Achamo Orshiso** and submitted in partial fulfillment of the requirements for the degree of Doctor of Philosophy in Applied Chemistry **(Bioinorganic Chemistry)**. Therefore, we recommend the final submission of the dissertation to the department.

Dr. Enyew Amare	_____	_____
Supervisor	Signature	Date
Dr. H. C. Ananda Murthy	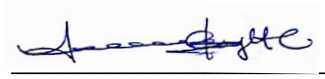	_____
Co-supervisor	Signature	Date

Approval Page

We hereby certify that the recommendations and suggestions made by the board of examiners are appropriately incorporated into the final version of the dissertation entitled "**Phytochemical Mediated CuO, ZnO and MgO Based Mono, Bi and Trimetallic Oxide Nanomaterials for Biological Applications"** by Temesgen Achamo.

Supervisor	Signature	Date
Co-supervisor	Signature	Date

We, the undersigned, members of the Board of Examiners of the dissertation open defense by Temesgen Achamo have read and evaluated the dissertation entitled "**Phytochemical Mediated CuO, ZnO and MgO Based Mono, Bi and Trimetallic Oxide Nanomaterials for Biological Applications"** and examined the candidate during open defense. This is, therefore, to certify that the dissertation is accepted for partial fulfillment of the requirement of the degree of Doctor of Philosophy in Bioinorganic Chemistry**.**

Chair Person	Signature	Date
Internal Examiner I	Signature	Date
Internal Examiner II	Signature	Date
External Examiner I	Signature	Date
External Examiner II	Signature	Date

Finally, approval and acceptance of the dissertation is contingent upon submission of its final copy to the Office of Postgraduate Studies (OPGS) through the candidate's Department Graduate Council (DGC) and School Graduate Committee (SGC).

Department Head	Signature	Date
School Dean	Signature	Date
Office of Postgraduate Studies, Dean	Signature	Date

ACKNOWLEDGMENT

First, I would like to praise the Almighty God and His Begotten Son, Jesus Christ for bestowing upon me health, strength, patience and protection.

I want to express my heartfelt gratitude to my supervisors, Dr. Enyew Amare and Dr. H. C. Ananda Murthy for their daily follow-up, priceless guidance, suggestions, and fatherly consultancy throughout the work. This dissertation couldn't have appeared in its current form without their strong support and guidance. They, indeed, have taught me both formal and informal ways, which I could never find in formal education.

I would like also to acknowledge Professor Tegene Desalegn and Dr. Fedlu Kedir for their constructive comments and guidance. Moreover, I recognize the Ministry of Education for sponsoring my Ph.D. study, Haramya University, and Adama Science and Technology University for financial and material support. The Department of Applied Chemistry, Department of Applied Biology, and Department of Materials Science and Engineering for providing laboratory space and facility to accomplish this work.

I would also like to thank Dr. Ravikumar, Research Centre, Department of Science, East West Institute of Technology, India, for supporting SEM-EDX and TEM-SAED analysis. Mr. Surash Ghotekar, Chettinad, Academy of Research and Education, India, is highly acknowledged for doing Cytotoxicity analysis. My special thanks go to Dr. Taye B. Demissie, University of Botswana, for his kind support of analysis of molecular docking studies. I thank Guta Amanu, Bontu Tiki, Eticha Abdisa, and Mariam Kufa for their technical support during laboratory work.

I would also like to thank my family for their unreserved moral and financial support. Last but not least, my sincere gratitude goes to all my friends for their unwavering support and contributions throughout the work.

CONTENTS **PAGES**

LIST OF TABLES

LLIST OF FIGURES

LIST OF APPENDIXES

LIST OF ABBREVIATIONS

AIDS	Acquired immunodeficiency syndrome
ATCC	American Type Culture Collection
ATP	Adenosine Triphosphate
BMO	Bimetallic Oxide
CFU	Colony Forming Unit
CLSI	Clinical and Laboratory Standards Institute
CuO NPs	Copper Oxide Nanoparticles
DIW	Deionized Water
DMH	1,2-dimethyl hydrazine
DMEM	Dulbecco's Modified Eagle Medium
DMSO	Dimethyl Sulphoxide
DNA	Deoxyribonucleic acid
DPPH	2,2-diphenyl-1-picrylhydrazyl
DTA	Differential Thermal Analysis
ED_{50}	Half Maximum Effective Dose
EDX	Energy-dispersive X-ray
FBS	Fetal Bovine Serum
FRAP	Ferric Reducing Antioxidant Power
FTIR	Fourier Transform Infrared
IARC	International Agency for Research on Cancer
ICSD	Inorganic Crystal Structure Database
IC_{50}	Half Maximal Inhibitory Concentration
LEAA	Leaf Extract of *Artemissia abysinica*
MC	MgO-CuO
MgO NPs	Magnesium Oxide Nanoparticles
MHA	Mueller-Hinton Agar
MIC	Minimum Inhibitory Concentration
MO NPs	Metal Oxide NPs

MTT	[3-(4,5-dimethylthiazol-2-yl)-2,5-diphenyltetrazolium bromide]
NA	Nutrient Agar
NCs	Nanocomposities
NMs	Nanomaterials
NPs	Nanoparticles
OD	Optical Density
PBM	peripheral blood mononuclear
PBS	Phosphate Buffer Saline
PDA	Potato Dextrose Agar
pH	Power of Hydrogen
ROS	Reactive Oxygen Species
RNS	Reactive Nitrogen Species
SAED	Selected Area Electron Diffraction
SDA	Sabouraud Dextrose Agar
SEM	Scanning Electron Microscopy
SPR	Surface Plasmon Resonance
HRTEM	High Resolution Transmission Electron Microscopy
TEM	Transmission Electron Microscopy
TGA	Thermo Gravimetric Analysis
TMO	Trimetallic Oxide
TSA	Tryptic Soy Agar
UV-Vis	Ultra Violet-Visible
WHO	World Health Organization
XRD	X-ray Diffraction
ZnO NPs	Zinc Oxide Nanoparticles
ZC	ZnO-CuO
ZMC	ZnO-MgO-ZnO

ABSTRACT

Due to their unique physicochemical properties, metal oxide nanomaterials (MO NMs) have recently emerged as promising materials for various biological applications. However, effective utilization of MO NMs in biological applications is determined by synthetic conditions including optimal reaction parameters and synthesis methods. Phytochemical-mediated synthesis of MO NMs has a significant role in biological applications. In this study, one-pot greener technique was used for the synthesis of mono (CuO, ZnO, and MgO), bi (ZnO-CuO, MgO-CuO, and MgO-ZnO) and trimetallic (ZnO-MgO-CuO) NMs using the leaf extract of Artemisia abyssinica (LEAA). The physicochemical properties of biosynthesized MO NMs were characterized using TGA/DTA, FTIR, XRD, UV-visible, SEM, EDX, TEM, and SAED techniques. From the TGA/DTA results, the thermal stabilities of nanomaterials were determined. XRD analysis revealed the synthesis of pure CuO, ZnO, and MgO NPs and mixed phases ZnO-CuO, MgO-CuO, MgO-ZnO and ZnO-MgO-CuO nanocomposities (NCs) with average crystallite sizes ranging from 11-15 nm. FTIR analyses have shown the involvement of functional groups from LEAA during the synthesis of NMs. The optical properties of mono, bi and trimetallic oxide NMs were investigated using UV-visible spectroscopic analysis. The EDX analysis confirmed the presence of a predictable composition of the NMs. The SEM and TEM/HRTEM-SAED analysis revealed that the synthesized NMs have a spherical morphology and crystalline nature with average particle sizes ranging from 12-16 nm. In-vitro antioxidant activity analysis of synthesized MO NMs was studied using DPPH and FRAP assays. DPPH assay results indicated that all the synthesized MO NMs have radical scavenging activity ranging from 81-97% at 200 μg/mL with respective IC_{50} of 2.08-7.76 μg/mL. Likewise, the biosynthesized MO NMs have exhibited the ferric reducing antioxidant power (FRAP) with an absorbance of 1.312±0.012-1.964±0.003 at 200 μg/mL. Antibacterial activity of biosynthesized MO NMs against two gram-negative (Pseudomonas aeruginosa and Escherichia coli) and two gram-positive (Staphylococcus aureus and Streptococcus pneumonia) bacterial strains were evaluated. As the result demonstrated MO NMs have the zone of inhibitions between 25±0.02-35±0.03 mm at 200 μg/mL against the tested bacterial strains. Antifungal activity evaluations showed that all the synthesized MO NMs are active against pathogenic (Aspergillus flavus, Aspergillus niger and Candida albicans) fungal strains with inhibition zones 22±0.11-31±0.03 mm at 200 μg/mL. Anticancer activity results of

ZC, MC, MZ, and ZMC NPs showed promising cytotoxicity against MCF-7 cell lines with the respective IC_{50} values of 33.12, 35.24, 37.47, and 24.83 μg/mL. Moreover, the in silico molecular docking simulation of tested MO NMs has shown strong binding affinity against amino acid residues of S. aureus dihydrofolate reductase (PDB: 2w9h), E. coli DNA gyrase B (PDB: 6F86) and estrogen receptor alpha (ERα; PDB: 5GS4). These findings suggested that the biosynthesized MO NMs could be promising antioxidant, antibacterial, antifungal and anticancer (particularly for breast cancer) therapeutic agents. However, the in-vivo biological efficacies of MO NMs would be recommended to ensure the clinical use of NMs.

Keywords: *Artemisia abyssinica; MO NMs; antioxidant, antibacterial, antifungal, anticancer, Molecular docking.*

1. INTRODUCTION

1.1 Background of Study

Infectious diseases and cancer are major contributors to the global health burden and have been the leading cause of morbidity and mortality worldwide (Deo, Sharma, & Kumar, 2022; Ikuta et al., 2022). According to the World Health Organization (WHO), infectious diseases account for approximately 17% of global deaths each year (Kojom & Singh, 2021). In low- and middle-income countries, infectious diseases are responsible for a higher proportion of deaths than in high-income countries. Several antimicrobials (antibiotics) have been investigated and utilized broadly in clinical fields to combat various infectious diseases (Aghamohammad & Rohani, 2023). However, antimicrobial resistance (AMR) or multi-drug resistance is another aspect of the emerging global burden of the 21st century (Murray et al., 2022). AMR is caused by modification in the ability of microorganisms to resist antimicrobial agents either by inactivating them or by causing a decrease in their therapeutic efficacy (Cucci et al., 2020). Inappropriate use or abuse of antibiotics considerably induces genetic modifications in microorganisms that favor drug resistance (Palma, Tilocca, & Roncada, 2020). A study reported that the burden of AMR is comparable to the combined effect of influenza, tuberculosis and HIV/AIDS (human immunodeficiency/acquired immunodeficiency syndrome). It is also reported that the impact is highest in infants and the elderly. Disturbingly, the study also reported that 39% of all AMR were caused by bacteria and fungi that are resistant to last-line antibiotics, making them very difficult or impossible to treat (Cassini et al., 2019; Organization, 2020). As per the report of WHO, new resistance mechanisms are emerging and spreading globally, threatening the ability of scientists in the field to treat common infectious diseases, resulting in prolonged illness, disability, and death (MacNair, Rutherford, & Tan, 2024).

Cancer has been a growing health problem next to infectious diseases. Several factors both inside (genetic factors) and outside the body (environmental factors) contribute to the development of cancer (Bahrami & Tafrihi, 2023). It is usually a fatal disease which contributes an enormous burden on society in both economically developed and developing countries. According to WHO projections, cancer in the near future will be the overall leading cause of death worldwide (Siegel, Miller, & Jemal, 2019). Currently available estimates by GLOBOCAN (an International

Agency for Research on Cancer-IARC) show that about 19.3 million new cancer cases and 10 million about 1 in every 6 deaths worldwide, more than AIDS, tuberculosis, and malaria combined occurred in 2020. Furthermore, 38.6 million people were living with cancer, within 5 years of diagnosis by 2020 (Ferlay et al., 2019). Overall, 57 % of new cancer cases, 65 % of cancer deaths, and 48 % of the 5-year prevalent cancer cases occurred in less developed countries. The numbers are projected to double by 2040 due to the ageing, fast growth of the population, and adoption of behaviors and lifestyles associated with economic development (Bray et al., 2018). Breast cancer is one of the leading malignancies among women, which has caused significant morbidity, and leads to a tremendous burden on the healthcare system worldwide. According to GLOBOCAN 2020, (Sung et al., 2021) there are 2.3 million newly diagnosed cases (accounting for 11.7% of all newly diagnosed breast cancer cases) and 685,000 deaths in 2020. Almost two-thirds of those deaths were recorded in less-developed regions (Deo et al., 2022).

Reactive oxide species (ROS) such as superoxide ($O_2^{\cdot-}$), hydroxyl (·OH), peroxyl ($RO_2\cdot$), and alkoxyl (RO-) as well as hypochlorous acid (HOCl), ozone (O_3), singlet oxygen ($^1O_2$), and hydrogen peroxide (H_2O_2) are the middle products of normal metabolism and play a crucial role in cell signaling transduction. On the contrary, accumulation of excess reactive oxide species results in oxidative stress that often brings multifarious impairment to cells, including a decrease of adenosine triphosphate (ATP) level in cells, elevation of cytosolic Ca^{2+}, damage to cell membranes, membranes of subcellular organelles, proteins, lipids, and deoxyribonucleic acid (DNA), and thus subsequently leading to mutations, apoptosis, and failure within these systems (Raut & Khullar, 2023). These effects have the potential to lead to many types of diseases including cancer, diabetes, cardiovascular diseases, Alzheimer's and Parkinson's disease, acute renal failure, acute lung injury, radiation injury, cancer, arthritis, and even aging (Jomova et al., 2023). Both endogenous routes generally induce ROS and reactive nitrogen species (RNS) such as nitric oxide ($NO^{\cdot}$) peroxynitrite ($ONOO^{-}$), nitrogen dioxide (NO_2), including ROS-generating enzymes, such as nitric oxide synthase xanthine oxidase, and metabolism (e.g., secretion by macrophages, as well as by-product formation by the electron transport chain), and external sources including environmental stress (e.g., ionizing radiation, redox, and heavy metals, excess UV-radiation responsible to oxidative stress (Koltover, 2010). In the current decade, antioxidants have drawn attention due to their potential to minimize oxidative stress, which is defined as the

pathophysiological response created due to the imbalance between the production of oxidants and endogenous antioxidants to counteract (Sandhir, Yadav, Sunkaria, & Singhal, 2015).

Numerous antimicrobial, anticancer and antioxidant drugs have been introduced in clinical field in last decades. However, the majority of them have encountered cytotoxicity to a healthy body, poor water solubility, restricted membrane transport, and limitations in rapid clearance in the bloodstream (Del Genio et al., 2022). Hence, these combined complications urged researchers to explore new strategies and pioneering means of dealing with infectious disease, cancer and oxidative stress. Nanotechnology has recently sparked tremendous research, with applications to biotechnology, medicine, and biology (Contera, Bernardino de la Serna, & Tetley, 2020; Zain et al., 2022). Because of their diverse, physicochemical and structural properties such as small size, large surface area, optical and electrical activity, and mechanical and magnetic features metal and metal oxide nanomaterials (NMs) have been gaining the attention of researchers in the biological field (Abdelghany et al., 2023; Augustine & Hasan, 2020; Kannan, Radhika, Sadasivuni, Reddy, & Raghu, 2020). As the result, over the last few decades, many metal and metal oxide NMs have been studied extensively and introduced in biological fields including drug delivery, cancer treatment, infectious disease treatment, and antioxidative therapies (Jaffri & Ahmad, 2018; Srinoi, Chen, Vittur, Marquez, & Lee, 2018).

Metal oxide nanomaterials (MO NMs) have unique properties such as facile surface chemistry, colloidal stability, and enhanced surface reactivity compared to their metallic counterparts (Anjum et al., 2021; Chavali & Nikolova, 2019). These characteristics make them promising candidates for various applications in the clinical field. With proper engineering, MO NPs can be localized in any system of the body and mimic the activity of biomolecules, thus hacking the biological system of the body according to the need for human benefit (Zambonino et al., 2023). Currently, various types of MO NPs are used in clinical practice as antioxidant, antibacterial, biosensors and anticancer agents (S. Murthy, Effiong, & Fei, 2020; Negrescu et al., 2022; Shalaby, Shanab, El-Raheem, & Hanafy, 2022). Among these MO NMs iron oxide (Fe_2O_3), magnetite (Fe_3O_4), cerium oxide (CeO_2), aluminum oxide (Al_2O_3), titanium oxide (TiO_2), silver oxide (Ag_2O), gold oxide (AuO), zinc oxide (ZnO), palladium oxide (PdO), magnesium oxide (MgO), manganese oxide (MnOx), platinum oxide (PtO), copper oxide (CuO), cuprous oxide

(Cu_2O), nickel oxide (NiO), zirconium oxide (ZrO NPs) and cadmium oxide (CdO) NPs are the most promising candidates for use in biological applications (Gebre, 2023; Rana et al., 2023)

From those biologically benign MO NMs that have been introduced into clinical fields, ZnO, CuO, and MgO NPs are economically viable, eco-friendly, remarkably bioavailable, and biocompatible in biological applications (Gao et al., 2019; Ginting, Maulana, & Karnila, 2020; Vidhya, Vijayakumar, Prathipkumar, & Praseetha, 2020). Due to the semi-conductive nature and surface crystal defects of ZnO and CuO NPs the electrons freely move from the valance band to conduction bands and hence react with oxygen species to form free radicals which cause oxidative damage in microbial and cancerous cells. ZnO NPs are more appropriate in cancer therapy due to their inherent electrostatic nature and selective toxicity (Hadi, Nayef, Mutlak, & Jabir, 2023; Meer et al., 2022). ZnO NPs have exhibited significant anticancer efficacies against a variety of cancer types, including lung cancer (Rani et al., 2022), breast cancer (Ahamed, Lateef, Khan, Rajanahalli, & Akhtar, 2023), ovarian cancer (Mousa, Moawad, Abdallah, Abdel-Rasheed, & Zaher, 2023), and colorectal cancer (Efati et al., 2023). The anticancer potency of ZnO NPs is mainly through zinc-mediated protein activity disequilibrium and oxidative stress (Aboul-Soud et al., 2023; Naser et al., 2023). CuO NPs have shown enhanced cytotoxicity against breast cancer (Dolati, Tafvizi, Salehipour, Komeili Movahed, & Jafari, 2023), hepatocellular carcinoma (Younas et al., 2023), lung cancer (Doman, Gharieb, Abd El-Monem, & Morsi, 2023), and cervical cancer (M. S. Mohammad & Shyam, 2023). The anticancer mechanism of CuO NPs is mainly through genotoxicity and apoptotic death in cancerous cells due to its ability to generate enhanced ROS (Sathiyavimal et al., 2023). The exceptional features of MgO NPs such as biocompatibility, recycling activity, low density, hygroscopic nature, and good functionality make it a promising anticancer remedy (Saheb Ali et al., 2023; Fathy & Mahfouz, 2021; Fouda et al., 2022). Moreover, MO NPs of Zn, Cu, and Mg have been broadly utilized in microbial infections and oxidative stress-induced ailments (Ahamad Khan et al., 2023; Stanić & Tanasković, 2020).

Moreover, CuO is a p-type semiconductor with a narrow energy bandgap, ZnO is n-type semiconductor has medium bandgap and MgO has wide band gap hence combining different bandgap metal oxides to form nanocomposites is an efficient approach to enhance their physicochemical properties by modifying their bandgap. The interaction between various

constituent oxides with different band potentials leads to increased charge transferability, increased carrier lifetime, and charge separation efficiency that open up a new avenue of research for their biological applications (Joghee, Ganeshan, Vincent, & Hong, 2019; Panchal et al., 2019; Varshney et al., 2022). Due to immensely improved synergistic effects, enriched surface area, multiple reactive sites, higher charge flow, and mass transfer, metal oxide nanocomposities (MO NCs) exhibit enhanced biological activities than their monometallic counterparts (Abid et al., 2021; Basavegowda & Baek, 2021; Cao et al., 2021). For example, the bi and tri-metallic MO NCs display higher catalytic activity (Fauzia et al., 2019), modified morphology (Rodríguez-Proenza et al., 2018), highly selective and sensitive detection (Jiao et al., 2019), enhanced drug encapsulation efficiency (Ryu et al., 2021), good stability and chemical transformation (Adekoya, Dare, & Mesubi, 2014) and enhanced antimicrobial action (N. Yadav et al., 2018). Therefore, the fabrications of MO NCs more precisely enhance the biological activities of their monometallic oxide counterparts.

MO NMs have been synthesized using physical, chemical and biological approaches (Habibullah, Viktorova, & Ruml, 2021). However, synthesis of MO NMs using physical method has drawbacks including high cost, high energy and time consumption (Madhyastha et al., 2019). Chemical synthesis approach also utilizes toxic chemicals which cause harmful effects in environment and biological entities (Ramanathan, Gopinath, Arshad, Poopalan, & Perumal, 2021). Due to these limitations, there is a growing focus on "biological" methods in current materials science and technology research and development. Biological (green) synthesis techniques prevent the fabrication of unwanted or hazardous byproducts using efficient, accessible, and ecofriendly synthesis techniques as well as enhance the biocompatibility of NMs and hence can be utilized in biological applications (Augustine & Hasan, 2020; Dowlath et al., 2021).

Biological synthesis of MO NMs using various entities (e.g., bacteria, fungi, algae, and plant extracts) has been reported. Using plant extracts (phytochemical) to synthesize MO NMs is a simple and convenient method for producing nanoparticles on a large scale compared to using bacteria or fungi (Dauthal & Mukhopadhyay, 2016). Plant biodiversity is a valuable resource for synthesizing MO NMs, as it offers a wide range of effective phytochemicals like alkaloids, flavonoids, saponins, terpenoids, phenols, carbohydrates, proteins, carboxylic acids, and ascorbic

acid. These compounds play a crucial role in converting metal salts into MO NMs and maintaining their stability (Marslin et al., 2018). Furthermore, the diverse functional groups from phytochemicals of plant extracts, including NH_2, SH, COOH, C=O, and OH are used as greener reducing and capping agents (Akbar et al., 2020; Ogunyemi et al., 2020). Using medicinal plants to synthesize of MO NMs can also exhibit further synergistic effects on biological activity (M. Majeed, Hakeem, & Rehman, 2022; Sathiyavimal et al., 2022). It has been documented that biosynthesized MO NMs are mostly biocompatible and highly suitable for biological applications (Barui, Das, & Patra, 2019). The essential features of such nanomaterial have been investigated for use in biomedical diagnostics, antimicrobial, anticancer, antioxidant, anticoagulant, antiviral, catalysis, molecular sensing, optical imaging, and labeling of biological systems (R. Singh & Nalwa, 2011; Wahid, Khan, Shehzad, Ul-Islam, & Kim, 2014).

This work focuses on the fabrication of facile and eco-benign mono- (CuO, ZnO, and MgO) and bi- (CuO-ZnO, CuO-MgO, and ZnO-MgO) and trimetallic (CuO-MgO-ZnO) oxide NMs using the leaf extract of *Artemisia abyssinica* (LEAA) and the evaluation of their biological efficacies. *Artemisia abyssinica* (Figure 1) family *Asteraceae* (chekugn -Amharic) endemic to Ethiopia is a short-lived perennial, aromatic, grey, silky hairy plant commonly used in Ethiopia for traditional medicine and rituals. From nearly 400 species occurring primarily in northern temperate regions of the world, the genus *Artemisia* constitutes one of the 1535 genera in the family Asteraceae/Compositae. Among four species, including the endemic *Artemisia abyssinica* grow in Ethiopia (Chekole, 2017). It is a well-known stimulant and an analgesic; its leaves are ternate and grey-green and grow up to 10 cm long. It is widely grown in higher altitudes from 2000 cm to 3300 cm. Stems are sparingly branched and are superiorly grooved. Artemisia abyssinica treats intestinal problems, bronchitis and other inflammatory disorders, cold and fever, anorexia, colic, infectious diseases (bacterial, protozoa), headache, amenorrhea, and dysmenorrhea (Asfaw & Demissew, 2015). The plant has also been used as an anthelmintic, antispasmodic, antirheumatic, antioxidant, antitumor and antibacterial agent (d'Avigdor, Wohlmuth, Asfaw, & Awas, 2014). Besides these, essential oils of *Artemisia abyssinica* were reported to produce sesquiterpene lactones, coumarins, and acetylenes as primary bioactive metabolites. The major phytochemicals screened in *Artemisia abyssinica* are alkaloids, flavonoids, saponins, phenolic compounds, tannins, and essential oils (Letha, Ganesan, Nair, & Gani, 2016).

Figure 1. Photograph of *Artemisia Abyssinica* plant (ጭቁኝ).

1.2 Statement of the Problem

Infectious diseases and cancer are among the top ten health threat and second leading cause of death, respectively, worldwide. Microbial infection, cancer and oxidative stress are closely linked with one another since cancer could be induced by oxidative stress and microbial infection as well cancer can induce oxidative stress. The increasing prevalence of multi-drug resistant strains of bacteria and the appearance of strains with reduced susceptibility to antibiotics resulted in extended infection periods, increased mortality rates, and further economic burden on health systems. Currently, most conventional antibiotics, such as, erythromycin, aminoglycosides, quinolones, fluoroquinolone, carbapenems, penicillin and cephalosporin, have become obsolete due to the increased resistance of many bacterial strains. In addition, some of these antibiotics also have problems with cytotoxicity to healthy tissues, low water-solubility, poor membrane transport ability, and rapid clearance and degradation (Assis, Nedeljković, & Dessen, 2017).

Accumulation of excess reactive oxygen species (ROS) such as superoxide ($O_2^{\cdot -}$, $OOH^{\cdot}$), hydroxyl ($OH^{\cdot}$), and peroxyl ($ROOH^{\cdot}$) radicals, reactive nitrogen species (RNS), and sulfur-centered radicals results in oxidative stress that often brings multifarious impairment to cells, including decrease of ATP level in cells, elevation of cytosolic Ca^{2+}, DNA damage, dysfunction of biological function in lipid bilayer among others. These effects will finally lead to several

kinds of chronic diseases, such as inflammation, cancer, reperfusion injury, rheumatoid arthritis, diabetes, neurological and cardiovascular diseases (Koltover, 2010).

In addition to the above stated, the prevalence of cancer is increasing because of the growth and aging of the population, as well as an increasing pervasiveness of established risk factors such as smoking, overweight, physical inactivity, and changing reproductive patterns associated with urbanization and economic development. Currently, several therapies are available, such as surgery, radiotherapy, and chemotherapy and adjuvant therapy, to treat various types of cancer. Nevertheless, most of these therapeutic approaches are linked to severe challenges such as short drug circulation times, localization of the therapy to tumor sites, cytotoxic effects, and drug resistance by tum (de Martel, Georges, Bray, Ferlay, & Clifford, 2020; Wu, Powers, Zhu, & Hannun, 2016).

Natural compounds isolated from medicinal plants are believed to be promising leads in the developing of antimicrobial, antioxidant, and anticancer drugs. Screening medicinal plants and their active constituents for various biological activities, such as antimicrobial, antioxidant, and anticancer activity, has been a significant interest for the last few decades. However, phytochemical mediated synthesized MO NMs from medicinal plants have become a keen interest of researchers because of their minimal size, high surface-to-volume ratio, high solubility, biocompatibility, broad optical properties, and facile surface chemistry. MO NMs also play a critical role in refining the absorption, distribution and compatibility of natural products in treating several infectious, metabolic, and chronic diseases, including cancer (Lucky et al., 2016; J. Zhang et al., 2021).

MO NMs exhibit potent antimicrobial effects against bacteria and fungi at lower doses due to their small size and high surface area-to-volume ratios. They limit oxidative stress by scavenging free radicals, inhibiting oxidation, and activating enzymes of the antioxidant defense system. The unique characteristics of MO NMs make them effective in targeting and penetrating cancerous cells, potentially enhancing the efficacy of cancer treatments while minimizing harm to healthy cells. They can induce DNA damage and gene mutations in abnormal cells. However, CuO, ZnO and MgO NPs are economicaly viable, more bioavialble and biocompatible. Combining these metal oxides to create multiphase MO NMs, show promise for biological applications, surpassing that of monometallic counterparts due to synergistic effects, broad range

of physiochemical properties, and diverse mechanisms of action. This study aims to synthesize CuO, ZnO and MgO based pure and mixed-phase oxide NMs using phytochemicals from *Artemisia abyssinica* plant extracts and investigate their antimicrobial, antioxidant, and cytotoxic effects on drug-resistant pathogens and breast cancer cells.

1.3 Hypothesis

Advances in nanoscience and nanotechnology to modulate materials at the nanoscale level have continued to have a significant impact on the medical field. The surge in the utilization of benign and non-toxic biomolecules to engineer enhanced biocompatible nanomaterials is contributing to the applications of nanomaterials in healthcare, an emerging sub-discipline termed nanomedicine, to a large extent. Among the several nanomaterials that have been produced, MO NMs occupy prime positions owing to their optical, catalytic and biological characteristics. Chemical constituents of various phytochemicals provide powerful synergistic chemical reduction potential, maintain their stability, and enhance medicinal properties during phyto-mediated synthesis of MO NMs. Furthermore, they modify the physicochemical properties (shape, size, and surface chemistry) and the lipophilicity of MO NMs, which is a significant factor in designing a drug (Sukri et al., 2019).

The antibacterial activity mechanisms of CuO, ZnO, and MgO NPs are often based on their ability to induce excess ROS generation as well as the accumulation of nanoparticles in in bacterial cells' outer membrane or cytoplasm, which leads to bacterial cell membrane disintegration, membrane protein damage, and genomic instability, resulting in the death of bacterial cells. ZnO NPs destroy lipids and the proteins of the membrane, which can cause cell death, and they also form Zn^{2+} ions and ROS, including hydrogen peroxide (H_2O_2), which damage the bacterial cell. CuO NPs can produce ROS on the bacterial cells and interact with amine and carboxyl groups, present on the membrane of microbes. MgO NPs also cause lipid peroxidation of the microbial cell envelope by generating ROS and a drop in cytoplasmic pH, which raises membrane potential (B. R. Mohammad, Algburi, & Alzubaidy, 2020; Ogunyemi et al., 2020).

MO NMs possess inherent antioxidant activities by limiting oxidative stress by scavenging free radicals, inhibiting oxidation, and activating enzymes of the antioxidant defense system

(glutathione peroxidase, superoxide dismutase, and catalase). Phytochemical constituents from plant extracts, such as phenolic compounds and ascorbic acids, also play a crucial role in the synergistic antioxidant activity of MO NMs. Their primary action involves the protection of cell constituents against oxidative damage through the scavenging of free radicals, thereby averting their deleterious effects on nucleic acids, proteins, and lipids in cells (B. R. Mohammad et al., 2020).

Each single MO NPs will also have unique features, making them a novel and efficient for anticancer agents. CuO NPs are effective cytotoxic agents in cancer by causing growth inhibition and apoptotic cell death by enhanced ROS generation. Moreover, CuO NPs can be utilized as DNA cleavage agents and potent anticancer therapeutics due to their binding capacity and modifiable surface properties through conjugation with various bio-molecules, including enzymes and proteins. ZnO NPs can be used for selective cytotoxicity towards cancer cells by zinc-dependent protein activity disequilibrium, ROS induction, enhanced permeability, and retention (EPR) effect and electrostatic interaction. MgO NPs are highly interesting because they are extremely stable in very harsh conditions and causes cell membrane damage due to the release of reactive oxygen species (ROS), which affect the essential enzymes in the cell by producing the oxidative distress that results in the destruction of the DNA inside the cell (Sonbol et al., 2021; Tabrez et al., 2022a, 2022b).

Mixing these two or more MOs enhances medicinal efficiency due to the synergism, biocompatibility, and ability to tune the surface chemistry between the two or more MO NMs. The pharmacological activity depends on the nature of metal ions, phytochemical scaffold, physicochemical properties of MO NMs, and specific DNA binding sites. Consequently, this study expected to discover new advanced mono, bi, and tri-metallic oxide therapeutic agents from indigenously existing plant sources and put possible remedies in fighting pathogenic bacteria and fungi, scavenging free radicals which boost chronic diseases like cancer and cause exposure to infectious diseases and strongly fight oxidative stress of the body with enhanced efficacy. The outcome of this study will also be expected to pave the way for the scientific communities to carry on further studies on drug designing and clinical applications by providing novel technology and scaffolds (Cao et al., 2021; Dobrucka, Kaczmarek, Łagiedo, Kielan, & Dlugaszewska, 2019).

1.4 Objective of the Study

1.4.1 General objective

The main objective of this work was to synthesize and characterize mono- (CuO, ZnO and MgO) bi- (CuO-ZnO, CuO-MgO, ZnO-MgO), and tri-metallic (CuO-MgO-ZnO) oxide NMs using leaf extract *Artemisia abyssinica* and to assess their biological activities.

1.4.2 Specific objectives

The specific objectives of the present dissertation were to:

- Prepare leaf extracts of *Artemisia abyssinica* using deionized water, 50 % Ethanol and n-hexane.
- Synthesize *Artemisia abyssinica* leaf extract mediated mono- (CuO, ZnO and MgO), bi- (CuO-ZnO, CuO-MgO, ZnO-MgO), and tri-metallic (CuO-MgO-ZnO) oxide NMs.
- Characterize the synthesized MO NMs using UV-Visible, FTIR, TGA/DTA, XRD, SEM, EDX, and TEM/HRTEM/SAED techniques.
- Study *in vitro* antioxidant activities of the synthesized MO NMs using DPPH and FRAP assays.
- Evaluate *in vitro* antibacterial activity of the synthesized MO NMs against sellected standard gram-negative and gram-positive bacterial strains.
- Examine *in vitro* antifungal activity of the synthesized MO NMs against selected standard fungal strains.
- Assess in *vitro* cytotoxicity of the synthesized MO NMs against breast cancer (MCF-7) and peripheral blood mononuclear cells (PBM) cell lines.
- Assess the *in silico* molecular docking interactions of the synthesized MO NMs against dihydrofolate reductase (PDB: 2w9h) (DHR), *E. coli* DNA gyrase B (PDB ID 6F86) and estrogen receptor alpha (ERα; PDB: 5GS4).

1.5 Significance of the study

Oxidative stress, antimicrobial resistance, and cancer are interrelated and continue to be the burden of all age groups worldwide. Pharmacy, chemistry, and biomedicine researchers have been working to provide wide-spectra nanometal therapeutics. In this study, we have reported

the fabrication of facile, eco-benign, and one-pot synthesis of mono (CuO, ZnO, and MgO), bi (CuO-ZnO, CuO-MgO, and ZnO-MgO), and trimetallic (CuO-MgO-ZnO) NMs using a greener reducing and capping agents from the LEAA and the evaluation of their biological activity. More significantly, mono- (CuO, ZnO, and MgO), bi- (CuO-ZnO, CuO-MgO, and ZnO-MgO), and tri-metallic (CuO-MgO-ZnO) nanoparticles with promising antioxidant, antibacterial, antifungal and anticancer activities are reported. Likewise, molecular interactions of the synthesized MO NMs with selected proteins of bacteria and breast cancer were evaluated and used to sustain the experimental findings. Therefore, the output of this work may give directions to pharmacists, medicinal chemists, biologist, inorganic and material chemists. Moreoevr, from this waork the researchers, industries and soceities could be benifieted.

1.6 Delimitation of the study

In this work, mono- (CuO, ZnO, and MgO), bi- (CuO-ZnO, CuO-MgO, and ZnO-MgO), and tri-metallic (CuO-MgO-ZnO) oxide NMs using the medicinal plant *Artemisia abyssinica* have been synthesized. However, there are more biologically active MO NMs and diverse indigenous medicinal plants of Ethiopia, and hence, it would be viable to include more bioactive metals and medicinal plants. Regarding size, morphology, structure, and compositions characterization of synthesized MO NMs, including more instruments would also be necessary. However, due to time-bound, budget limitations and the need for more resources, this work was limited to the synthesis of listed MO NMs and *their in-vitro* antioxidant, antimicrobial (selected bacterial and fungi strains) and anticancer (breast cancer) applications. Based on the results obtained from the tested activities, it would be an opportunity to include the anticancer activity of other cancer types as well as the biological efficiency of the synthesized MO NMs against other pathogenic species. Because of the unavailability of instruments and reagents, this work was limited to cytotoxicity test of breast cancer, and antimicrobial evaluation of selected pathogenic species.

2. LITTERATURE REVIEW

In the past two decades, the field of nanotechnology has grown exponentially and has made an immense impact on physical, chemical, and biological sciences, due mainly to the specific size-dependent properties exhibited by the resulting nanomaterials (Chavali & Nikolova, 2019; S. Yadav & Maurya, 2021). Amongst the already in use nanomaterials, metallic nanomaterials and metal oxide nanomaterials (MO NMs) have received a great deal of attention due to their unique physco-chemical properties (Chavali & Nikolova, 2019), which provide researchers with novel ways of diagnosing and treating diseases that prior to this were thought to be unapproachable due to the size limitations. Moreover, MO NMs have multiple advantages such as high stability, simple preparation methods, excellent engineering control over aspects ranging from size, shape, porosity, etc. and cellular penetration capability. MO NMs have grown into valuable materials for the drug and health-related industry (S. Yadav & Maurya, 2021). Through the design and development of engineered MO NMs, the limitations imposed by their bulk counterparts could be finally overcome, allowing researchers to make astounding breakthroughs in fields such as specific drug delivery, bio-imaging, and biomedicine (Nikolova & Chavali, 2020).

2.1 Metal Oxide Nanomaterials

There has been an immense extension of MO NMs applications and uses as a result of basic and applied researches from scientists all over the world. MO NMs possess unique physical and chemical properties linked to their nanometer size, shape and morphology. MO NMs have grown into key constituents in biological applications including drug delivery, sensing, and diagnosis (S. Murthy et al., 2020). Beyond these uses, MO NMs have received much attention recently for the applications of antimicrobial, antioxidant and anticancer therapies (Naseem & Durrani, 2021; Suresh, Doss, Praveen Pole, & Devika, 2023). Based on their different electronic structures, MO NMs exhibit metallic, semiconductor and insulator characteristics. The semiconductors are further classified into i-, n- and p-types (Ananya Dey, 2018). Intrinsic semiconductors are i-type semiconductors having properties both of insulators and conductors. The n-types are electron-excess semiconductor oxides with free electrons as charge carriers and will have either excess cations or deficient anions. The p-types are electron-deficit semiconductors with a cation-deficient oxide and this cation vacancy provides the additional electrons for reactivity. These features confer unique chemical and physical properties to MO NMs through which they interact

with biological systems (Mahmood et al., 2022). The different properties of MO NMs are the major contributors to their biological activity.

2.1.1 Properties of MO NMs

Size: Size is one of the key properties of MO NMs. A size range of 10-100 nm is considered good for biological application. The lower scale of this size range is based on the measurement of the sieving coefficient for the glomerular capillary wall, as the threshold for first pass elimination by the kidneys is estimated to be 20 nm in diameter. The upper scale of the size range is based on the result of various studies showing that, up to 100 nm, nanoparticles show better efficacy. However, some research articles show that nanoparticles smaller than 30 nm diameter accumulate more efficiently and penetrate more deeply in tumors than their larger counterparts (Saw et al., 2018). Nano size allows MO NMs to enter inside the cell easily and manipulate the cellular function of the cell, leading to cytotoxicity. Nanoparticles can interact with biological molecules and manipulate various cellular cycles, disrupting cellular homeostasis and inducing apoptosis, due to their small size, which cannot be checked by the plasma membrane (Shang, Nienhaus, & Nienhaus, 2014).

Tissue resident macrophage in the liver and spleen rapidly clears most particles entering into blood vessels. A blood protein called ‘opsonins’ absorbs any foreign particles entering blood and macrophage targets these adsorbed opsonins. Research has suggested that size is related to blood circulation time of particles. The smaller the size, the more the blood circulation time will be occurred. In addition, small size, i.e., less than 20 nm shows increased cytotoxicity by means of increased diffusion through cytoplasm. These ultra-sized particles even enter the nucleus and show toxicity through nucleus aberration (Toy, Hayden, Shoup, Baskaran, & Karathanasis, 2011).

High surface area to volume ratio: Nanoparticles have high surface area to volume ratio due to their small size. This property of nanoparticles allows increased surface contact and increased reactivity as well as other wide ranges of application. Various ligands and targeting molecules can be conjugated in the surface of NMs, which is an essential aspect of NM -mediated drugs (Sapsford et al., 2013).

The surface charge of MO NMs also has an important effect on its fate. High surface charges lead to increased macrophage scavenging activity, resulting in rapid clearance of nanoparticles from blood vessels. Similarly, surface charge should be maintained in such a way that it should have minimal self-self and self-nonself interaction while displaying selectivity towards tumor cells. The ultimate fate of nanoparticles depends upon their interaction with their surrounding environment, which ultimately depends upon the size and surface properties of nanoparticles (Stark, 2011). The other properties of nanoparticles also include chemical composition of high purity, crystallinity, and quantum effects that can affect chemical reactivity.

High dislocation density: In MO NMs, the high surface-to-volume ratio and smaller grain sizes can lead to an increase in dislocation density compared to bulk materials. The presence of dislocations can affect the surface properties of nanomaterials, such as their roughness and reactivity, which in turn can impact their biological activity (Thakur & Bharti, 2023).

Solubility: MO NMs have appreciable solubility with both organic and inorganic solvents. Particularly they are highly soluble in aqueous media when compared with bulk solutes due to their enhanced surface area to volume ratio. Their small size also have significant contribution to interaction with solvent molecules and their solubility can be further increased by proper surface modification (Ceylan, Jastrzembski, & Shah, 2006).

Interaction of NMs with Biological Components: Understanding the interaction of nanoparticles with the cell surface is important in understanding the mechanism of their action and manipulating it for medical and biological applications. The nano-bio is a dynamic physicochemical interaction between the nanomaterial surface and the surface of biological components, which deals with the kinetic and thermodynamic exchanges between the interfaces (Stark, 2011). It includes the interaction between the nanoparticles' surfaces, the solid-liquid interface and the solid-liquid interface contact zone with the biological membrane.

Besides the nano-bio interface, another, meaningful, significant interaction that defines the role of MO NMs s is the interaction between them. Various forces, such as van der Waals forces, electrostatic, solvation, solvophobic, and depletion, act on these interactions, which affect the rate of agglomeration of nanoparticles in media. Van der Waals and depletion forces act as attractive forces, whereas electrostatic force is repulsive. Van der Waals forces arise from

changes in the dipole moment of electrons, which induce a dipole moment in the adjacent atoms. It arises from the quantum mechanical motion of electrons. These different forces play an important role in the adhesive interaction of nanoparticles on the cell surface and their passive uptake inside the cell (Ceylan et al., 2006). The optimizable surface area of MO NMs favors this adhesive interaction to the cell surface according to the cell surface receptor, and the comparative size of MO NMs to that of ligands/ biomolecules, leading to adhesive interaction and passive uptake inside the cell, boycotting the phagocytic process (Saw et al., 2018). With this passive uptake, nanoparticles can directly interact with cytoplasm proteins and cell organelles, increasing cytotoxicity. They can localize anywhere inside the cell, including the outer membrane, cytoplasm, lipid vesicles, mitochondria, nuclear membrane, nucleus, DNA, etc., damaging these cell organelles and ultimately leading to cell death (De La Cruz et al., 2018).

Selective targeting nature: MO NMs have an inherent nature of showing selective cytotoxicity against cancerous cells in vitro conditions compared with conventional anticancer agents. Due to their selective targeting nature, MO NMs can specifically release a therapeutic payload onto the target, reducing the side effects on normal cells (Sutradhar & Amin, 2014).

Enhanced cytotoxicity: While extracellular MO NMs show biocompatibility, elevated levels of administered intracellular MO NMs show enhanced cytotoxicity through metal-mediated protein activity disequilibrium and oxidative stress (De La Cruz et al., 2018). MO NMs have the unique ability to induce oxidative stress in cancer cells, which is e one of the mechanisms of their cytotoxicity towards cancer cells. This property is due to the semiconductor nature of MO NMs. Metal oxide nanoparticles induce ROS generation, leading to oxidative stress and eventually cell death when the anti-oxidative capacity of the cell is exceeded(Wan et al., 2012).

Owing to the listed unique properties, MO NMs have received a great deal of attention of researchers nowadays. With multiple advantages such as high stability, simple preparation methods, excellent engineering control over aspects ranging from size, shape, porosity, etc. and cellular penetration capability, MO NMs have grown into valuable materials for biological applications. The constraints imposed by their bulk counterparts could finally be overcome through the design and development of engineered MO NMs, allowing researchers to make

astounding breakthroughs in fields such as specific drug delivery, bio-imaging, biomolecule sensors, etc. (S. Yadav & Maurya, 2021). Moreover, due to their reduced size, MO NMs can interact more in-depth with various cellular structures compared to their bulk counterparts, and, more importantly, they do not cause systemic toxicity due to their highly improved biocompatibility (Waghchaure & Adole, 2023). Currently, various types of MO NMs are used in clinical practice as antibacterial and wound healing dressings, biosensors and anticancer and antidiabetic agents (Velsankar et al., 2022; S. Yadav & Maurya, 2021).

2.1.2 Synthesis methods of MO NMs

The synthesis approach of MO NMs is grouped into three categories, namely the (1) physical methods (2) chemical methods, and (3) biological methods (Nyabadza et al., 2023). On the other hand, the synthetic methods are grouped under top-down and bottom-up approaches (Figure 2). All the physical methods are grouped under the top-down approach. Likewise, the biological and chemical methods are grouped under the bottom-up approaches (Gebre, 2023; Nyabadza et al., 2023). However, some physical methods consume high energy, temperature, and pressure and require expensive apparatus with tedious experiments to bring the atoms or molecules together which hinders the complete synthesis of the MO NMs. The low production rate of MO NMs is another limitation of the physical methods. On the other hand, the chemical approach is simple, economical for large-scale production, and effective for the synthesis of materials. However, it uses both inorganic and organic reactive reducing agents such as sodium borohydride, hydrazine, *N*,*N*-dimethylformamide (DMF), polymers, hydrazine, etc., that can cause environmental damage due to the harmful by-products and may also adsorb on the surface of the NMs thereby limiting their clinical or biological applications (Nikam, Prasad, & Kulkarni, 2018). Flammable organic solvents are also used in the chemical method. Among the chemical methods, coprecipitation and hydrothermal methods are relatively, straightforward, low-cost, and effective for preparing MO NMs. Researchers use a biological method to synthesize MO NMs to alleviate the above disadvantages.

The biological (green) synthesis method is beneficial over chemical and physical methods because it is safe, modest, economical, reproducible, and often results in more stable materials. In the natural environment, plants and microorganisms reduce metal ions to MO NMs with their bioactive compounds to mitigate the toxicity of the metal ions and use them as a nutrient for their

growth. Therefore, several researchers endeavored to develop unpolluted, biocompatible, non-toxic, and eco-friendly techniques for the synthesizing of metal and metal oxide NMs (Sonbol et al., 2021). The biological synthesis of nanoparticles has being carried out using different biomaterials such as bacteria, fungi and yeast, microalgae, arthropods and their exudates, enzymes and plant biomass/extract (Ghaffar et al., 2023). Plant-mediated synthesis of MO NMs is better than microbes-mediated as the process doesn't include any synthetic protocols and toxic chemicals as well as has high reaction rate since need to grow microbes is eliminated (J. O. Adeyemi, Onwudiwe, & Oyedeji, 2022). Moreover, plant-mediated synthesis approach is a simple, fast, and forward method, whereas the use of microorganisms requires further isolation and culture, which results in a low yield of MO NMs synthesis. Furthermore, phyto-mediated synthesized MO NMs are biocompatible and bioavailable hence safer to use in biological applications (Akbar et al., 2020; Alhujaily et al., 2022).

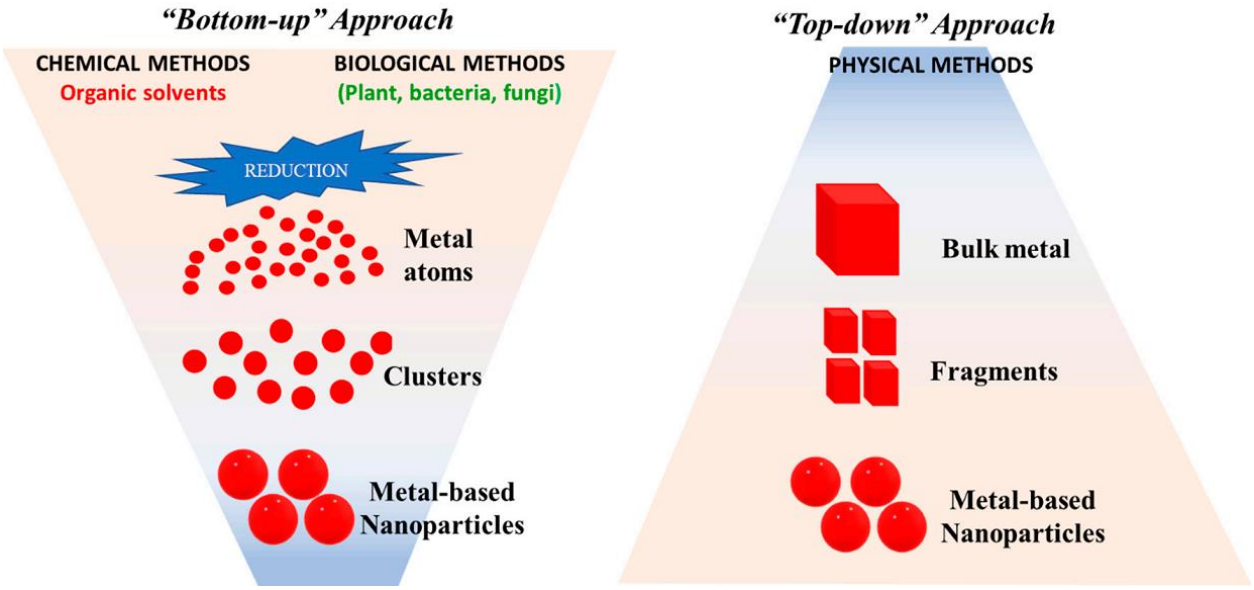

Figure 2. Botom-up and top-down methods used for the synthesis of MO NMs (Hasan et al., 2018).

2.1.2 1 Phytochemical mediated synthesis of MO NMs

Different terms such as phyto-mediated synthesis, phytogenic synthesis, biogenic synthesis, biological synthesis, green synthesis, and biosynthesis are used for the synthesis of MO NMs from plant sources. Phytochemical mediated synthesis is collectively used for the fabrication of

MO NMs using plants phytochemicals as reducing and stabilizing agents (Alhujaily et al., 2022). Phytochemicals present in plant extracts, diverse primary and secondary metabolites such as terpenoids, alkaloids, flavonoids, polyphenols, monosaccharaides, polysaccharides, proteins, and organic acids are responsible for the reduction of metal ions to nanostructure form (Abdelghany et al., 2023). The phytochemicals are used both as reducing and capping agents in biosynthesis as presented in Figure 3. Functional groups of the plant-derived biomolecules, mostly polar groups such as amine, hydroxyl, carboxylic acids, thiol, and carbonyl groups, react with the metal ions and are reduced via electrons that flow from the extract to the metal in order to activate nucleation. All plant parts, including leaves, fruit, stems, bark, roots, flowers, buds, and latex, are used in the biosynthesis of NPs (Alnehia et al., 2023). The plant extract phytochemicals are used as donors of electrons to the metal ion to convert into MO NMs. Flavonoids, amine groups of protein, hydroxyl groups of polyphenols, carboxylic groups, polysaccharides, and carbonyl groups, etc. possess a potential chelating site to form stable metal cations during synthesis MO NMs (Küünal, Rauwel, & Rauwel, 2018).

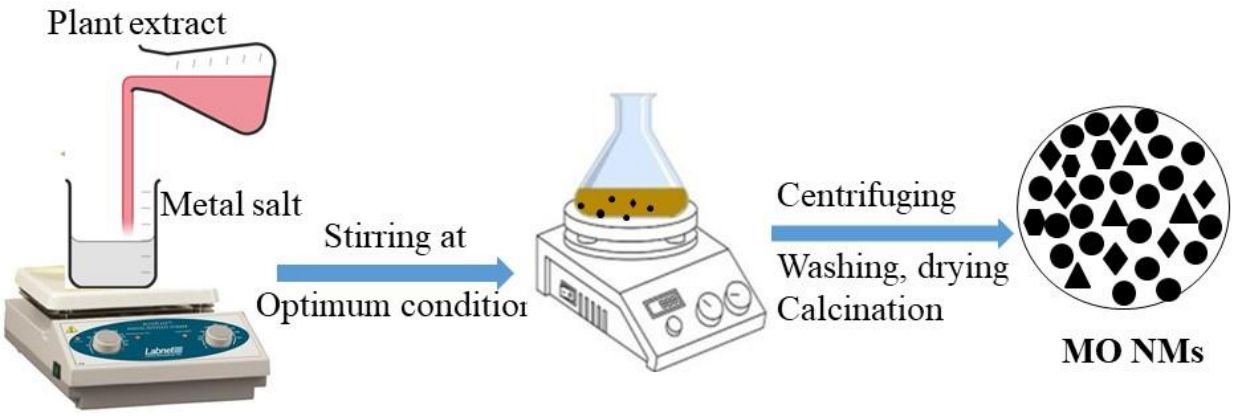

Figure 3. The schemes of plant-mediated synthesis of MO NMs (Küünal et al., 2018).

MO NMs such as CuO, ZnO and MgO NPs are among the most investigated ones using phyto-mediated synthesis techniques for biological applications. Due to its semiconducting nature, CuO NPs has revealed unique electrical, optical, and magnetic features and are utilized for various biological applications (Joshi, Sharma, Bachheti, Husen, & Mishra, 2019). It exists in two stoichiometry of oxides, namely cuprous oxide (Cu_2O) which has a cubic structure and the other form, cupric oxide (CuO), which has a monoclinic structure (Joshi et al., 2019).

Various phytochemicals from plants are used for the synthesis of CuO NPs as revealed in Table 1. Using aqueous leaf extract of the plant *Artemisia deserti* stable CuO NPs with average particle size of 7.2 nm was synthesized and used for anticancer activity (Shahriary, Tafvizi, Khodarahmi, & Shaabanzadeh, 2022). The aqueous extract contains metabolites such as alkaloids, phenols, saponins, flavonoids, protein, amino acids, and carbohydrates, which are responsible for the reduction of copper salt to CuO NPs. Similarly, Renata Dobrucka reported the synthesis of ultrafine CuO NPs with average particle size 10 ± 5 nm using extract of *Galeopsidis herba* for antioxidant and catalytic activities (Dobrucka, 2018). The presence of quercetin, kaempferol, ellagic acid, cyanidin-3-glucoside, and cyanidin-3-rutinoside are responsible phytochemicals for the fabrication of the NPs. In another study, Vinothkanna *et al*. used an aqueous *Rubia cordifolia* bark extract for the synthesis of CuO NPs. The bark extract of the plant were rich in phenolic compounds used as reducing and stabilizing agents in biosynthesis (Vinothkanna, Mathivanan, Ananth, Ma, & Sekar, 2023). *Hylotelephium telephium* flower extract-mediated synthesized CuO NPs were reported by Karunakaran *et al*. (Karunakaran, Jagathambal, Kumar, & Kolesnikov, 2020). The phytochemicals present in the flower extract were used as an internal reductant for the biogenic synthesis of CuO NPs. (Thandapani et al., 2023) reported the *Spinacia oleracea* leaf extract assisted synthesized spherical shape CuO NPs for biological application. The carboxyl functional groups of proteins, phenolic compounds, flavonoids, vitamins, alkaloids, terpenes, tannins, and saponin were responsible for the bioreduction of copper nitrate into CuO NPs. Fine spherical shaped nanoparticles with the size of 5-20 nm was reported using the leaf extract of *Aloe-vera* (S. Sharma & Kumar, 2021). Successful synthesis of CuO NPs using *Psidium guajava* leaf extract (Sathiyavimal et al., 2021), *Salacia reticulata* leaves (Sabeena et al., 2022), *Diantum lunulatum* leaves (Sarkar et al., 2020), *Spirulina platensis* (Alsamhary, Al-Enazi, Alhomaidi, & Alwakeel, 2022), and *Annona muricata* (Mahmood et al., 2022) mediated synthesis of CuO NPs were also reported.

Plant mediated synthesis of CuO NPs using various phytochemicals are presented as reported in Table 1.

Table 1. Phyto-mediated synthesized CuO NPs with their proposed responsible phytochemicals.

Plant used	Responsible phytochemicals	Precursor used	Particle size	Ref.
Artemisia deserti, leaf	Polyphenols, alkaloids, flavonoids, terpenoids	Copper sulphate	7.2 nm	(Shahriary et al., 2022)
Gloriosa superba, leaf extract	Alkaloids, flavonoids, phenols	Copper nitrate	5-10 nm	(Dobrucka, 2018)
Rubia cordifolia, bark	Alkaloids, tannins, terpenoids, flavonoids	Copper sulphate		(Vinothkanna et al., 2023)
Hylotelephium telephium, flower	Alkaloids, glycosides, steroids, phenolics, sesquiterpenoid, aliphatic compounds and polysaccharides	Copper nitrate	6-8 nm	(Karunakaran et al., 2020)
Spinacia oleracea leaf extract	Alkaloids, tannins, flavonoids, phytosterols, phenols, terpenes and carbohydrates	Copper nitrate	48 nm	(Thandapani et al., 2023)
Aloe-vera leaf extract	Phenols, terpenoids, proteins	Copper acetate	5-20 nm	(S. Sharma & Kumar, 2021).
Psidium guajava	Flavonoids, alkaloids, phenols, terpenoids and essential oils	Copper Sulfate	40-100 nm	(Sathiyavimal et al., 2021)
Salacia reticulata leaves	Phenols, heterocyclic compounds and flavonoids	Copper nitrate	13 nm	(Sabeena et al., 2022)
Adiantum lunulatum	Aromatic and phenolic compounds	Copper Sulfate	2-20 nm	(Sarkar et al., 2020)
Spirulina platensis, leaf	Phenols, terpenes and carbohydrates	Copper nitrate	20-30 nm	(Alsamhary et al., 2022)
Annona muricata	Flavonoids, alkaloids, polyphenols	Copper nitrate	10-25 nm	(Mahmood et al., 2022)

The phytochemical mediated synthesis of ZnO NPs using *Passiflora caerulea* leave leaf extract for antimicrobial application were reported (Alnehia et al., 2023). The leaf extract is rich in organic acids, tannin, amides and other biomolecules which are highly responsible for antioxidant activity are acting as reducing agents in the conversion of zinc ions into ZnO NPs. Further, the amide groups are acting as a capping agent used to prevent agglomeration. Shalaby *et al*. reported the successful synthesis of hexagonal wurtizite ZnO NPs with size range of 57 nm

use *Moringa oleifera* extracts for biological applications (Shalaby et al., 2022). The *Moringa oleifera* extract contains phytochemicals such as phenolic acids, flavonoids, and vitamin-based compounds which are responsible for the reduction and stabilizations of ZnO NPs. *Azadirachta indica* (Neem) leaf extract mediated-synthesis of spherical ZnO NPs with particle size 20-40 nm was reported by Singh *et al*. (Amit Singh & Kaushik, 2019). A large number of hydroxy and carbonyl constituents are responsible for the reduction and stabilization of the ZnO NPs. Muthuvel *et al*. (Muthuvel, Jothibas, & Manoharan, 2020) also reported effective synthesis of ZnO NPs *using Solanum nigrum* leaf extract. The presence of the phytochemical functional groups on the surface of the NPs acts as a surfactant and stabilizes to improve the activity of the plant-mediated NPs. The *Anchusa italic* flower extract has been used for the synthesis of ZnO NPs at 100 °C and 200 °C annealing temperatures. A stable NPs in the range of 8-14 nm average size, and hexagonal shape was obtained (Azizi et al., 2016). Moreover, bioiosynthesis of zinc oxide nanoparticles have been reported from different plants such as *Aloe vera* peel extract (Chaudhary, Kumar, Kumar, & Salar, 2019), *Acalypha indica*, leave extract (S. Karthik et al., 2017), *Hagenia abyssinica*, leaf extract (Zewde & Geremew, 2022), *Cnidoscolus aconitifolius*, leaf extract (Dangana, George, & Agboola, 2023), *Solanum rantonnetii*, leaves (Salem & Awwad, 2022), and *Andrographis alata* (Dappula et al., 2023).

Plant mediated synthesis of ZnO NPs using various phytochemicals are presented as reported in Table 2.

Table 2. Phytochemical mediated synthesized ZnO NPs with their proposed responsible phytochemicals.

Plant used	Responsible phytochemicals	Precursor used	Particle size	Ref.
Passiflora caerulea, leaf	Terpenoids, flavonoids, alkaloids	Zinc nitrate	30-50 nm	(Alnehia et al., 2023)
Moringa oleifera, leaf	Flavonoids, alkaloids, phenols	Zinc nitrate	57 nm	(Shalaby et al., 2022)
Azadirachta indica (Neem), leaf	Flavones, organic acids, ketones, amides, aldehydes	Zinc acetate	20-40 nm	(Amit Singh & Kaushik, 2019)
Solanum	Glycoalkaloids,	Zinc	20-30 nm	(Muthuvel et al., 2020)

nigrum, leave	glycoproteins, polysaccharides	acetate		
Anchusa italic, flower	Alkaloids, flavonoids tannins, saponins, oil, and triterpenes	Zinc nitrate	8-14 nm	(Azizi et al., 2016)
Aloe vera, peel extract	Phenolic compounds, terpenoids, proteins	Zinc sulphate	50 nm	(Chaudhary et al., 2019)
Acalypha indica, leave	Chitosan		20 nm	(S. Karthik et al., 2017)
Hagenia abyssinica, leaf extract	Phenolic compounds, saponins, alkaloids, flavonoids	Zinc acetate	27 nm	(Zewde & Geremew, 2022)
Cnidoscolus aconitifolius, leaf	Sugars, proteins, essential amino acids, fats	Zinc acetate	100 nm	(Dangana et al., 2023)
Solanum rantonnetii, leaves	Flavonoids polyphenols, tannins, alkaloids	Zinc acetate	5-12 nm	(Salem & Awwad, 2022)
Andrographis alata	Phenolic compounds	Zinc acetate	35–53 nm	(Dappula et al., 2023)

Phytochemical mediated synthesis of MgO NPs by using Moringa oleifera leaf extract was introduced by Vijayakumar *et al*. (Sekar Vijayakumar et al., 2023). Moreover, Amor and his co-workers investigated the antibacterial properties of NPs and the synthesis of MgO nanoparticles using *Pimelia payraudi latreille* extract without the intervention of chemical catalysts (Amor et al., 2023). It was declared that NPs significantly inhibited bacterial growth, biofilm formation and motility. In another study, Poonguzhali and co-workers used lemon juice to synthesis MgO nanostructures, as citric acid in lemon juice can act as a reducing agent (Cheviron, Gouanvé, & Espuche, 2014). In their study, MgO NPs were synthesized for use in gas sensing by a combustion technique using lemon juice as a natural source of citric acid. The exothermic reaction between lemon juice and metal nitrates and the very rapid self-combustion nature were influenced by the acidic lemon juice, which resulted in the production of NPs. The results showed that lemon juice as a natural fuel plays an important role in the production of MgO nanorods with a smaller size. In another intriguing study, the effect of MgO NPs synthesized by the green method using *Saussurea costus* plant roots on breast cancer was investigated (Amina et

al., 2020). Their findings show that the synthesized NPs have high toxicity on MCF-7 breast cancer cells and cause cell death. Moreover, *Pterocarpus marsupium* heartwood extract was used to synthesis MgO NPs due to its richness in polyphenolic compounds and flavonoids; additionally, its antibacterial effects against *Escherichia coli* and *Staphylococcus aureus* were evaluated (Ammulu et al., 2021). Green tea (*Camellia sinensis*) extracts contain many polyphenols which can act as reducing, chelating and capping agents for synthesis of MgO nanoparticles is reported. Membranes containing reactive nanoparticles were immobilized on PVDF membrane. Reactivity of nanoparticles in membrane was observed even after three months of repeated usage (S. A. Kumar et al., 2022). Moreover, *Limonia acidissima* fruits (Sakthivel, Nivetha, & Prabha, 2022), *Prosopis farcta* leaf extract (Abdullah & Mohammed, 2021), *Emblica officinalis*, fruits extract (Sakthivel et al., 2022), *Trachyspermum ammi* leaf extract (Dabhane et al., 2022), *Hagenia abyssinica*, flower extract (Hirphaye, Bonka, Tura, & Fanta, 2023), *Allium cepa*, leaf extract (Periakaruppan et al., 2023), *Citrus aurantium* fruit peels (Ringwal, Bartwal, & Sati, 2022) mediated-fabrication of MgO NPs were also reported. Plant mediated synthesis of MgO NPs using various phytochemicals are presented as reported in Table 3.

Table 3. Phytochemical mediated synthesized MgO NPs with their proposed responsible phytochemicals

Plant used	Responsible phytochemicals	Precursor used	Particle size	Ref.
Moringa oleifera, leaf	Flavonoids, alkaloids, phenols	Magnesium nitrate	17 nm	(Sekar Vijayakumar et al., 2023)
Pimelia payraudi latreille	Polyphenols, saponins, alkaloids	Magnesium chloride	20-70 nm	(Amor et al., 2023)
Lemon Juice	Citric acid, alkaloids polyphenols	Magnesium sulphate	15-30	(Cheviron et al., 2014)
Limonia acidissima fruits	Flavonoids, alkaloids, polyphenols	Magnesium nitrate	92.8 nm	(Sakthivel et al., 2022)
Phyllanthus emblica, fruits extract	Polyphenols, terpenes, carbohydrates	Magnesium nitrate	27 nm	(Ananda et al., 2022)
Trachyspermum ammi leaf extract	Phenols, terpenes and carbohydrates	Magnesium chloride	10-11 nm	(Dabhane et al., 2022)
Hagenia	Phenolic compounds,	Magnesium	12.8 nm	(Hirphaye et al., 2023)

abyssinica, flower extract	saponins, alkaloids, flavonoids	nitrate		
Allium cepa, leaf extract	Flavonoids, alkaloids, polyphenols	Magnesium nitrate	12 nm	(Periakaruppan et al., 2023)
Citrus aurantium fruit peels	Flavones, organic acids, amides	Magnesium nitrate	50-60 nm	(Ringwal et al., 2022)
Saussurea costus plant roots	Polyphenols, alkaloids,terpenes,	Magnesium nitrate	30 nm	(Amina et al., 2020)
Pterocarpus marsupium heartwood extract	polyphenolic compounds and flavonoids	Magnesium nitrate	10-20 nm	(Ammulu et al., 2021)
Camellia sinensis (green tea) leaf extracts	Polyphenols	Magnesium sulphate	35 nm	(S. A. Kumar et al., 2022)
Prosopis farcta leaf extract	polyphenolic compounds	Magnesium nitrate	30-50 nm	(Abdullah & Mohammed, 2021)
Allium cepa, leaf extract	Flavonoids, alkaloids, polyphenols	Magnesium sulphate	20 nm	(Periakaruppan et al., 2023)

2.1.2.2 Mechanism of acttion of plant extracts for synthesis of MO NMs

For nanoparticle synthesis mediated by plant extract, the extract is mixed with metal precursor solutions at different reaction conditions (El Shafey, 2020). The parameters determining the conditions of the plant extract (such as types of phytochemicals, phytochemical concentration, metal salt concentration, pH, and temperature) are admitted to control the rate of nanoparticle formation as well as their yield and stability (S. Ali et al., 2020). The phytochemicals present in plant extracts have uncanny potential to reduce metal ions in a much shorter time as compared to fungi and bacteria, which demands the longer incubation time. Therefore, plant extracts are considered to be an excellent and benign source for metal as well as metal oxide nanoparticle synthesis. Additionally, plant extract play a dual role by acting as both reducing and stabilizing agents in nanoparticles synthesis process to facilitate nanoparticles synthesis. The composition of the plant extract is also an important factor in nanoparticle synthesis, for example different plants comprise varying concentration levels of phytochemicals. The main phytochemicals present in plants are flavones, terpenoids, sugars, ketones, aldehydes, carboxylic acids, and amides, which are responsible for biopreparations of MO NMs (Figure 4) (El Shafey, 2020).

Flavonoids contain various functional groups, which have an enhanced ability to reduce metal ions. The reactive hydrogen atom is released due to tautomeric transformations in flavonoids by which enol-form is converted into the keto-form. This process is realized by the reduction of metal ions into metal nanoparticles. In sweet basil (*Ocimum basilicum*) extracts, enol- to keto transformation is the key factor in the synthesis of biogenic silver nanoparticles (Ahmad et al., 2010). Sugars such as glucose and fructose exist in plant extracts can also be responsible for the formation of MO NMs. Note that glucose was capable of participating in the formation of MO NMs with different size and shapes, whereas fructose-mediated gold and silver nanoparticles are monodisperse in nature (Ovais et al., 2018).

An FTIR analysis of green synthesized nanoparticles via plant extracts confirmed that nascent nanoparticles were repeatedly found to be associated with proteins. Different researchers observed that amino acids (viz cysteine, arginine, lysine, and methionine are proficient in binding with silver ions. Some studies also showing that all of the 20 natural α-amino acids to establish their efficient potential behavior towards the reduction of metal ions (Marslin et al., 2018). Plant extracts are made up of carbohydrates and proteins biomolecules, which act as a reducing agent to promote the formation of metallic nanoparticles. Also, the proteins with functionalized amino groups ($–NH_2$) available in plant extracts can actively participate in the reduction of metal ions (Ovais et al., 2018). The main types of plant metabolites involved in the synthesis of MO NMs are presented in Figure 4.

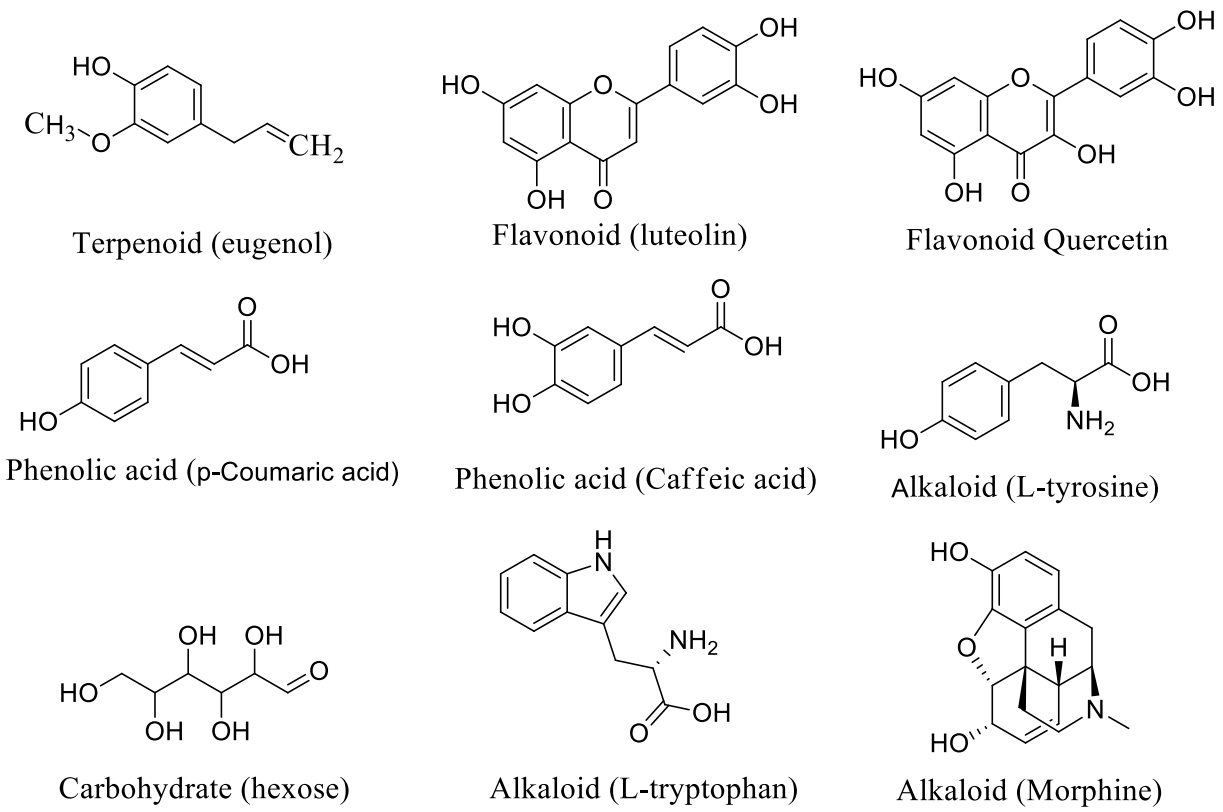

Figure 4. The main types of plant metabolites involved in the synthesis of MO NMs (Makarov et al., 2014).

The functional groups (such as –O-H, –C–O–C–, –C–O–, –C=C–, and –C=O) present in phytochemicals such as flavones, alkaloids, phenols, and anthracenes can help to generate metallic nanoparticles (Gebre, 2023; Marslin et al., 2018). According to Huang et al. (J. Huang et al., 2007), the absorption peaks of FTIR spectra at (1) 1042 and 1077, (2) 1606 and 1622, and (3) 1700-1800 cm^{-1} imply the stretching of (1) –C–O–C– or –C–O–, (2) –C=C– and (3) –C=O, respectively. Based on FTIR analysis, they confirmed that functional groups like –C–O–C–, –C–O–, –C=C–, and –C=O, are the capping ligands of the nanoparticles (J. Huang et al., 2007). The main role of the capping ligands is to stabilize the nanoparticles to prevent further growth and agglomeration. The process of nanoparticle formation by plant extract is depicted in Figure 5.

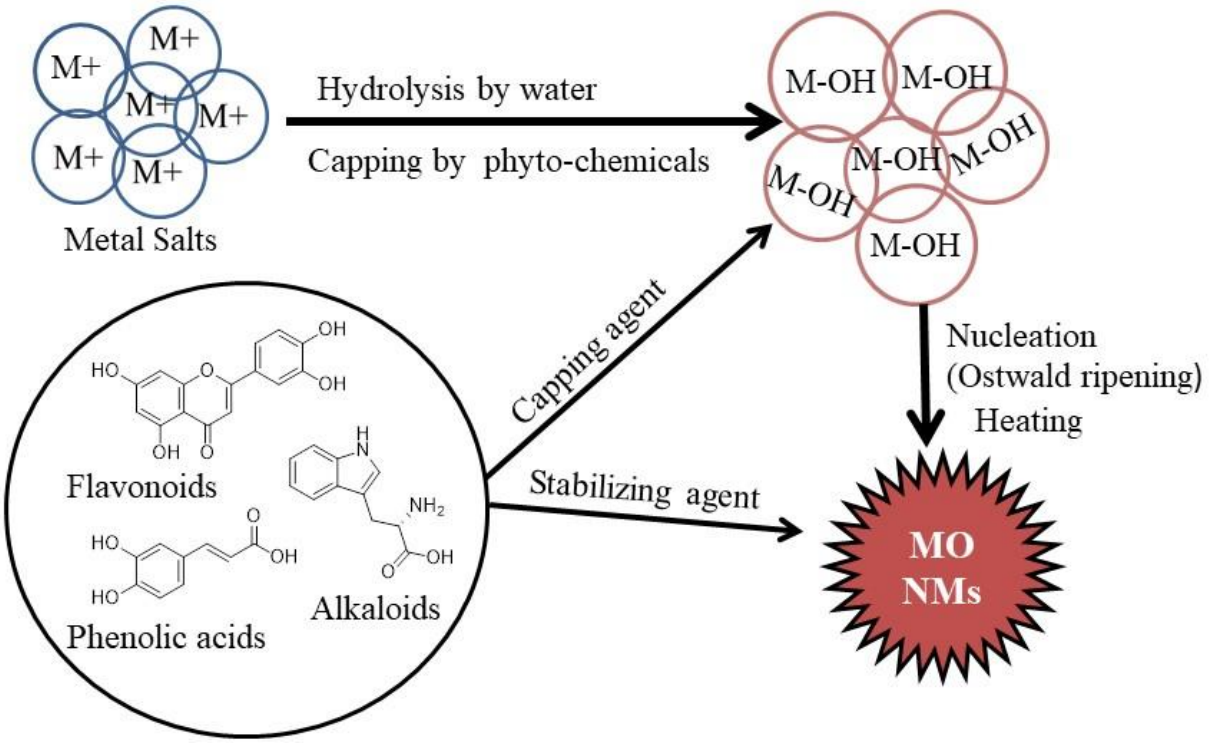

Figure 5. Mechanism of Phyto-mediated synthesis of MO NMs (Shah, Fawcett, Sharma, Tripathy, & Poinern, 2015).

It has already been well established that numerous plant phytochemicals including alkaloids, terpenoids, phenolic acids, sugars, polyphenols, and proteins play a significant role in the bioreduction of metal salt into metallic nanoparticles. For instance, Shanakr *et al*. (Shankar, Ahmad, Pasricha, & Sastry, 2003) confirmed that the terpenoids present in geranium leaf extract actively take part in the conversion of silver ions into nanoparticles. Eugenol is a main terpenoid component of *Cinnamomum zeylanisum* (cinnamon) extracts, and it plays a crucial role for the bioreduction of $HAuCl_4$ and $AgNO_3$ metal salts into their respective metal nanoparticles. FTIR data showed that –OH groups originating from eugenol disappear during the formation of Au and Ag nanoparticles. After the formation of Au nanoparticles, carbonyl, alkenes, and chloride functional groups appeared. Several other groups [e.g., R–CH and –OH (aqueous)] were also found both before and after the production of Au nanoparticles (A. K. Singh, Talat, Singh, & Srivastava, 2010). Nonetheless, the exact fundamental mechanism for MO NMs preparation via plant extracts is still not fully tacit. In general, there are three phases of metallic nanoparticle synthesis from plant extracts: (1) the activation phase (bioreduction of metal ions/salts and

nucleation process of the reduced metal ions), (2) the growth phase (spontaneous combination of tiny particles with greater ones) via a process acknowledged as Ostwald ripening, and (3) the last one is termination phase (defining the final shape of the nanoparticles) (Shah et al., 2015).

2.2. Characterizations of MO NMs

MO NMs are characteristically categorized by their size, surface area, and shape and dispersity nature. The common procedures implemented in their characterization are UV-visible spectrophotometry, Fourier transform infrared spectroscopy (FTIR), scanning electron microscopy (SEM), transmission electron microscopy (TEM), atomic force microscopy (AFM), X-ray diffraction (XRD), dynamic light scattering (DLS) and energy dispersive X-ray spectroscopy (EDX). The development of various metallic nanoparticles from their precursor metal salts gives representative peaks at different absorptions that can be examined using UV-visible spectrophotometry. For instance, noble metallic nanoparticles like Ag and Au absorb strongly within the visible region producing λmax of 400-450 nm and 500-560 nm, respectively, as a function of surface plasmon resonance (SPR) phenomenon occurring in metallic nanoparticles (Vijayaraghavan & Ashokkumar, 2017).

SPR originates from the resonant combined oscillations of the conduction electrons along the transversal pathway of the electromagnetic field. SPR band intensity and band width are predisposed by the dielectric constant of the medium, particle shape, and temperature. Hence, UV-vis spectrophotometry examination is typically the first practice in characterization of metallic nanoparticles to monitor the formation of nanoparticles. On making contact with the metal salt, the color of biomolecular extract suspension employed for the synthesis changes and this is due to excitation of surface Plasmon vibrations in the MO NMs. The arrays of color that developed depend on number of factors that include nature of the bioreductant, the mixing ratio and the particle size. Investigating the suspension using UV-vis spectrophotometry typically reveals a band having a determinable adsorption peak and from which the formation of respective metal can be confirmed. A progressive rise in the characteristic peak with increased reaction time and ratio of concentration of biomolecular extract with respect to the metallic salt solution clearly indicates the formation of nanoparticles (Shukla & Iravani, 2017).

Fourier transform infrared (FTIR) spectroscopy is a surface chemical analytical method, which evaluates the infrared intensity against wave-number or wavelength of light. The nature of the functional groups and their participation through the bioreduction process can be roughly estimated using the FTIR spectroscopy. Elemental arrangement of metal nanoparticles can be recognized using energy dispersive X-ray spectroscopy (EDX). Each element has a distinctive atomic structure that produce a unique set of peaks on its spectrum which also leads to the characterization of the elements (Shukla & Iravani, 2017). The identification of the biomolecules involved in bioreduction is vital to develop new pathways in synthesis of MO NMs. Generally, FTIR spectrum of crude extract and that of synthesized nanoparticles will be compared to collect facts about X-ray diffraction (XRD) system is used to understand the structural information about crystalline nature of MO NMs. The X-rays can penetrate deep into the materials and give relevant information about the structure of the bulk. If the nanoparticles are fashioned in an amorphous structure, there will be no diffraction peak detected (Vijayaraghavan & Ashokkumar, 2017). The widening of the peaks in XRD endorses the formation of particles in nano size. The sizes of MO NMs can thus be estimated using the Debye Scherer approach (Shukla & Iravani, 2017).

Scanning electron microscopy (SEM) affords information about the structure and morphology of the MO NMs. Additionally, electron microscopic technique is used for the determination of mean size of nanoparticles using statistical software. Some researchers also employed atomic force microscopy (AFM) to unravel the structure of MO NMs (Ruggeri, Šneideris, Vendruscolo, & Knowles, 2019). TEM technique has superior resolution and magnification than SEM and the images give more precise information concerning shape, size and crystallography of the MO NMs. Another benefit of TEM investigation over SEM images relates to the ability of TEM to differentiate between crystalline and amorphous structures with the aid of selected area electron diffraction technique (SAED) (Altenhoff, Aßmann, Teige, Huber, & Will, 2020).

2.3 Biological Applications of Phytochemical Mediated MO NMs

Different factors can affect biological efficacies (interactions with biofluids, cells, biomolecule, etc.) of MO NMs, such as size, aggregation state, morphology and stability. For example, the physical and chemical properties of MO NMs that have an impact on the interactions with cells are the (i) MO NMs morphology (shape, size), which controls aspects such as overcoming cell

barrier, internalization and toxicity; (ii) NPs surface area and surface energy, as this influences the number of active sites and can control reactivity (J. O. Adeyemi et al., 2022; Akbar et al., 2020); (iii) crystal structure, which together with size, defects, media composition and aggregation, influences the dissolution of the metal ions, which can cause toxic effects (Chouke et al., 2022); (iv) surface chemistry, such as surface charge (zero-point of charge, acidity constant), dispersibility and aggregation, influence surface cascade reactions consequential for healing and subsequent bio integration (Gebre, 2023); (v) chemical composition of the MO NMs, as some nanoparticles can generate hydroxide or peroxide radicals and, furthermore, can (photo) release metal ions that may either facilitate favorable/unfavorable localized '-cidal' effects (Kannan et al., 2020). Phyto-fabricated MO NMs were designed to produce MO NMs with controlled morphology, size and stability and hence they have transformed physo-chemical properties for biological applications.

2.3.1 Antimicrobial Activity

Drug/antibiotic resistance is an increasing phenomenon and there is necessity for the development of new and more effectual drugs against microbes. Resistance in bacteria can be attributed to horizontal gene transfer of the antibiotic resistance genes, adjustment in the antibiotic target, mutational changes in the biofilm formation and efflux pumps (Zayed, Mahfoze, El-kousy, & Al-Ashkar, 2020). Antibiotic resistance patterns of microorganisms have led to the dread about the emergence and re-emergence of multidrug resistant (MDR) parasites and pathogens. Therefore, modification in antimicrobial compounds to augment their latent bactericidal prospective is a main area of research in modern era and nanotechnology provides an excellent platform to transform and develop the important properties of metal in the form of nanoparticles having potential applications as cell labelers, biomarkers, contrast agents for bioimaging, antimicrobial agents, and drug delivery schemes (Ghahremani, Sharifi, & Haghi Ghahremanloi Olia, 2020).

The unique physicochemical characteristics of nanomaterial have positioned them to exercise multiple actions against multidrug resistant bacteria for broader applications. It was predicted that the particles rendered the drug-resistant isolates vulnerable by a series of attacks; comprising deformation of structural integrity of bacterial cell wall to stimulate entry of particles, in addition to the enhancement of the entry of antibiotic via the carrier action of the particles (Zayed et al.,

2020). There are two core manner of nanoparticles action on microbial cells. First, it directly damages the cell membrane and components. Second, it induced the release of reactive oxygen species (ROS) that destroys the molecular machinery of the cell by oxidative damage. ROS production may lead to inactivation of proteins, RNA and DNA within the cell (Estevez, Mitchell, Faccio, & Alborés, 2020). Metallic nanoparticles of silver, gold, copper, titanium, cerium oxide, magnesium and zinc have been proven to be bactericidal at nano-levels (Ghahremani et al., 2020).

CuO NPs synthesized using the fruit extract of lemon and *Phyllanthus embilica* displayed antibacterial activities against some clinical bacterial isolates. The green synthesis of spherical CuO NPs of 5-10 nm using the extract of *Gloriosa superba* was also reported to display antibacterial potentials (Naika et al., 2015). Spherically shaped greenly synthesized ZnO NPs displayed significant antibacterial activities. The crystalline nanoparticles synthesized using *Citrus hystrix* leaf extract and potent antibacterial activities (Krishnamoorthy et al., 2023). Phyto-assisted ZnO NPs were using different plants extract have showed enhanced bacterial activities against different bacterial strains (S. Karthik et al., 2017; Ravichandran et al., 2022; Amit Singh & Kaushik, 2019). The spherical nanoparticles were averagely 32nm and showed agglomerations. Moreover, promising antibacterial activities of phyto-fabricated MgO NPs were also reported by different studies (Amor et al., 2023; Augustine & Hasan, 2020). MgO NPs were also synthesized using the leaf extract of *Trachyspermum ammi* (Dabhane et al., 2022), *Hagenia abyssinica,* flower extract (Hirphaye et al., 2023), *Allium cepa,* leaf extract (Periakaruppan et al., 2023), *Citrus aurantium* fruit peels (Ringwal et al., 2022) showed likely antibacterial potencies.

The antifungal activity of biosynthesized metallic nanoparticles has more potential than commercial antibiotics such as fluconazole and amphotericin. The plant derived CuO NPs have clearly showed the membrane damage in *Candida sp*. and damage in fungal intercellular components and finally cell function was destroyed (Logeswari, Dineshkumar, Usha, & Kumar, 2012). Most of the commercial antifungal agents have limited applications clinically and in addition, there are more adverse effect and less recovery from the microbial disease. Subsequently, the commercial drugs induce side effect such as renal failure, increased body temperature, nausea, liver damage, and diarrhea after using the drugs. Nanoparticles were developed for novel and effective drug against microbes. The fungal cell wall is made up of high

polymer of fatty acid and protein. The multifunctional ZnO NPs have shown a promising activity against spore producing fungus and effectively destroy the fungal growth (Abdelghany et al., 2023). The fungal cell membrane structure significant changes were observed by treating it with MgO nanoparticles (Saheb Ali et al., 2023; Jamdagni, Khatri, & Rana, 2018)

Bimetallic oxide NMs also serve as great antimicrobials. Bimetallic nanoparticles as antimicrobials can complement the role of antibiotics in combating with bacteria. These nanoparticles can interfere with bacterial growth either by disrupting their membrane or by producing ROS (reactive oxygen species) that cause destruction of DNA and also impede its protein functioning machinery (Zhao et al., 2020). ZnO-CuO NCs synthesized from leaf extracts of *Dovyalis caffra* exhibited enhanced antibacterial activity (J. O. Adeyemi et al., 2022). Also, CuO-AgO bimetallic NCs synthesized from *Oscimum basilicum* (Basil) flower and leaf extracts have antibacterial activity against *Pseudomonas aeruginosa*, *Staphylococcus aureus*, *Bacillus subtilis*, *Escherichia coli* (Malapermal, Mbatha, Gengan, & Anand, 2015). AgO-CuO bimetallic NCs prove to be promising anti-microbials against gram positive bacteria *Bacillus subtilis*. Therefore their synergistic effects with antibiotics and sulfa drugs can be exploited for preparation of medicines against bacteria (Ashishie et al., 2018). Ag-ZnO NCs show anti-bacterial activity against *Staphylococcus aureus* and *Bascillus subtilis* by altering MIC (Minimum Inhibition concentration) especially in case of *S.aureus.* CuO-NiO bimetallic NCs have shown bacteriostatic effect against certain bacterial strains like *Escherichia coli, Staphylococcus aureus, and Staphylococcus mutans.* FeO-ZnO magnetic bimetallic NCs show very good antifungal and anti-bacterial effect against a number of pathogenic micro-organisms (Al-Asfar, Zaheer, & Aazam, 2018).

Adeyemi *et al*., (J. O. Adeyemi et al., 2022) synthesized CuO-ZnO NCs using a co-precipitation method. Compared to pure CuO and ZnO, the enhanced antibacterial activities of CuO-ZnO NCs were confirmed. The antibacterial activity of the composite increases as the concentration of NiO increases. The results of the disc diffusion assay establish the susceptibility order of the exposed bacteria against CuO-ZnO to be *E. coli* > *B. subtilis* > *S. aureus* > *S. typhi*. The Phytoextract mediated ZnO/MgO nanocomposites synthesized using *Ricinus communis L.* plant seedless fruit extract (SFE) also showed good antibacterial activity against *E. coli* and *Klebsiella* bacteria. In comparison to the pure NPs and NCs, the ZnO/MgO-NCs (1:1) exhibited an enhanced

antibacterial activity and resulted in 1.5-2.8 times and 1.27-3.5 times larger radius for zone of inhibition in case of *E.coli and Klebsiella* respectively (Panchal et al., 2019). Using *Ricinus communis* L. plant seedless fruit extract as a green synthesis procedure Panchal et al. also synthesized a granular nanoflakes morphology of MgO clusters, irregular morphology of ZnO, and granular nanoflakes shaped MgO/CuO NCs (B. R. Mohammad et al., 2020). The antibacterial activity conducted on *E.coli* and *Klebsiella* photogenic bacteria show enhanced ZOI for the MgO/CuO NCs compared to single MgO and ZnO. The obtained highest ZOI on *E. coli* bacteria was 28 mm.

Trimetallic oxide NMs exhibited efficient and promising antimicrobial potentials than the mono and bi-metallic counterparts. As an example, glycine-mediated CuO-Fe_2O_3-MgO NCs against *Staphylococcus aureus* and *Escherichia coli* bacteria revealed comparable activity to that of Azithromycin standard drug(Alnahari, Al-Sharabi, Al-Hammadi, Al-Odayni, & Alnehia, 2023). Using SEM analysis, the materials were confirmed to have less than or equal to 100 nm-sized semi-globular-ovoid shapes. The antibacterial activity of the composites against *E. coli ATCC 8739, S. paratyphi ATCC 9150, S. aureus ATCC 33862,* and *L. monocytogenes ATCC 15313* bacteria shows good results. Compared to the composite, TiO_2 showed poor antibacterial activity on all bacteria (only 5–9 mm inhibition zone). The highest ZOI obtained on *S. paratyphi* bacteria is 18 mm. The ROS generation and electrostatic force interaction were suggested to be the probable antibacterial mechanism that led to bacterial death.

CuO-NiO-ZnO mixed metal oxide NCs (~7 ± 2 nm) displayed good antibacterial activities and damaging effects against *E. coli* and *S. aureus* bacterial strains; the NPs attached to the bacterial cell wall and totally annihilated the cells (Alnahari et al., 2023). In another study, the green-synthesized trimetallic microwave assisted CdO-NiO-ZnO mixed metal oxide NCs exhibited enhanced antimicrobial activities against *S. aureus, E. coli, Enterococcus faecium, Enterococcus faecalis*, and *Candida albicans*. It was revealed that inhibition responses of trimetallic nanomaterial were higher than mono-metallic and bi-metallic ones, as in the case of CdO-NiO-ZnO tri-metallic NCs synthesized by phyto-mediated synthesis techniques (Munawar, Iqbal, Yasmeen, Mahmood, & Hussain, 2020).

Munawar et al. synthesized ZnO-Yb_2O_3–Pr_2O_3 ternary NCs that showing a highly enhanced antibacterial activity (31 mm) on the *S. aureus* bacteria (Munawar, Yasmeen, et al., 2020). The

ternary ZnO-Pr_2O_2-Yb_2O_3 NC that was synthesized using a co-precipitation technique has porous morphology. The high surface area and porous nature of the material were reported to have good contact with the bacteria. Moreover, the dual-Z-scheme ZnO-Er_2O_3-Yb_2O_3 NCs synthesized using co-precipitation techniques was also reported to be highly effective on *S. aureus* bacteria (Munawar, Yasmeen, et al., 2020). The generation of ROS was suggested to be the mechanism of bacterial deactivation (Hussein et al., 2022). Ishaque *et al*. synthesized a spherical ternary CuO-NiO-ZnO NCs for antibacterial test against *S. aureus* and *E. coli* bacteria (Ishaque et al., 2023). The obtained result from growth curve analysis and colony-forming unit reduction study showed promising antibacterial activity, specifically an enhanced number of colony counts of bacterial strains reduction on *S. aureus* bacteria. FESEM analysis result also shows the effect of CuO-NiO-ZnO NCs that causes rupturing, cracking, and release of intracellular components. CuO-MgO-ZnO NCs prepared by coprecipitation techniques also revealed enhanced antibacterial activity against *Escherichia coli, Klebsiella pneumoniae, Proteus Vulgaris, Staphylococcus aureus*, and *Pseudomonas aeruginosa bacteria* with the zones of inhibition 30, 31, 30, 30, and 30 mm, respectively (Munawar et al., 2021). Some important mentioned mechanisms for antibacterial effects of these nanomaterial are the formation of reactive oxygen species (ROS) (as the main cause of cellular death), membrane modifications, and a decrease in ATP level and inhibition of tRNA (Nasrollahzadeh, Sajjadi, Iravani, & Varma, 2020).

2.3.1.1 Methods for antimicrobial activity test

The in vitro antibacterial activity test of NPs have been performed using different methods such as broth dilution followed by colony count, disk diffusion assay, agar dilution method microtiter plate-based method, flow cytometer viability assays, and conductometric assay (Gopal et al., 2018). Agar disk-diffusion method is the official method used in many clinical microbiology laboratories for routine antimicrobial susceptibility testing. Nowadays, many accepted and approved standards are published by the Clinical and Laboratory Standards Institute (CLSI) for bacteria and fungi testing (Yaqub et al., 2020). In this well-known procedure, agar plates are inoculated with a standardized inoculum of the test microorganism. Then, filter paper discs (about 6 mm in diameter), containing the MO NPs at a desired concentration, are placed on the agar surface. The Petri dishes are incubated under suitable conditions. Generally, antimicrobial agent diffuses into the agar and inhibits germination and growth of the test microorganism and

then the diameters of inhibition growth zones are measured. The growth media, temperature, incubation time and inoculum size required by CLSI standards. Antibiogram provides qualitative results by categorizing bacteria as susceptible, intermediate or resistant (Fathy & Mahfouz, 2021). Therefore, it is a typing tool based on the resistance phenotype of the microbial strain tested, its outcomes also guide clinicians in the appropriate selection of initial empiric treatments, and antibiotics used for individual patients in particular situations (Hashem & El-Sayyad, 2023).

Moreover, disk-diffusion assay offers many advantages over other methods: simplicity, low cost, the ability to test enormous numbers of microorganisms and antimicrobial agents, and the ease to interpret results provided. Furthermore, several studies have demonstrated the great interest in patients who suffer from bacterial infection of an antibiotherapy based on the antibiogram of the causative agent (Hashem & El-Sayyad, 2023). This fact is due to the good correlation between the *in vitro* data and the *in vivo* evolution, currently, a standardized antifungal disk-diffusion approach is used to test non-dermatophyte filamentous fungi. The above-mentioned advantages of this method, mainly simplicity and low cost, have contributed to its common use for the antimicrobial screening of MO NPs and other drugs (Anand et al., 2022).

The antimicrobial activity of MO NMs has been tested using disk-diffusion methods against both Gram-positive bacteria such as *B. subtilis* and *S. aureus* and Gram-negative bacteria such as *P. aeruginosa*, *C. jejuni*, and *E.coli*. In addition to a thin peptidoglycan layer, Gram-negative bacteria have an outer membrane lipopolysaccharide. This layer acts as a barrier that prevents from entering negatively charged ROS (Joghee et al., 2019). On the contrary, the cell membrane of Gram-positive has a less negative charge (Karthik, Dhanuskodi, Gobinath, Prabukumar, & Sivaramakrishnan, 2018) that allows penetration of negatively charged ROS (Maheo et al., 2023). MO NPs shows good antibacterial properties on both Gram-positive and Gram-negative bacteria. Yet, the antibacterial activity of MO NPs is highly dependent on the particle size. It was reported that decreasing the particle size results in enhancing the antibacterial activity of MO NMs (B. R. Mohammad et al., 2020). To indicate, Jones et al. compared the antibacterial activities of MgO, TiO_2, Al_2O_3, CeO_2, and ZnO against *S. aureus RN6390* bacteria. To check the effects of ZnO particle size on the antibacterial activities, differently sized MO NMs materials,

namely >1 μm, 8 nm, and 50-70 nm were studied. Compared to the other, the antibacterial activities of small-sized 8 nm MO NMs was found to be superior (M. Li et al., 2023).

2.3.1.2 Mechanisms of antimicrobial activities of MO NMs

For the antimicrobial activities of MO NMs, several mechanisms have been proposed. The antimicrobial activity mechanism of MO NMs may follow three mechanisms including the release of antimicrobial ions (Narendhran & Sivaraj, 2016), the interaction of NPs with microorganisms (Sonbol et al., 2021), and the formation of ROS (Vinothkanna et al., 2023). However, the release of antimicrobial ion/solubility of metal oxides is dependent on different factors such as the concentration of metal oxides, time of interaction, and the nature of microorganisms (Santhosh et al., 2023).

The antibacterial activity of MO NMs stems from their high solubility and metal ion release, which, once in contact with the bacterial cells, will end up being absorbed. At this intracellular level, the free metal ions will interact with the thiol group of respiratory enzymes and inhibit their action, leading to an overproduction of ROS and free radicals, which in turn will cause oxidative stress. This will result in membrane, mitochondria and DNA damage and ultimately bacterial cell death (Makvandi et al., 2020). Data from the specialized literature indicate the bactericidal effect of ZnO NPs against both Gram-positive and Gram-negative bacteria, but also against spores, which in general possess resistance against high pressures and temperatures (Ravichandran et al., 2022). Moreover, it was reported that the antibacterial activity of MO NMs is tightly related to their size and concentration. For example, (*i*) Jiang *et al*. (Jiang, Lin, & Cai, 2020) showed that the bactericidal activity of ZnO NPs increased with the decrease in particle size, while (*ii*) Sonbol and his co-investigators reported that the bacterial response to CuO NPs is both dose- and time-dependent, with positive results being observed in low-dose ranges and smaller exposure periods (Sonbol et al., 2021); similarly, (*iii*) Li *et al*. (X. Li, Feng, Li, & Zhang, 2022) reported a decrease in the number of bacteria with the decrease in the MgO NMs size.

Due to their unique physicochemical and biological characteristics, antibacterial activities and low cost of preparation, CuO NPs have attracted the attention of researchers all over the world (Lv et al., 2018). Mahapatra et al., 2008, investigated the antibacterial activity of

CuO NPs against various bacteria including *Salmonella paratyphi*, *Shigella strains*, *Klebsiella pneumonaie* (*K. pneumonaie*) and *P. aeruginosa* and reported that these nanoparticles were able to reduce the number of bacteria through membrane crossing and enzyme damage, which in turn led to cell death. In another study, Azam et al., 2012, evaluated the effect of CuO NPs against two Gram-positive bacteria and two Gram-negative bacteria and the results showed that the antibacterial effect against both groups of bacteria was size and concentration-dependent. Moreover, CuO NPs exhibited significant antibacterial activity against a wide range of bacterial strains such as *Enterococcus faecalis, K. pneumonaie, E. coli, P. aeruginoasa*, *Shigella flexneri, S. aureus, Proteus vulgaris, S. typhimurium,* etc. (Varshney et al., 2022).

Data from the literature highlight a strong antibacterial activity of MgO NPs, which can be correlated to their ability to generate superoxide on their surface and increase the pH of the microenvironment by particle hydration with water (Varshney et al., 2022). In addition, Vijayakumar and his friends (S Vijayakumar, Punitha, & Parameswari, 2022) demonstrated that this type of MO NPs is capable of damaging the membrane, resulting in a leakage of the intracellular contents and, in the end, cell death. MgO NPs exhibit antibacterial effects against both Gram-positive and Gram-negative bacteria (Poonguzhali et al., 2022). For example, Vijayakumar et al. (S Vijayakumar et al., 2022) reported that MgO NPs possess antibacterial effectiveness against *S. aureus* and *E. coli*, while another study proved the particles' efficiency against *E. coli* and *Salmoella stanely*, but in a concentration-dependent manner (Ahmed et al., 2021). Panchal et al. investigated the antibacterial potential of a combined nanostructure of ZnO-MgO NCs and their results indicated a high antibacterial activity against the Gram-positive bacterium, *B. subtilis*, while the pure MgO NPs revealed a moderate activity against both *B. subitlis* and *E. coli* bacteria (Panchal et al., 2023).

2.3.2 Antioxidant activities

Studies on the capacities of biosynthesized MO NMs to scavenge free radicals gave an initiative about the relationship and activity of the nanoparticles with the biomolecules that exist in living systems. Antioxidants mostly play a dynamic role in the performance of biological systems by scavenging toxic free radicals. Antioxidants check oxidative injuries that are generated by oxidative stress to cellular components such as DNA, proteins and lipids, and minimize the risk of age-related chronic diseases. Measurements of antioxidant potentials are still to a large extent

restricted to biological moieties. Various studies on antioxidant activities of MO nanoparticles have been earlier reported (Ge, Cao, & Chu, 2022; N. Mohamed, Hessen, & Mohammed, 2021).

Reactive oxygen species (ROS) are said to excite or stimulate auto-oxidation and thermal oxidations of lipids which are connected with damage of membrane and aging in living organisms (Koltover, 2010). Hydrogen peroxide is a weak oxidizing agent that can deactivate some enzymes directly by the oxidation of important thiol groups. It crosses cell membrane swiftly, and inside the cell, it can possibly react with Fe^{2+} and Cu^{2+} to form hydroxyl radicals. Hydroxyl (OH) radicals have very short half-life and are among the most lethal and reactive free radicals with huge oxidative power, which combines rapidly with virtually all molecules in its immediate vicinity. It hastens several biological disorders such as cataracts, carcinogenesis, inflammation, atherosclerosis, mutation, ageing and cell death (Mao, Gu, Chen, Yu, & He, 2017). It can freely react with superoxide radicals, resulting to vascular system impairment which then leads to conditions such as multiple sclerosis and juvenile diabetes. Nitric oxide (NO) is involved in many biological processes or functions, such as: smooth muscle relaxation, neurotransmission, antitumor, blood pressure regulation, and antimicrobial activities. However, it also adds to oxidative damage, because it has the ability to react with superoxide to form the peroxynitrite anion, which can produce DNA fragmentation and initiate lipid peroxidation (Ribeiro et al., 2014). Thus, production of nitric oxide must be tightly controlled to restrain the harmful effects.

Nanotechnology has expanded the range of materials that can scavenge free radicals in the environment and in living entities. The nano-scaled inorganic particles could be well developed for their further application of antioxidant effects in many fields, such as medicine, cosmetic and functional foods additives. The smaller sizes of inorganic nanoparticles could offer more feasibility to function as antioxidants due to the high surface to volume ratio. Although metallic and metallic oxide nanoparticles were considered to potentially induce oxidative stress and lead to undesirable health problems, some of the nanoparticles exhibit excellent behavior in antioxidants, such as ZnO, CeO_2, TiO_2, AgO, MgO, CuO, and Fe_3O_4 NPs in recent research works (Ge et al., 2022). TiO_2 were widely used in many products due to their low toxicity, and has to be considered as a nano-material on cellular antioxidant defense(Q. Li et al., 2021). Also, CeO_2 nanoparticles may function as a free radical scavenger regeneratively to defect oxygen with

their lattice structure (Filippi et al., 2019). Fe_3O_4 could be further modified to carbon paste electrode to form nanoparticles for electrosensitive determination of antioxidant components, such as sinapic acid, syringic acid and rutin (Bouafia, Laouini, Khelef, Tedjani, & Guemari, 2021). Subbaiya and Selvam (Subbaiya & Selvam, 2015) reported the antioxidant activities of spherically shaped greenly synthesized CuO NPs using *Hibicus rosasinensis* leaf extract as the bioreductant and stabilizer. Also, ZnO NPs synthesized using stem extract of *Ruta graveolens* reported by were reported to display potent antioxidant activities (Bharathi & Bhuvaneshwari, 2019). Spherical MgO nanoparticles biosynthesized using *Amaranthus spinosus* leaf extract with sizes ranging from 58-530 nm were also reported to possess antioxidant properties (Sandhir et al., 2015).

2.3.2.1 Methods for antioxidant activity test

There are several techniques of assessing the antioxidant potentials of MO NMs. Of the *in-vivo* and *in-vitro* assessment of antioxidant activities, *in-vitro* assays are simple, cost-effective, reproducible and convenient. The 2, 2-diphenyl-1-picrylhydrazyl (DPPH) is basically used for testing initial radical scavenging potentials of a compound or extract, and it offers a speedy and uncomplicated way to assess antioxidant activity. The DPPH is a stable nitrogen free radical which accepts hydrogen atom or electron from antioxidant materials. A change of color in the ethanoic solution of DPPH is detected once it reacts with an antioxidant, which is as a consequence of the scavenging action of antioxidant on DPPH by liberating or donating hydrogen to form the stable DPPH which is yellow-colored (Ge et al., 2022). DPPH (Figure 6) is one of a few stable and commercially available organic nitrogen radicals due to the delocalization of the spare electron on the whole molecule (Pisoschi & Negulescu, 2011). It has a UV-vis absorption maximum at 515 nm. It involves preparation of a solution of DPPH in methanol (3.9 mL, 25 mg/L) and follow the reaction progress at 515 nm after 30 minutes reaction of time with the 0.1 mL sample volume (D. Huang, Ou, & Prior, 2005).

The DPPH assay is technically simple, but some disadvantages limit its applications. Besides the mechanistic difference from the HAT reaction that normally occurs between antioxidants and peroxyl radicals, DPPH is long-lived nitrogen radical, which bears no similarity to the highly reactive and transient peroxyl radicals involved in lipid peroxidation. Antioxidants that react quickly with peroxyl radicals may react slowly or may even be inert to DPPH. In recent years,

this method was modified to methanolic solution of DPPH (5×10^{-5} mol/L), 40 minutes of reaction times with the samples and absorbance reading at 517 nm (Sirivibulkovit, Nouanthavong, & Sameenoi, 2018).

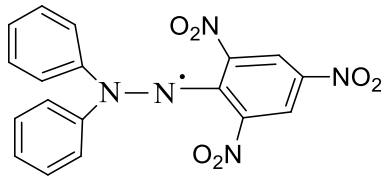

Figure 6. Structure of DPPH

Also, ferric ion reducing antioxidant power (FRAP) is an antioxidant assay employed to estimate the degree of the antioxidant competence of drugs, and nutritional supplements comprising polyphenols. The use of FRAP assay gives rapid and easy way to calculate antioxidant activities (Dudonne, Vitrac, Coutiere, Woillez, & Mérillon, 2009). Moreover, ABTS radicals are produced from the oxidation of ABTS by potassium persulfate and it is an excellent tool for appraising the antioxidant potential of the hydrogen-donating and chain-breaking antioxidants (R. Zhang et al., 2021).

2.3.3. Anticancer activities

Cancer is not a solitary disease; rather it is a group of diseases with every organ or system having the capability to develop a distinct set of diseases. It is developed through diverse signaling mechanisms including cell proliferation, angiogenesis and metastasis. The currently available anticancer therapies have adverse effect by affecting the functions of normal cells while administering excess drug and exposure to radiation; thereby necessitating the need to develop new anticancer strategies (A. Sharma, Goyal, & Rath, 2018). In order to address these therapeutic requirements, nano-sized molecular tools capable of distinguishing between malignant and non-malignant cells and also deliver lethal payload are being developed (Gmeiner & Ghosh, 2014).

Current anticancer research has been devoted to the discovery of novel transition metal compounds rather than the platinum based pharmaceutical with various toxic side effects including gastrointestinal and hematological toxicity (Abdel-Fattah & Ali, 2018). Metal oxide

nanoparticles have been used in drug delivery especially in the treatment of cancer. Given to their large surface area and area to volume ratio, MO NPs display a number of specific physicochemical attributes making them valuable by inducing cytotoxicity in the treatment of cancer cells, and have therefore become formidable tool against cancers (H. Sharma, Mishra, Talegaonkar, & Vaidya, 2015). In medicine, MgO is used for the alleviation of heartburn, stomach sore, and for bone regeneration. Nowadays, MgO NPs are applied in tumor inhibition and additionally, have remarkable potential as an antimicrobial agent. Other experimental results revealed the possible utility of ZnO NPs and CuO NPs in the treatment of cancer, including colorectal and breast cancer cell lines (Dolati et al., 2023; Efati et al., 2023).

It has been documented that biosynthesized MO NMs are mostly biocompatible and highly suitable for anticancer applications. CuO NPs biosynthesized from *Alchornea cordifolia* Leaf Extract inhibited the proliferation of human cervical carcinoma (Hela) cells and induced apoptosis in concentration dependent manner (Elemike, Onwudiwe, & Singh, 2020). Spherical copper oxide nanoparticles of 26-30 nm in dimension were synthesized by biological method using extract of *Acalypha indica* leaf and the cytotoxicity activity of the CuO NPs was confirmed by MTT assay against MCF-7 breast cancer cell lines. The cytotoxic effect of the CuO NPs was determined by sulforhodamine-B assay and results indicated that an increase of the mitochondria-derived reactive oxygen species (ROS) and initiation of the lipid peroxidation of the liposomal membrane, which influences the cytokinetic movements of cells and regulates the several signaling pathways. Also, clonogenic assay established that the NPs-incubated cancer cells were unable to proliferate well. CuO NPs synthesized using different plant extracts obtained from the leaves of *Azadirachta indica, Murraya koenigii, Hibis cus rosa-sinensis, Moringa oleifera, Tamarindus indica,* have reaveled cytotoxic effect against four cancer cell lines such as cervical (HeLa), human breast (MCF-7), epithelioma (Hep-2) and lung (A549), and one normal human dermal fibroblast (NHDF) cell line (Nagajyothi, Muthuraman, Sreekanth, Kim, & Shim, 2017; Rehana, Mahendiran, Kumar, & Rahiman, 2017).

ZnO NPs have been reported to possess anticancer properties in a couple of studies. For instance ZnO NPs considerably declined elevated levels of oxidative stress markers and hepatocyte integrity, and also reduced high levels of serum of tumor alpha-l-fucosidase and markers alphafetoprotein when used against hepatocellular carcinoma HepG2, non-small cell human

A549 (lung cancer), MCF-7 (breast cancer) and PC3 (prostate cancer) cell lines (Kanagamani, Muthukrishnan, Saravanakumar, Shankar, & Kathiresan, 2019; Rajeshkumar et al., 2018). And also the efficacy of ZnO NPs in inhibiting ERK enzyme and other cancer associated kinases such as AKT, p70S6 K and CREB has reported (Arumugam et al., 2021). ZnO NPs has also been reported as an anticancer agent against human HCT-116 (colon cancer), and HeLa (cervical cancer) among others (Anjum et al., 2021; S. Majeed, Danish, Ismail, Ansari, & Ibrahim, 2019). ZnO NPs was doped with rare earth metals such as lanthanum, Cerium and Neodymium facilitated by *Gymnema sylvestre* leaves extract, and they were reported to display anticancer activities *in vitro* against A498 (human kidney carcinoma) cell line and normal vero (African monkey kidney) cell lines (Karthikeyan, Ahamed, Karthikeyan, & Kumar, 2019).

In another study, MgO NPs were produced using leaf extract of *Sargassum wightii*, which displayed effective cytotoxic activity against A549 (lung cancer) cell lines in a dose dependent manner with the IC_{50} value of 37.5 ± 0.34 µg/ml (Pugazhendhi, Prabhu, Muruganantham, Shanmuganathan, & Natarajan, 2019). Karthik *et al* reported microwave assisted green synthesized MgO NPs using *Andrographis paniculata* (*A. paniculata*) extract which caused reduction of cell viability and exercised improved cytotoxicity against human breast adenocarcinoma (MCF-7) cells with IC_{50} of IC_{50}:15.76 µg/mL (Karthik, Dhanuskodi, Kumar, Gobinath, & Sivaramakrishnan, 2017). MgO NPs are synthesized using wheat bran fermented by *Erysiphe cichoracearum* and gamma irradiation with elevated cytotoxic activity against human Prostate cancer cell lines (PC3) with IC_{50} of IC_{50} value of 11.17 µg/mL (Fathy & Mahfouz, 2021). In another report, MgO NPs synthesized using using grains extract of *Oryza sativa* L. *indica* (black rice), displayed activities against HCT-116 cells (Velsankar et al., 2023).

Bi- and tri-metallic oxides NCs have promising usage in field of biological applications. Tunable chitosan-capped spiky urchin like bimetallic CuO-ZnO NCs created via single reactor synthesis process, when targeted against cancer in photothermal cancer therapy gave promising results in ablating cancer cells (J. O. Adeyemi et al., 2022; Orshiso et al., 2023). MgO-ZnO bimetallic NCs synthesized using gallic acid and quercitin as standard phenolics and flavonoids have seen to be toxic against cancer cells and therefore can be used in preventing or at least lowering oxidative stress related to degenerative diseases (Rafie & Meshkini, 2021). Bi- and tri-metallic oxide NCs can be effectively used in drug delivery as they have high surface area to volume ratio, hence can

cross blood-brain barrier and epithelial cell junction to reach target site (Abd El-Aziz & Farahat, 2023; Shujat Ali et al., 2021).

2.3.3.1 Methods for cytotoxicity evaluation

Cytotoxicity assays quantify the chemotherapeutic agents' capacity to inflict damage or death on a target cell. Cytotoxicity is the toxicity that results from the impact of medicines on living cells. A cytotoxicity evaluation method involves the use of dyes: tetrazolium, trypan blue, alamar blue, neutral red, and coomassie blue. This procedure distinguishes different cells by color based on the ratio of color uptake in both live and dead cells (Arsianti et al., 2020). The 3-(4,5- dimethyl-2-thiazolyl)-2,5-diphenyl-2H-tetrazolium bromide (methyl thiazolyl tetrazolium) also called as MTT assay is a colorimetric cytotoxicity assay for rapid assessment of cell proliferation and measurement of metabolism or function of the cells used. It is based on the reduction of a yellow tetrazolium salt (3-(4,5-dimethylthiazol-2-yl)-2,5-diphenyltetrazolium bromide or MTT) to purple formazan crystals by metabolically active cells (Ghasemi, Turnbull, Sebastian, & Kempson, 2021). Living cells contain NAD(P)H-dependent oxidoreductase enzymes that reduce methyl thiazolyl tetrazolium (MTT) to purple formazan crystals. Formazan crystals are soluble in DMSO and the resulting-colored solution can be quantified by measuring absorbance at 570 nm. Briefly, it involves the incubation of plate cells at approximately 104 cells/well in 96 well plates for 24 hr at 37^0C, aspirate old media (add 100 µL of treatment media to all wells and incubate for a further 24 hr), addition of 100 µL of working MTT solution diluted from 50-100 mg/mL stock solution to each well to achieve 0.5 mg/mL. After 4hr carefully aspirate MTT solution from each well and dissolve the formazan precipitate by addition of 100 µL DMSO and finally read absorbance at 570 nm in plate reader and blank (no cells). Figure 7 displays the mechanism of enzymatic reduction of MTT to formazan.

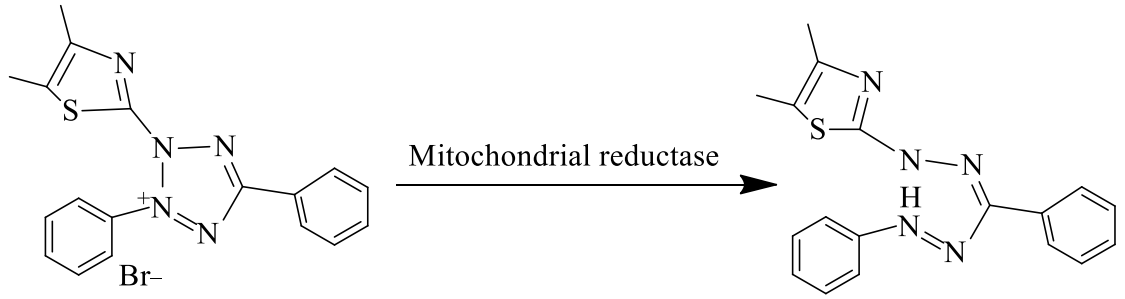

3-(4,5-Dimethylthiazol-2-yl)-2,5-diphenyl-2H-tetrazolium bromide **(MTT)**

(E,Z)-5-(4,5-dimethylthiazol-2-yl)-1,3-diphenylformazan **(Formazan)**

Figure 7. Enzymatic reduction of MTT to formazan (Ghasemi et al., 2021).

2.4 Molecular Docking

Molecular docking is one of the most frequently used methods in structure-based drug design, due to its ability to predict the binding-conformation of compounds to the appropriate target binding site (Khan, Ahemad, Chuah, Naidu, & Htar, 2020). Molecular docking assists in the process of computer-aided drug designing by considering every possible conformation of the protein and targeted molecules (Salmaso & Jacobson, 2020). Molecular docking techniques aim to predict the best matching binding mode of a ligand to a macromolecular partner (Dubey et al., 2022). Ligand binding to macromolecules plays a key role in biology and medicine as guiding mechanism in biological processes. The binding of drugs to proteins and DNA has led to vast structural studies using both experimental and theoretical methods. Because of the major role of DNA in replication and transcription, DNA has been a major 39 target for antibiotic, anticancer and antiviral drugs (Peluso & Chankvetadze, 2023). Nucleic acid binding drugs are known for various diseases such as cancer, malaria, AIDS and other viral, bacterial and fungal infections (Dubey et al., 2022). The different modes of drug binding to DNA include intercalation between adjacent base pairs, intrusion into the minor groove and into the major groove. Intercalation and minor-groove binding are the predominant DNA-binding modes of small molecules (Peluso & Chankvetadze, 2023). Molecular docking or computer-simulated ligand binding is a powerful technique for investigating intermolecular interactions. It is an attractive scaffold to understand drug biomolecular interactions for the rational drug design and discovery, as well as in the mechanistic study by introducing a molecule (ligand) into the preferred binding site of the target specific region of the DNA/protein (receptor) mainly in a non-

covalent fashion to form a stable complex of potential efficacy and more specificity. The information obtained from the docking technique can be used to suggest the binding energy, free energy and stability of complexes. At present, docking technique is utilized to predict the tentative binding parameters of ligand-receptor complex beforehand (Khalil et al., 2018; Morris et al., 2009).

3. MATERIALS AND METHODS

3.1 Experimental Site

Synthesis of mono (CuO, ZnO, and MgO), bi (CuO-ZnO, CuO-MgO, and ZnO-MgO), and tri metallic (CuO-ZnO-MgO) oxide NMs, were done at Department of Applied Chemistry, Adama Science and Technology University (ASTU). X-ray diffraction (XRD) analysis was done at Department of Material Science and Engineering, and UV-Vis absorption edge determination of the nanomaterial were done at Applied Biology Department, ASTU. Antioxidant activity test was done at Applied Chemistry, ASTU. Antimicrobial activity was done at College of Agriculture, and Department of Agronomy, Plant Pathology Laboratory Haramaya University (HU). TEM/HRTEM/SAED and SEM/EDX analyses were done at Bangalore University, India. Anticancer activities were done at the University of Mumbai College of Commerce and Science Department of Chemistry, India.

3.2 Chemicals and Reagents

All the chemicals, and reagents used in this work were of analytical grade and used without further treatment. Magnesium nitrate ($Mg(NO_3)_2 \cdot 6H_2O$, 99.9%), zinc nitrate ($Zn(NO_3)_2 \cdot 4H_2O$, 99.9%), copper nitrate ($Cu(NO_3)_2 \cdot 3H_2O$, 99.8%), ethanol (C_2H_6O, purity ≥ 99.9%), and sodium hydroxide (NaOH, 97%) (Sigma Aldrich) were purchased from Addis Ababa, Ethiopia. The bacteria strains; *Escherichia coli* (*E.coli*, ATCC 25922), *Pseudomonas aeruginosa* (*P.aeruginosa*, ATCC 27823), *Streptococcus pneumoniae (S. pneumoniae*, ATCC 11778), and *Staphylococcus aureus* (*S. aureus* ATCC 25923) and fungal strains; *Aspergillus flavus*, *Aspergillus niger*, and *Candida albicans* were obtained from the Institute of Public Health (IPH), Addis Ababa, Ethiopia. Mueller Hinton broth (MHB), Potato Dextrose Agar (PDA), Sabouraud Dextrose Agar (SDA), dimethyl sulfoxide (DMSO), 2,2-diphenyl-1-picryl-hydrazyl-hydrate (DPPH), ascorbic acid, ferric chloride, potassium ferricyanide, 0.2 M potassium phosphate buffer, trichloroacetic acid, chloramphenicol, Fluconazole (Sigma-Aldrich) were purchased from Addis Ababa, Ethiopia. MCF-7 cells, peripheral blood mononuclear cell (PBMC), Fetal Bovine Serum (FBS), Dulbecco's Modified Eagle Medium (DMEM), PenStrep, Trypsin, 3-(4,5-dimethylthiazol-2-yl)-2, 5diphenyltetrazolium bromide (MTT), and Doxorubicin (Invitrogen, USA) were obtained from National Center for Cell Sciences (NCCS), India.

3.3 Instruments and Apparatus

The instruments and apparatus used in this work were: UV-visible spectrophotometer (Shimadzu UV-vis, SM-1600) , XRD (SHIMADZU model: XRD-7000 X-RAY DIFFRACTOMETER) (X-ray tube target: CuKα(λ=1.5406 nm)), TGA (Shimadzu DTG-60H) and DTA (Perkin Elmer, DSC 4000, USA), FTIR (Perkin Elmer FT-IR, Spectrum 65), SEM-EDX (EVO 18 with low vacuum facility and ALTO 1000 Cryo attachment), TEM/HRTEM (JEOL TEM2100 HRTEM), analytical balance (OHAUS, Switzerland), Oven (Contherm 260M), furnace (BiBBY, Stuart), hot plate (SM6, India), Centrifuge (K_2 series, CENTERION SCIENTIFIC LTD, West Sussex. U.K), deionizer (ELGACAN, Germany), mechanical shaker, sonicator, pH meter, reactor tube, Agate mortar, ceramic crucible, volumetric flasks, measuring cylinders, beakers, pipettes, magnetic stirrer, test tubes and desiccators.

3.4 Plant Extract Preparation

Fresh leaves of the medicinal plant *Artemisia abyssinica* Sch. Bip. ex A. Rich were collected from Tiyo Woreda, Arsi Zone in March 2022. Tiyo Woreda, located at ($7^o45'55''$ and $8^o02'02''$N latitude and $38^o56'42''$ to $39^o18'31''$E longitude), is found in Arsi Zone, Oromia Region, Ethiopia, which is 175 km Southeast of Addis Ababa (Aman, Asfaw, & Dalle, 2020). The collected plant was authenticated by a botanist in Addis Ababa University, with voucher specimen number YG006. The leaves of *A. abyssinica* were washed repeatedly with tap and distilled water and dried for 13 days in the dark to remove moisture content. After grinding with a mechanical grinder, 10 g of powdered leaves were mixed with 100 mL n-hexane, 50 % ethanol (water and ethanol, 1:1 *v*/*v*), and deionized water (DIW) in each 250 mL conical flasks (J. Singh, Kumar, Kim, & Rawat, 2019). The mixtures were shaken for 90 minutes at 120 rpm and 25.0 °C in a mechanical shaker and then heated for 1 hour at 60.0 °C with a magnetic stirrer, and finally the mixtures were cooled at room temperature overnight. The obtained crude extracts were filtered through Whatman filter paper, and then centrifuged to produce clear soltution as illustrated in Figure 8. The clear brown color extracts obtained and preserved at 4^oC for further study (Ananda et al., 2022).

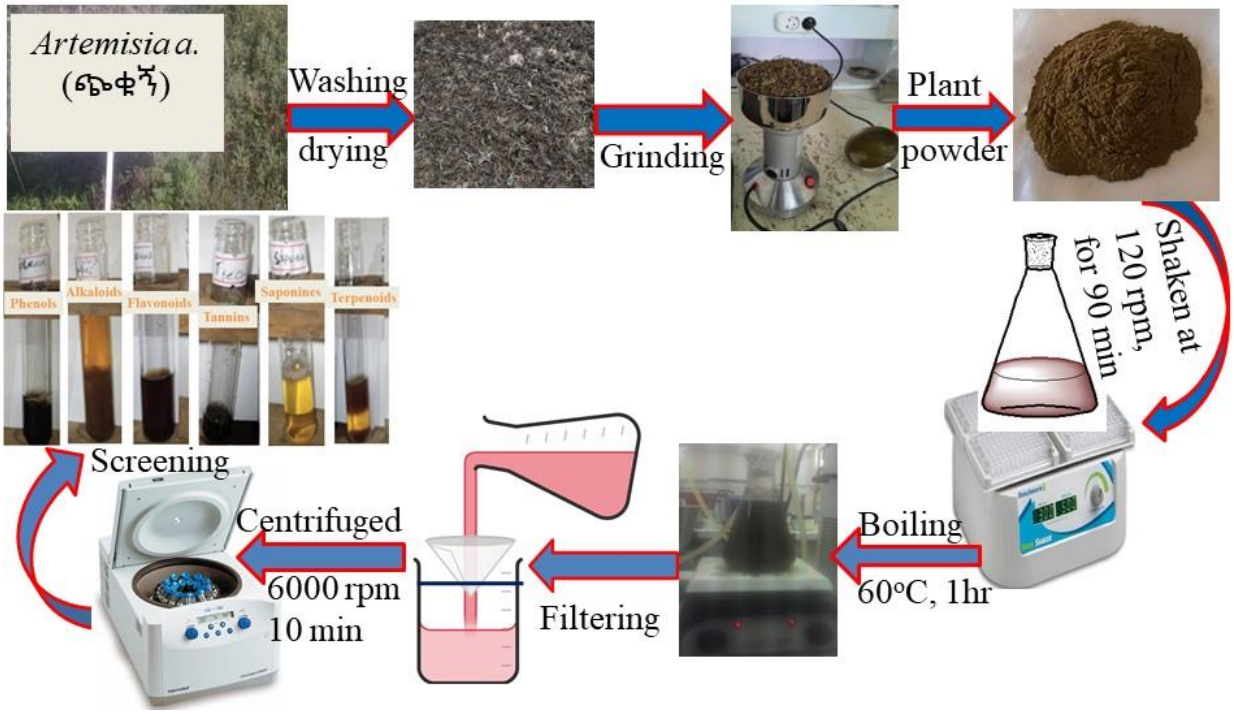

Figure 8. Schematic representation for LEAA preparation and Phytochmeical scheering

3.4.1 Phytochemical screening of the extracts

The aqueous, 50 % ethanol and n-hexane LEAA were subjected to phytochemical screening, and major secondary metabolites such as alkaloids, polyphenols, flavonoids, terpenoids, saponins, protein, and amino acids, carbohydrates, anthraquinones, glycosides, tannins, steroids, and resins were analyzed by following the standard methods.

Test for alkaloids

To 1 mL of aqueous, 50% ethanol and n-hexane LEAA in three separate test tubes 3 mL distilled water and 1 mL 35% HCl were added. The mixtures were warmed for 15 min in a water bath, then cooled and filtered. After that, 1 mL of the filtrates was tested with 0.5 mL each of Dragendorff's reagents and Mayer's (De Silva, Abeysundara, & Aponso, 2017).

- ***Dragendroff's Test:*** Two drops of Dragendroff's reagent (solution of Potassium Bismuth Iodide) were added to aqueous, 50% ethanol and n-hexane LEAA. The presence of alkaloids is indicated by the production of a crimson precipitates.
- ***Mayer's Test***: One mL of aqueous, 50% ethanol and n-hexane LEAAswere measured into watch glasses and small amount of dilute hydrochloric acid and Mayer's reagent (solution

of potassium mercuric iodide) were added to the solutions; the formation of a white precipitates indicated the presence of alkaloids.

Test for flavonoids

The presence flavonoids were determined by two alternative tests (De Silva et al., 2017):

- ***Alkaline reagent test*:** A few drops of sodium hydroxide solution were added to 2 mL aqueous, 50% ethanol and n-hexane LEAA. The presence of flavonoids is revealed by producing a bright yellow color that fades to colorless when dilute acid is added.
- ***Lead acetate test*:** A few drops of lead acetate solution were added to the 2 mL aqueous, 50 % ethanol and n-hexane LEAA. The presence of flavonoids is shown by the production of a yellow color precipitate.

Test for proteins and free amino acids

Biuret test: Equal amounts of 5% sodium hydroxide and 1% copper sulfate solutions were added to two mL of aqueous, 50% ethanol and n-hexane LEAA. The presence of proteins and free amino acids were observed by the formations of pink or purple color (De Silva et al., 2017).

Test for phenols

Ferric Chloride Test: 2 mL of ferric chloride solution was added to three mL of warm LEAAs' in a water bath. The blue color indicated the presence of phenols (Shaikh & Patil, 2020).

Test for Anthraquinones

***Borntragor's Test*:** A few drops of magnesium acetate solution were added to one mL of the aqueous, 50% ethanol and n-hexane LEAA, and the formation of the pink color showed the presence of anthraquinone (R. Kumar, Sharma, & Devi, 2018).

Test for Tannins

Wohler's Test: A few drops of 0.1% ferric chloride ($FeCl_3$) were added to 5 mL of pure aqueous, 50% ethanol and n-hexane LEAA in a test tube and allowed to stand for some time. The brownish-green color indicated the presence of tannins. A few drops of basic lead acetate

solution were added to 1.6 mL of each LEAA; the appearance of a white precipitate indicated the presence of tannin (Shaikh & Patil, 2020).

Test for Saponins

Foam test: A drop of sodium bicarbonates solution was added to test tubes containing five mL of aqueous, 50% ethanol and n-hexane LEAA. The test tubes were firmly shaken for three minutes. The appearance of honeycomb-like foam indicates the presence of saponins (De Silva et al., 2017).

Tests for steroids

Salkowski test: A few drops of chloroform were added to one mL of each aqueous, 50% ethanol and n-hexane LEAA and shaken vigorously, and then a small amount of sulphuric acid was added gradually. The appearance of red color indicates the presence of steroids (R. Kumar et al., 2018).

Test for Terpenoids

***Salkowski test*:** To five mL of the aqueous, 50% ethanol and n-hexane LEAA in a test tube, two mL chloroform and three mL of saturated H_2SO_4 were added. A reddish-brown coloring confirmed the presence of terpenoids near the interface (Shaikh & Patil, 2020).

Test for Glycosides

***Molisch's Test*:** To 0.5 mL of the aqueous, 50% ethanol and n-hexane LEAA, ten mL of water was added, shaken, and then filtered; the filtrates were concentrated over a steam and reacted with two to 3 drops of Molisch's test and carefully added with two mL of concentrated H_2SO_4, through the side of the test tube. The formation of a reddish violet ring indicates the presence of glycosides (R. Kumar et al., 2018).

Test for Steroids

***Salkowski Reaction*:** Two mL aqueous, 50% ethanol and n-hexane LEAA shaken with one mL of chloroform and added with sulfuric acid in a slow manner along the sides of the test tubes.

The formation of red color indicates the presence of steroids (Oloya, Namukobe, Ssengooba, Afayoa, & Byamukama, 2022).

Test for Resins

***Turbidity Test*:** 0.5 mL of the aqueous, 50% ethanol and n-hexane LEAA were dissolved in one mL of acetone and the solutions were poured into five mL of distilled water. The formation Turbidity indicates the presence of resins (Oloya et al., 2022).

Test for Carbohydrates

***Benedict's test*:** In each of 0.5 mL aqueous, 50% ethanol and n-hexane LEAA, 10 mL of water was added, shaken and then filtered, concentrates the filtrate over a steam, added five mL Benedict's reagent, and boiled for 5 minutes. Formation of brick red precipitate indicates the presence of carbohydrates (Shaikh & Patil, 2020).

3.5 Phytochemical Mediated Synthesis of MO NMs

3.5. 1 Optimization of reaction parameters

The effects of reaction parameters such as precursor salt concentration, pH, volume of ethanolic (50% ethanol v/v) LEAA and temperature on the formation of MO NMs were optimized. The effect of precursor salts concentration ($Cu(NO_3)_2 \cdot 3H_2O$, $Zn(NO_3)_2.4H_2O$ and $Mg(NO_3)_2.6H_2O$) on the synthesis of CuO, ZnO, and MgO NPs were studied by varying (0.01, 0.1, 0.3, 0.5, and 1M) of each salts while keeping LEAA to precursor salts ratio (10:40 mL), temperature (60±2 °C) and the pH (7.5 units) constant at that time. Similarly, the effect of pH (at varying pH of 3, 5, 7.5, 9, and 11units) (adjusted using 0.1 M NaOH), while using precursor salts concentration (0.1 M), LEAA to precursor salts ratio (10:40 mL), temperature (60±2 °C) on the synthesis of MO NPs were studided. The effect of LEAA to precursor salts ratio on the the synthesis of MO NPs by varying from (5:40, 10:40, 20:40, 30:40 and 40:40 mL) and keeping precursor salts concentration (0.1 M), pH at 5 and temperature (60±2 °C) were analyzed. Finally, the effect of temperature (at varying values of 30, 40, 50, 60, 70, and 80 °C) by keeping precursor salts concentration (0.1 M), pH at 5, and LEAA to precursor salts ratio (10:40 mL) on the absorbance and band gap (Eg) values of MO NMs were also studied for optimizing the synthesis methodology.

3.5.2 Synthesis of CuO, ZnO and MgO NPs

For the phyto-mediated synthesis of CuO NPs, 100 mL of 0.1 M ($Cu(NO_3)_2.3H_2O$ in DIW) solution was prepared and added with 25 mL of ethanolic (50% ethanol v/v) LEAA drop wise. The mixed solution was adjusted (using 0.1 M NaOH) at pH 5 and heated for 1 hour at 70 °C on a hot plate with a magnetic stirrer (according to our optimization). Visual observation of blue-black to deep brown color was used to assess the formation of CuO NPs in the solution. Next, the reaction mixture was sonicated at room temperature for 30 minutes at 60 rpm to maintain particle dispersion. The precipitated particles formed were isolated by centrifuging at 6000 rpm for 20 minutes and washed with ethanol following DIW to eliminate any impurities. The isolated precipitates were oven-dried at 80 °C for eight hours, calcinated at 300 °C in muffle furnace for two hours. The black-colored powder obtained and stored in an airtight sample holder for next use (Elemike et al., 2020; Sonbol et al., 2021).

For the synthesis of ZnO NPs, 100 mL of 0.1 M ($Zn(NO_3)_2.4H_2O$ in DIW) solution was added with 25 mL ethanolic (50% ethanol v/v) LEAA dropwise. The mixed solution was adjusted (using 0.1 M NaOH) at pH 7.5 and heated for 1 hour at 70 °C on a hot plate with a magnetic stirrer (according to our optimization). Following the color change from light brown to pale yellow was observed which was used to assess the formation of ZnO NPs in the solution. Next, the reaction mixture was sonicated at room temperature for 30 minutes at 60 rpm and the precipitates were isolated by centrifuging at 6000 rpm for 20 minutes and washed with ethanol following DIW. Then the precipitates were collected, oven-dried at 80 °C for ten hours, calcinated at 400 °C for two hours. The white-colored powder was obtained and stored in an airtight sample holder (Amor et al., 2023; Mthana, Mthiyane, Onwudiwe, & Singh, 2022).

Similarly, for the synthesis of MgO NPs, 100 mL of 0.1 M ($Mg(NO_3)_2.6H_2O$ in DIW) solution was prepared and added with 25 mL ethanolic (50% ethanol v/v) LEAA. Then the pH of mixed solution was adjusted (using 0.1 M NaOH) at 5 and heated at 70 °C for 1 hour on a hot plate with magnetic stirrer. The visual observation of light brown to milky color was used to assess the formation of MgO NPs in the solution. Then, the reaction mixture was sonicated at room temperature for 30 minutes at 60 rpm and the precipitates were isolated by centrifuging at 6000 rpm for 20 minutes and washed with ethanol following DIW. Then the precipitates were oven

dried at 80 °C for eight hours, calcinated at 350 °C for 2 hours and the fine milky-colored powder was collected and stored airtight sample holder (Dabhane et al., 2022).

3.5.3 Synthesis of ZnO-CuO, MgO-CuO and MgO-ZnO nanocomposites

Phyto-mediated fabrication of ZnO-MgO (ZC) NCs using ethanolic (50% ethanol v/v) LEAA was follows. 0.1 M of $Zn(NO_3)_2.4H_2O$) and 0.1 M of ($Cu(NO_3)_2.3H_2O$) solutions were prepared separately by stirring on hot plate at 30 ± 2 °C for ten minutes to obtain a homogeneous solution and then mixed together by (1:1) ratio. Then 100 mL mixed salt solution was taken and 25 mL of ethanolic (50% ethanol v/v) LEAA was added dropwise in a proportion of 4:1 (v/v). Then mixed solution was adjusted (using 0.1 M NaOH) at pH 5, and heated for 1 hour at 70 °C on a hot plate while heating with a magnetic stirrer (Cao et al., 2021). The light black to reddish-brown color change has been observed for the formation of ZC NCs. Next, the reaction mixture was sonicated at 25 ± 2 °C for 1 hour at 60 rpm to maintain particle dispersion and then centrifuged for 20 minutes at 6000 rpm. The obtained precipitates were washed with ethanol following DIW and then oven-dried at 80 °C for 12 hours, then calcinated for 2 hours at 400 °C. The fine reddish-brown powder was obtained and stored in the airtight sample holder.

For the synthesis of bimetallic MgO-CuO (MC) NCs, 0.1 M of $Mg(NO_3)_2.6H_2O$ and 0.1 M $Cu(NO_3)_2 \cdot 3H_2O$ were prepared separately by stirring on hot plate at 30 ± 2 °C for ten minutes and then mixed together by (1:1) ratio. 100 mL of mixed solution was added with 25 mL of ethanolic (50% ethanol v/v) LEAA dropwise in a proportion of 4:1 (v/v). Then mixed solution was adjusted (using 0.1 M NaOH) at pH 5, and heated for 1 hour at 70 °C on a hot plate containing a magnetic stirrer. The color change from greenish-black to milky-brown color was observed which indicated the formation of MC NCs. Then the solution was sonicated at 25 ± 2 °C for 1 hour at 60 rpm and then centrifuged for 20 minutes at 6000 rpm. The obtained precipitates were washed with ethanol following DIW and then oven-dried at 80 °C for 10 hours, then calcinated at 350 °C for 2 hours. The milky precipitates were obtained and stored in the airtight sample holder (Abbas et al., 2022).

For the synthesis of bimetallic MgO-ZnO (MZ) NCs, 0.1 M of $Mg(NO_3)_2.6H_2O$ and 0.1 M $Zn(NO_3)_2.4H_2O$ were prepared separately by stirring on hot plate at 30 ± 2 °C for ten minutes and then mixed together by (1:1) ratio. 100 mL of mixed salt solution was added with 25 mL of

ethanolic (50% ethanol v/v) LEAA dropwise in a proportion of 4:1 (v/v). Then mixed solution was adjusted (using 0.1 M NaOH) at pH 5, and heated for 1 hour at 70 °C on a hot plate containing a magnetic stirrer. The color change from yellowish-brown to reddish-white color was observed which indicated the formation of MZ NCs. Then the solution was sonicated at 25 ± 2 °C for 1 hour at 60 rpm and then centrifuged for 20 minutes at 6000 rpm. The obtained precipitates were washed with ethanol following DIW and then oven-dried at 80 °C for 10 hours, then calcinated at 400 °C for 2 hours. Then fine white powder was obtained and stored in the airtight sample holder (Panchal et al., 2019).

3.5.4 Synthesis of ZnO-MgO-CuO (ZMC) nanocomposities

Phytochemical mediated synthesis of trimetallic ZnO-MgO-CuO (ZMC) NCs involves the following steps: $Zn(NO_3)_2.4H_2O$ (100 mM), $Mg(NO_3)_2.6H_2O$ (100 mM) and $Cu(NO_{3)2}\cdot 3(H_2O)$ (100 mM) were prepared as three separate solutions. Each solution was stirred for 10 min at 30 ± 2 °C to obtain a homogeneous solution and then mixed together. Then 25 mL of ethanolic (50% ethanol v/v) LEAA prepared has been added drop wise to 100 mL of mixed salt solution in a proportion of 1:4 (v/v). The mixed solution was adjusted (using 0.1 M NaOH) at pH 5, and heated for 1 hour at 70 °C on a hot plate while string with a magnetic stirrer and formation of deep brown precipitate was observed. Then the solution was sonicated at 25 ± 2 °C for 1 hour at 60 rpm and then centrifuged for 20 minutes at 6000 rpm. The obtained precipitates were washed with ethanol following DIW and then oven-dried at 80 °C for 12 hours, then calcinated at 350 °C for 2 hours. Then the fine brown powder was obtained and stored in the airtight sample holder (Abbas et al., 2022; Batool et al., 2022). Figure 9 represents the schemes of phyto-mediated synthesis of MO NMs from ethanollic (50% ethanol v/v) LEAA.

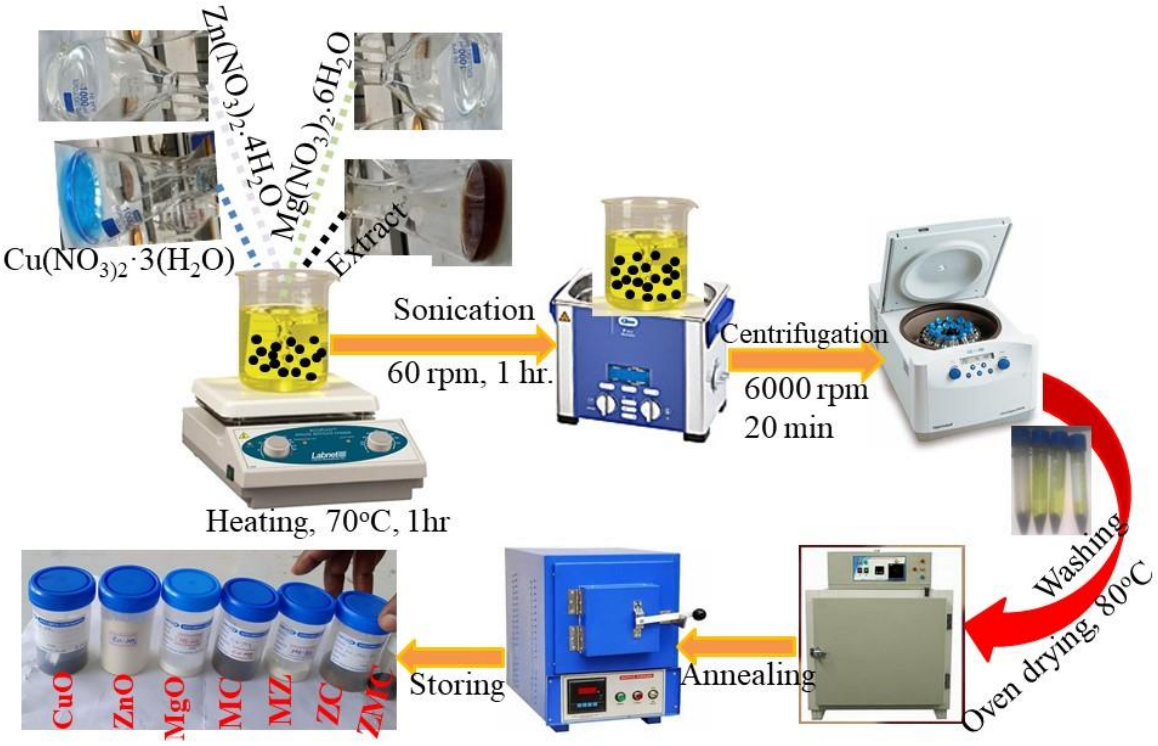

Figure 9. Schematic representation of phytochemical mediated synthesis of MO NMs using LEAA.

3.6 Characterizations of MO NMs

Phytochemical mediated synthesized mono (CuO, ZnO, and MgO), bi (ZC, MC and MZ) and trimetallic (ZMC) NMs were characterized by the following techniques.

3.6.1 Thermogravimetric/Differential thermal analysis of MO NMs

The TGA (Shimadzu TGA-60H) and DTA (Perkin Elmer, DTA 4000, USA) techniques under an N_2-atmosphere (20 mL/minute) using an eight mg dried samples between 35-800 °C with a heating rate of 10 ^{o}C/min were used to study the weight loss, and thermal stability of as-synthesized MO NMs.

3.6.2 UV-visible spectroscopy analysis of MO NMs

Biosynthesized MO NMs and LEAA are characterized by the UV-visible spectroscopy (Shimadzu, Tokyo, Japan). 1 mL of LEAA and MO NMs were taken in 10 mL flasks and diluted

with DIW and phosphate buffer at pH 7.4 was taken as blank and UV-visible spectra are obtained in the range of 200–800 nm.

3.6.3 Fourier transform-infrared spectroscopy analysis of MO NMs

Fourier transform infrared spectroscopy was carried out to examine the formation of MO NMs mediated by the functional groups in LEAA. The spectra of the considerable number of test samples (LEAA and MO NMs) were reported by KBr pellet production at room temperature spectrometrically (Shimadzu FT-IR spectrophotometer). The range was preserved at a resolution of 4 cm^{-1}, between 4000 and 400 cm^{-1}. FTIR analysis was conducted to classify the biomolecules essential for capping and stabilizing biosynthesized MO NMs.

3.6.4 X-ray diffraction study of MO NMs

The X-ray diffraction (XRD, Shimadzu, and XRD-7000) equipped with a Cu target for generating Cu Kα radiation (wavelength 1.5406 Å) was used to study the phase crystallinity and crystallite sizes of phytochemical mediated MO NMs. The measurements were made at room temperature, and the accelerating voltage and the applied current were 40 kV and 30 mA, respectively. The instrument was operated under step scan type with step time and degree (2θ) of 1s and 0.020°, respectively, over 2θ range of 10° to 80°. The crystallite sizes of MO NMs were calculated by Debye-Scherer equation and Williamson-Hall (W-H) approaches.

3.6.5 Scanning electron microscopy/energy-dispersive X-ray spectroscopy analysis of MO NMs

The surface morphological characteristics such as shape, size, and compostion of MO NMs are charceterized by scanning electron microscopy coupled energy-dispersive X-ray spectroscopy (SEM-EDX) (SEM, JEOL-JSM 6500F, made in Japan) machine with spectral imaging system and transmission electron microscopy. The test samples (MO NMs) for SEM investigation were developed by placing the filtered lyophilized nanoparticles on the network, which was allowed to dry under a mercury light after 10 min of drying for SEM study.

3.6.6 Transmission electron microscopy analysis of MO NMs

The internal morphology, particle size, and interplanar distance of synthesized MO NMs were characterized by transmission electron microscopy (TEM/HR-TEM/SAED, Tecnai F20 G2, Philips, and the Netherlands). Sample for TEM investigation was prepared by placing a small drop of suspended nanoparticles on a carbon-covered copper grid and enabling the dissipation of water into a vacuum dryer. TEM images were scanned on the grid containing MO NMs.

3.7 Biological Activity Test

3.7.1 Antioxidant activity test

The antioxidant activity of LEAA and biosynthesized MO NMs were evaluated using 1, 1-diphenyl-2 picrylhydrazyl (DPPH) and ferric-reducing antioxidant power (FRAP) assays.

3.7.1.1 DPPH assay

The *in vitro* antioxidant activity of LEAA and the MO NMs was evaluated using DPPH assay (Achamo, Zereffa, Murthy, Ramachandran, & Balachandran, 2022; Sirivibulkovit et al., 2018). The DPPH stock solution was prepared by dissolving 4 mg DPPH in 100 mL methanol and stored at 4°C in the dark condition for three hours to test the stability of the solution. Constant λ max of the solution observed at 517 nm revealed that the solution was stable throughout the experiment. 2 mL of 0.1 mM DPPH solution was mixed with 1 mL (200, 100, 50, 25, and 12.5 µg mL^{-1}) of LEAA, MO NMs, and ascorbic acid solutions. The reaction solutions were mixed and incubated for 30 minutes at 27±2 ^{o}C in the dark. Ascorbic acid and methanol were used as positive control and a blank, respectively. The absorbance of each solution was recorded at 517

nm using a UV-visible spectrophotometer in triplicate, and the results were expressed as mean ± standard deviation. Equation (1) was used to compute the DPPH radical scavenging abilities of LEAA, MO NMs, and ascorbic acid.

$$\text{DPPH scavenging activity (\%)} = \frac{AB-AS}{AB} \text{ x } 100 \qquad (1)$$

AB is the absorbance of the blank, and *AS* is the absorbance of the sample.

3.7.1.2 Ferric reducing antioxidant power assay

The *in vitro* antioxidant activities of biosynthesized MO NMs were evaluated using the ferric reducing antioxidant power (FRAP) assay (Benzie & Strain, 1996; Chau et al., 2022). Different concentrations (200, 150, 100, 50, 25, and 12.5 μg/mL, in H_2O) of each sample were mixed with 0.2 M potassium phosphate buffer (2 mL, pH 6.6) and potassium ferricyanide (2.5 mL, 10% w/v) solutions followed by incubation at 40 °C for 30 min. After centrifuging the incubated solutions for 10 minutes at 3000 rpm with trichloroacetic acid (2.5 mL, 10% w/v) added, a supernatant (5 mL) of each solution was combined with distilled water (2 mL) and ferric chloride (0.5 mL, 0.1% w/v). The absorbance of each solution was measured by a UV-visible spectrometer at 700 nm in triplicate and used to calculate the mean ± standard deviation of the ferric ion-reducing power of each sample.

3.7.2 Antimicrobial test

3.7.2.1 Antibacterial test

The agar disc diffusion method was used to evaluate the antibacterial activities of LEAA and the NPs. Muller Hinton Agar and Mulberry Hinton Broth as solid and liquid media, respectively, were used, according to the Clinical and Laboratory Standards Institute standard protocols (CLSI) (Yaqub et al., 2020). The density of bacteria was adjusted to 0.5 McFarland standard reagents and swabbed on a plate encompassing Muller Hinton culture media from a suspension of fresh bacterial cultures such as *E. coli*, *P. aeruginosa*, S. *pneumoniae*, and *S. aureus* added to the liquid medium to obtain turbidity similar to the McFarland standard. The disks were soaked with 50 μL of each sample (12.5 25, 50, 100, and 200 μg/mL). Chloramphenicol (positive control) impregnated standard discs (50 μg/mL) was used as standard antibiotics and DMSO as

(negative control). The cultures were incubated at 37 °C for 24 hours and then the zone of inhibition was measured with a ruler (in mm) to estimate the bacterial strains' liability to the samples. Also, every experiment was conducted in a triplicate petri dish, and the results were expressed as mean ± standard deviation using statistical analysis software (SPSS) (version 20).

3.7.2.2 Antifungal test

Agar well diffusion technique was used to analyze the antifungal test of LEAA and biosynthesized MO NMs (A. I. Adeyemi, Vincent, & Olujenyo, 2018). Sabouraud dextrose agar (SDA) culture media plates were made, injected with the *Aspergillus flavus*, *Aspergillus niger*, and *Candida albicans* fungal strains, and incubated at 25 °C for ten days to observe fungus growth. After ten days, a core borer was used to punch wells in the agar plate, and each well was injected with 12.5, 25, 50, 100, and 200 μg/mL DMSO dissolved samples. Standard drug fluconazole (50 μg/mL) and DMSO were positive and negative controls, respectively. The plates were left at 25 °C for one hour to allow the test sample to diffuse before being incubated at 25 °C for three days. The zones of inhibition were measured with a ruler (in mm) to estimate the liability of fungal strains to the samples. The experiment was conducted in triplicate, and the results were expressed as mean ± standard deviation.

3.7.2.3 Minimium inhibitory concentration

The minimium inhibitory concentration (MIC) of LEAA and biosynthesized MO NMs against bacterial (*E. coli*, *P. aeruginosa*, S. *pneumoniae* and *S. aureus)* and fungal (*Aspergillus flavus*, *Aspergillus niger*, and *Candida albicans) strains were deterimined* using the broth dilution method (Yaqub et al., 2020). Sterilized nutrient broth (5 mL) was taken into each test tube for minimum inhibitory concentration assay and inoculated with 100 μL of the freshly made test strain. Next, various concentrations of LEAA, and biosynthesized MO NMs (5, 10, 15, 20, 25, μg/mL) are added in the test tubes and incubated under an orbital shaker with 120 rpm for 24 hours at 37 °C. After 24 hours, each test tube was evaluated for turbidity at 600 nm using a Spectrophotometer. The bacterial and fungal colonies were concurrently treated with samples (LEAA and MO NMs), control (i.e., sterile media devoid of test solution), and blank (i.e., sterile media devoid of inoculums). MIC has been described to be the lowest samples concentration inhibiting bacterial and fungal growth. All the assays were conducted in triplicates.

3.7.3 Anticancer Test

3.7.3.1 Culturing of cells

Human peripheral blood mononuclear cells (HPBM) and breast cancer cells (MCF-7) were cultured according to the standard protocol (Sonbol et al., 2021). The standard cells were cultured in Dulbecco's Modified Eagle Medium (DMEM) added with inoculated Fetal Bovine Serum (FBS) 10% (v/v), penicillin (100 IU/ml), streptomycin (100 µg/mL) in impregnated conditions of 5% CO_2 at 37 ^oC while waiting for they become confluent. The cell was separated with cell separating solution (0.2% trypsin, 0.02% EDTA, 0.05% glucose in PBS (Fetal Bovine Serum). The viability of the cells is checked and centrifuged. Further, 50,000 cells /well were cultivated in a 96-well plate and nurtured for 24 hours at 37 ^oC, under 5% CO_2 in an incubator.

3.7.3.2 Cytotoxicity test of nanoparticles

3-(4,5-dimethylthiazol-2-yl)-2, 5diphenyltetrazolium bromide (MTT) assay was used to evaluate the *in vitro* cytotoxicity of NMs on PBM and MCF-7 cell lines (Elsayed et al., 2021; Sonbol et al., 2021). The standard cells were trypsinized and adjusted with $5x10^5$ cells/mL to count cells using respective media containing 10% FBS (v/v). To each well of the 96-well microtiter plate, 100 µL of the diluted cell suspension (50,000 cells/well) was added. The supernatant was removed 24 hours later, washed with medium, and 100 µL of different concentrations of samples were added to the partial monolayer in microtiter plates. The plates were then incubated at 37^oC for 24 hours under 5% CO_2 in an incubator. After incubation, the test solutions in the wells were rejected, and 0.05 mg MTT was added to each well. The plates were kept for four hours at 37 ^oC in 5% CO_2 atmosphere. The supernatant was removed, 100 µL of DMSO was added, and the plates were gently shaken to solubilize the formed formazan. The absorbance was measured using a microplate reader at 570 nm. The percentage growth inhibition was calculated using equation (2). The concentration of test drug needed to inhibit cell growth by 50% (IC_{50}) values was generated from the dose-response curves for each cell line.

$$\% \text{ Inhibition} = \frac{\text{OD of control} - \text{OD of samples}}{\text{OD of control}} \text{ x } 100 \qquad (2)$$

OD stands for optical density.

IC_{50} values for cytotoxicity tests were derived from a nonlinear regression analysis (curve fit) based on a sigmoid dose-response curve (variable) and computed using Graph Pad Prism 6 (Graph pad, San Diego, CA, USA).

3.8 Molecular Docking Study

The molecular interaction of the synthesized nanoparticles and the standard drugs (doxorubicin and chloramphenicol) were evaluated against the binding sites of estrogen receptor alpha (ERα; PDB: 5GS4), dihydrofolate reductase (PDB: 2w9h) (DHR) and *E. coli* DNA gyrase B (PDB ID 6F86) which are important targets of MCF7, *S. aureus*, and *E.coli* respectively AutoDock 4.2 (MGL tools 1.5.7) program (Khalil et al., 2018; Morris et al., 2009). The geometry of the standard drugs and nanoparticles was optimized using the B3LYP-GD3/6 311++G(d,p)/LanL2DZ approach before the molecular docking investigation, and it was then translated to PDB files using GaussView 6. The protein database was used to download the crystal structures of the estrogen receptor alpha (ER; PDB: 5GS4), dihydrofolate reductase (PDB: 2w9h), and *E. coli* DNA gyrase B (PDB ID 6F86). These structures were then processed by adding polar hydrogen and cofactors, and removing the co-crystallized ligand, and water molecules according to the AutoDock 4.2 (MGL tools 1.5.7) program. After cleaning the protein, only polar hydrogen and the Kollman charges were introduced. The grid center coordinates were 65, 65, and 65, pointing in the x, y, and z directions, respectively, with a grid point spacing of 0.375 Å. The center grid box was -12.055, -10.491, and 5.964 Å. 100 different conformation was generated for each targeted ligand and the nanoparticles. The conformation of the nanoparticles and the standard drugs with the lowest free binding energy were selected to analyze their interactions with the receptors using the Discovery Studio Visualizer.

3.9 Statistical Data Analysis

All the experimental results were conducted in triplicate and expressed as mean ± SD using the one-way analysis of variance (ANOVA) function of the statistical package for Social Science (SPSS) version 20. Data analysis was also done with ImageJ (imajej153-win java8imagejimagej.exe), Gatan Microscopy Suite software (GMS 64bit) version 2.x, and Origin software (Originpro 9.0 64bit). The docking studies of MO NMs and the target were analyzed by using the AutoDock 4.2 (MGL tools 1.5.7) program. IC_{50} values for cytotoxicity

tests were computed using Graph Pad Prism 6 (Graph pad, San Diego, CA, USA).

4. RESULTS AND DISCUSSION

In this work, an eco-friendly, cost-effective mono- (CuO, ZnO, and MgO), bi- (CuO-ZnO, CuO-MgO, ZnO-MgO), and tri-metallic (CuO-ZnO-MgO) oxide NMs using LEAA were successfully synthesized. The effects of reaction parameters such as precursor salts ($Cu(NO_3)_2.3H_2O$, $Zn(NO_3)_2.4H_2O$ and $Mg(NO_3)_2.6H_2O$) concentration, pH, volume of ethanolic (50% ethanol v/v) LEAA and temperature on the synthesis of MO NMs were optimized. The thermal stability, crystallinity nature, size as well as surface morphological characteristics such as shape, size, and composition of synthesized MO NMs were characterized using TGA, XRD, FTIR, UV-vis, SEM, EDX, and TEM techniques. Finally, the biological applications of the synthesized MO NMs against FRAP and DPPH radical, gram-negative and gram-positive bacterial strains, pathogenic fungal strains, and *breast cancer* (MCF-7) cell lines were evaluated. The binding affinity of phytochemical mediated synthesis MO NMs against *S. aureus* dihydrofolate reductase (PDB: 2w9h), *E. coli* DNA gyrase B (PDB: 6F86), and estrogen receptor alpha (ERα; PDB: 5GS4) via *in-silico* molecular docking simulations. In this chapter, details of the results and discussion are presented.

4.1. Phytochemical Screening

The qualitative phytochemical analysis of *Artemisia abyssinica* (LEAA) was carried out using coloring and precipitating chemical reagents. The phytochemical screening presented in Table 4 revealed positive results for polyphenols, flavonoids, alkaloids, tannins, terpenoids, and saponins in aqueous, 50% ethanol (water and ethanol, 1:1 v/v), and n-hexane extracts. The absence of proteins, anthraquinones, carbohydrates, steroids, resins, and glycosides was also observed in the LEAA prepared from the three solvents. Nevertheless, the presence of more significant level of phyto-constituents were observed (Table 4) in ethanolic (water and ethanol, 1:1 v/v) LEAA than aqueous and n-hexane LEAA. Therefore, using the ethanolic extract to synthesize MO NMs is preferable to aqueous and n-hexane LEAA.

Consequently, polyphenols, flavonoids, alkaloids, tannins, terpenoids, and saponins present in ethanolic (water and ethanol, 1:1 v/v) LEAA have roles on synthesis and stabilizations of MO NMs. However, due to the presence of the polyhydroxy groups, polyphenols, flavonoids, and alkaloids are more reactive and responsible for the reduction and stability of MO NMs.

Moreover, functional groups of polyphenols with aromatic and aliphatic properties and low molecular weight have more of a role in MO NMs synthesis (Santhosh et al., 2023). Flavonoids and alkaloids could also be involved in the synthesis of NMs, since their terminal hydroxyl groups have ability to convert divalent metals to MO NMs (Tabrez et al., 2022a). Similarly, the involvement of polyphenols, flavonoids, and alkaloids in the synthesis and stability of MO NMs were reported in different studies (Król, Railean-Plugaru, Pomastowski, & Buszewski, 2019; Letchumanan, Sok, Ibrahim, Nagoor, & Arshad, 2021).

Table 4. Phytochemical screenings of LEAA using aqueous, 50% ethanol (water and ethanol, 1:1 v/v) and n-hexane.

Phytochemicals	**Test used**	**LEAA tested**		
		Aqueous	**(50%, v/v) Ethanol**	**Hexane**
Polyphenols	Ferric Chloride Test	**	***	***
Alkaloids	Mayer's Test and Dragendroff's Test	**	***	**
Flavonoids	Alkaline reagent test and Lead acetate test	**	***	**
Proteins	Biuret test	-	-	*
Anthraquinones	Borntragor's Test	-	-	-
Carbohydrates	Benedicts Test	-	-	-
Tannins	Wohler's Test	*	*	**
Steroids	Salkowski's Reaction	-	-	-
Saponines	Foam test	**	*	-
Resins	Turbidity test	-	-	-
Terpenoids	Salkowski test	*	**	***
Glycosides	Molisch's Test	-	-	-

(***) = present in significant level, (**) = present in medium level, (*) = present in trace amount, and (-) = absent.

4.2 Phyto-mediated Synthesis of MO NMs

Synthesis of mono (CuO, ZnO, and MgO), bi (CuO-ZnO, CuO-MgO, ZnO-MgO), and trimetallic (CuO-ZnO-MgO) oxide NMs were performed using phytochemicals from ethanolic (water and ethanol, 1:1 v/v) LEAA as a reducing and stabilizing ligands (Figure 10). The preliminary confirmations of the formation of the MO NMs were acquired by the decrease in the

color intensity of the LEAA. This is ascribed to the fact that the phytochemicals of the LEAA get degraded when carrying out the reduction and stabilization processes for the formation of MO NMs. Apart from the color transition of the LEAA, the appearance of characteristic surface plasmon resonance (SPR) peaks of UV-vis spectra presente in (Figure 25) affiliated with the MO NMs further confirmed the formation of the NMs through the utilized green route. Moreover, successful synthesis of MO NMs using LEAA were also confirmed using further analysis as discussed in characterization section.

The proposed reaction mechanism of the phytochemical mediated synthesis of MO NMs from precursor salts and LEAA is presented in Figure 10. The major phytochemicals present in LEAA are phenolic compounds such as polyphenols, alkaloids, flavonoids, and terpenoids, which are used as ligand agents (Sonbol et al., 2021). These major active compounds, as also confirmed in the discussion parts from FTIR of this study, are the possible agents that participate as reducing and capping ligands. In light of this, a proposed reaction scheme for forming MO NMs is presented as follows.

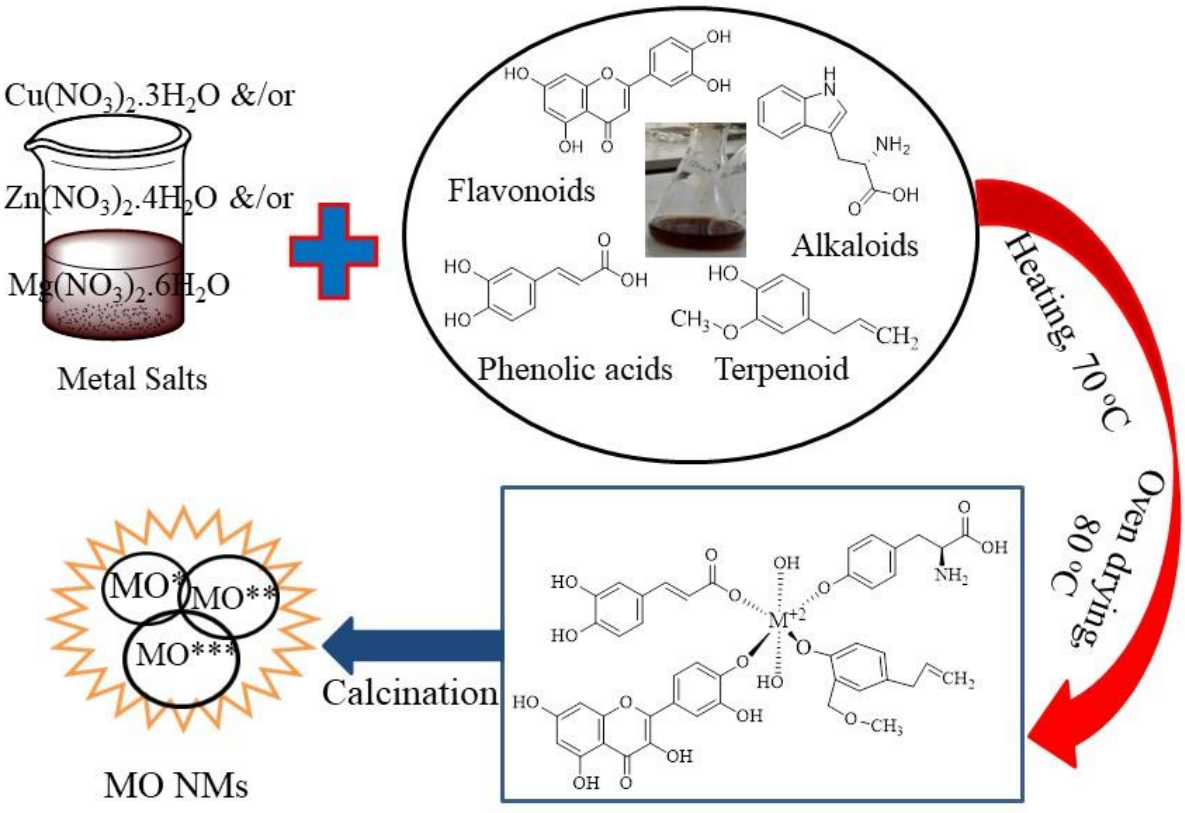

Figure 10. Scheme of the proposed reaction mechanism of MO NMs formation.

Note: MO* = monomeyallic, MO** = bimetallic and MO*** = trimetallic oxide NMs

4.2.1 Optimization of the reaction parameters

The effects of precursor salts ($Cu(NO_3)_2 \cdot 3H_2O$, $Zn(NO_3)_2.4H_2O$ and $Mg(NO_3)_2.6H_2O$) concentration, pH, volume of ethanolic (50 % ethanol v/v) LEAA and temperature on the size and yields MO NMs were optimized and discussed below.

4.2.1.1 Optimization of precursor salts concentration

The effect of $Cu(NO_3)_2 \cdot 3H_2O$ concentration on the synthesis of CuO NPs was investigated by varying the concentration (0.01, 0.1, 0.3, 0.5, and 1M) while keeping the pH (7.5 units), volume of LEAA to precursor salts ratio (10:40 mL) and temperature (60±2 °C) (De, Das, Jain, & Kaur, 2022). The characteristic SPR absorption peak of CuO NPs at a wavelength of 400-410 nm was observed in three out of five tests of the UV-Vis spectrum (Figure 11a), indicating that the concentration range of 0.01 to 0.3 M was appropriate for the synthesis of CuO NPs. However, no SPR peaks were observed for 0.5 and 1 M $Cu(NO_3)_2 \cdot 3H_2O$ using similar volumes of LEAA. Therefore, using the salt at a concentration above 0.3 M is not recommended because an increment in the salt concentrations does not favour the formation of CuO NPs.

Besides the appearance of the characteristic SPR spectrum regarding the synthesis of the CuO NPs, the intensity of the absorption peak can be used to carry out the quantitative analysis of yields of nanoparticles (Sonbol et al., 2021). Since the absorbance of the peak is directly proportional to the concentration of the absorbing species in the medium. The SPR peak at 405 nm when using 0.1 M of salt is more intense, and the maximum yield of CuO NPs was achieved compared to the yields when using 0.01 and 0.3 M of salt. Consequently, using 0.1 M of $Cu(NO_3)_2 \cdot 3H_2O$ was preferred for the phytochemical mediated synthesis of CuO NPs using the fixed volume of LEAA.

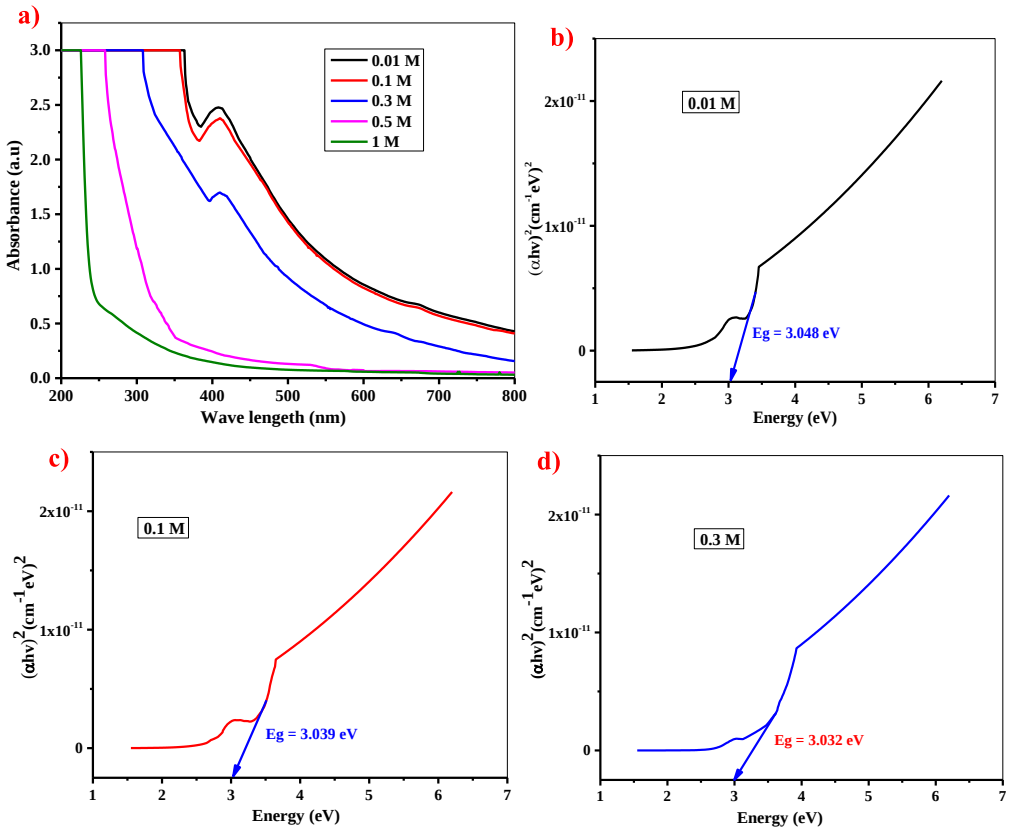

Figure 11. a) UV–Vis absorbance for CuO NPs prepared at different precursor concentrations; Tauc plot for CuO NPs prepared at precursor concentration of b) 0.01 M, c) 0.1 M and d) 0.3 M

The effect of $Mg(NO_3)_2 \cdot 6H_2O$ concentration on the synthesis of MgO NPs was also evaluated using various (0.01, 0.1, 0.3, 0.5, and 1 M) concentrations while keeping the pH at 7.5, the volume of LEAA to precursor salts ratio (10:40 mL) and temperature (30±2 °C). Three out of five (0.01, 0.1 and 0.3 M) concentrations exhibited the characteristic SPR absorption peaks of the MgO-NPs at a wavelength of 265-284 nm (M. I. Khan et al., 2020b), presented in Figure 12a. However, at 0.5 and 1 M of $Mg(NO_3)_2 \cdot 6H_2O$ with a fixed volume of LEAA, no SPR peaks of MgO NPs were observed. As a result, the concentration range from 0.01 to 0.3 M was adequate for synthesizing the MgO-NPs. However, the SPR absorption peaks at 265 and 267 nm generated using 0.01 and 0.1 M concentrations are relatively higher than the SPR produced using 0.3 M. Therefore, the maximum yield of MgO NPs was expected using 0.01, and 0.1 M than 0.3 M. As a result, 0.01, and 0.1 M of $Mg(NO_3)_2.6H_2O$ are the optimum concentrations for synthesizing MgO NPs with a fixed volume of LEAA.

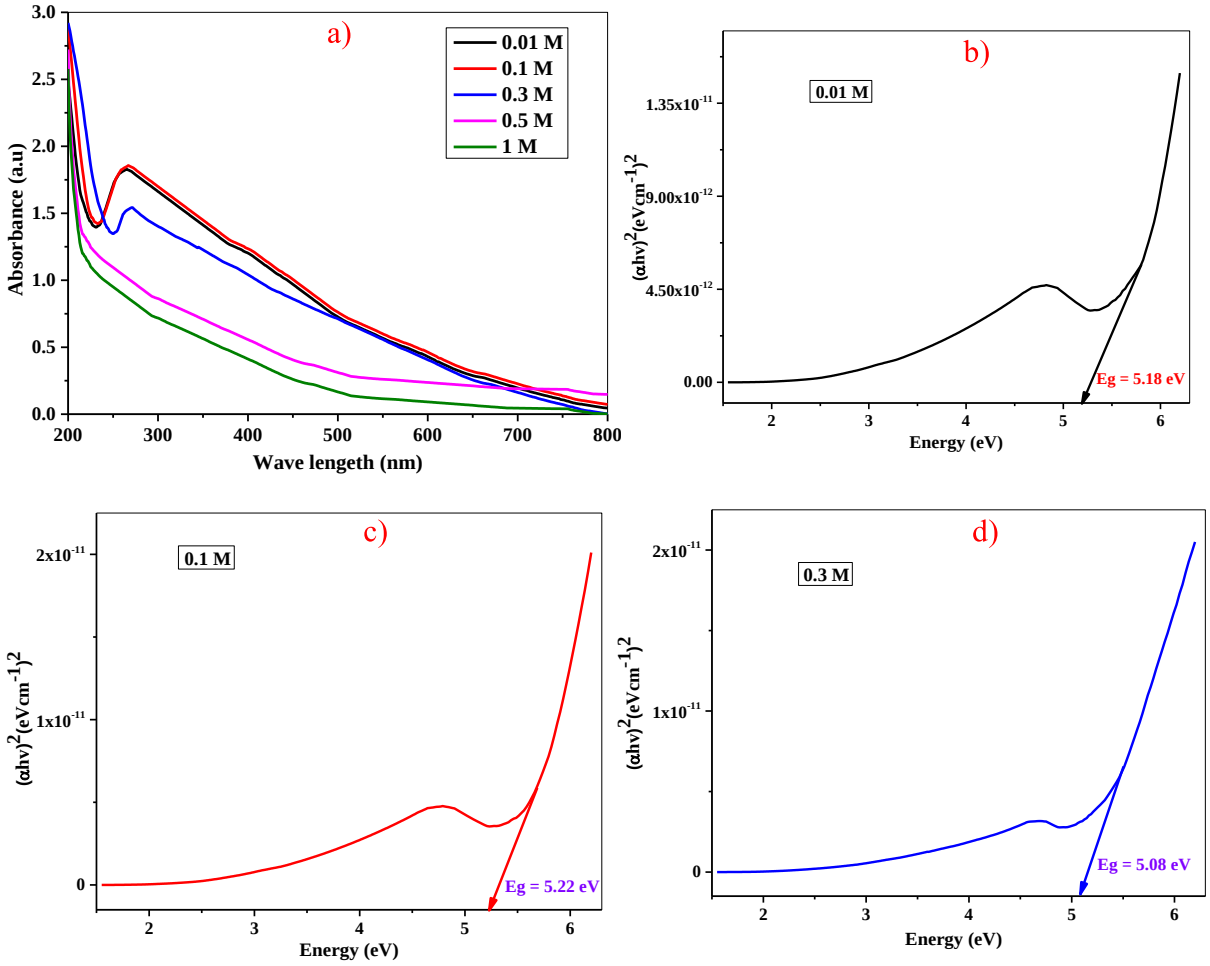

Figure 12. a) UV–Vis absorbance for MgO NPs prepared at different precursor concentrations; Tauc plot for MgO NPs prepared at precursor concentration of b) 0.01 M, c) 0.1 M and d) 0.3 M

Similarly, the optimization of $Zn(NO_3)_2 \cdot 4H_2O$ concentrations on the formations of ZnO NPs was also assessed by varying from 0.01 to 1M (0.01, 0.1, 0.3, 0.5, 1 M) and keeping the pH at 7.5, volume of LEAA to precursor salts ratio (10:40 mL) and temperature (30 ± 2°C). The results in Figure 13a have revealed that the characteristic SPR bands of ZnO NPs at wavelength of 360-372 nm (Mthana et al., 2022) have been seen at concentrations of 0.01, 0.1, and 0.3 M. Among the three concentrations, the most intense SPR peak was at 0.1 M, and as a result, more yields were obtained than the rest. However, at high concentrations (0.5 and 1 M), no SPR peaks were

revealed; hence, these concentrations are not feasible for synthesizing ZnO NPs.

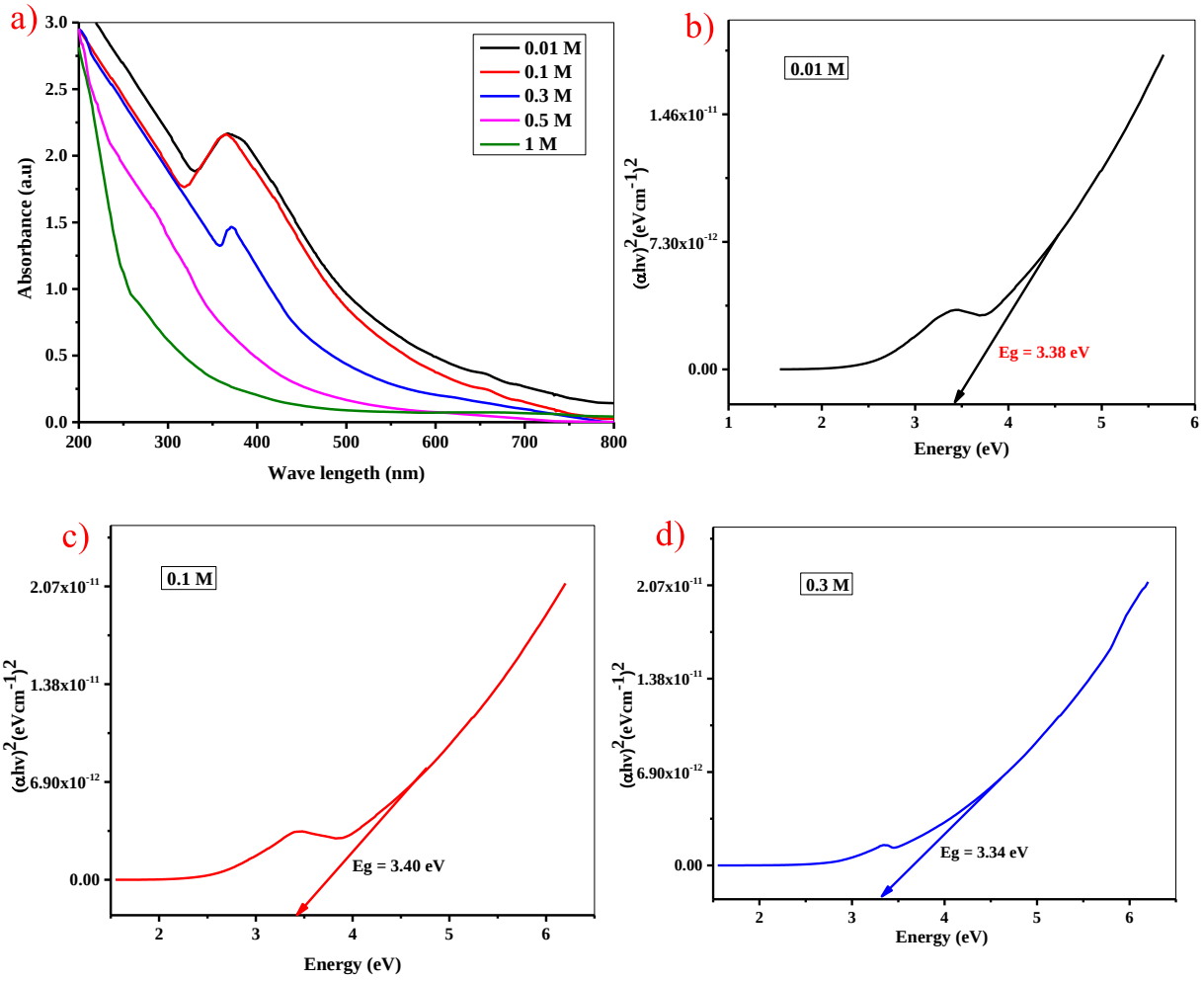

Figure 13. a) UV–Vis s absorbance for ZnO NPs prepared at different precursor concentrations; Tauc plot for ZnO NPs prepared at precursor concentration of b) 0.01 M, c) 0.1 M and d) 0.3 M

In general, exceedingly high concentrations (0.5 and 1 M) of salts were found undesirable for the synthesis of CuO NPs, MgO NPs, and ZnO NPs using fixed volume of LEAA. This was attributed to the fact that phytochemicals in the extract were unable to completely reduce the excess amounts (0.5 and 1 M) of precursor salts present in the reaction medium. Furthermore, the minimum nanostructures generated could also be agglomerated with the unreacted salt solutions present in the reaction medium for achieving surface stability. This led to the formation of very large-sized clusters in the reaction medium, making this reaction condition inappropriate for the synthesis of the MO NPs (Siddiqui, Parra, & Haque, 2018).

The UV–Vis spectrum of the MO NMs was further utilized to calculate the Eg values (eV) of the synthesized nanostructures by using the following empirical formula (Equation 3) (Ngom, Ngom, Sackey, & Khamlich, 2021):

$$(\alpha h\nu)^2 = (h\nu\text{-}Eg) \quad (3)$$

hν represents the optical energy, and α represents the absorptivity coefficient of the material.

The Tauc plots of CuO NPs illustrated in Figure 11 (b-d) indicated that band gap energy (Eg) values using 0.01, 0.1, and 0.3 M were 3.048, 3.039, and 3.032 eV, respectively. The band gaps obtained when using 0.01 and 0.1 M of salts are slightly higher than that of 0.3 M, which results in the formation of smaller CuO NPs. However, using 0.1 M, small NPs with high yields are expected. Figure 12 (b-d) presents the Tauc plots of MgO NPs showing Eg values of 5.18, 5.22, and 5.08 eV using 0.01, 0.1, and 0.3 M respectively. As a result, using 0.01 and 0.1 M, small NPs with greater yields are produced. However, using 0.1 M, small-sized MgO NPs with high yields were produced comparably. The Eg values using 0.01, 0.1, and 0.3 M from the Tauc plots of ZnO NPs in Figure 13 (b-d) are 3.38, 3.40, and 3.34 eV respectively. The results show that small NPs with high yields are produced using 0.1 M. Regarding the size and yields of NPs, 0.1 M of precursor salts is optimum for synthesizing MO NMs.

4.2.1.2 Optimization of pH

The effect of pH on the synthesis of CuO, MgO, and ZnO NPs were also investigated by varying the pH (3, 5, 7.5, 9, and 11) and keeping the precursor salts concentration (0.1 M), volume of LEAA to precursor salts ratio (10:40 mL) and temperature (60±2 °C). As UV-vis spectra of CuO, MgO, and ZnO NPs are illustrated in (Figures 14-16). The characteristic SPR bands were observed at three of the tested pH (3, 5 and 7.5). The results indicated that the three pH values are essential for the synthesis of CuO, MgO, and ZnO NPs. However, higher absorbances with sharp peaks were observed at pH 5 than the rest. Therefore a maximum yield of NPs was achieved at pH 5 and is optimum for the synthesis of MO NMs.

On the other hand, at high values of pH (9 and 11), the formations of NPs were inhibited. This observation is attributed to the fact that the increment in pH values directly affects the nature of charge present at the secondary metabolites of the LEAA. This change in the nature of charge affects the binding and reducing capability of the phyto-constituents (Thamer, Muftin, & Al-

Rubae, 2018). At low pH values, the active form of the phytochemicals demonstrated the capability to reduce the precursor metal salts, which is in agreement with the nature of the metabolites present in the LEAA. As the metabolites belong to the polyphenolic, alkaloid and flavonoid classes, the acidic nature of these compounds was quenched in the basic environment owing to neutralization and hydrolytic reactions. Thus, the greater concentration of the hydroxyl ions (OH^-) in the basic medium electrostatically favored the aggregation over the reduction processes, leading to the inability of the metabolites to form MO NPs at higher pH values (Tabrez et al., 2022a).

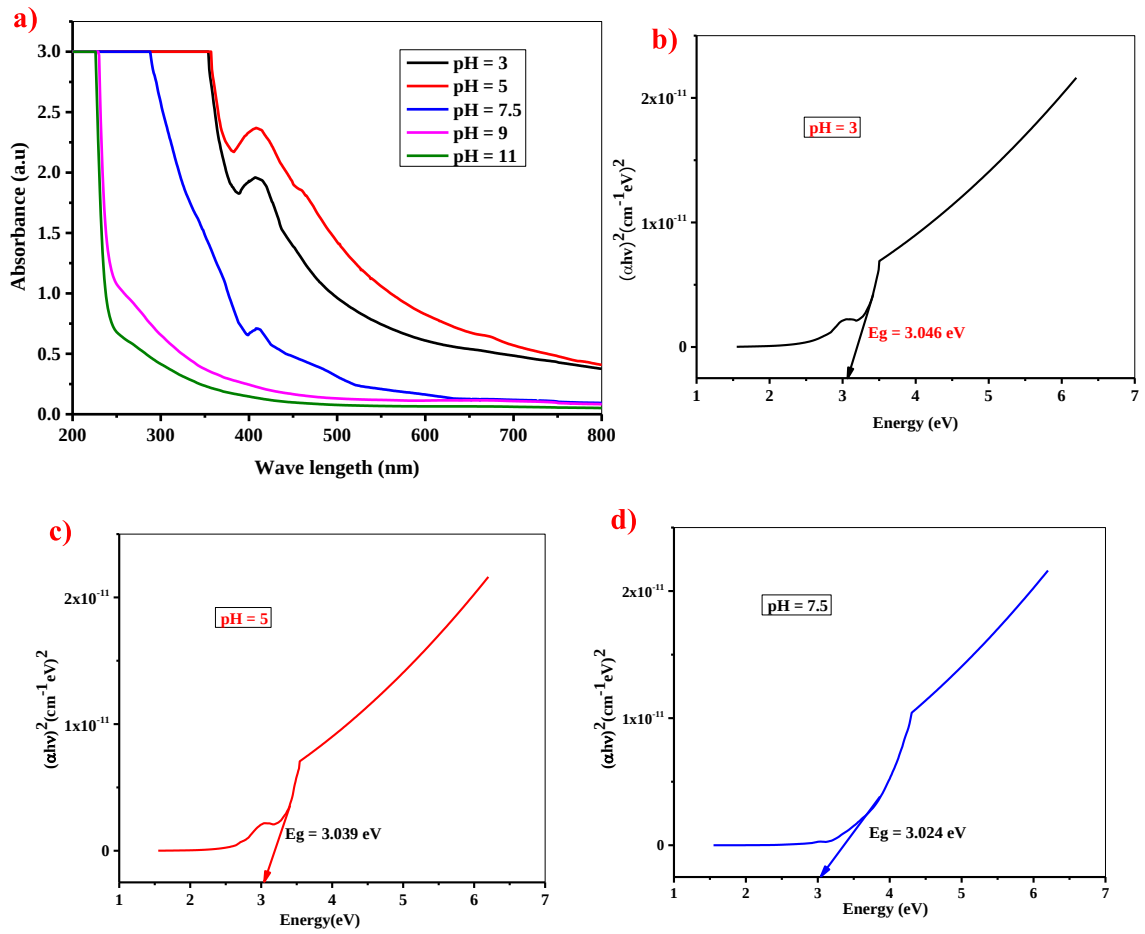

Figure 14. a) UV–Vis absorbance of CuO NPs prepared at different pH values; Tauc plot for CuO NPs at pH b), 3 c) 5 and d) 7.5.

Furthermore, SPR absorption peaks and Tauc plots in Figures 14(b-d), 15(b-d), and 16(b-d) showed at pH 5 the existence of more intense peaks with moderate band gaps than pH (3 and 7.5). As a result, small-sized CuO, MgO, and ZnO NPs with high yields have been produced at pH 5 (M. I. Khan et al., 2020a). Therefore, the optimized pH for the synthesis of MO NMs using LEAA was found to be 5.

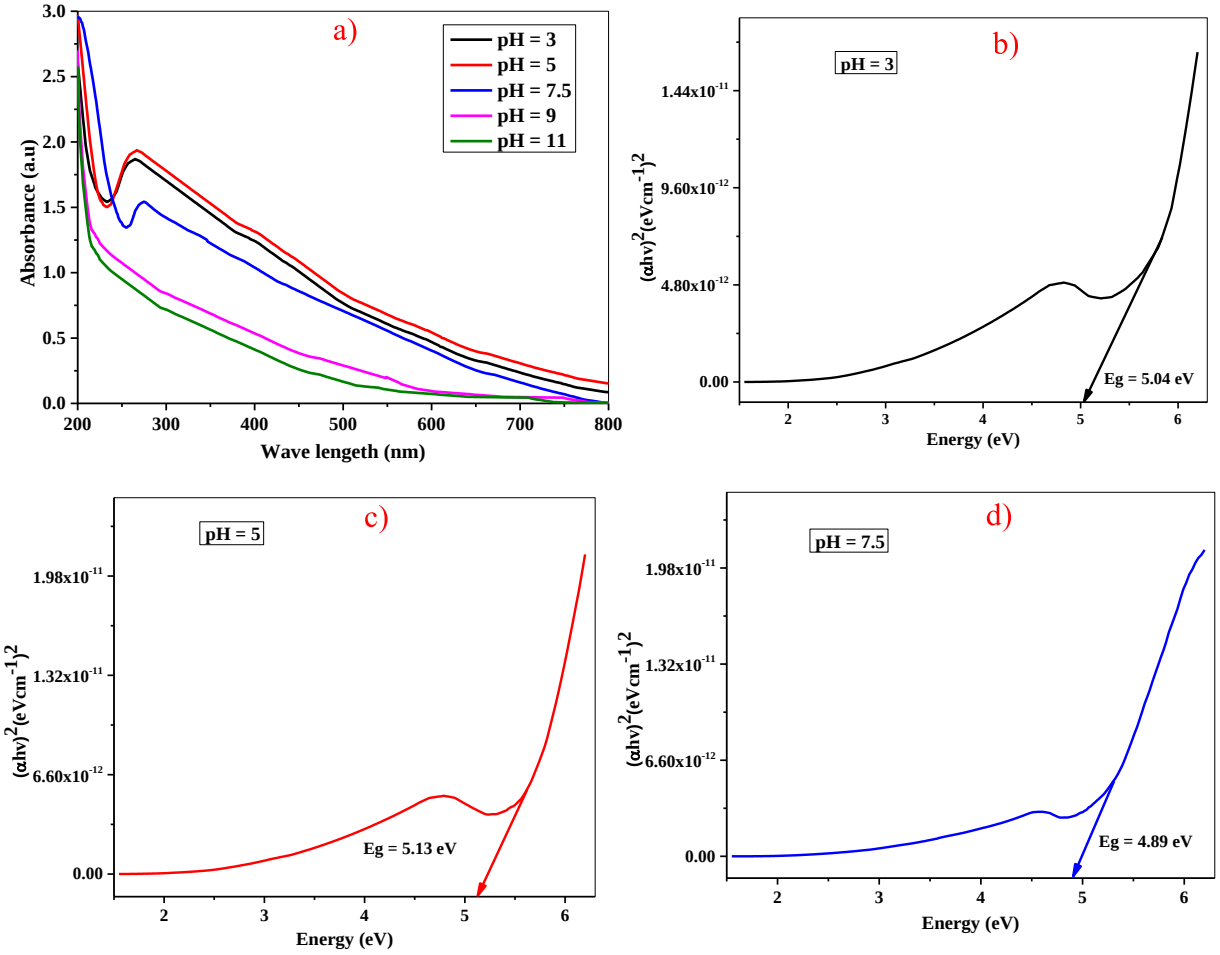

Figure 15. a) UV–Vis absorbance of MgO NPs prepared at different pH values; Tauc plot for MgO NPs at pH b), 3 c) 5 and d) 7.5.

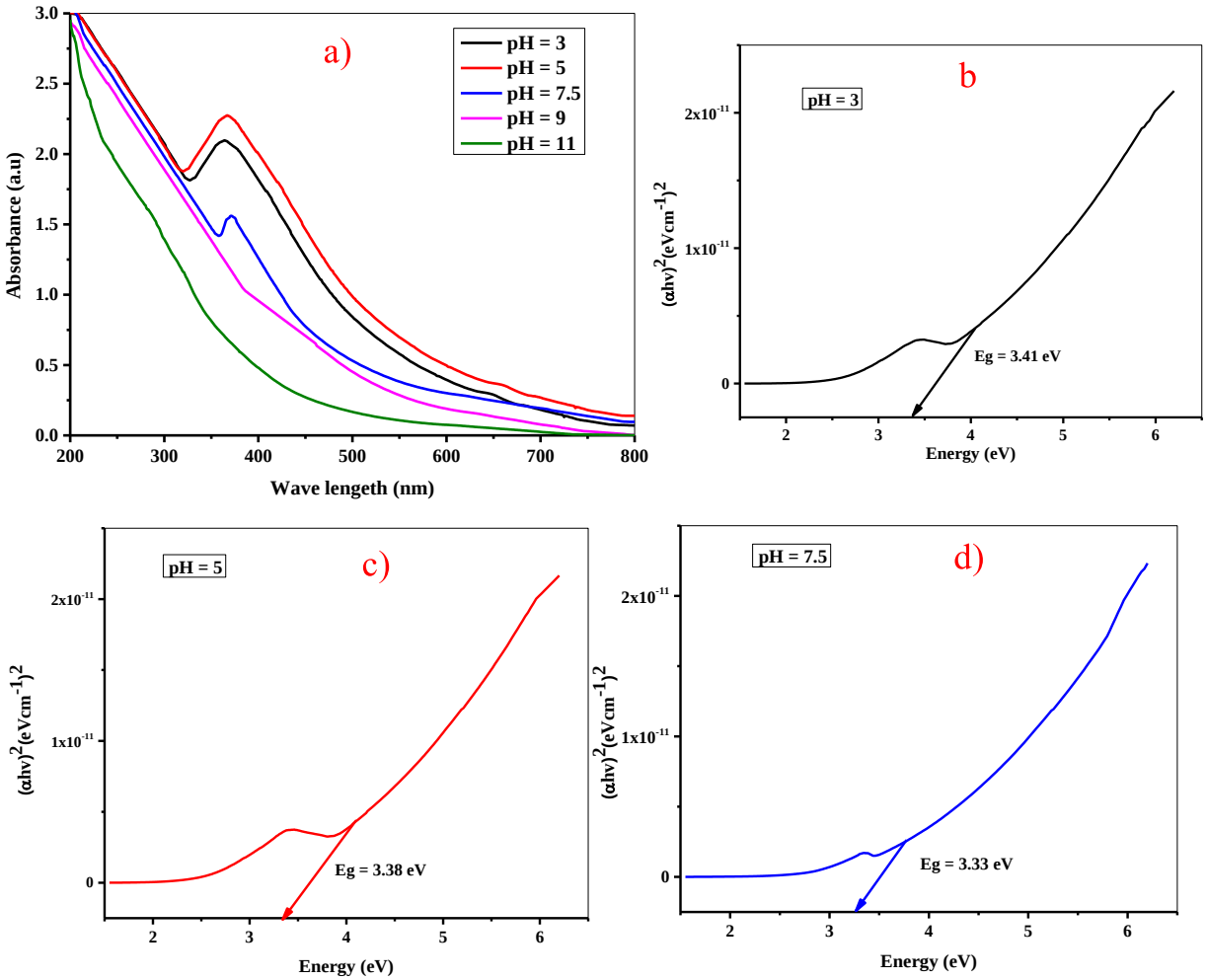

Figure 16. a) UV–Vis absorbance of ZnO NPs prepared at different pH values; Tauc plot for ZnO NPs at pH b), 3 c) 5 and d) 7.5.

4.2.1. 3 Optimization of LEAA volumes

The effect of LEAA volume (5, 10, 20, 30, and 40 mL) was assessed by varying the ratios (5:40, 10:40, 20:40, 30:40, and 40:40 mL (v/v)) of 0.1 M precursor salts $Cu(NO_3)_2{\cdot}3H_2O$, $Mg(NO_3)_2{\cdot}6H_2O$, and $Zn(NO_3)_2{\cdot}4H_2O$ while keeping pH at 5 and temperature at (60±2 °C). From Figures 17-19, it is seen that SPR peaks of CuO, MgO, and ZnO were observed at LEAA-to-precursor salt ratios of 10:40 and 20:40, which implied the successful formation of CuO, MgO, and ZnO NPs. As the LEAA volumes in the reaction media rose, the characteristic peaks shifted to longer wavelengths. The SPR peaks of CuO, MgO, and ZnO NPs were not revealed at higher LEAA-to-precursor salt ratios of 30:40 and 40:40 and at the lower LEAA-to-precursor

salt ratio of 5:40. According to the findings, a moderate amount (10:40 and 20:40) of LEAA is required to synthesize MO NPs because a sufficient amount of phytochemicals were available in the reaction medium to enable the synthesis and stability of nanostructures. At a lower volume of LEAA (5:40), the amount of existing phytochemicals could not stabilize the particles; however, by raising the phytochemical amounts to higher volumes (30:40 and 40:40), the small-sized NPs owing to their higher instability aggregated leading to large-sized CuO, MgO, and ZnO NPs (Tabrez et al., 2022a).

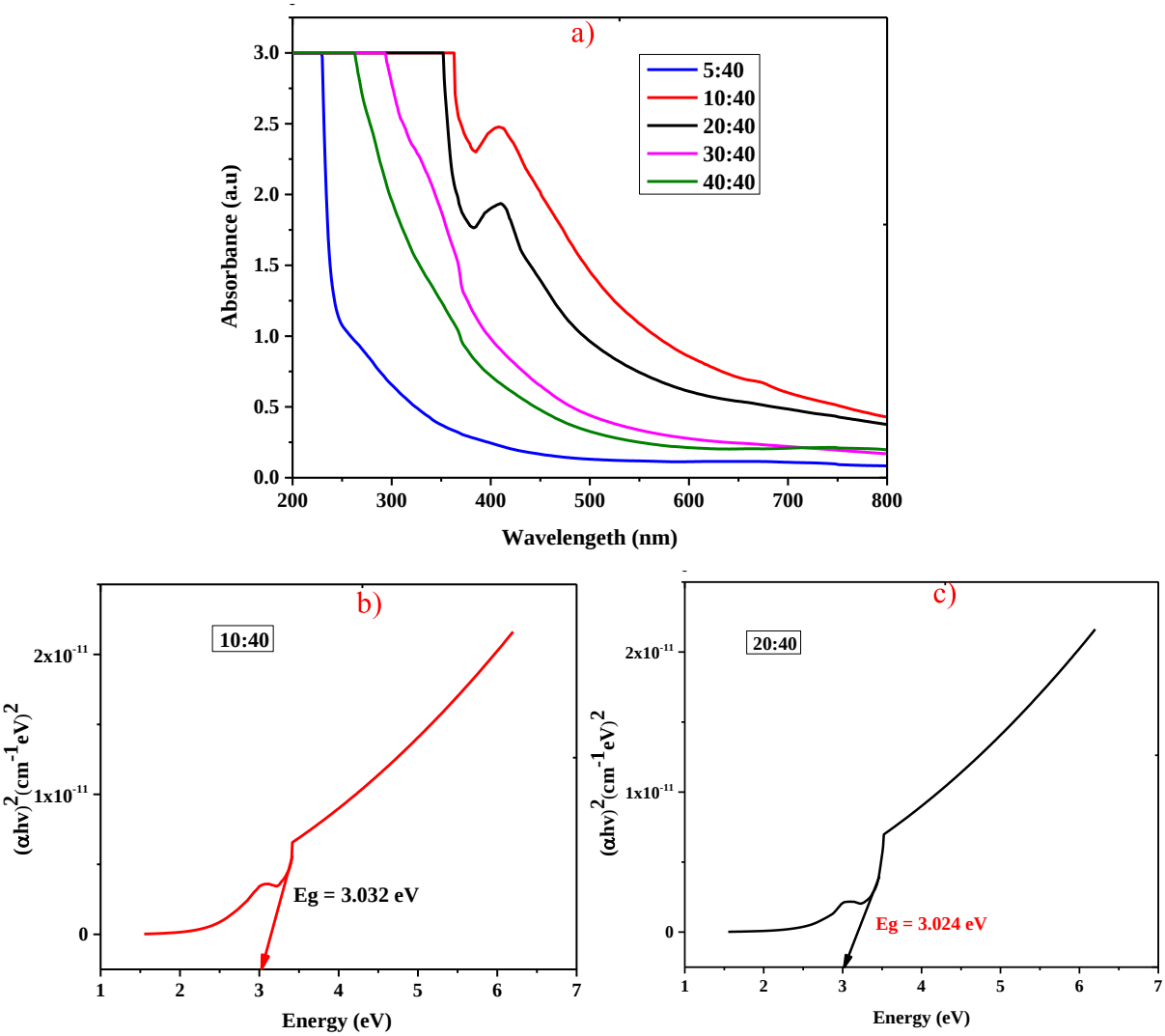

Figure 17. a) UV–Vis absorbance of CuO NPs prepared at different LEAA volumes; Tauc plot for CuO NPs at b) 10:40 and c) 20:40 mL LEAA-to-$Cu(NO_3)_2 \cdot 3H_2O$ ratios.

The Tauc plots, Figure 17(b-c), illustrate the band gap energy (Eg) values of CuO NPs using LEAA-to-precursor salt ratios (10:40 and 20:40) were 3.032 and 3.024 eV, respectively. The results signify that by using 10:40 ratio, band gap energy (3.032 eV) is slightly larger than the band gap at 20:40 (3.024 eV) ratio and hence the smaller CuO NPs have been produced. Similarly, from the Tauc plots of MgO and ZnO NPs in Figures 18(b-c) and 19 (b-c) small NPs with high yield are synthesized using a ratio of 10:40. Thus, LEAA-to-precursor salts ratios of 10:40 is optimum for the synthesis of CuO, MgO and ZnO NPs using LEAA (El-Saadony et al., 2020).

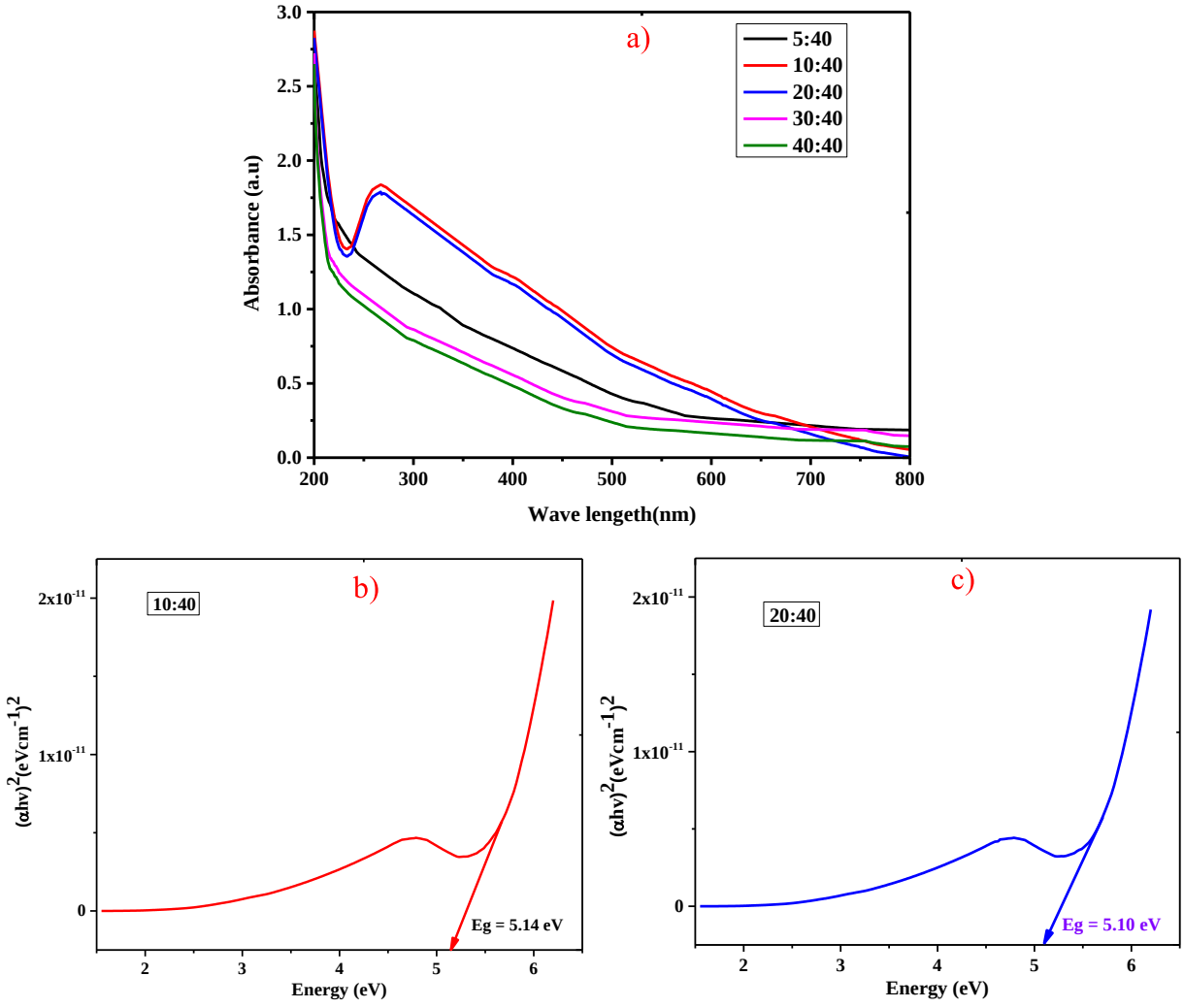

Figure 18. a) UV–Vis absorbance of MgO NPs prepared at different LEAA volumes; Tauc plot for MgO NPs at b) 10:40 and c) 20:40 mL LEAA-to-$Mg(NO_3)_2 \cdot 6H_2O$ ratios.

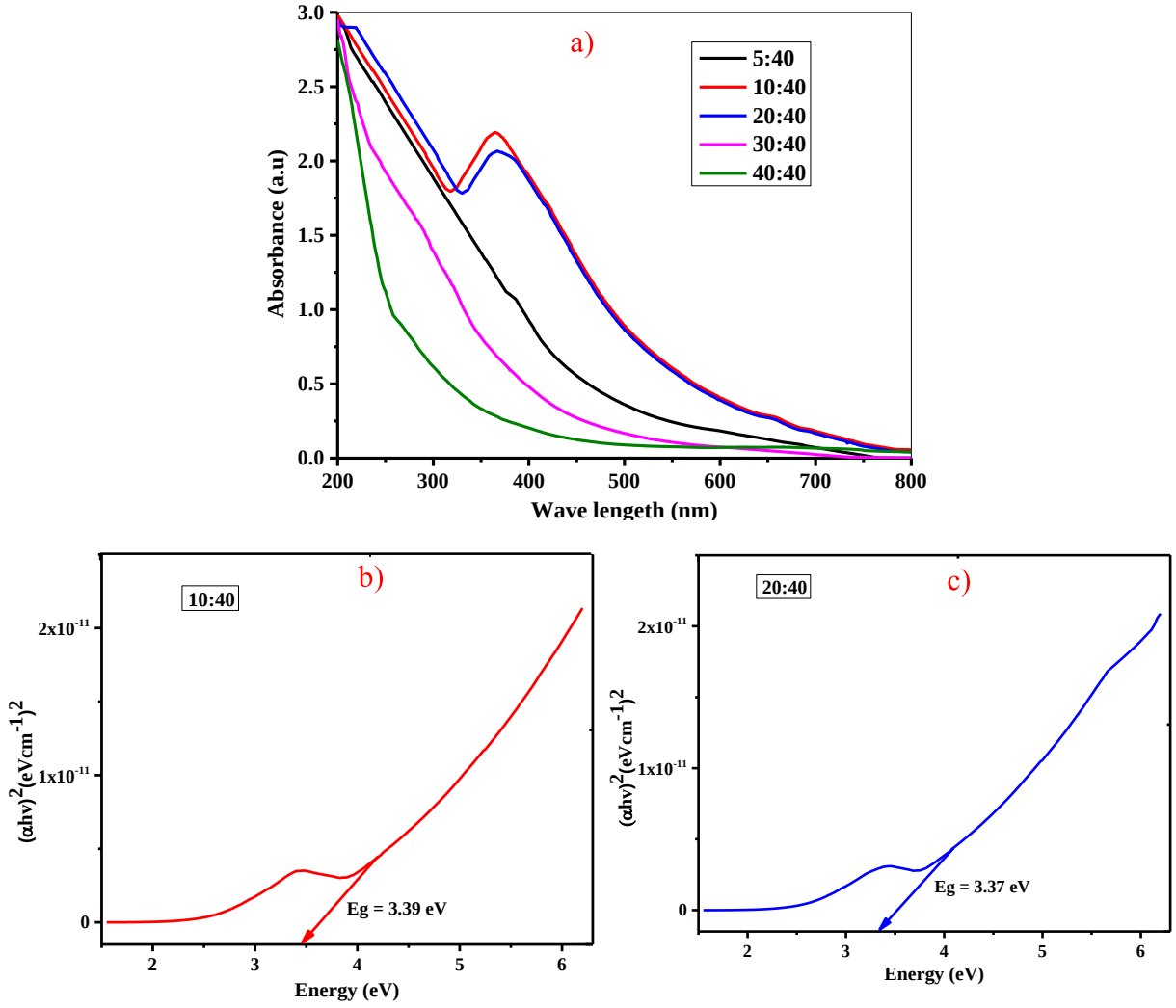

Figure 19. a) UV–Vis absorbance of ZnO NPs prepared at different LEAA volumes; Tauc plot for ZnO NPs at b) 10:40 and c) 20:40 mL LEAA-to-$Zn(NO_3)_2 \cdot 4H_2O$ ratios.

4.2.1.4 Optimization of reaction temperatures

The synthesis of the MO NPs can further be optimized by varying the reaction temperature of the medium from 30 to 80 °C while keeping precursor salts concentration at 0.1 M, pH at 5, and LEAA-to-precursor salts ratio 10:40 mL (v/v). The spectral analyses of the synthesis reaction carried out at numerous temperatures are presented in Figures 20-22. Similar to the factor of precursor salts, pH, and extract volume, the temperature variation directly influenced the reaction constituents of the medium (Fayaz, Balaji, Kalaichelvan, & Venkatesan, 2009). Therefore, the heat stability of the phytochemicals was critical for the biosynthesis of CuO, MgO, and ZnO

NPs. If the appropriate temperature is not used during the synthesis, the phytochemicals could be decomposed, and the nanostructure reduction and stabilization process would be suppressed (Biswal & Misra, 2020).

The UV–Vis spectra of CuO, MgO, and ZnO NPs (Figures 20-22) depicted the appearance of SPR peaks in all tested temperatures. However, the three temperatures (50 °C, 60 °C and 70 °C) highly influenced the biosynthesis of CuO, MgO, and ZnO NPs. Among the three temperatures relatively maximum absorbance was observed at 70 °C and moderate absorbance were observed in the case of 50 °C and 60 °C. As a result, biosynthesis of MO NPs with high yields was expected at 70 °C using LEAA. Low absorbances were observed at 30 °C, 40 ^{o}C and 80 ^{o}C temperatures. This was attributed to the fact that the lower temperatures (30°C and 40^{o}C) were unable to efficiently initiate phytochemicals to carry out the process of reduction and stabilization. While at higher temperature conditions (80 ^{o}C), the phytochemicals destabilize, and the collision frequency of the nanocrystals increases, leading to the aggregation of the nanostructures and as a result lower absorbances were detected (Mohammadi & Ghasemi, 2018).

The Eg values calculated by using Tauc plots depicted in Figures 20(b-d), for CuO NPs at 50, 60 and 70 °C were found to be 3.071, 3.078 and 3.147 eV, respectively. The Eg values presented in Figures 21(b-d) for MgO NPs at 50, 60 and 70 °C were 5.087, 5.104 and 5.139 eV, respectively. Similarly, the Eg values computed in Figures 22 (b-d) for ZnO NPs at 50, 60 and 70 °C were 3.27, 3.32 and 3.39 eV, respectively. Thus, a temperature of 70 °C was considered to be optimum for the synthesis of CuO, MgO, and ZnO NPs using LEAA in terms of size and yield of the NMs (Biswal & Misra, 2020).

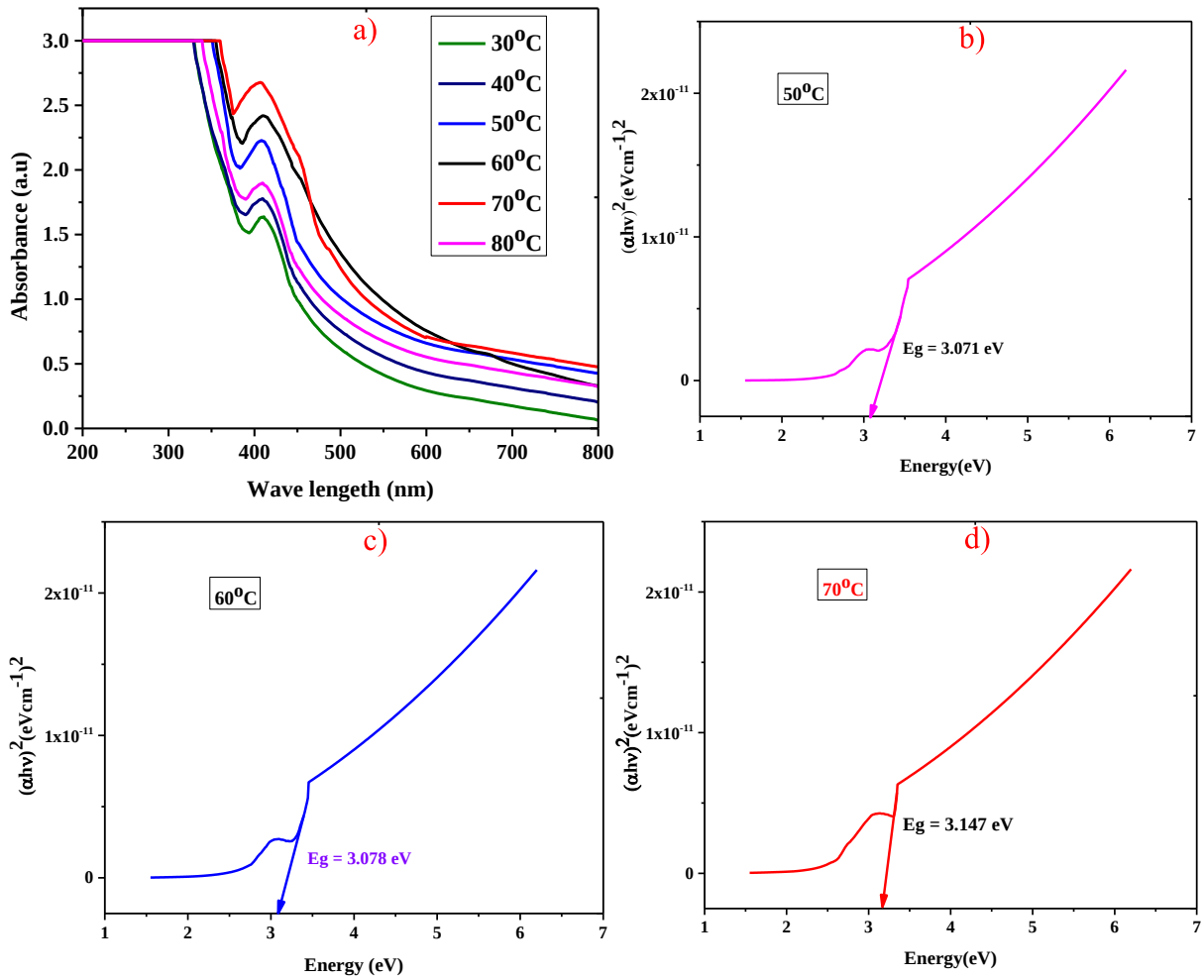

Figure 20. a) UV–Vis absorbance of CuO NPs prepared at different temperatures; Tauc plot for CuO NPs at b) 50, c) 60, d) 70 ^{o}C.

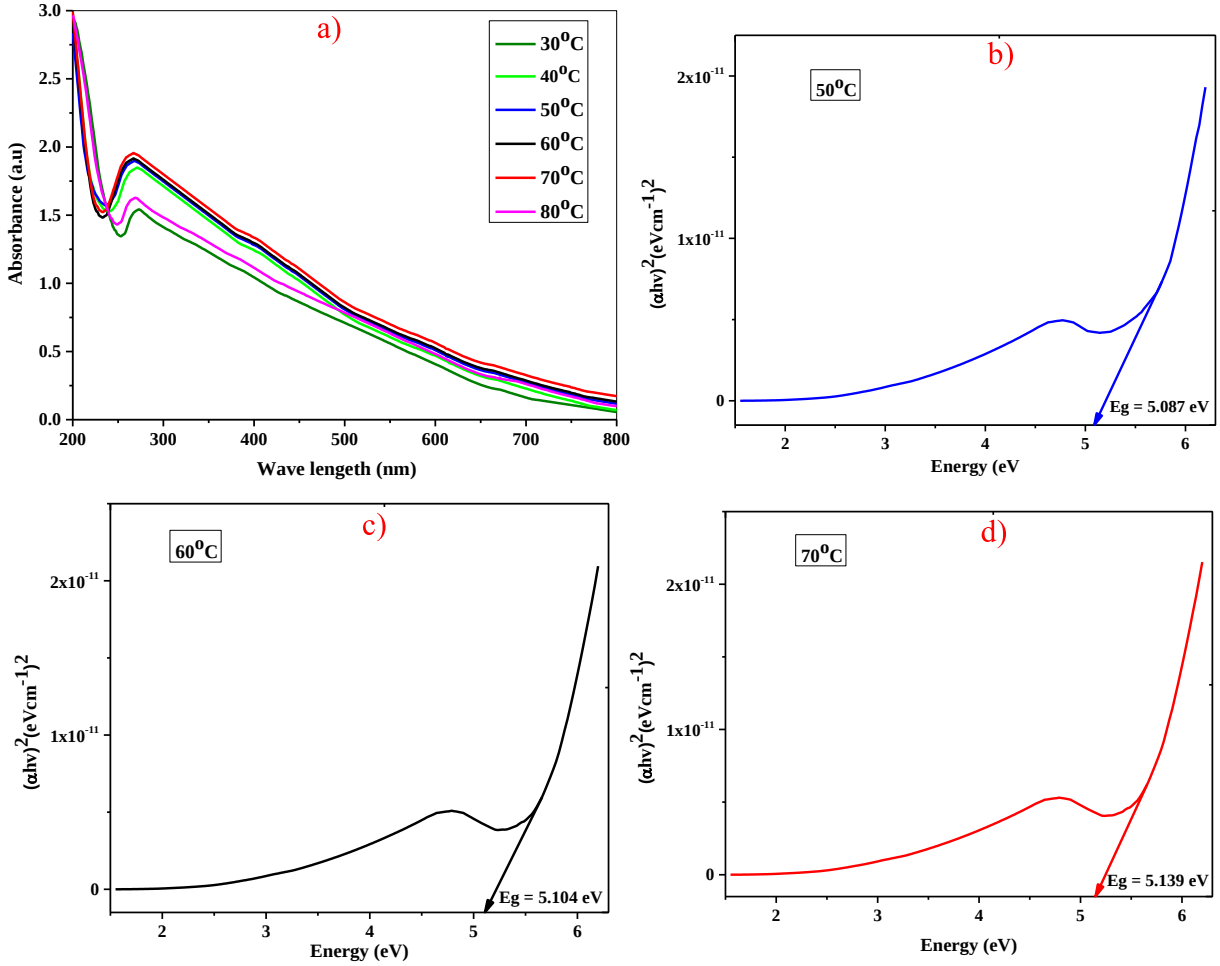

Figure 21. a) UV–Vis absorbance of MgO NPs prepared at different (30-80 ^{o}C) temperatures; Tauc plot for MgO NPs at b) 50, c) 60 and d) 70 ^{o}C.

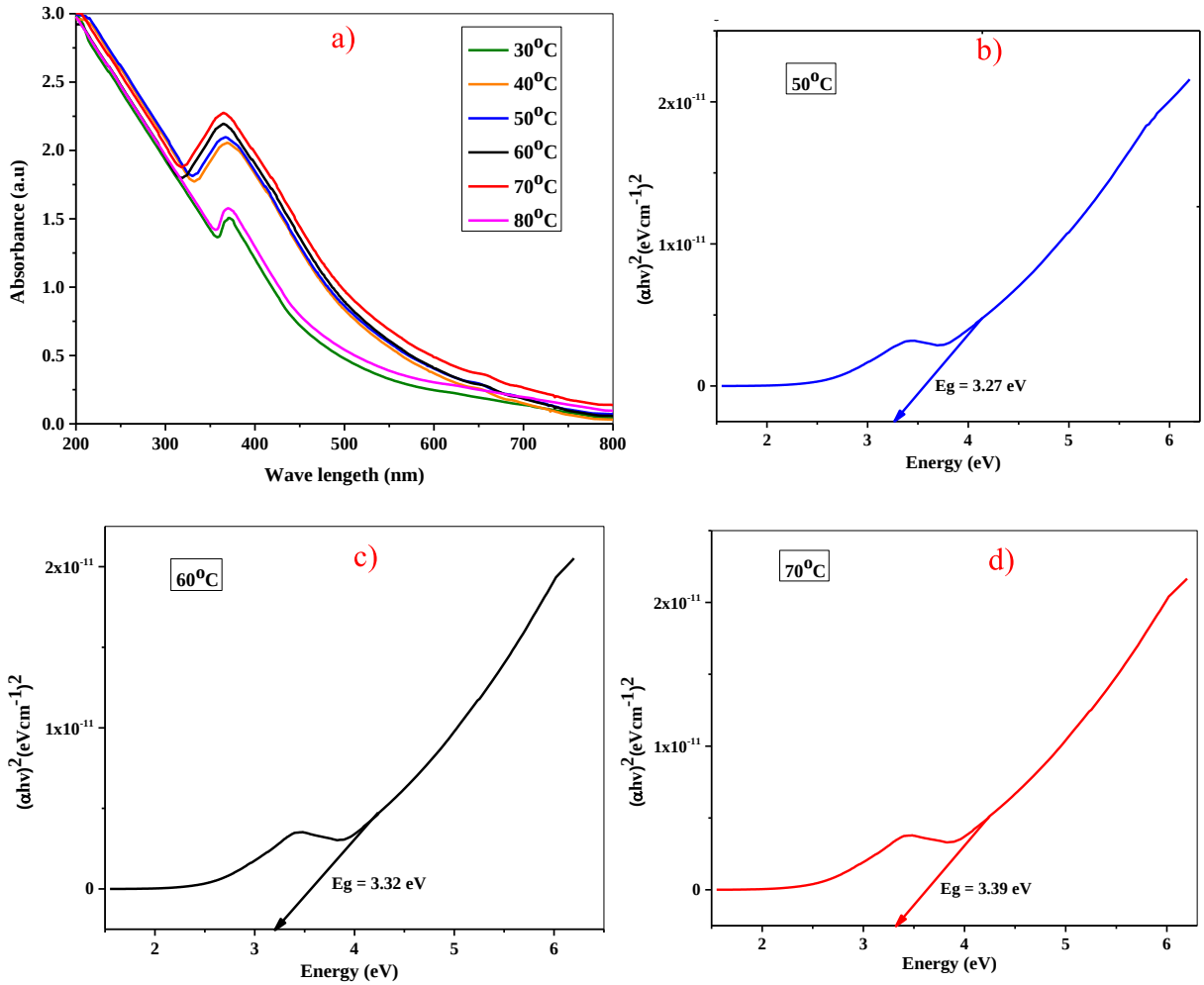

Figure 22. a) UV–Vis absorbance of ZnO NPs prepared at (30-80 ^{o}C) different(30-80 ^{o}C) temperatures; Tauc plot for ZnO NPs at b) 50, c) 60, and d) 70 ^{o}C.

4.3 Characterizations of MO NMs

4.3.1 TGA/DTA analysis

Thermogravimetric analysis (TGA) combined with differential thermal analysis (DTA) is widely used to investigate the thermal stability and compositions of nanomaterials. The TGA-DTA thermograms of phytochemical mediated mono (ZnO, CuO, and MgO) NPs and bi and trimetallic (ZC, MZ, MC and ZMC) NCs are presented in Figure 23 (a-c) and Figure 24 (a-d).

The DTA curve of CuO NPs (Figure 23a) shows three distinct peaks in the temperature range of 40.0°C to 800.0 °C. The first minor peak at 48.61 °C in the curve corresponds to a weight loss of 1.82% in the TGA curve due to the desorption of physically adsorbed moisture on the surface of

the NPs (J. Singh et al., 2019). The second, a minor peak, and the third, a major peak, at 207.25 °C and 285.06 °C correspond to 3.56 and 16.18% weight losses in the TGA curve, respectively. These weight losses are due to the decomposition of biomolecules that partake in the synthesis and stabilization of the NPs (Desalegn, Murthy, Ravikumar, & Nagaswarupa, 2021). Above 308.0°C, no weight loss occurs, inferring stability of the CuO NPs.

The TGA thermogram of MgO NPs (Figure 23b) shows three peaks in the temperature range of 35.0 °C to 800.0 °C. The first and second peaks at 110.23 °C and 198.94 °C correspond to weight losses of 6.89% and 14.95%, respectively, in the TGA curve. These weight losses are due to desorption of physically adsorbed moisture and biomolecules on the surface of the NPs. The third peak at 274.03 °C corresponds to 16.91% weight loss due to the decomposition of biomolecules involved in the reduction and stabilizing of the NPs (Poonguzhali et al., 2022). Above 335.0°C, there is no significant weight loss, inferring thermal stability of the MgO NPs.

The DTA curve of ZnO NPs (Figure 23c) shows two peaks in the temperature range of 32.0 °C to 800.0 °C. The first, a broad peak between 84.0 °C and 220.0 °C in the DTA curve, corresponds to 11.76% weight loss in the TGA curve and is associated with the desorption of physically bound moisture and volatile biomolecules (Poonguzhali et al., 2022). The second exothermic peak at 297.2 °C corresponds to 34.88% weight loss in the TGA curve and is also associated with the decomposition of biomolecules involved in the reduction and stabilization of the NPs (Faisal et al., 2021). Above 400 °C there is significant weight loss and thermal stability was observed in the sample.

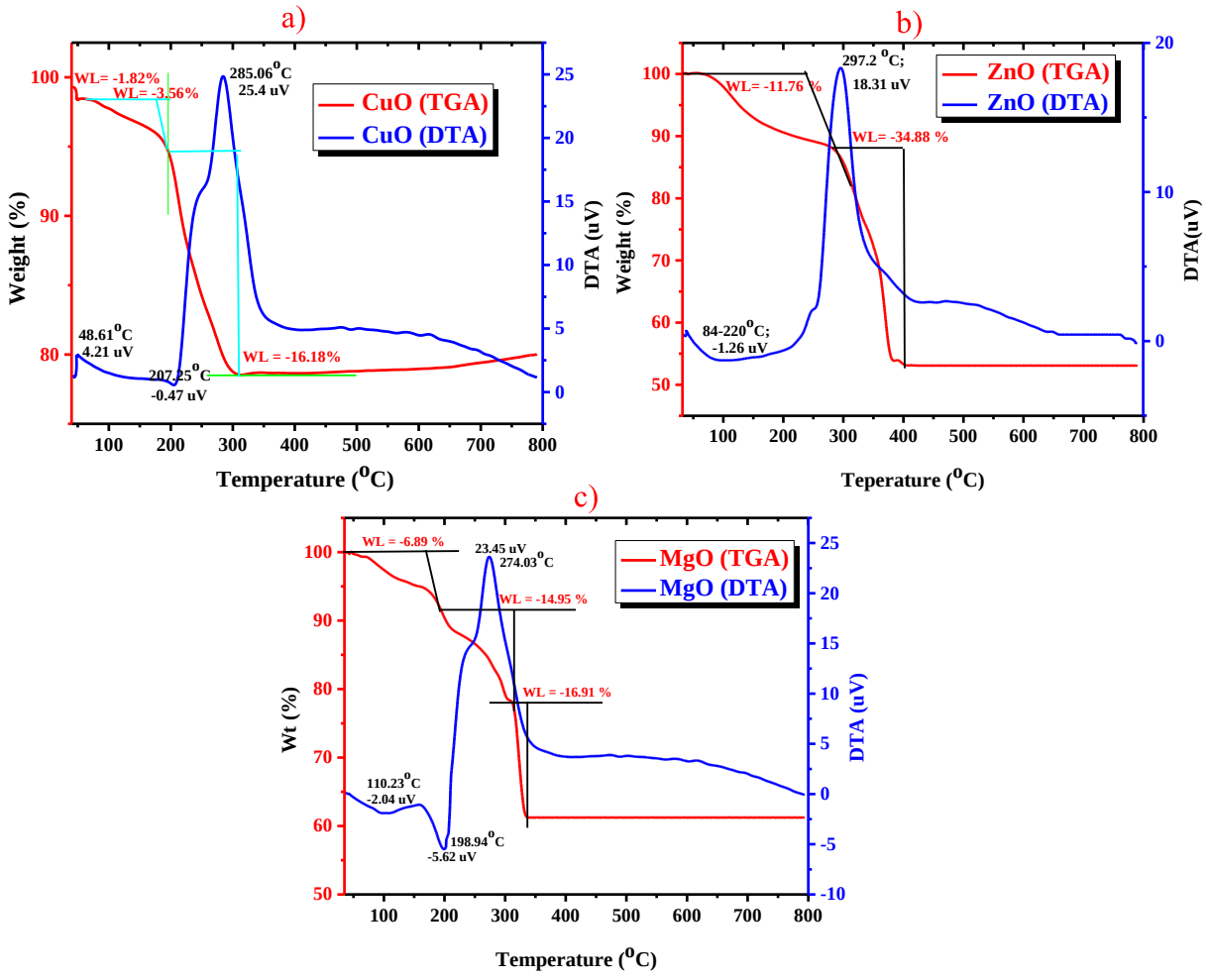

Figure 23. TGA/DTA thermograms of a) biosynthesized CuO NPs, b) MgO NPs and c) ZnO NPs

Figure 24 (a-d) illustrates the TGA-DTA thermograms of biosynthesized bi- (ZC, MC, MZ), and trimetallic ZMC NCs. Three weight loss transitions are observed in the TGA curves of bimetallic ZC NCs (Figure 24a): 35-124.30 ºC, 125-208 ºC, and 209-384 ºC. The first peak in the DTA curve at 44.07 ºC corresponds to a weight loss of 13.73% in the TGA curve due to the vaporization of physically adsorbed moisture on the surface of the NMs (Poonguzhali et al., 2022). The second peak at 199.78 ºC is complemented by a weight loss of 31.49% due to the decomposition of biomolecules on the surface of the NMs (Faisal et al., 2021). The third peak at 274.01 ºC corresponds to a weight loss of 6.56% in the TGA curve. It is attributed to the decomposition of certain biomolecules involved in the synthesis of the NMs (Desalegn et al., 2021). Beyond 384.0 ºC, there is no significant weight loss, inferring the thermal stability of the ZC NCs.

For the bimetallic MC NCs, the three weight loss transitions are observed in the TGA curve (Figure 24b). These occur in the temperature ranges of 37-167.51 ºC, 168-276 ºC, and 277-341 ºC. The first DTA peak at 122.39 ºC is complimented by a weight loss of 2.22 %, corresponding to loss of physically adsorbed moisture. The second peak at 276.93 ºC, complimenting a weight loss of ca. 3.3%, is attributed to the desorption and degradation of biomolecules on the surface of the NCs (Poonguzhali et al., 2022). The third DTA peak at 276.93ºC complements a weight loss of 5.32% in the TGA curve and is attributed to the degradation of the biomolecules (Sukumar, Rudrasenan, & Padmanabhan Nambiar, 2020). No significant weight loss is observed beyond the temperature of 341.0 ºC, inferring the stability of the MC NCs.

The TGA thermogram of bimetallic MZ NPs (Figure 24c) shows the three weight loss transitions in the temperature ranges of 37-212 ºC, 213-312.5 ºC, and 313-341 ºC. The first and second DTA peaks at 174.75 ºC and 218.98 ºC, are complimented by weight losses of 11.58 and 10.16% in the TGA curve, respectively, and correspond to evaporation of physically adsorbed moisture and volatilization and degradation of biomolecules on the MZ NCs (Faisal et al., 2021). The third DTA peak at 315.73 ºC is complimented by a weight loss of 16.87%, attributed to the complete decomposition of the biomolecules involved in synthesizing the MZ NCs.

Similarly, the TGA thermogram of trimetallic ZMC NCs (Figure 24d) shows three weight loss transitions in temperature ranges of 37-225 ºC, 226-328.81 ºC, and 329-374 ºC. The first DTA peak at 191.73 ºC complements a weight loss of 11.72% due to the vaporization of physically adsorbed moisture and volatile phytochemicals, and the second DTA peak at 335.72 ºC complements a weight loss of 10.11%. The third weight loss transition of 17.92% is also part of the second DTA peak; this loss is due to the decomposition of the biomolecules. Beyond a temperature of 360 ºC, there is no weight loss, indicating the thermal stability of biosynthesized ZMC NCs (Sukumar et al., 2020). In conclusion, the TGA-DTA data revealed that, all the biosynthesized mono-, bi- and trimetallic MO NMs have insignificant weight loss beyond 300-400 ºC and they are thermally stable.

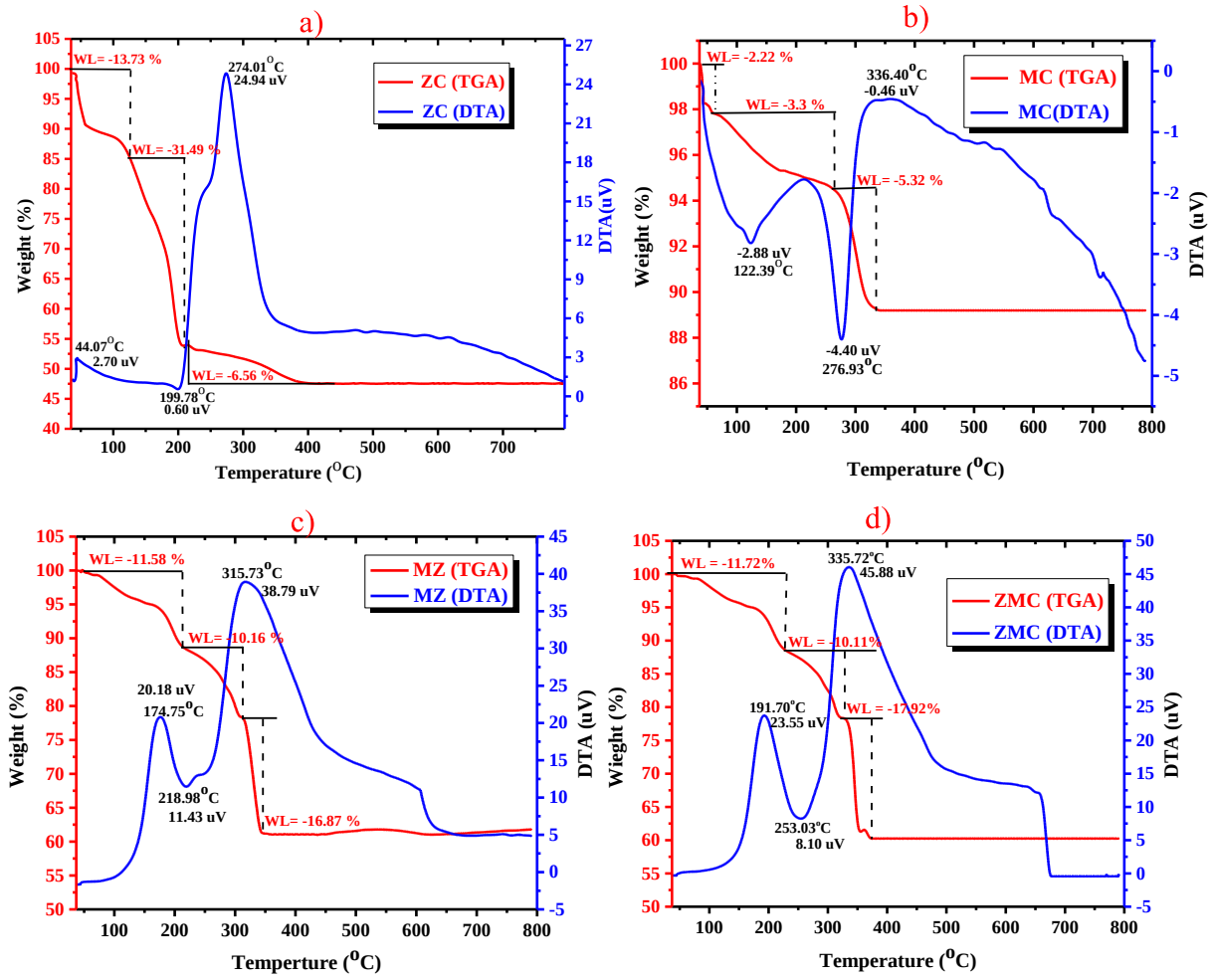

Figure 24. TGA/DTA thermograms of a) ZC, b) MC, c) MZ and d) ZMC NCs.

4.3.2 UV-visible analysis

UV-visible spectroscopy is an important technique for determining NPs' physicochemical and optical properties. 5 mL of LEAA and phytochemical mediated mono- (ZnO, CuO and, MgO), bi- (ZC, ZM, and MC) and trimetallic (ZMC) NMs aqueous solutions were prepared, and their respective absorption peaks were measured using UV-visible spectroscopy. The absorption spectra of LEAA and biosynthesized mono- (ZnO, CuO, and MgO) NPs bi- (ZC, MC, and ZM) and trimetallic (ZMC) NMs are illustrated in Figure 25(a-d). LEAA (Figure 25a) shows different absorption peaks at 235, 355, and 412 nm attributed to different active biomolecules present in LEAA, responsible for the reduction and stability of the synthesized NPs (Thamer et al., 2018). Monometallic (CuO, ZnO, and MgO) NPs display strong SPR peaks at 406, 365, and

267 nm edges, respectively (Figure 25a). The bi- (ZC, MC, and ZM) and trimetallic (ZMC) NMs (Figure 25c) also show broad SPR peaks at 380, 342, 295, and 367 nm respectively. Similar patterns of SPR were reported in the range of 200-800 nm for mono and bimetallic oxide NMs of CuO, ZnO and, MgO in previous studies (Annathurai, Chidambaram, Baskaran, & Prasanna Venkatesan, 2019; Majhi & Kuiri, 2021). The observed SPR peaks are due to the interaction of free electrons of the NPs and light, indicating successful NMs synthesis (Annathurai et al., 2019; Majhi & Kuiri, 2021). However, the SPR bands of mono-, bi-, and trimetallic oxide NMs occur at various edges because the SPR bands of NMs depend on their physicochemical properties such as shape, size, and surface distribution as well as the dielectric properties of the medium (Achamo et al., 2022; Vinu et al., 2021).

Recent studies report that anisotropic NPs show two or more SPR bands, while spherical NPs show only a single SPR band depending on the shape of the nanoparticles (Majhi & Kuiri, 2021). Hence, the single SPR peaks in the spectrum of NPs infer the synthesis of iso-morphological particles (Majhi & Kuiri, 2021). The capping agents regulate the functionalization and stabilization of the MO NMs in the medium in which they are suspended (Ajitha, Reddy, Reddy, Jeon, & Ahn, 2016; Orshiso et al., 2023). The SPR bands' symmetrical shapes also suggest that the synthesized MO NMs have well-dispersed and uniform sizes (Samari, Baluchi, Salehipoor, & Yousefinejad, 2019). Since non-uniform particles will have a broad absorption peak with a split Plasmon bands (Ajitha et al., 2016), the higher intensity in the UV-vis spectra of NPs could also be used to carry out the quantitative analysis of yields of MO NMs (Khani, Roostaei, Bagherzade, & Moudi, 2018). Hence, absorbance of a peak has direct relation to the concentration of the absorbing species in the medium. Therefore, the UV-vis spectra of MO NMs revealed the formation of well-dispersed, iso-morphological particles with high yields.

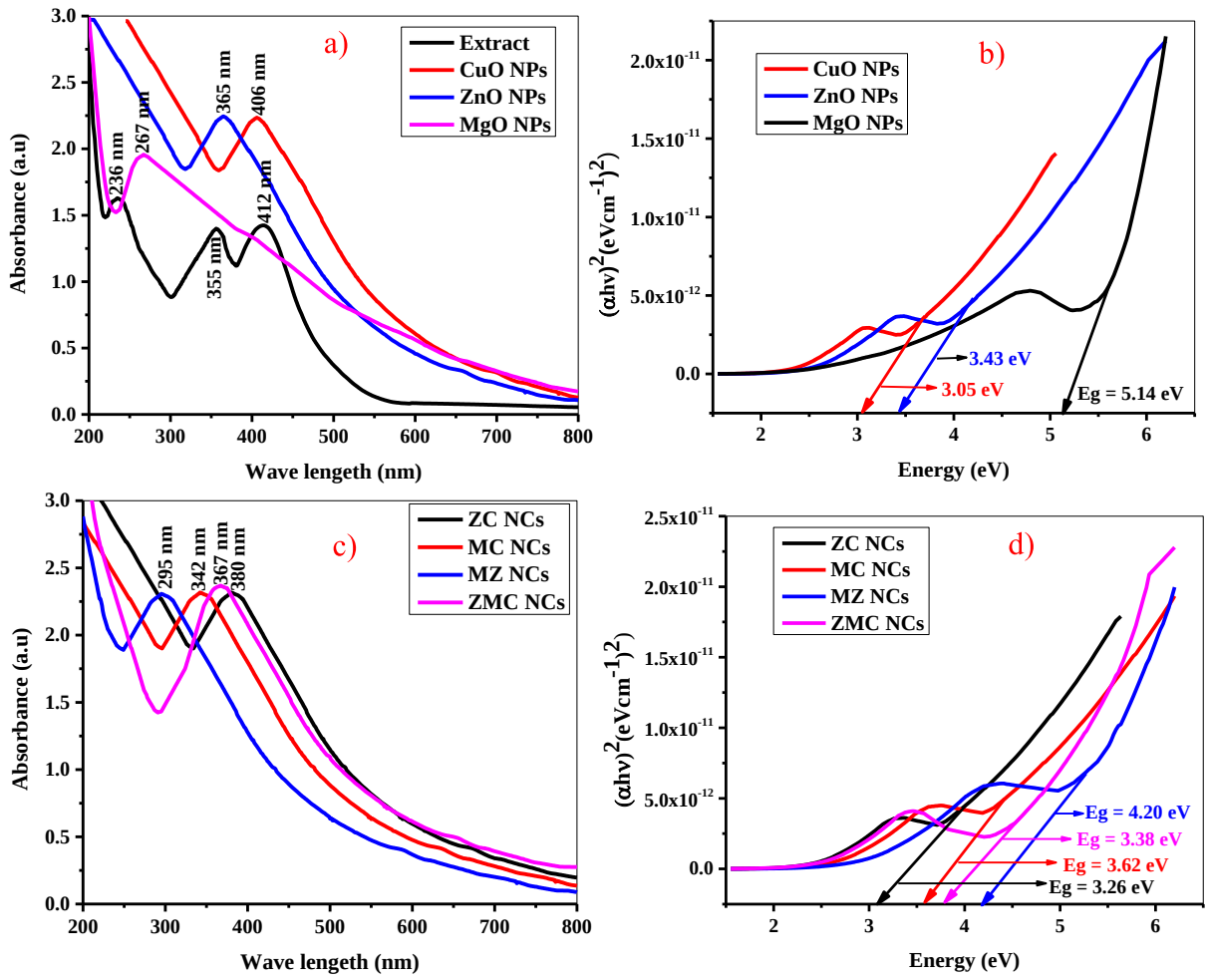

Figure 25. a) UV–Vis s absorbance of LEAA, CuO, ZnO, and MgO NPs, b) Tauc plot for CuO, ZnO, and MgO NPs, c) UV–Vis spectrum of ZC, MC, MZ and ZMC NCs, and d)Tauc plot for ZC, MC, MZ and ZMC NCs.

The band gap energy (Eg) of the mono- (ZnO, CuO, and MgO), bi- (ZC, MC, and MZ) and trimetallic (ZMC) NMs for the direct electronic transition between the valence band (VB) and conduction band (CB) were computed using Tauc's relation as illustrated in Figure 25 (b and d). The Eg values of the CuO, ZnO, and MgO NPs (Figure 25 b) were 3.05, 3.43 and, 5.14 eV, respectively. The Eg values of ZC, MC, MZ, and ZMC NCs (Figure 25 d) were 3.26, 3.62, 4.20, and 3.38 eV respectively. The slight change in Eg values of bi- and trimetallic NCs show moderately amended values compared to their monometallic counterparts. The change in the band gap energy of the bi- and trimetallic oxide NCs compared to the individual metal oxides is

likely due to the formation of new energy states at the interfaces between the different metal oxides (Achamo et al., 2022; Vinu et al., 2021), which can result in a shift in the electronic structure and a change in the band gap energy. The presence of multiple metal oxides in the bi- and trimetallic oxide NCs can also lead to increased electron-hole separation and improved charge transport properties, which can further affect the band gap energy. Moreover, several factors, such as the size-induced quantum confinement, charge carrier concentration, grain size, morphology, lattice strain, and orbital hybridization by combining different atoms from bi- and trimetallic NCs, may contribute to the change in band gap value from monometallic counterparts (Annathurai et al., 2019).

4.3.3 FTIR analysis

FT-IR spectroscopy studies of LEAA and phytochemical mediated synthesized MO NMs using LEAA were performed to characterize the chemical nature of the materials as illustrated in Table 5 and Figures 26 (a&b). The absorbtion band positions (Figure 26a) at 3425, 2914, 2072, 1693, 1392, 1268, 1076, and 614 cm^{-1} represent the FTIR spectra of the LEAA. The bending and stretching vibrational frequencies of phenolic O−H is assumed to be involved in the absorbtion band at 3425 cm^{-1} (Rajagopal et al., 2021). The bands at 2914 and 2072 cm^{-1} are also ascribed due to the bending and stretching frequency of C−H from vinyl groups and −C≡C− from terminal alkyne groups respectively (Lv et al., 2018). The intense band at 1392 is associated with the vibrational stretching of C=O groups from phenolic compounds (Lv et al., 2018). The small bands at 1693 and 1268 cm^{-1} could be associated with the deformation of C−O from methoxyl and carboxylic groups, respectively (Sarwar et al., 2021; Umaralikhan & Jamal Mohamed Jaffar, 2018). The band at 1076 cm^{-1} could also be associated with the C−N stretching frequency. The broad band at 614 cm^{-1} could be connected to the C−O−C stretching of esters groups (Sarwar et al., 2021). The FT-IR response proves the presence of phenolic compounds, alkaloids, and flavonoids in the LEAA and confirms this work's phytochemical screening test result.

FTIR spectrum of the biosynthesized mono- (ZnO, CuO, and MgO), bi- (ZC, ZM, and MC), and trimetallic (ZMC) NCs are illustrated in Figure 26 (b). All the MO NMs showed similar absorption bands at 3398-3172, 2918, 2077, 1391, 1107, 835 614, and 514 cm^{-1}. Moreover, common absorption bands at 1107, 835, and 514 cm^{-1} were observed in the FTIR spectra of CuO,

ZnO, and MgO NPs, respectively. The broad peaks at 3354-3206 cm^{-1} and 2914 cm^{-1} were attributed to the vibrational stretching frequency of O−H and C−H phenolic compounds and vinyl groups, respectively (Sarwar et al., 2021). The intense band 2077 cm^{-1} were due to the stretching vibration of −C≡C− from terminal alkyne group (Lv et al., 2018). The intense band at 1392 cm^{-1} were due to stretching vibrations of C=O from polyphenols groups. and C-O-C from ester groups, respectively (Sarwar et al., 2021; Umaralikhan & Jamal Mohamed Jaffar, 2018). The FT-IR bands at 1107, 835, and 514 cm^{-1} corresponded to the stretching vibrations of the Cu−O, Mg−O and Zn−O bonds, respectively (Murali et al., 2021; H. Murthy, Desalegn, Kassa, Abebe, & Assefa, 2020; Umaralikhan & Jamal Mohamed Jaffar, 2018). The band at 614 cm^{-1} could be connected to the C−O−C stretching of esters grops (Sarwar et al., 2021). In general, the FT-IR spectra of the NPs showed that they were coated with active phytochemicals, particularly with the O−H, C=O, and N−H residues of phenolic compounds and alkaloids. These residues, bond with the MOs by coating their surface and minimizing agglomeration, which is crucial for stabilization (Ansari & Asiri, 2021; Rodríguez-Félix et al., 2022).

Table 5. Assignment of characteristic absorption peaks from FTIR spectra of AALE and ZMC NMs.

AALE (band position cm^{-1})	**Assignments**	**MO NMs (band position cm^{-1})**	**Assignments**
3425	O−H stretching	3354-3206	O−H stretching (phenols)
2914	C−H stretching	2914	C−H stretching (vinyl)
2072	C≡C stretching	2072	C≡C stretching (terminal alkyl)
1392	C=O vibration	1381	C=O vibration (polyphenols)
1693	C−O vibration	1107	Cu−O bond vibration
1268	C−O stretching	835	Mg−O bond vibration
1076	C−N stretching	514	Zn−O bond vibration
614	C−O−C stretching	614	C−O−C stretching (ester)

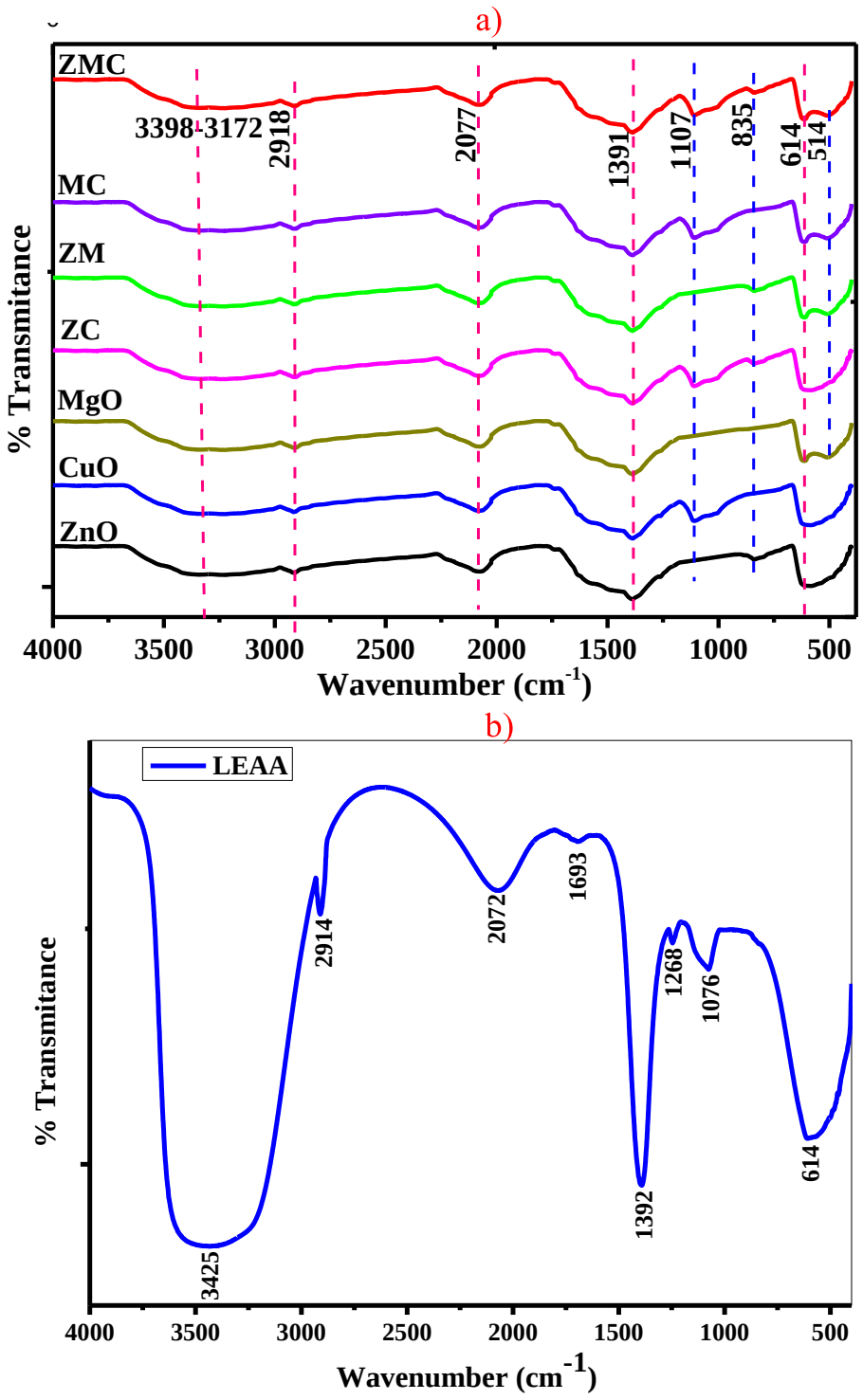

Figure 26. FTIR spectra of a) MO NMs and b) LEAA.

4.3.4 XRD analysis

The structural composition and crystallographic nature of the monometallic (ZnO, CuO, and MgO) NPs were examined using an X-ray diffractometer (XRD), as illustrated in Figure 27 (a-c). The XRD pattern of ZnO NPs (Figure 26a) shows intense diffraction peaks at 2θ values of 31.76°, 34.46°, 36.22°, 47.51°, 56.50, and 67.89° corresponding to the Miller indices (hkl) (100), (002), (101), (102), (110), and (112) respectively matches ICSD card No. 00-036-1451, Zincite-P63mc (Narendhran & Sivaraj, 2016). These observations confirmed the formation of crystalline ZnO NPs with hexagonal wurtzite phase. Figure 27b illustrates the XRD pattern of CuO NPs with characteristic diffraction peaks at 2θ values of 36.40, 38.71, 42.60°, 48.72°, 61.51°, and 73.64° corresponding to (002), (111), (200), (202), (220) and (311) planes, respectively. The observed planes confirming the formation of crystalline CuO NPs with monoclinc phase which are similar to reflections presented by different literatures and ICSD Card No.00-048-1548, Tenorite-C2/c (Shahriary et al., 2022; Amrita Singh, Gaud, & Jaybhaye, 2020). The XRD diffraction pattern of MgO NPs (Figure 27c) shows diffraction peaks with 2θ values of 36.22°, 38.44°, 42.76°, 62.51°, 74.40° and 77.74° corresponding to the Miller indices (hkl) of (111), (0020), (202), (220), (311), and (222) planes, respectively, confirming the formation cubic phase MgO NPs (ICSD Card No. 00-045-0946, Periclase-Fm-3m) (Noori & Kareem, 2019).

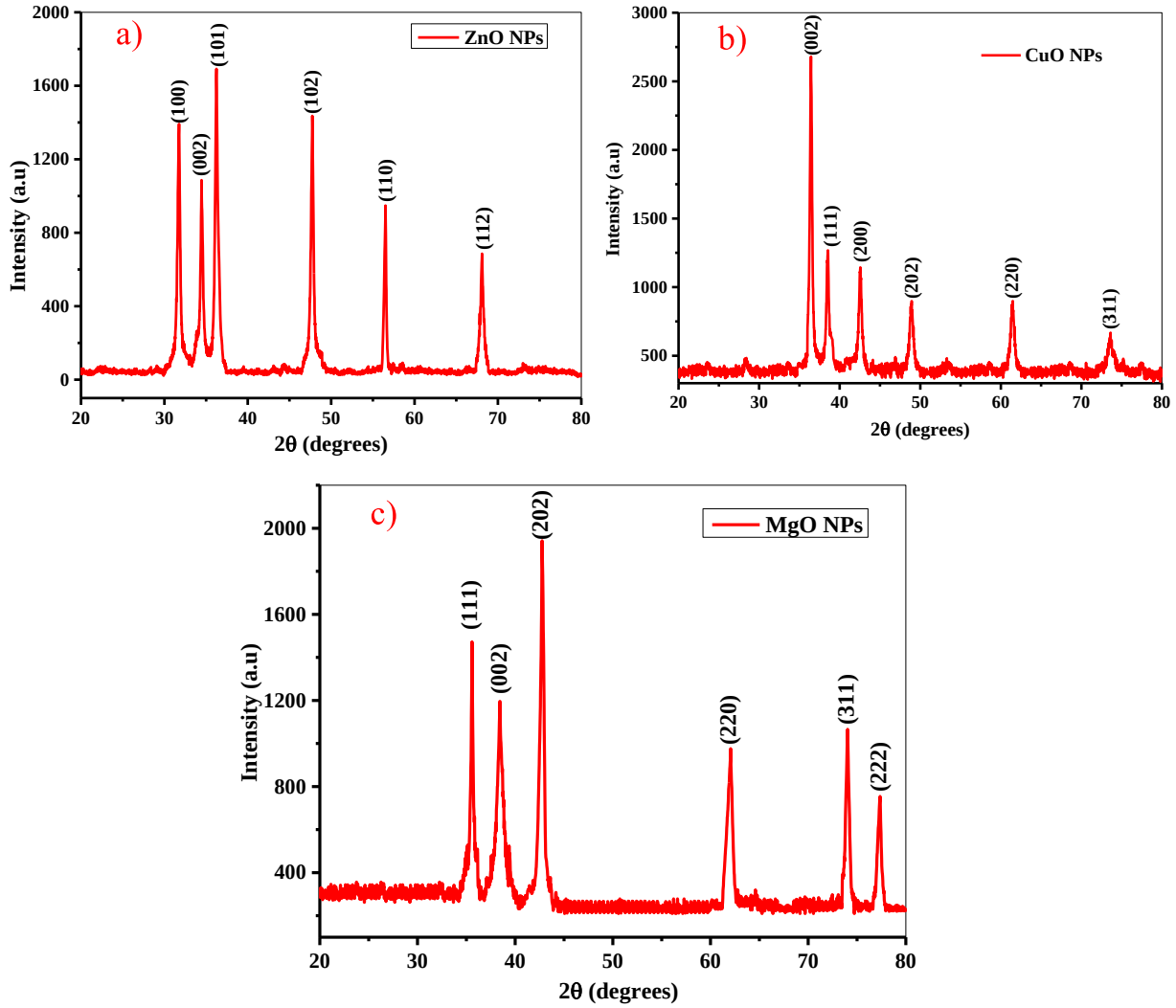

Figure 27. XRD pattern of monometallic a) ZnO NPs, b) CuO NPs and c) MgO NPs.

The X-ray patterns of the bimetallic (MgO-ZnO, MgO-CuO, and ZnO-CuO) NCs are illustrated in Figures 28a-c. The diffraction peaks of MgO-ZnO (MZ) NCs (Figure 28a) at 2θ values of 31.76°, 34.46°, 36.22°, 38.44°, 42.76°, 47.74°, 56.52°, 62.51°, 68.18°, 74.40° and 77.74° correspond to Miller indices (hkl) values of (100), (002), (101), (111), (200), (102), (110), (220), (112), (311), and (222), respectively. The typical peaks of both monometallic MgO and ZnO NPs are present in bimetallic MZ NCs, confirming the successful synthesis of bimetallic ZM NCs. The sharper to broader diffraction peaks corresponding to Miller indices (100), (002), (101), (111), (200), (102), (110), (220), (112), (311), and (222 planes indicate the formation of hexagonal lattice structures with monoclinic symmetry of MZ NCs (Mandal et al., 2022; Wong

et al., 2020). Figure 28b illustrates the XRD diffraction peaks of MgO-CuO (MC) NCs with 2θ values of 36.35, 38.43, 42.67, 48.88, 61.40, 62.63, 74.52 and 77.74° correspond to Miller indices of (002), (111), (202), (202), (220), (220), (311), and (222) planes. The characteristic diffraction peaks confirm the crystalline hexagonal structural lattice with the orthorhombic structure of the MC NCs (Amor et al., 2023). The XRD pattern of ZnO-CuO (ZC) NCs is illustrated in Figure 28c. The characteristic diffraction peaks with 2θ values of 31.71°, 34.41°, 35.56, 36.18°, 38.79, 47.51°, 56.50, 62.83, 67.89°, and 73.06 nm correspond to Miller indices (hkl) of (100), (002), (102), (101), (111), (102), (021), (103), (112), and (311), and respectively. The sharper to broader diffraction peaks and the (101), (100), (002), (002), (111), (200), (102), (110), (220), (311), and (222) planes indicate the formation of the highly crystalline, hexagonal lattice structures with monoclinic symmetry of ZC NCs (Cao et al., 2021).

The XRD pattern of biosynthesized trimetallic ZnO-MgO-CuO (ZMC) NCs is illustrated in Figure 28d. The prominent peaks at 2θ values of 18.57°, 31.73°, 34.36°, 36.12°, 38.74°, 42.98°, 47.58°, 57.10°, 61.82°, 73.06° and 78.54° correspond to the Miller indices (hkl) values of (101), (100), (002), (002), (111), (200), (102), (110), (220), (311), and (222) planes respectively. The typical diffraction peaks at (100), (002), (102), and (110) planes with 2θ values 31.73°, 34.36°, 47.58°, and 57.10° are associated with the crystalline structure of ZnO NPs and match ICSD Card No. 00-036-1451, Zincite-P63mc (Pillai et al., 2020). The characteristic diffraction peaks at (002), (111), (220), and (311) planes with 2θ values of 36.12°, 38.74°, 61.82°, and 73.06° are the CuO NPs matching ICSD Card No. No.00-048-1548, Tenorite-C2/c (Amrita Singh et al., 2020). The prominent diffraction peaks with 2θ values of 27.62°, 42.98°, and 78.54° corresponding to Miller indices of (110), (200), and (222) planes are associated with the MgO NPs matching ICSD Card No. 00-045-0946, Periclase-Fm-3m (Noori & Kareem, 2019). The XRD pattern shows the successful synthesis of highly crystalline ZMC NCs. The sharper to broader diffraction peaks and the (101), (100), (002), (002), (111), (200), (102), (110), (220), (311), and (222) planes perfectly coincide with the monoclinic phase of CuO, the cubic phase of MgO, and the wurtsize phase of ZnO NPs (Mandal et al., 2022; Wong et al., 2020).

Moreover, it was observed that the average D values of ZnO-MgO-CuO NCs were larger compared with individual NPs due to the agglomeration of particles caused by the presence of MgO. The MgO particles act as nucleation sites for the CuO and ZnO NPs, resulting in

aggregation into larger clusters. This phenomenon is known as the Ostwald ripening effect, wherein smaller particles dissolve and re-deposit on larger particles, increasing their size. Hence, the presence of MgO in the NCs increases the particle size of CuO and ZnO NPs (Al-Hammadi, Alnehia, Al-Sharabi, Alnahari, & Al-Odayni, 2023).

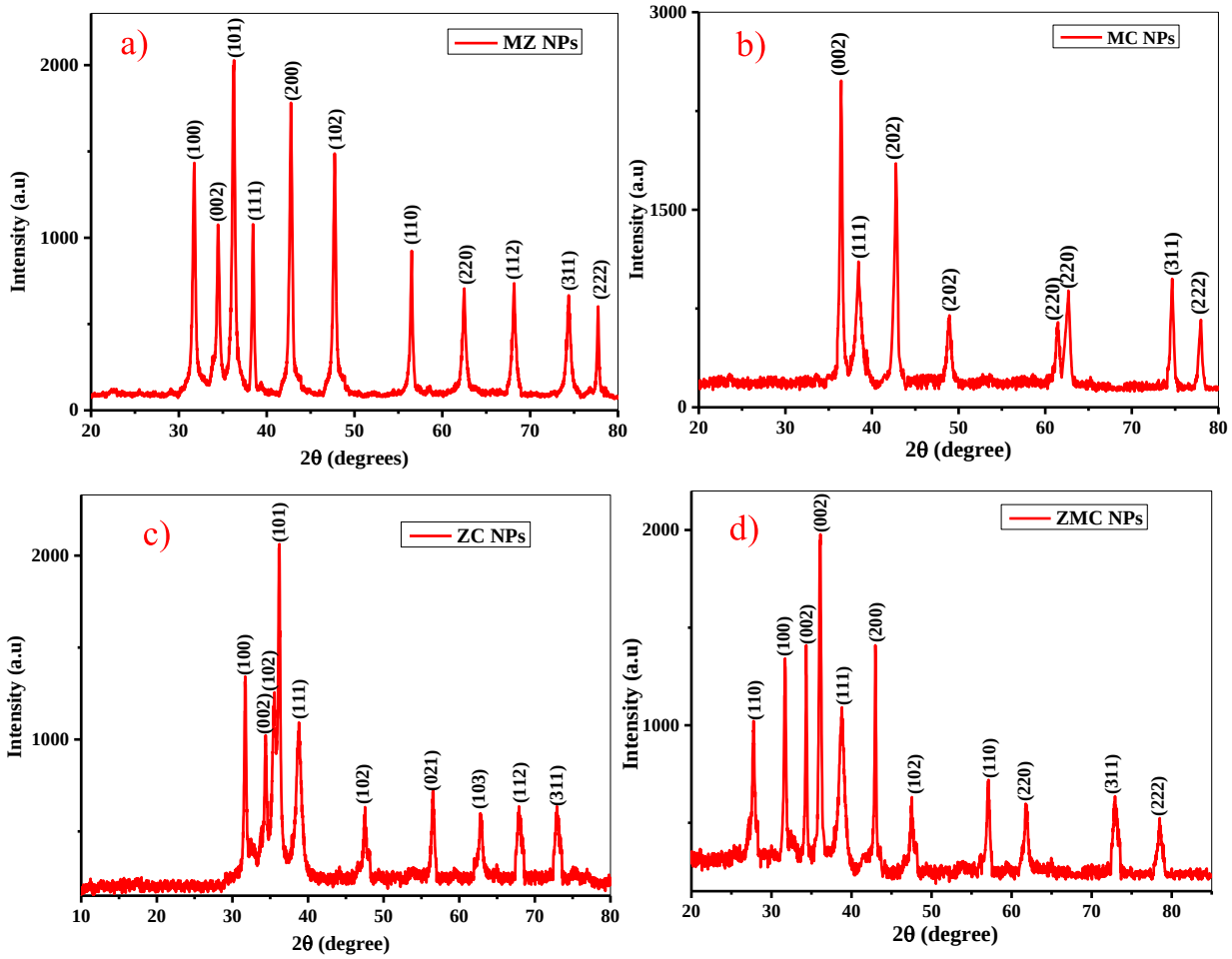

Figure 28. XRD pattern of bi and trimetallic a) MgO-ZnO (MZ) NCs, b) MgO-CuO (MC) NCs, c) ZnO-CuO (ZC) NCs, and d) ZnO-MgO-CuO (ZMC) NCs.

The average crystallite sizes of phytochemical mediated MO NMs were calculated, using the Debye-Scherer equation (4) and Williamson-Hall (W-H) plot equation (5), respectively, and presented in Table 6.

$$D = \frac{K\lambda}{\beta\cos\theta} \qquad (4)$$

D, k, λ, β, and θ are the average crystallite size, the Scherer constant (0.9), wavelength of X-ray (Cu Kα = 0.15418 nm), FWHM (full width at half maximum), and Bragg's diffraction angle, respectively.

$$\beta Cos\theta = \frac{k.\lambda}{D} + 4\varepsilon Sin\theta \qquad (5)$$

β is the full width of the Bragg peak at half maximum (FWHM), θ is peak angle, D is mean crystallite size, k is the Scherer constant, λ is the wavelength of X-ray and ε is (micro-strain).

The dislocation densities (δ) of MO NMs (Table 6) were calculated using equation 6 as folows:

$$\delta = \frac{1}{D^2} \qquad (6)$$

The dislocation density (δ) is inversely proportional to the crystallite size (D) of MO NMs calculated from Debye-Scherer approaches.

Table 6. Average crystallite size (D) by Debye-Scherer, W-H equations, Microstrain (ε) and dislocation density (δ) of MO NMs.

MO NMs	Average crystallite size (nm)		Microstrain (ε) x 10^{-4}	δ(x 10^{-2} nm) Debye-Scherer	Phase
	Debye-Scherer	Williamson-Hall			
CuO	11.69	12.27	7.42	0.732	Tenorite
ZnO	10.17	11.43	5.63	0.967	Wurtizite
MgO	12.04	13.82	7.33	0.690	Periclase
MZ	13.98	14.87	8.45	0.512	W-P
ZC	13.85	14.94	8.32	0.521	W-T
MC	14.02	15.22	9.83	0.509	P-T
ZMC	14.67	15.38	9.49	0.465	W-P-T

By the Debye-Scherer equation, the average crystallite sizes of the CuO, ZnO, MgO, MZ, ZC, MC, and ZMC NMs were 11.69, 10.17, 13.04, 13.98, 13.85, 14.02, and 14.67 nm, respectively. The average crystallite sizes of CuO, ZnO, MgO, MZ, ZC, MC, and ZMC NMs, by the W-H equation approach, were 12.27, 11.43, 13.82, 14.87, 14.94, 15.22, and 15.38, respectively. The

crystalline sizes computed for Debye-Scherer and W-H approaches were not shown large variation and both approach fitted well for the determination of crystallite sizes of MO NMs. However, the average crystallite sizes of MO NMs obtained for W-H analysis showed slightly higher than Debye-Scherer approach. This variation could be due to differences in average crystallite distribution from various peaks and considering the effects of peak expansion as the result of strain (ε) in W-H approach (Mustapha et al., 2019). The micro-strains of CuO, ZnO, MgO, MZ, ZC, MC, and ZMC NPs were 7.42, 5.63, 7.33, 8.45, 8.32, 9.83, and 9.49 x 10^{-4} respectively. The obtained positive micro-strains (slopes) and extrapolation of the linear fit to the y-intercept indicate that the distances between the relevant crystal planes are not the same, presumably due to tensile stress (Munguti & Dejene, 2021).

The dislocation density, δ, measures the number of defects and vacancies in the crystal that is determined from the crystallite sizes using Debye-Scherer approach (Table 6). The calculated dislocation densitis (δ) of CuO, ZnO, MgO, MZ, ZC, MC, and ZMC NMs were 0.732, 0.967, 0.690, 0.512, 0.521, 0.509 and 0.465 x 10^{-2} nm, respectively. There were the deacrements in dislocation densities in W-H approach than Debye-Scherer approach. It is evident that the decrease in crystallite size causes an increase in the dislocation density. The presence of dislocations can affect the surface properties of nanomaterials, such as their roughness, surface area and reactivity, which in turn can impact their biological activity. Ingeneral, the presence of dislocations can influence the release of ions or reactive species from nanomaterials, which can contribute to their biological activity by disrupting microbial and cancer cell membranes or interfering with cellular processes (Erol et al., 2023).

4.3.5 SEM-EDX analysis of MO NMs

The SEM-EDX is an instrument that creates magnified images that reveal microscopic-scale information on a specimen's size, morphology, composition, crystallography, and other physical and chemical properties (Goldstein et al., 2018).

4.3.5.1 SEM-EDX analysis of CuO, MgO and ZnO NPs

The SEM images of CuO, MgO and ZnO NPs are shown in Figure 29 (a-c), respectively. In the SEM microgram of CuO NPs Figure 29a, the morphology of particles was nearly spherical. Moreover, the particles are dispersed across the surface with random aggregation, which might

be associated with bioactive molecules from LEAA. The SEM micrograms of MgO and ZnO NPs are illustrated in Figures 29b and 29c, respectively. The surface morphology of the MgO NPs (Figure 29b) revealed the presence of flower-like spherical shape nanoparticles with some aggregation. Similarly, the particle morphology of the ZnO NPs, Figure 29c, was nearly spherical with random agglomeration.

The elemental compositions of the CuO, MgO and ZnO NPs were obtained from energy dispersive X-ray (EDX) analysis as illustrated in Figure 30 (d-f). The appearance of intense optical absorption peaks at 0.5 keV (O), 1, 8 and 9 keV (Cu), in the EDX spectrum of CuO NPs (Figure 29d), confirmed the the formation of crystalline CuO NPs. The weight percentages of Cu and O in the CuO NPs were found to be 64.94, and 28.90 %, respectively. The presence of minor peaks at 2.6 keV (nitrogen) and 3.4 keV (carbon) with weight percentages of nitrogen 2.74%, and carbon 3.42% could be due to the presence of the biomolecules bonded to the CuO NPs' surface. The EDX spectra (Figure 29e) showed intense peaks of Mg and O with weight percentages of 46.32 and 40.40%, respectively, confirming the synthesis of crystalline MgO NPs. Moreover, the minor peaks of C and N with weight percentages of 8.47 and 4.81 %, respectively, may be of the biomolecules adsorbed on the MgO NPs surface from LEAA. Moreover, the weak peak of Ca in the EDX spectra of MgO NPs might be from the reaction conditions as an impurity. Similarly, the formation of crystalline ZnO NPs was confirmed by EDX analysis (Figure 29f), which showed intense optical absorption peaks with weight percentages of 76.5 and 16.9 % of Zn and O, respectively. The low percentages of C and N (4.6 and 2.0, respectively) indicated the precence of bonded phytochemicals in ZnO NPs from LEAA.

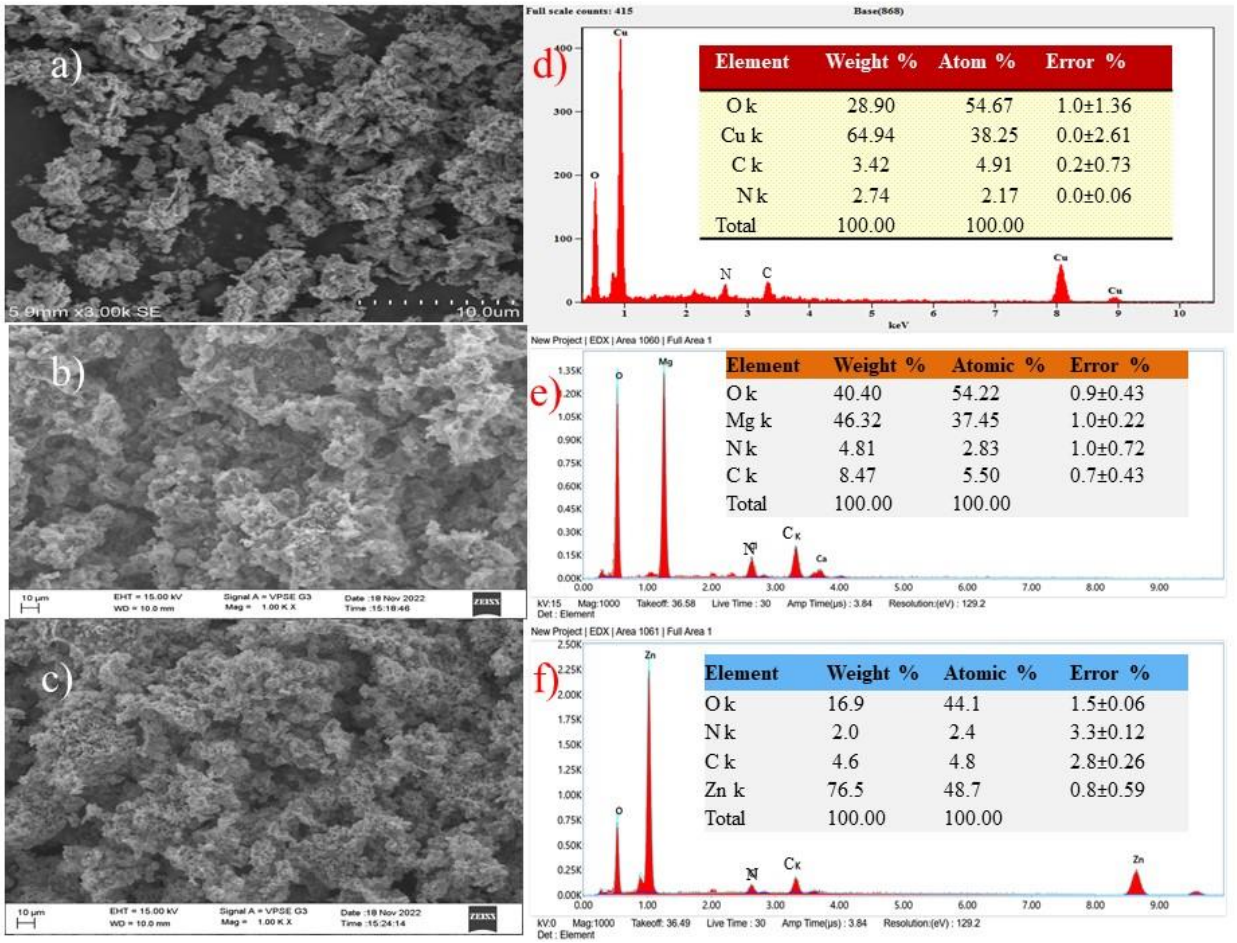

Figure 29. SEM micrographs a) CuO NPs, b) MgO NPs, C) ZnO NPs and EDX spectrum of d) CuO NPs, e) MgO NPs, f) ZnO NPs.

4.3.5.2 SEM-EDX analysis of ZC, MC and MZ NCs

The surface morphology and elemental compositions of the bimetallic ZC, MC and MZ NCs are illustrated in Figure 30 (a-f). SEM micrograph of ZC NCs in Figure 30a was found to show that the synthesized nanomaterial has flower-like structures with spherical morphology. Furthermore, the particles are dispersed across the surface with random aggregation, which is associated with the presence of biomolecules from the LEAA. The SEM micrograph of MC NCs is illustrated in Figure 30b. The micrograph revealed flower-like structures with spherical morphology of MC NCs. Sporadic agglomeration as indicated by a few large clusters present at the bottom of the SEM micrographs, is attributed to the adopted synthesis route and biological incapacitation capabilities of the phytochemicals from the LEAA. Figure 30c illustrates the SEM micrograph of MZ NCs. The surface morphologies of granules and mono-dispersive clusters in the shape of

assemblies are visible in the SEM image. The spherical-shaped MZNCs with random agglomeration of the particles throughout the surface were observed which may be due to the biomolecules from the LEAA.

The elemental compositions of ZC, MC and MZ NCs were obtained from EDX analysis Figure 30 (d-f). The intense optical absorption peaks at 0.5 keV (O) and 1(Cu and Zn) keV in EDX (Figure 30d) confirm the the formation of crystalline ZC NCs. The presence of Zn, Cu, and O with weight percentages of 39.35, 27.42, and 26.75 %, respectively confirmed the successful preparation of bimetallic ZC NCs. The minor peaks at 2.5 and 3.5 keV indicate the weight percentages of C and N, from the biomolecules adsorbed on the ZC NCs' surface. The EDX analysis, Figure 30e, also confirmed the formation of the MC NCs showing the characteristic peaks for the Mg, Cu, and O in the map. The Cu, Mg, and O percent weights in the MC NCs were 29.14, 18.37, and 33.35 %, respectively. Minor peaks of C and N at 2.5 and 3.5 keV with weight percentages of 13.43 and 5.31 are due to the biomolecules adsorbed on the surface of MC NCs. The intense optical absorption peaks in Figure 30f at 0.5, 1.2, 1.4, and 8.7 keV with weight percentages of 47.80, 26.52, and 15.40 for Zn, O, and Mg, respectively also confirm the formation of crystalline bimetallic MZ NCs. The presence of 7.4 and 3.0 % of C and N, respectively, could be attributed to the adsorbed biomolecules on the surface of MZ NCs.

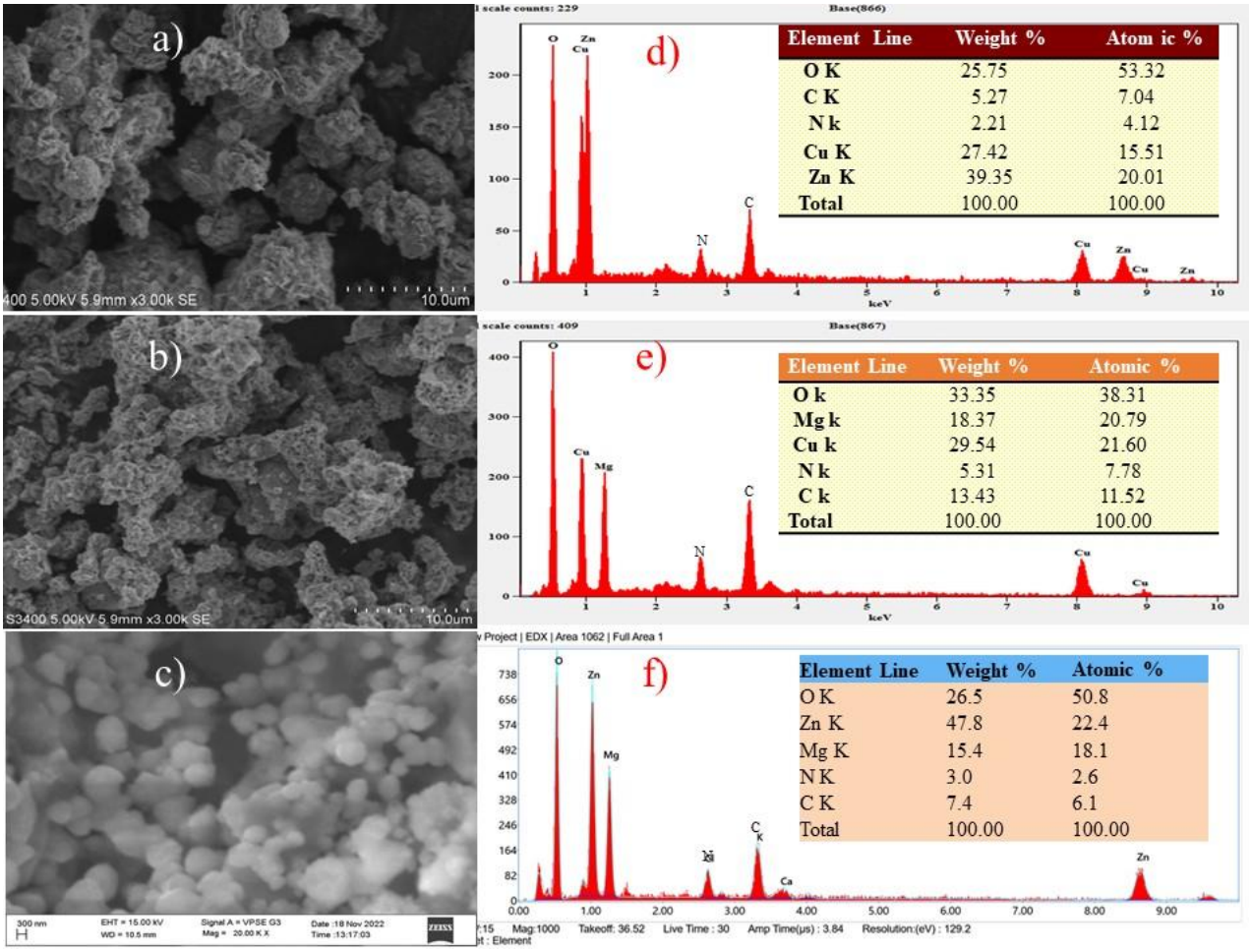

Figure 30. SEM micrographs a) ZC NCs, b) MC NCs, C) MZ NCs and EDX spectrum of d) ZC NCs, e) MC NCs, f) MZ NCs.

4.3.5.3 SEM-EDX analysis of ZMC NCs

The SEM micrographs of ZMC NPs at different magnifications are illustrated in Figure 31 (a, b) and show a spherical morphology of the NCs. Furthermore, the particles are dispersed across the surface uniformly with a low level of agglomeration/clustered structures due to the presence of phytochemicals from the LEAA on the particle surfaces. The EDX analysis, illustrated in Figure 31c, indicates the presence of Zn, Cu, Mg, and O in weight percentages of 22.46, 20.56, 13.87, and 26.50, respectively. The composition of these elements indicated the successful synthesis of pure ZMC NPs, and the presence of 13.30 and 3.31 % of C and N suggested that active biomolecules were adsorbed onto the surface of ZMC NPs. The intense optical absorption peaks

at 0.5, 1.2, 1.4, 8.2, and 8.7 keV also confirm the crystalline nature of the bio-prepared ZMC NCs.

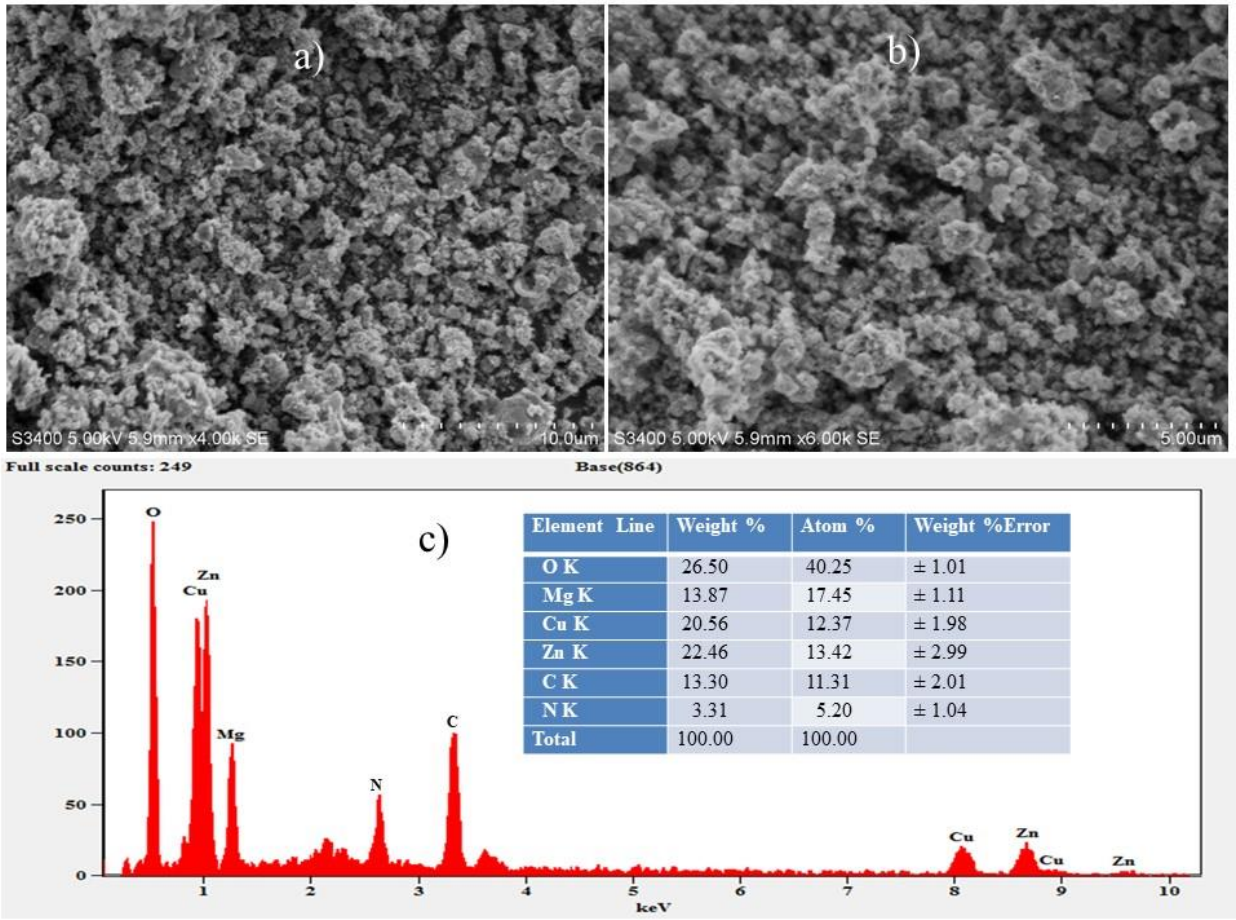

Figure 31. SEM micrographs of ZMC NPs with (a) 10 μm, (b) 5 μm and (c) EDX spectrum.

4.3.6 TEM/HRTEM/SAED analysis

The size, surface morphology, and crystallinity of the monometallic (CuO, ZnO, MgO) NPs, bimetallic (ZC, MZ, and MC) NCs, and trimetallic (ZMC) NCs are analyzed using using TEM, HRTEM, and SAED as illustrated in Figures 32-38. From the TEM images, the sizes of the synthesized NPs in the range of 4-26 nm, this agrees with the XRD analysis. From the TEM-HRTEM and SAED images the surface morphology and crystallinity of the synthesized MO NMs have also been observed.

4.3.6.1 TEM analysis of CuO, ZnO and MgO NPs

TEM/HRTEM/SAED images of the CuO NPs are illustrated in Figure 32 a-f. Figure 32 (a, b) shows that the CuO NPs have nearly spherical shapes and sizes ranging from 6 to 20 nm, with an average particle size of 12.30 nm as computed by ImageJ software. The five spots on the SAED pattern (Figure 32c) corresponded to specific CuO NPs crystal planes observed in XRD (Figure 27b). Colored concentric circles were used to show the most prominent five (002), (111), (200), (202), and (311) planes visualized in the XRD pattern, which evidenced the synthesis of monocrystalline CuO NPs. The HRTEM image analysis was performed using Gatan microscopy suite software, as illustrated in Figure 32 d-f. The obtained d-spacing value (Figure 32 e-f) of 0.271 nm is cooresponds to the (002) plane of CuO NPs in XRD analysis (Figure 27b) (H. Mohamed, Thema, & Dhlamini, 2021).

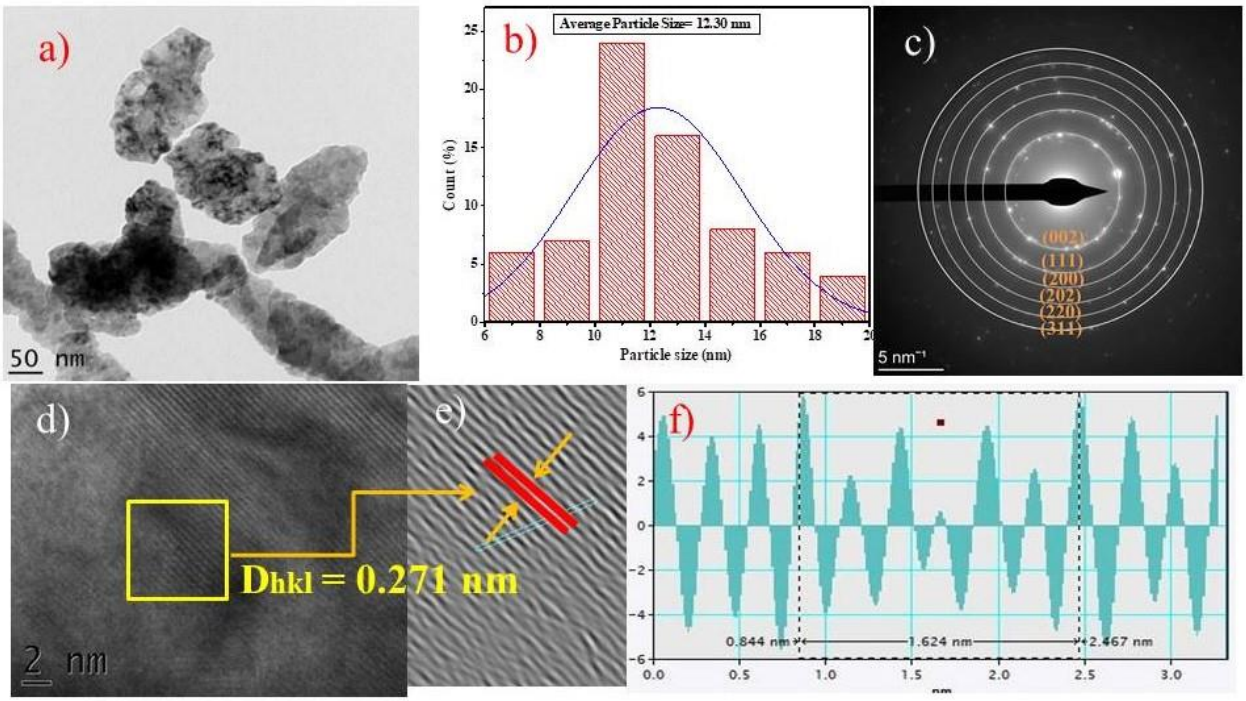

Figure 32. a) TEM micrograph of CuO NPs at 50 nm, b) Histogram of particle size distribution, c) SAED pattern, d) HRTEM at 2 nm, e) IFFT patterns with d-spacing and f) Profile of IFFT with d-spacing distance.

The surface morphology, size and crystalline of the ZnO NPs was analyzed as illustrated in Figure 33 a-f. The TEM images (Figure 33 a-b) evidenced the synthesis of spherical ZnO NPs

with an average particle size of ca, 10.03 nm. It has also been observed that the ZnO NPs were well distributed, homogeneous, spherical, and crystalline, as illustrated in Figure 33 a-c. The six ringed spots in the SAED pattern (Figure 33c) correspond to (100), (002), (101), (102), (110), and (112) crystal planes in the XRD pattern (Figure 27a). Figure 35 (c-f) also shows the polycrystalline nature of ZnO NPs with an inter-planer spacing (IPS) of 0.283 nm in the significant plane (101) (PP, 2020).

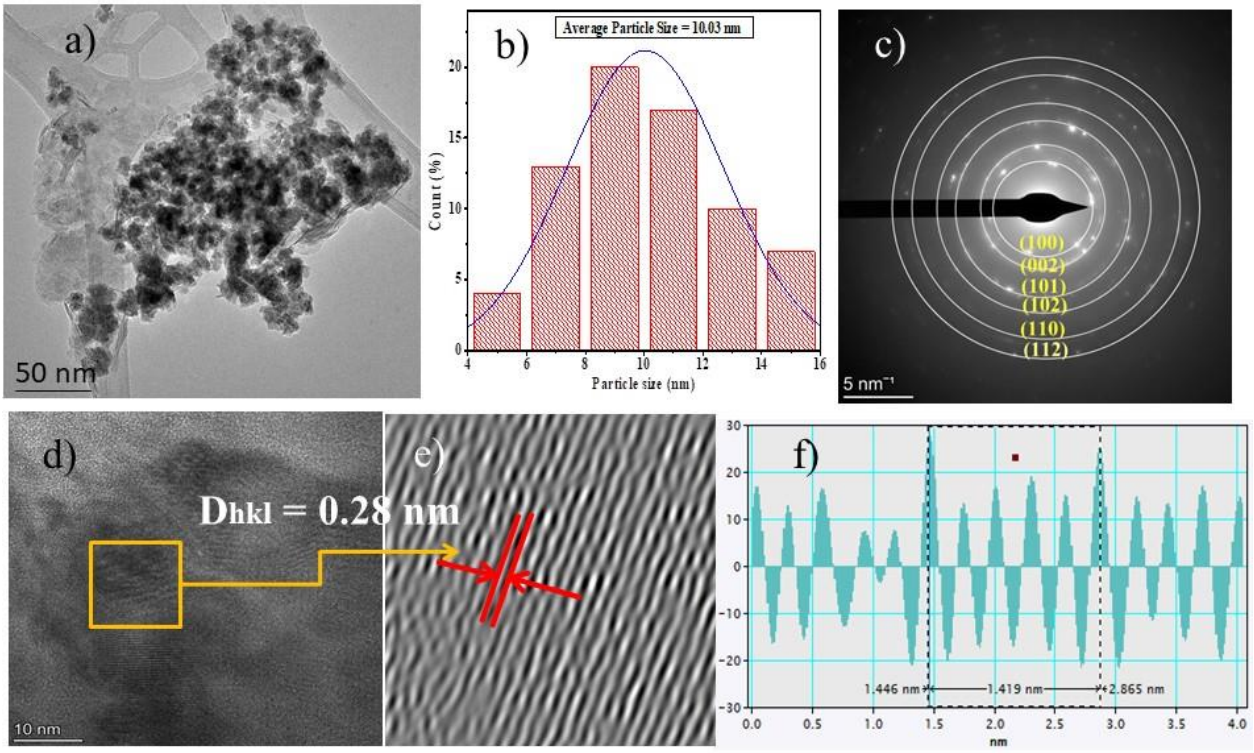

Figure 33. a) TEM micrograph of ZnO NPs at 50 nm, b) Histogram of particle size distribution, c) SAED pattern, d) HRTEM at 10 nm, e) IFFT patterns with d-spacing and f) Profile of IFFT with d-spacing distance.

The TEM/HRTEM/SAED images of MgO NPs have been presented in Figure 34 (a-f). The TEM micrograph at 50 nm resolution (Figure 34 a, b) show the spherical morphology and dispersed particles of MgO NPs with a size range of 6-18 nm and a average particle size of 11.34 nm. Figure 34c displays the selective area electron diffraction (SAED) pattern of MgO NPs, where the six white spot arrays support the NPs' crystalline nature. The six bright spots in the SAED pattern also correspond to (111), (002), (200), (220), (311) and (222)] crystal planes in the XRD

pattern (Figure 27c). Figure 34 (c-f) also illustrate the crystalline nature of MgO NPs with an inter-planer spacing of ca. 0.21 nm in the (111) plane (Velsankar et al., 2023).

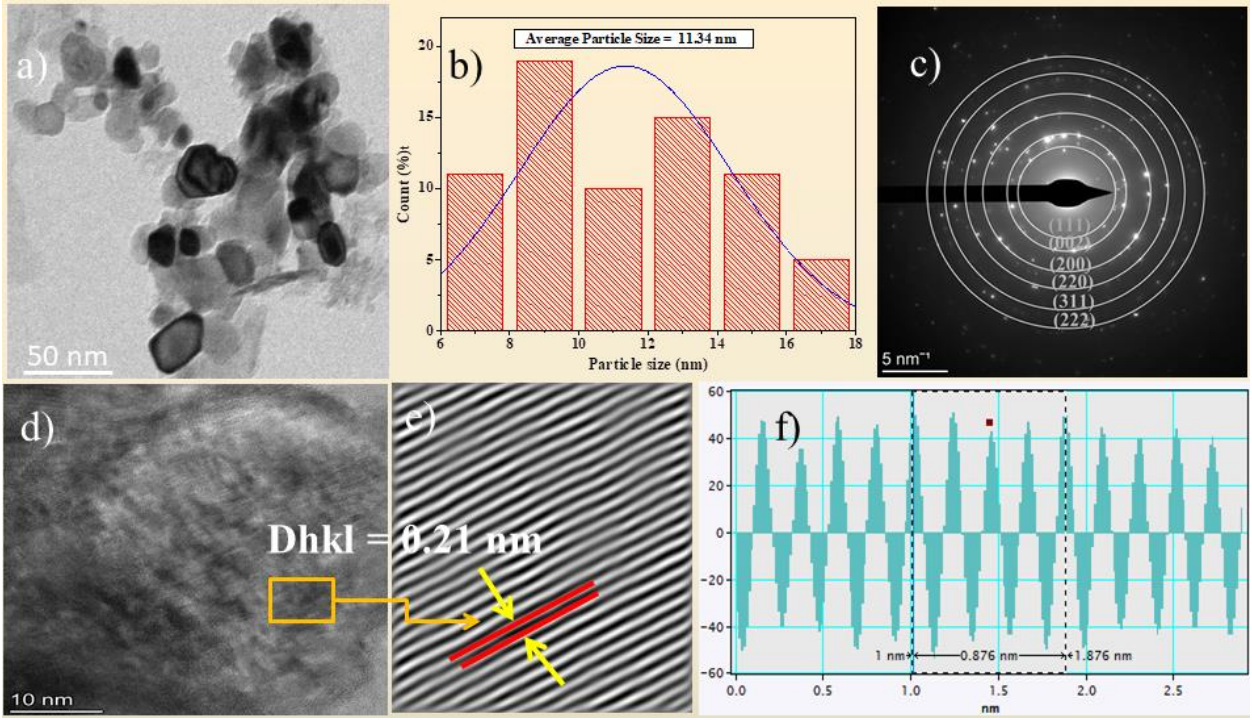

Figure 34. a) TEM micrograph of MgO NPs at 50 nm, b) Histogram of particle size distribution, c) SAED pattern, d) HRTEM at 10 nm, e) IFFT patterns with d-spacing and f) Profile of IFFT with d-spacing distance.

4.3.6.2 TEM analysis of ZC, MZ, and MC NCs

The particle size, surface morphology, and crystallinity nature of bi-(ZC, MZ, and MC) and trimetallic (ZMC) NCs are illustrated in Figures 35-38.

From the TEM micrographs, Figure 35 (a-b), it was observed that the ZC NCs had nearly spherical shape and size ranging from ca, 4.2 to 22.7 nm, with an average particle size of 13.09 nm. The nine major ringed spots in the SAED pattern (Figure 35c) showed specific ZC NCs crystal planes corresponding to the XRD pattern (Figure 28c). The concentric circles correspond to the prominent nine (101), (100), (102), (111), (002), (021), (112), and (102) crystal planes in the XRD pattern. The SAED pattern illustrated in Figure 35 (d-h) showed a d-spacing value of ca. 0.255 nm, which corresponds to the (102) plane of CuO and ca. 0.261 nm for the (101) plane of the ZnO NPs.

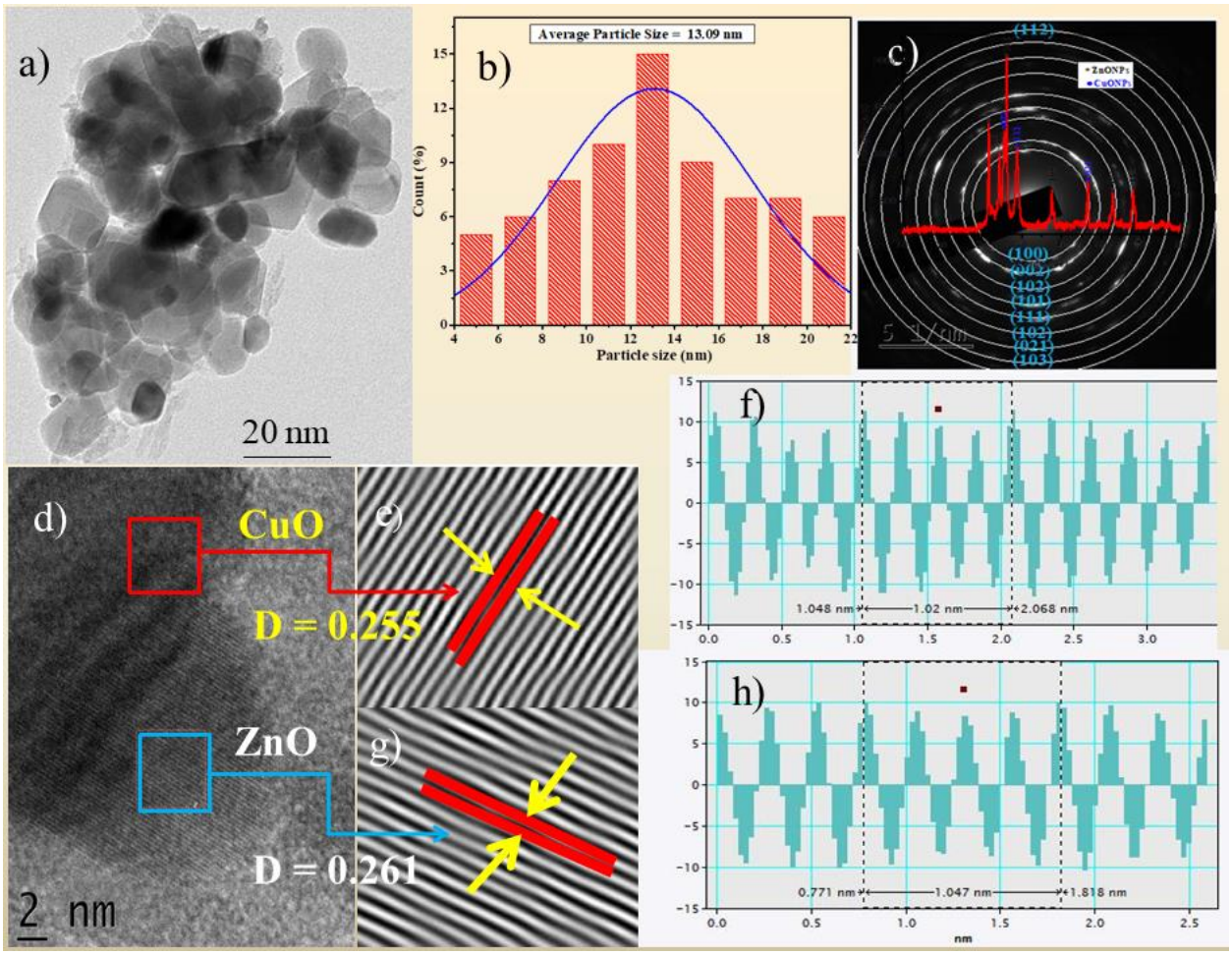

Figure 35. TEM images of ZC NCs a) at 20 nm, b) Histogram of particle size distribution c), SAED pattern, d) HRTEM at 2 nm e) IFFT patterns with d-spacing of CuO, and f) IFFT patterns with d-spacing of ZnO NPs, g) Profile of IFFT of CuO with d-spacing distance, and h) Profile of IFFT of ZnO with d-spacing distance.

The TEM/HRTEM-SAED analysis of MC NCs is illusrated in Figure 36 (a-h). Figure 36 (a,b) shows that the MC NCs are nearly spherical, with sizes ranging from 6 to 24 nm with an average particle size of 14.54 nm. The eight spots in the SAED pattern (Figure 36c) evidenced the polycrystalline nature of MC NCs and the concentric circles in the SAED pattern, which corresponded to the (002), (111), (200), (202), (220), (220), (311), and (222) crystal planes of the eight diffraction peaks in the XRD pattern (Figure 28b). Figure (36 d-h) illustrates the enlarged lattice fringes, patterns, and profiles of IFFT with d-spacing values of 0.23 nm for the (002) plane of CuO NPs, and 0.21 nm for the (111) plane of MgO NPs respectively.

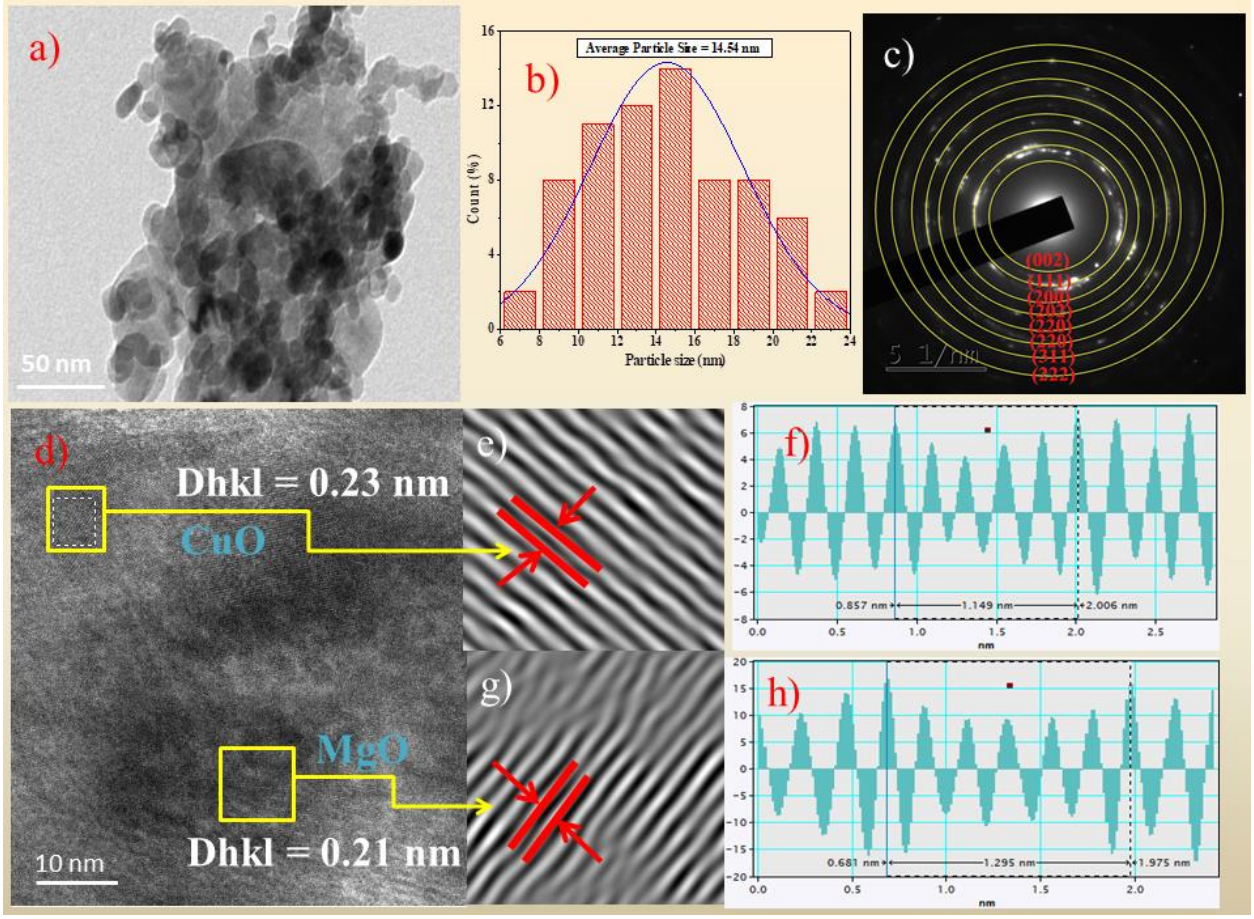

Figure 36. TEM images of MC NCs a) at 50 nm, b) Histogram of particle size distribution c), SAED pattern, d) HRTEM at 2 nm e) IFFT patterns with d-spacing of CuO, and f) Profile of IFFT of CuO with d-spacing distance, g) IFFT patterns of MgO with d-spacing distance, and h) Profile of IFFT of MgO with d-spacing distance.

The particles' size, crystal structure, and morphology of MZ NCs were described with TEM/HRTEM-SAED. The synthesized MZ NCs are nearly spherical, as seen in TEM images IN Figures 37 (a&b), with sizes ranging from 4 to 20 nm and an average particle size of 12.23 nm. The eight spots on the SAED pattern (Figure 37e) revealed the polycrystalline nature of MZ NCs, and the concentric circles of the SAED pattern corresponded to the (100), (002), (101), (200), (111), (1032), (110), and (220) crystal planes, of the eight prominent peaks in the XRD pattern (Figure 28a). Figure 37 (d-h) revealed the HRTEM micrographs with magnified lattice fringes, patterns, and profile of IFFT with d-spacing values for specified planes (100) and (111), respectively, as analyzed by Gatan Digital Micrograph Software. The average inter-planer

spacing of 0.28 nm (Figure 37 d-h) corresponds to the (100) plane of ZnO NPs and 0.23 nm with the (200) plane of MgO NPs.

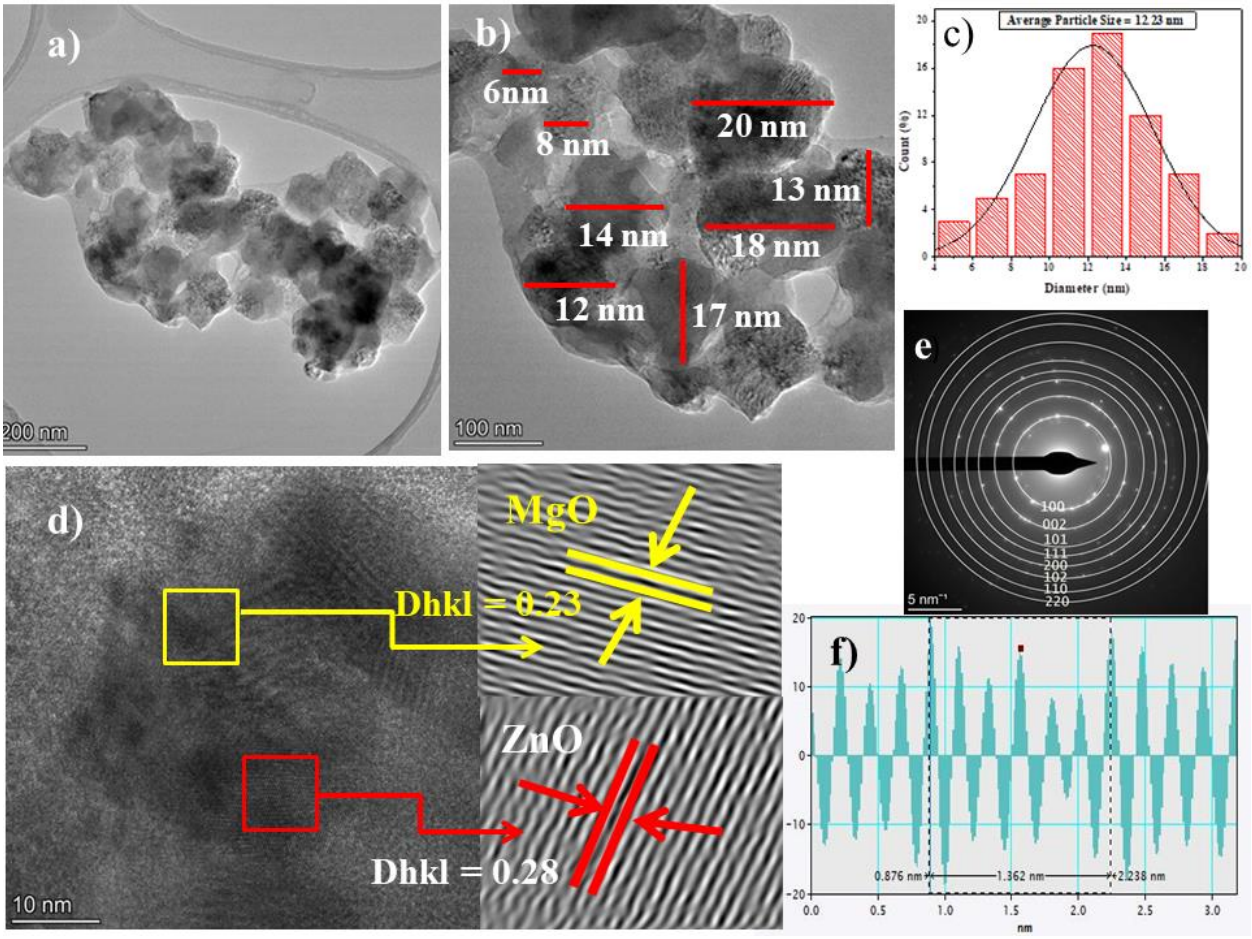

Figure 37**.** TEM micrograph of MZ NPs a) at 200 nm, b) at 100 nm, c) HRTEM at 10 nm d) SAED pattern, e) Profile of IFFT with inter-planner distance

4.3.6.3 TEM analysis of trimetallic ZMC NCs

The morphology, particle size, and crystallinity of ZMC NCs are illustrated in TEM-HRTEM-SAED images (Figure 38 a-f). The ZMC NCs have well-defined spherical morphology with sizes ranging from 4 to 26 nm and an average particle size of 15.13 nm, as presented in Figures (38 a, b). The presence of small particles with a size of 4 nm demonstrates the effectiveness of biomolecules from the LEAA as capping and stabilizing agents. The nine major circular concentric circles in the SAED pattern (Figure 38c) correspond to (110), (100), (002), (002), (111), (200), (102), (110), (220) and (311) crystal planes in the XRD pattern (Figure 24d)

(Figure 28d). The average inter-planer spacing values of ca. 0.276, 0.261, and 0.211 nm (Figure 38d) computed from profile IFFT (Figure 38 e-g) correspond to the (002), (100) and (110) planes of CuO, ZnO, and MgO NPs respectively. The stacking faults in the HRTEM (IFFT) image and the bright circular spots in the SAED pattern confirm the synthesis of polycrystalline ZMC NCs (Maheo et al., 2023; Vindhya & Kavitha, 2023).

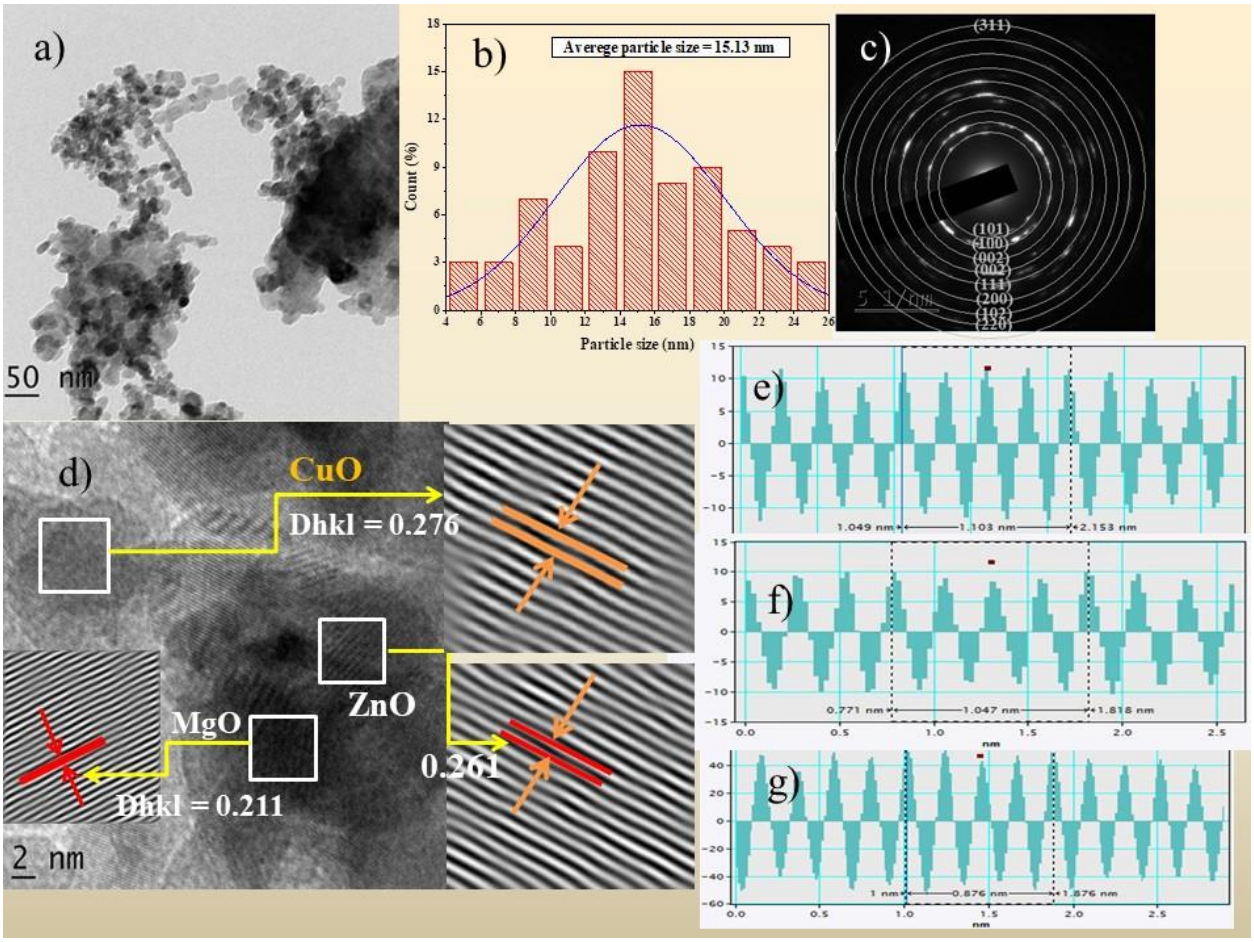

Figure 38. TEM images of ZMC NPs a) at 200 nm, b) at 50 nm, c) HRTEM at 5 nm, d) magnified lattice fringes, e) Profile of IFFT with d-spacing distance, f) SAED pattern, and g) Average particle size of ZMC NPs.

4.4 Biological Activities

4.4.1 Antioxidant activity

The DPPH and FRAP assays were carried out to assess the *in-vitro* antioxidant activity of LEAA and biosynthesized mon- (CuO, ZnO, and MgO), bi- (ZC, MZ, and MC) and tri-metallic (ZMC)

NMs. Different concentrations (200, 100, 50, 25, and 12.5 μg/mL) of samples were prepared from their respective stock solutions (1 mg/mL). Each solution was subjected to the UV-vis spectrophotometer to measure their absorbance against DPPH and FRAP assays at 517 and 700 nm, respectively. The average values of triplicate outcomes for each sample were expressed as mean ± standard deviation.

4.4.1.1 DPPH assay

DPPH free radical scavenging potential of LEAA and MO NMs compared to ascorbic acid (AA) were depcied in Figure 39 and Table 7. The results showed that the activity of LEAA and MO NMs against DPPH radical were dose-dependent, in which the DPPH scavenging activity percentage was directly correlated to concentration. LEAA showed a low DPPH radical scavenging percentage of 39.88 at 12.5 μg/mL and a high percentage of 65.02 at 200 μg/mL with a corresponding IC50 value of 38.60 μg/mL. The CuO NPs exhibited the highest DPPH radical scavenging activity of 88.81, with a corresponding IC50 value of 5.75 at 200 μg/mL concentration. The highest DPPH radical scavenging activity of ZnO NPs was 86.28 with a corresponding IC50 value of 6.53 at 200 μg/mL concentration. The highest DPPH radical scavenging activity of MgO NPs was 84.67 with a corresponding IC50 value of 7.76 at 200 μg/mL concentration.

The DPPH radical scavenging percentages of ZC, MC and MZ NCs at 200 μg/mL were 94.71, 96.42 and 92.93, respectively. The IC50 values of ZC, MC and MZ NCs were 3.28, 3.12 and 5.26 μg/mL respectively. The results revealed that the DPPH radical scavenging activity of MC NCs is relatively higher than that of ZC and MZ NCs. The trimetallic ZMC NCs showed a scavenging percentage 98.41 with a corresponding IC50 value of 2.08 μg/mL at 200 μg/mL. The standard drug (ascorbic acid) has shown a scavenging percentage of 94.56 with a corresponding IC50 value of 3.78 μg/mL at 200 μg/mL. From the results, trimetalic ZMC NCs has the highest anti-DPPH radical scavenging percentages of all the tested samples including ascorbic acid.

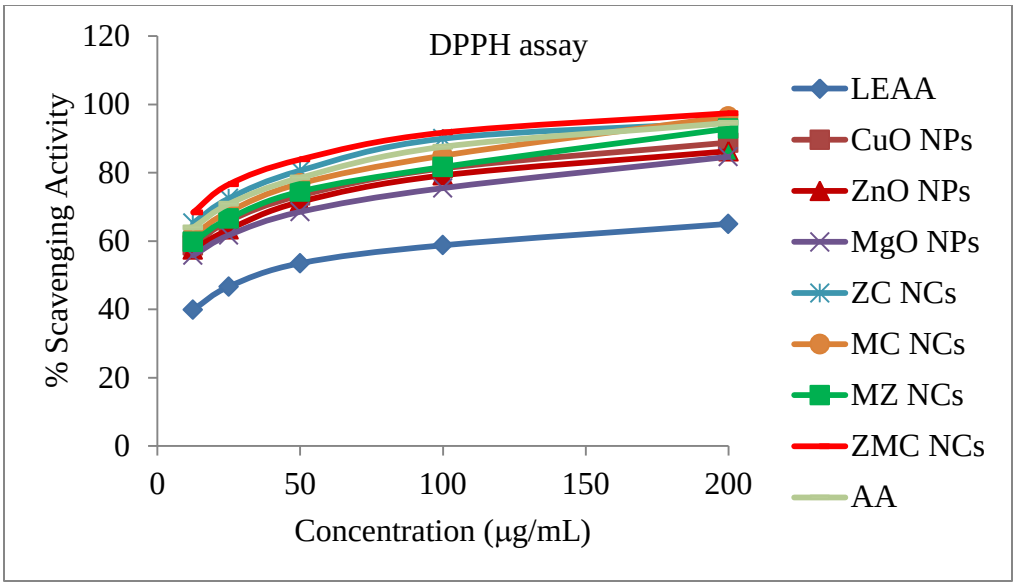

Figure 39. The scatter graph of DPPH radical scavenging activity of LEAA, phytochemical mediated (CuO, ZnO, MgO, ZC, MC, MZ, and ZMC) NMs and Ascorbic acid (AA).

Table 7. DPPH radical scavenging percentage activity (mean±SD) of LEAA, phytochemical mediated MO NMs and ascorbic acid.

Samples	**Concentrations (µg/mL)**					
	12.5	25	50	100	200	IC50
LEAA	39.88±0.04^{de}	46.66±0.01^{d}	53.49±0.02^{cd}	58.75±0.01^{cd}	65.02±0.02^{c}	36.97
CuO NPs	58.67±0.00^{cd}	65.86±0.02^{c}	73.32±0.01^{bc}	81.26±0.03^{ab}	88.81±0.02^{ab}	5.75
ZnO NPs	57.48±0.04^{cd}	63.37±0.02^{c}	71.46±0.03^{bc}	79.22±0.00^{bc}	86.28±0.04^{ab}	6.53
MgO NPs	55.76±0.00^{cd}	61.72±0.03^{c}	68.55±0.02^{bc}	75.49±0.04^{bc}	84.67±0.01^{ab}	7.76
ZC NCs	65.26±0.11^{c}	72.46±0.06^{bc}	80.62±0.03^{b}	89.96±0.04^{ab}	94.71±0.00^{a}	3.28
MC NCs	63.72±0.04^{c}	71.59±0.02^{bc}	81.83±0.01^{b}	88.99±0.03^{ab}	96.42±0.02^{a}	3.12
MZ NCs	61.77±0.03^{c}	68.59±0.01^{bc}	76.47±0.04^{b}	83.68±0.06^{ab}	92.93±0.01^{a}	5.26
ZMC NCs	68.37±0.11^{c}	76.57±0.01^{bc}	83.88±0.06^{b}	91.27±0.02^{ab}	98.41±0.01^{a}	2.08
A. acid	63.91±0.03^{c}	70.83±0.00^{bc}	78.51±0.06^{b}	87.58±0.01^{ab}	94.56±0.02^{a}	3.78

Note: The scavenging percentages (%) are the means of five individual triplicates ± the standard deviation (SD). The letter(s) on the means in each column are not significantly different as per Tukey's HSD analysis.

In general, the DPPH radical scavenging capacity of the samples were in decreasing order of ZMC NCs > MC NCs > ZC NCs > ascorbic acid > MZ NCs > CuO NPs > ZnO NPs > MgO NPs > LEAA. According to the results, at the same dose (200 μg/mL), monometallic oxide NPs and bimetallic MZ NCs have a higher DPPH radical scavenging activity than LEAA and slightly lower activity than ascorbic acid. Moreover, ZMC NCs, MC NCs, and ZC NCs have higher DPPH radical scavenging activity than ascorbic acid and all other NPs, which could be attributed to the synergistic effects of combined NCs (Haq et al., 2023). However, all the MO NMs synthesized using LEAA can be promising antioxidant therapeutic agents.

4.4.1.2 FRAP Assay

The potential of reducing ferric ($Fe^{3+)}$ ions to ferrous (Fe^{2+}) by LEAA and the MO NMs was observed by the change in color of the reaction solutions from yellow to green and measuring the absorbance at 700 nm (Benzie & Strain, 1996). The ability to reduce Fe^{3+} ions to Fe^{2+} ions (ferric-reducing power) by donor electrons presented in Table 8, was found to be in increasing order of LEAA < ZnO NPs < CuO NPs < MgO NPs < ZC NPs < MZ NPs < ascorbic acid < MC NPs < ZMC. The results show that at a 200 μg/mL concentration, LEAA has a ferric-reducing power of 0.227. The MO NMs and ascorbic acid have a ferric-reducing power between 1.194 and 1.964. LEAA has the lowest, and the ZMC NCs have the highest ferric-reducing power. Moreover, bimetallic NCs have higher ferric-reducing power than their monometallic counterparts. The strong ferric-reducing power of the bi- and trimetallic oxide NCs is attributed to free charge transferring between the combined NCs (Soleimani-Amiri, Hossaini, & Azizi, 2023). The MO NMs demonstrated significant ferric-reducing antioxidant power overall, which also agrees with earlier reports (Djamila, Eddine, Abderrhmane, Nassiba, & Barhoum, 2022; Soleimani-Amiri et al., 2023).

Table 8. The absorbance of FRAP of LEAA, MO NMs, and ascorbic acid.

Samples	Concentrations (μg/mL)				
	12.5	25	50	100	200
LEAA	0.152 ± 0.001^{e}	0.165 ± 0.003^{e}	0.183 ± 0.002^{ed}	0.204 ± 0.011^{d}	0.227 ± 0.010^{d}
CuO NPs	0.322 ± 0.003^{d}	0.507 ± 0.022^{dc}	0.683 ± 0.004^{c}	0.912 ± 0.002^{c}	1.204 ± 0.002^{bc}
ZnO NPs	0.302 ± 0.006^{d}	0.494 ± 0.010^{dc}	0.653 ± 0.002^{c}	0.882 ± 0.003^{c}	1.194 ± 0.011^{bc}
MgO NPs	0.332 ± 0.003^{d}	0.514 ± 0.012^{dc}	0.696 ± 0.004^{c}	0.922 ± 0.004^{c}	1.312 ± 0.012^{b}
ZC NCs	0.542 ± 0.001^{d}	0.884 ± 0.011^{c}	1.036 ± 0.001^{bc}	1.292 ± 0.003^{b}	1.826 ± 0.000^{a}
MZ NCs	0.554 ± 0.004^{d}	0.895 ± 0.012^{c}	1.047 ± 0.002^{bc}	1.297 ± 0.002^{b}	1.834 ± 0.001^{a}
MC NCs	0.723 ± 0.003^{cd}	0.933 ± 0.002^{c}	1.103 ± 0.004^{bc}	1.423 ± 0.001^{b}	1.893 ± 0.002^{a}
ZMC NCs	0.756 ± 0.002^{cd}	0.952 ± 0.001^{c}	1.114 ± 0.012^{bc}	1.515 ± 0.004^{b}	1.964 ± 0.003^{a}
A. Acid	0.654 ± 0.001^{d}	0.912 ± 0.003^{c}	1.069 ± 0.002^{bc}	1.304 ± 0.006^{b}	1.845 ± 0.001^{a}

Note: Absorbance values of five individual replicates ± standard deviation. The letter(s) on the means in each column are not significantly different as per Tukey's honestly significance difference (HSD) (SPSS 20.0).

4.4.2 Antimicrobial activity

The *in vitro* antimicrobial activity of LEAA and the MO NMs against selected bacterial and fungal strains using the Mueller-Hinton agar disc diffusion method was evaluated against drug-selected gram-positive and gram-negative bacterial strains (Uwizeyimana, Kim, Lee, Byun, & Yong, 2020; Yaqub et al., 2020). Chloramphenicol was used as the positive control and DMSO as negative control. In addition, the antifungal activity of LEAA and the MO NMs were also evaluated using pathogenic fungal strains, *Aspergillus flavus, Aspergillus niger, and Candida albicans.*

4.4.2.1 Antibacterial activity

Table 9, Figures 42 & 43 show that LEAA and the MO NMs showed excellent dose-dependent *in vitro* antibacterial activity against the selected drug-resistant bacterial strains compared to the standard drug Chloramphenicol. All samples showed a highest activity against *S. aureus* the lowest activity against *E. coli* bacterial strains.

Table 9. Zone of inhibition of LEAA and MO NMs against *S. pneumoniae*, *P. aeruginosa*, *E. coli*, and *S. aureus* bacterial strains.

Bacterial strains	**Conc. (µg/mL)**	**LEAA**	**CuO NPs**	**ZnO NPs**	**MgO NPs**	**ZC NCs**	**MC NCs**	**MZ NCs**	**ZMC NCs**	**Chloramphenicol (50 µg/mL)**
S. pneumoniae	25	11±0.21	19±0.17	18±0.13	17±0.04	20±0.22	21±0.02	19±0.03	23±0.02	29±0.04
	50	14±0.00	24±0.45	23±0.11	20±0.21	24±0.04	24±0.10	23±0.02	26±0.00	
	100	17±0.12	27±0.16	26±0.02	23±0.02	27±0.02	28±0.02	27±0.04	29±0.02	
	200	19±0.14	29±0.31	30±0.12	26±0.12	30±0.03	31±0.11	32±0.02	33±0.01	
MIC	(µg/mL)	20	12.5	10	12.5	10	10	10	10	
P .aeruginosa	25	12±0.13	19±0.33	18±0.11	18±0.22	22±0.13	20±0.01	18±0.01	24±0.02	30±0.03
	50	15±0.01	23±0.23	23±0.01	20±0.11	25±0.23	24±0.04	22±0.01	27±0.03	
	100	18±0.02	26±0.27	26±0.12	23±0.03	28±0.27	27±0.02	26±0.03	31±0.00	
	200	20±0.01	28±0.11	29±0.07	26±0.02	31±0.11	30±0.03	31±0.02	34±0.04	
MIC	(µg/mL)	20	15	15	15	10	15	10	10	
E. coli	25	10±0.11	17±0.28	15±0.11	17±0.03	19±0.28	18±0.04	18±0.02	22±0.00	27.5±0.06
	50	13±0.33	22±0.18	20±0.04	20±0.01	21.5±0.2	22±0.00	23±0.04	25.5±00	
	100	16±0.14	24±0.22	24±0.22	22±0.11	25±0.22	25±0.02	26±0.01	28±0.02	
	200	18±0.22	26±0.34	27±0.02	25±0.02	29±0.04	28.5±00	29±0.03	31±0.01	
MIC	(µg/mL)	20	15	15	15	10	10	10	10	
S. aureus	25	13±0.11	20±0.21	19±0.13	18±0.02	22±0.21	22±0.00	21±0.02	24±0.02	31±0.11
	50	16±0.04	24±0.27	23±0.11	21±0.01	26±0.27	25±0.04	25±0.11	27.5±00	
	100	19±0.12	27±0.09	27±0.02	24±0.21	30±0.09	28±0.01	29±0.01	31±0.02	
	200	21±0.00	30.5±0.0	31±0.17	28±0.11	32.5±0.0	32±0.02	33.5±0.1	35±0.03	
MIC	(µg/mL)	15	10	10	10	10	10	5	5	

The zone of inhibitions of LEAA and the b phytochemical mediated monometallic (CuO, ZnO and MgO) nanoparticles have presented in Figure 42 (a-d). The extract has revealed antibacterial activity (>10 mm to < 21 mm zone of inhibition) against all bacterial strains as presented in Figure 42a. At 200 µg/mL extract revealed the highest zone of inhibition (21±0.00) against *S. aureus* and lowest zone of inhibition (18.5±0.22) against *E.coli* bacterial strain with MIC of (15 and 25 µg/mL), respectively. Among the monometallic (CuO, ZnO and MgO) nanoparticles, ZnO NPs showed slightly the larger zone of inhibitions in all selected bacterial strains. At 200

µg/mL CuO NPs showed a highest zone of inhibition (30.5±0.02 with MIC 10 µg/mL) against *S. aureus* and the lowest zone of inhibition (26±0.34 with an MIC of 15 µg/mL) against *E.coli*. ZnO NPs revealed the highest zone of inhibition (31±0.17 with an MIC of 10 µg/mL) against *S. aureus* and the lowest zone of inhibition (27±0.02 with an MIC of 15 µg/mL) against *E.coli* strains at 200 µg/mL. MgO NPs revealed the highest zone of inhibition (28±0.11 with an MIC of 10 µg/mL) against *S. aureus* and the lowest zone of inhibition (25±0.02 with an MIC of 15 µg/mL) against *E.coli* strains at 200 µg/mL.

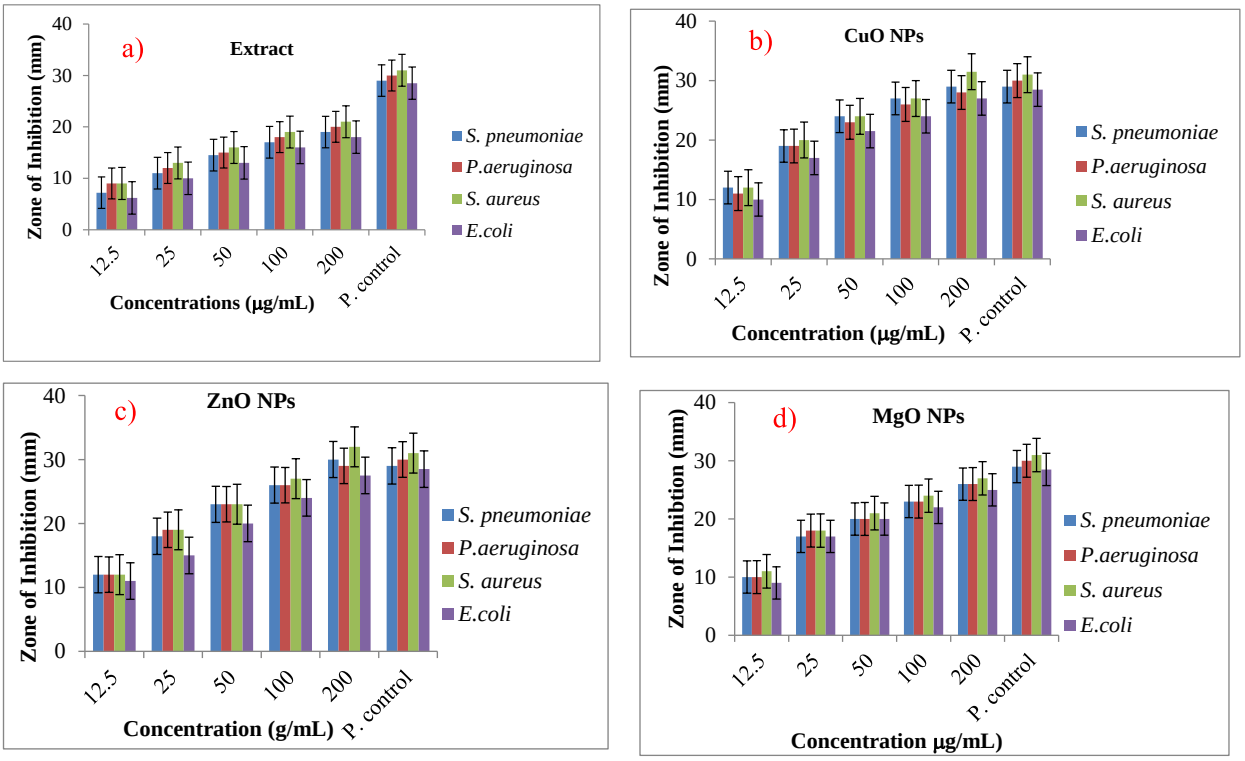

Figure 40. Antibacterial activity of a) LEAA, b) CuO NPs, c) ZnO NPs, and d) MgO NPs against selected bacteria strains.

The zone of inhibition of bimetallic (ZC, MC, and MZ) and trimetallic (ZMC) NCs are presented in Figure 43 (a-d). Among the bimetallic (ZC, MC, and MZ) NCs, MZ NCs showed considerably higher antibacterial activity than MC and MZ NCs at 200 µg/mL concentration. ZC NCs showed a zone of inhibition of 32.50 mm with MIC 10 µg/mL against *S. aureus* and a smaller zone of inhibition of 29.0 mm with MIC of 15 µg/mL against *E.coli*. MC NCs have a larger zone of inhibition of 32.0 and a MIC of 10 µg/mL against *S. aureus* and a smaller zone of inhibition of 28.5 mm with MIC of 15 mg/mL against E.coli. MZ NCs showed a larger zone of inhibition of

33.5 mm with MIC of 10 µg/mL against *S. aureus* and a smaller zone of inhibition of 29.5 mm with MIC of 15 µg/mL against *E.coli*. Trimetallic ZMC NCs exhibited a larger zone of inhibition of 35.0 mm with MIC of 5 µg/mL against and a smaller zone of inhibition of 31.0 mm with MIC of 10 mg/mL against E.coli. *S. aureus. Similarly*, the standard drug (Chloramphenicol) has exhibited a larger zone of inhibition (31±0.11) against *S. aureus* and a smaller zone of inhibion (27.5±0.06 mm) against *E.coli* among the tested strains.

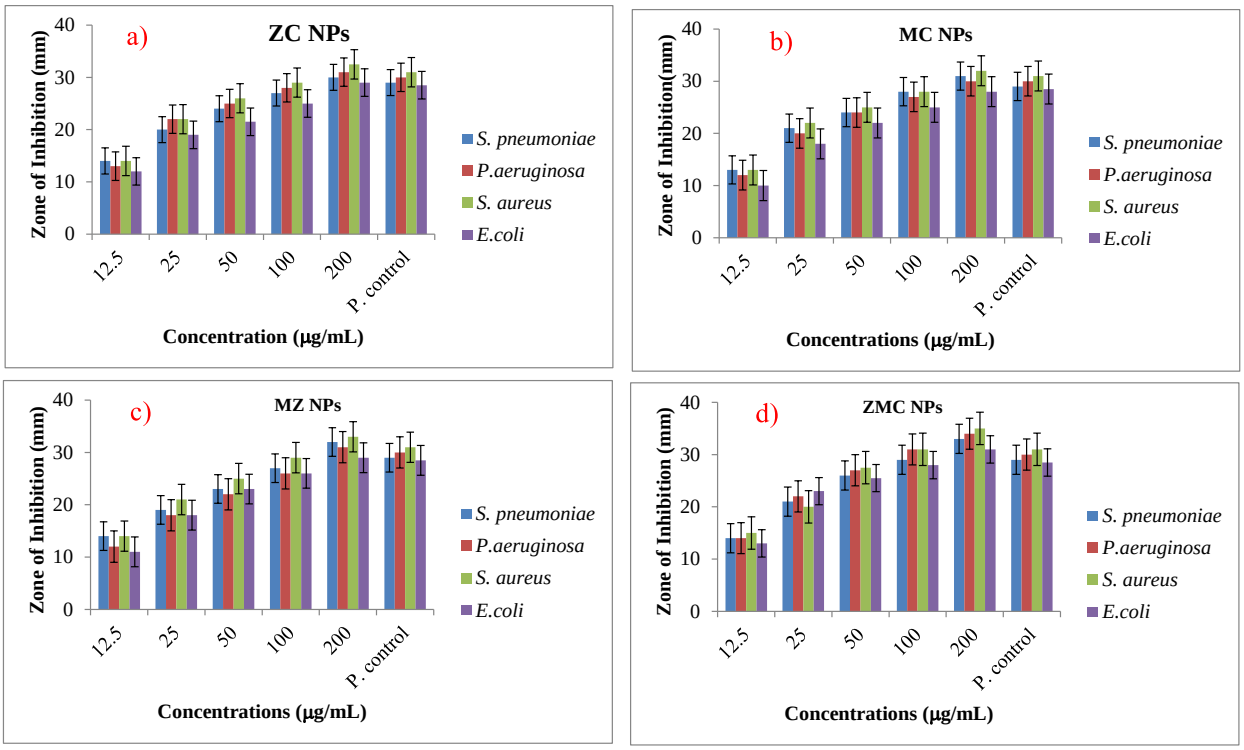

Figure 41. Antibacterial activity of a) ZC NCs, b) MC NCs, c) MZ NCs, and d) ZMC NCs against selected bacteria strains.

The results show that bi and trimetallic NCs have higher antibacterial activity against the gram-positive and gram-negative bacterial strains than their monometallic counterparts. Moreover, the antibacterial efficacy of ZMC NCs is highest amongst the synthesized MO NMs against all the bacterial strains. This is attributed due to the synergistic effect of the different metals incorporated in the bimetallic (ZC, MC, and MZ) and trimetallic (ZMC) NCs hence all bacterial starins have shown compariably less resistance to them (Gupta, Khare, & Sinha, 2021; Kim, Åberg, Salvati, & Dawson, 2012; Nieto-Maldonado et al., 2022). Nevertheless, all synthesized

MO NMs have antibacterial effeicacy and can be used as promising antibacterials for various contagious infections.

According to the literature, the characteristics of MO NMs, including size, shape, surface property, composition, and charge density, can affect how well they pass through biological barriers and interact with the cellular environment (R. Ali, Shanan, Saleh, & Abass, 2020). While the concise antibacterial mechanism of MO NMs is still debated, adhesion to bacterial surfaces, cell penetration, destruction of bacterial biomolecules, intracellular destabilization, and ROS generation are proposed mechanisms for cellular oxidative stress and variation of the bacterial signal transduction pathways are among the proposed mechanisms for their action (Athira, Gurrala, & Kumar, 2021). Because of the presence of negatively charged thick-layered peptidoglycan in the bacterial cell walls, MO NMs can be intracted easily and invade the cells and probably interact with sulfur (S) and phosphorous (P) contained in the DNA structure, leading to cytotoxicity and cell apoptosis (Gupta et al., 2021; Kim et al., 2012; Nieto-Maldonado et al., 2022).

4.4.2.2 Antifungal activity

The *in vitro* antifungal activity of LEAA and mono, bi, and trimetallic MO NMs against common pathogenic fungal strains were evaluated. The measured zone of inhibition of all the samples against *A. flavus, A. niger*, and *C. albicans* fungal strains are presented in Table 10 and Figures 44-45. It was observed that the organisms showed resistance toward LEAA and the MO NMs at lower concentrations. However, they showed dose-dependent antifungal activity.

LEAA showed a large zone of inhibition of ca. 13.0 mm with a MIC value of 25 µg/mL against *A. flavus* and the smallest zone of ca. 11.0 mm with a MIC value of 25 µg/mL against C.albicans as illustrated in Figure 44a. CuO NPs (Figure 44b) showed a large zone of inhibition of ca. 25.0 mm with a MIC value of 15.0 µg/mL against *A. flavus* and the smallest zone of ca. 22.0 mm with MIC value 15 of µg/mL against C.albicans. ZnO NPs (Figure 44c) showed a large zone of inhibition of ca. 26.0 mm with a MIC value of 10 µg/mL against *A. flavus* and the smallest zone of ca. 23.0 mm with MIC value of 15.0 µg/mL against C.albicans. MgO NPs (Figure 40d) showed a large zone of inhibition of ca. 23.0 mm with a MIC value of 15 µg/mL against *A. flavus* and the smallest zone of ca. 21.0 mm with a MIC value of 20 µg/mL against C.albicans.

The results indicated that monometallic (CuO, ZnO, and MgO) NPs have double-fold antifungal activity compared to the LEAA with similar concentrations. However, monometallic (CuO, ZnO, and MgO) NPs showed near comparable antifungal activity, except ZnO NPs, which showed slightly higher activity against all fungal strains.

Table 10. Antifungal activity of LEAA, and MO NMs against standard *Aspergillus flavus*, *Aspergillus niger*, and *Candida* albicans fungal strains.

Fungal strains	**Conc. (µg/mL)**	**LEAA**	**CuO NPs**	**ZnO NPs**	**MgO NPs**	**ZC NCs**	**MC NCs**	**MZ NCs**	**ZMC NCs**	**Fluconazole (50 µg/mL)**
Aspergillus flavus	25	8±0.11	12±0.28	13±0.02	11±0.03	15±0.22	14±0.02	14±0.0	16±0.11	29±0.02
	50	10.5±0.33	16.5±0.8	17±0.01	15±0.01	19±0.31	17±0.01	18±0.1	20±0.02	
	100	12±0.14	21.5±0.2	21±0.00	19±0.02	22±0.22	21±0.02	22±0.2	25±0.12	
	200	13±0.22	25±0.34	26±0.10	23±0.11	29±0.04	27±0.01	28±0.4	31±0.03	
MIC	(µg/mL)	25	15	10	15	10	10	10	10	
Aspergillus niger	25	7±0.01	11±0.07	11±0.03	11±0.11	14.5±0.1	13±0.0	12±0.01	15±0.12	26±0.21
	50	8.5±0.21	15.5±0.1	15±0.01	14±0.01	18±0.15	17±0.1	16±0.02	20±0.21	
	100	10±0.22	19±0.16	21±0.02	18±0.04	22±0.11	21±0.3	20±0.03	24±0.02	
	200	11.5±0.03	23.5±0.3	24±0.04	21±0.22	27±0.21	25±0.2	25.5±0.12	28±0.11	
MIC	(µg/mL)	25	15	15	15	10	15	15	10	
Candida albicans	25	6±0.13	10±0.33	12±0.11	10±0.03	14±0.01	13±0.2	13±0.02	15±0.02	27.5±0.11
	50	7.5±0.01	14.5±0.2	15±0.04	14±0.11	17.5±0.2	16±0.3	16±0.04	19.5±03	
	100	9±0.02	17.5±0.2	19±0.02	17±0.01	21±0.07	20±0.2	21.5±03	23±0.02	
	200	11±0.01	22±0.11	23±0.01	21±0.02	25.5±0.1	24±0.0	25.±0.02	27±0.11	
MIC	(µg/mL)	25	15	15	20	10	15	15	10	

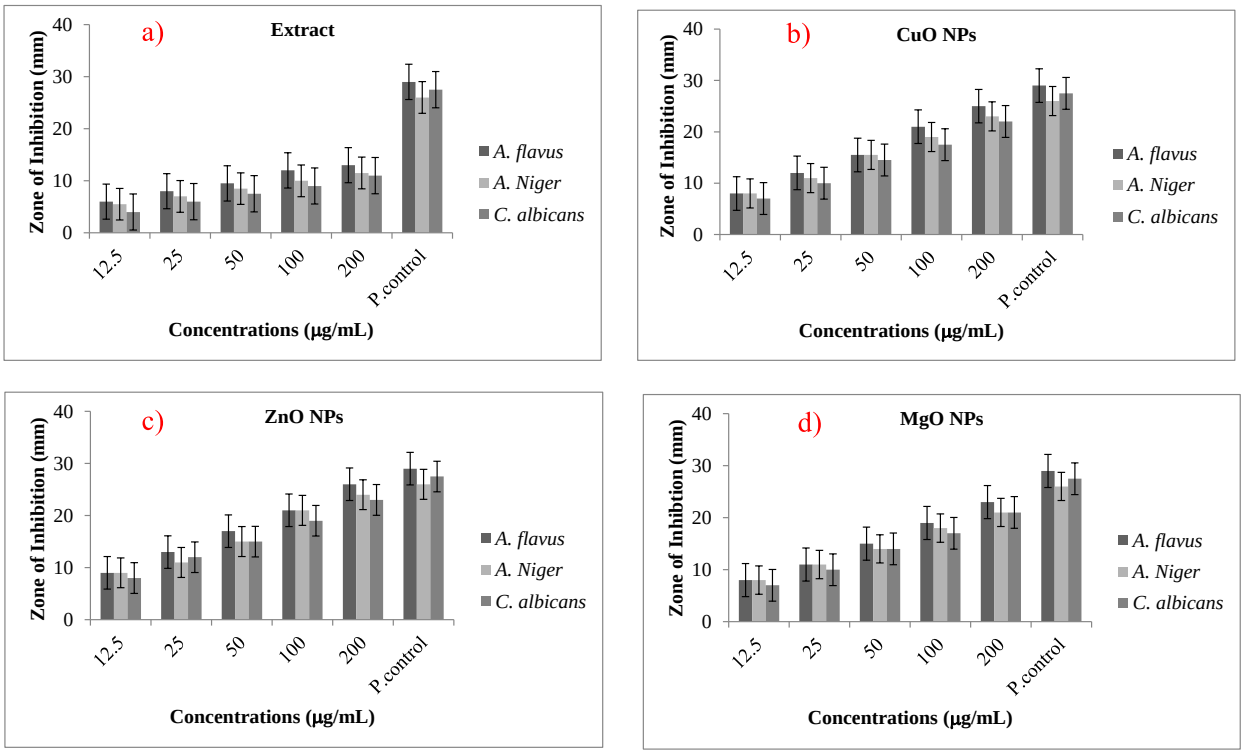

Figure 42. Antifungal activity of a) LEAA, b) CuO NPs, c) ZnO NPs, and d) MgO NPs against selected fungal strains.

At a concentration of 200 µg/mL, ZC NCs showed a large zone of inhibition of ca. 29.0 mm with a MIC of 10 µg/mL against *A. flavus* and a smaller zone of ca. 24.5 mm with a MIC of ca. 10 µg/mL against *A. niger* (Figure 44a). MC NCs showed a larger zone of inhibition of ca. 27.0 mm with MIC of ca. 10 µg/mL, and MZ NCs showed a larger zone of inhibition of ca. 28.0 mm with a MIC value of 10 µg/mL against *A. flavus*, Figure 44 (b, c). The results showed that the bimetallic (ZC, MC, and MZ) NCs have higher antifungal activity than their monometallic (CuO, ZnO, and MgO) NPs counterparts against the fungal strains. Trimetallic ZMC NCs showed a larger zone of inhibition of ca. 31.0 mm with a MIC of ca. 10.0 µg/mL against *A. flavus* and a smaller zone of ca. 27.0 mm with a MIC of ca. 10.0 mg/mL against *A.niger*. Similar to the antibacterial activity, ZMC NCs have the largest zone of inhibition compared to LEAA, mono, and bimetallic NCs against the tested fungal strains. This could be attributed to the trimetallic NPs' immensely modified physicochemical properties and synergistic effects (Kumaravel, Lalitha, Arunthirumeni, & Shivakumar, 2021).

Even though the MO NMs exhibited inspiring activity against both fungal and bacterial strains, the bacterial strains have shown less resistance than the fungal strains. This is related to the permeability of cells of the microorganisms. Fungi have chitin made up of polysaccharides with N-acetyl glucosamine, a nitrogen group, and a firmer cell wall. As a result, MO NMs cannot easily pass from the outside layer of the cell wall to the interior layer. However, bacteria's cell wall consists of peptidoglycan (a polymer containing sugars and amino acids), which is less rigid and allows for easier passage of the MO NMs (Kumaravel et al., 2021).

The antifungal activity of the MO NMs was possible because of their small sizes and higher surface area. Due to their smaller size, they might have disturbed the power functions like respiration and permeability of fungi by attaching them to the surface of their cell walls and membranes. Inactivation of enzymes, protein denaturation, DNA cleavage, and ribosome disassembly could be the possible mechanisms for antifungal activity (Gaber, Hashem, El-Sayyad, & Attia, 2023). MO NMs, due to their small size and large surface area, may invade fungal cells, which results in the production of ROS and apoptotic cell death. The complex formation of ergosterol may also damage the cell membranes, and the formation of aqueous pores causes the leakage of ions and cell lysis (Gaber et al., 2023). The inhibition of ergosterol synthesis that occurs by inhibiting the lanosterol conversion to ergosterol by MO NMs leads to changes in membrane fluidity and chitin synthase activity. Cell wall stress that arises by inhibiting 1, 3-β glucan synthase activity leads to the disruption of glucan synthesis, and finally, the cell wall disruption leads to fungal cell shrinkage.

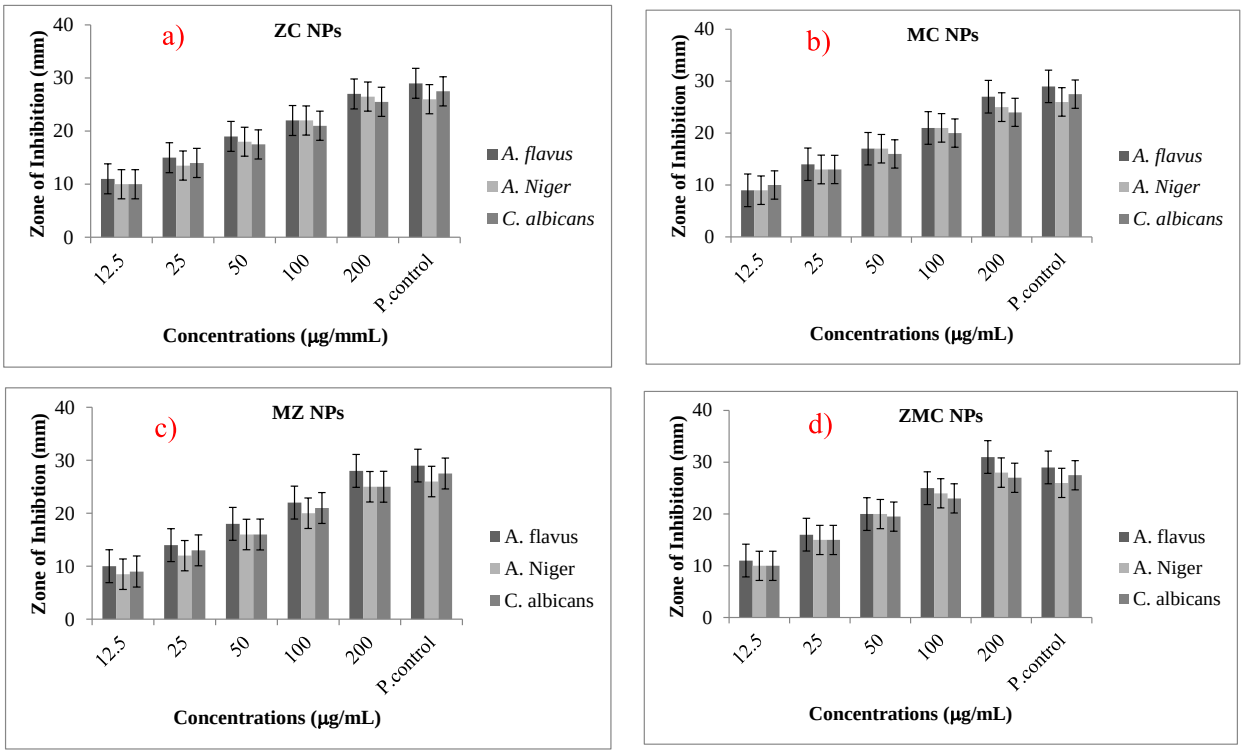

Figure 43. Antifungal activity of a) ZC NCs, b) MC NCs, c) MZ NCs, and d) ZMC NCs against selected fungal strains.

4.4.3 *In vitro* cytotoxicity and anticancer activity

The *in vitro* cytotoxicity of bio-prepared bi- and trimetallic (ZC, MC, MZ and ZMC) NCs including the standard drug (doxorubicin) have been assessed against PBM breast cancer (MCF-7) cell lines. Evaluating the cytotoxicity on normal human cell lines was thought to be the initial step in determining the safety of the fabricated NPs (Khonkarn, Okonogi, Ampasavate, & Anuchapreeda, 2010). As presented in in Table 11 and Figure 46 (a-d) the cytotoxicity of bio-prepared NPs and the standard drug were found to be in increasing order of MZ NCs < MC NCs < ZC NCs < ZMC NCs < doxorubicin. The obtained results indicated that at 250 µg/mL the % inhibition of MZ NCs, MC NCs, ZC NCs, ZMC NCs, and doxorubicin against PBM cell lines were 45.13±0.01, 49.54±0.10, 51.13±0.12, 52.82±0.11, and 56.49±0.02 respectively. From the results MZ NCs have slightly lower cytotoxicity and doxorubicin have higher cytotoxicity against PBM cell lines. The IC_{50} of MZ NPs, MC NPs, ZC NPs, ZMC NCs, and doxorubicin were 258.44, 252.23, 247.15, 227.69 and 175.56 µg/mL, respectively. The obtained high IC_{50} values confirmed noncytotoxic effects of the biosynthesized NCs against PBM cell lines (Ioset,

Brun, Wenzler, Kaiser, & Yardley, 2009). This could be due to the synthesis of NCs from biological precursors and nature of physiologically functioning (magnesium, zinc, and copper) metal ions, making them biocompatible and less cytotoxic to normal cells.

Table 11. Inhibition percent (%) of ZC, MC, MZ and ZMC NCs and standard drug against PBM Cell lines on MTT assay.

Concent. (μg/mL)	% Inhibitions of ZC, MC, MZ and ZMC NCs and Doxorubicin against PBM cell lines				
	ZC NCs	MC NCs	MZ NCs	ZMC NCs	Doxorubicin
Control	0	0	0	0	0
7.81	12.99 ± 0.22^{d}	11.68 ± 0.22^{d}	9.78 ± 0.22^{d}	14.69 ± 0.12^{d}	15.54 ± 0.02^{d}
15.62	19.77 ± 0.01^{cd}	17.08 ± 0.01^{cd}	16.67 ± 0.01^{cd}	20.62 ± 0.01^{cd}	21.47 ± 0.04^{cd}
31.25	27.68 ± 0.02^{c}	25.64 ± 0.02^{c}	23.44 ± 0.02^{c}	28.81 ± 0.04^{c}	30.23 ± 0.01^{bc}
62.5	33.89 ± 0.03^{bc}	31.48 ± 0.03^{bc}	29.37 ± 0.03^{bc}	35.02 ± 0.11^{bc}	35.31 ± 0.03^{bc}
125	41.52 ± 0.04^{b}	39.82 ± 0.12^{b}	36.52 ± 0.06^{b}	42.09 ± 0.04^{b}	45.20 ± 0.01^{b}
250	51.13 ± 0.12^{a}	49.54 ± 0.10^{a}	45.13 ± 0.01^{a}	52.82 ± 0.11^{a}	56.49 ± 0.02^{a}
IC50 (μg/mL)	247.15	252.23	258.44	227.69	175.56

The inhibition rates in (%) are the means of individual triplicates ± standard deviation (SD). The letter(s) on the means in each column are not significantly different as per Tukey's HSD analysis.

The anticancer activity of phytochemical mediated MO NCs and doxorubicin were also evaluated against human breast cancer (MCF-7) cell lines. The results in Table 12 and Figure 46 a-d have shown a decline in cell viability in a concentration-dependent manner. The anticancer efficacy of biosynthesized NPs and the standard drug were found to be in increasing order of MZ NCs < MC NCs < doxorubicin < ZC NCs < ZMC NCs. The % inhibition of MZ NCs, MC NCs, doxorubicin, ZC NCs and ZMC NCs, and at 250 μg/mL against MCF-7 cell lines were 73.82±0.08, 76.34±0.04, 79.58±0.04, 81.46±0.02, and 94.37±0.14 respectively. The microscopic images presented in Figure 45 a-d demonstrate the cell morphology of untreated MCF-7 cells and those treated with 7.81, 62.5, and 250 μg/mL respectively. After treatment with 7.81, 62.5, and 250 μg/mL nanoparticles, the cells displayed altered morphology and reduced cell density. Moreover, at 250 μg/mL, the epithelial morphology of MCF-7 was damaged and displayed very

low cell density. Generally, the obtained microscopic and cell viability results demonstrated the significant anticancer potency of MO NMs. The findings of this study are also well corroborated by previous studies that were reported in other works (Aditi Dey et al., 2019; Zughaibi et al., 2022).

Table 12. Inhibition percent (%) of ZC, MC, MZ and ZMC NCs and standard drug against MCF7 cell lines on MTT assay.

Concen. (µg/mL)	% Inhibitions of ZC, MC, MZ and ZMC NCs and Doxorubicin against MCF7 cell lines				
	ZC NCs	MC NCs	MZ NCs	ZMC NCs	Doxorubicin
Control	0	0	0	0	0
7.81	25.12 ± 0.04^{d}	22.34 ± 0.04^{d}	19.08 ± 0.04^{e}	$32.20\pm0.03d^{d}$	23.94 ± 0.02^{d}
15.62	35.92 ± 0.02^{cd}	33.28 ± 0.04^{cd}	28.42 ± 0.12^{d}	39.20 ± 0.06^{cd}	35.44 ± 0.01^{cd}
31.25	51.41 ± 0.01^{c}	47.34 ± 0.04^{c}	42.75 ± 0.06^{cd}	53.52 ± 0.00^{c}	49.76 ± 0.02^{c}
62.5	64.32 ± 0.03^{bc}	58.34 ± 0.04^{bc}	53.69 ± 0.22^{c}	66.67 ± 0.14^{bc}	63.85 ± 0.00^{bc}
125	71.12 ± 0.00^{b}	67.34 ± 0.04^{b}	62.74 ± 0.11^{bc}	75.82 ± 0.22^{b}	70.18 ± 0.02^{b}
250	81.46 ± 0.02^{ab}	76.34 ± 0.04^{ab}	73.82 ± 0.08^{b}	94.37 ± 0.14^{a}	79.58 ± 0.04^{ab}
IC50 (µg/mL)	33.12	35.24	37.47	24.83	35.94

The inhibition rates in (%) are the means of seven individual replicates ± standard deviation (SD). The letter(s) on the means in each column are not significantly different as per Tukey's HSD analysis.

The half maximal inhibitory concentration (IC50) is a measure of the effectiveness of a compoundin inhibiting biological or biochemical function. This quantitative measure indicates how much of a particular drug or other substance (inhibitor) is needed to inhibit a given biological process (or component of a process, i.e. an enzyme, cell, cell receptor or microorganism) by half. The IC50 of a drug can be determined by constructing a dose-response curve and examining the effect of different concentrations of antagonist on reversing agonist activity. IC50 values were calculated for a given antagonist by determining the concentration needed to inhibit half of the maximum biological response of the agonist. The IC_{50} of MZ NCs, MC NCs, ZC NCs, ZMC NCs, and doxorubicin were 37.47, 35.24, 35.94, 33.12, and 24.83 µg/mL, respectively. From the results MZ NCs have slightly lower IC_{50} value and ZMC NPs have IC_{50} value against MCF-7 cell lines. However, all synthesized NPs have revealed

comparably lower IC_{50} values than the standard drug that confirmed effectiveness of the biosynthesized MO NMs against MCF-7 cell lines. The result could be due to the synergism of different metals, improved surface-to-volume ratio, and richer electrochemical characteristics of NPs (Aditi Dey et al., 2019; Zughaibi et al., 2022). In conclusion, the bio-prepared MO NMs thus seem likely to be a good candidate for developing and designing therapeutic agents in breast cancer illnesses.

The proposed mechanism of action of MO NMs as an anticancer agent could be either Van der Waals interaction with different amino acids of protein targets of breast cancer. In addition to this, it could also be the apoptotic cellular death induced due to the generation of ROS in cellular environment and which result oxidative stress on the cancer cells. Furthermore, it might cause DNA binding as a result of an electrochemical interaction between a positive charge on the NPs and certain negative charges on the surface of the DNA of cancer cells. Moreover, NMs demonstrated greater cytotoxicity in the MCF-7 cell line due to their small size, improved surface-to-volume ratio, and richer electrochemical characteristics (Raj Preeth et al., 2019; Zughaibi et al., 2022). Therefore, NMs can be an effective therapeutic agent in cancer chemotherapy, particularly in breast cancer ailments and hence probably they will be a promising candidate for the development and design of anticancer drugs.

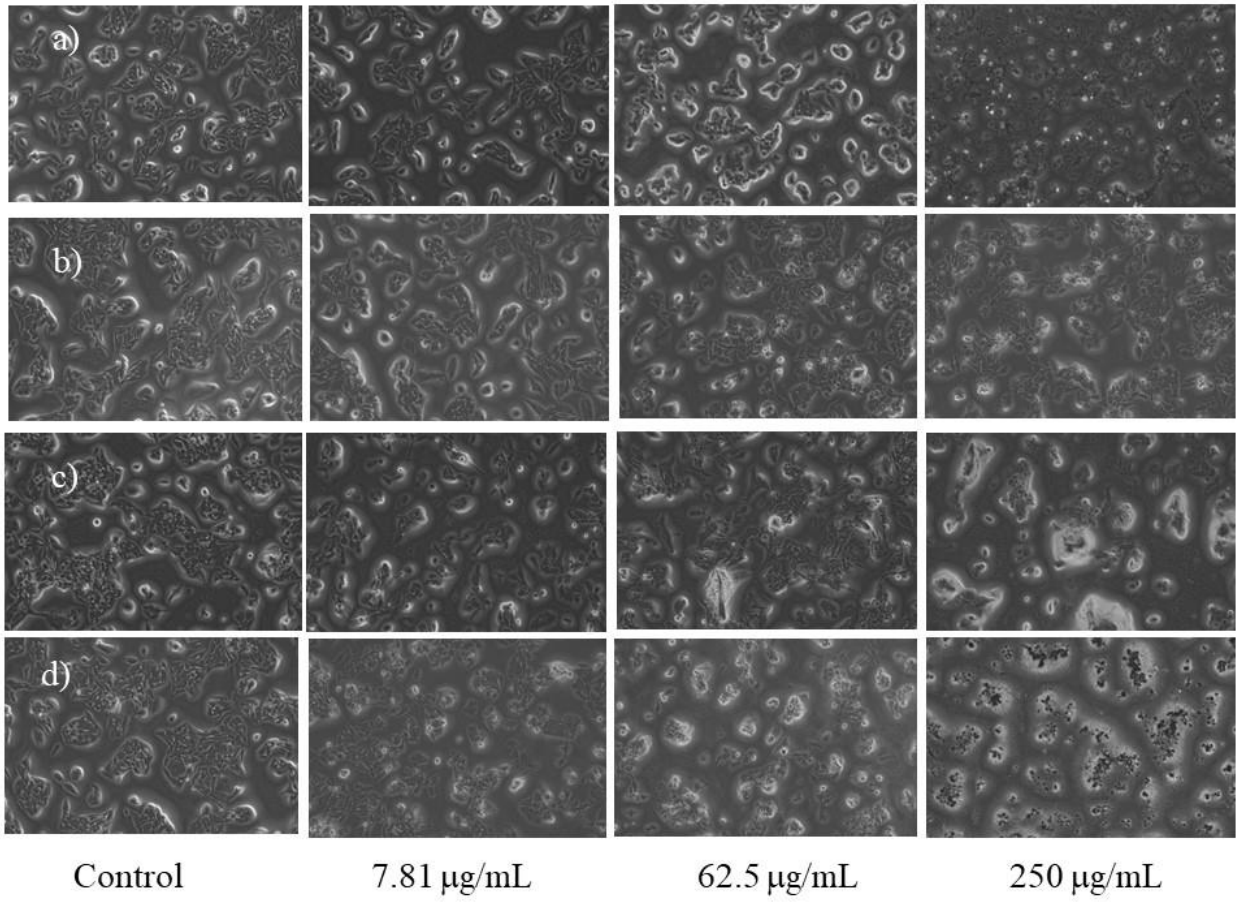

Figure 44. Micrograms of cytotoxicity of a) ZC NCs, b) MC NCs, c) MZ NCs, and d) ZMC NCs against MCF-7 cell lines: untreated (control), treated with 7.81μg/mL, treated with 62.5 μg/mL, and treated with 250 μg/mL.

4.4.5 Molecular docking study

Evaluations of the interaction efficiency and the binding affinity of molecules with specific targets are among the important factors in drug design and development. In order to propose the binding mechanism of phytochemical mediated mono (CuO, ZnO and MgO), bi (ZC, MC, and MZ), and trimetallic (ZMC) NMs including positive control (chloramphenicol) with bacterial cells, their binding affinity were evaluated against *S. aureus* dihydrofolate reductase and *E. coli* DNA gyrase B. Dihydrofolate reductase and DNA gyrase B are the most prominent enzymes for the survival of the *S. aureus* and *E. coli* bacterial species respectively (Anza et al., 2021; Morris et al., 2009). They are ubiquitously expressed in bacterial species and crucial for cell

growth and proliferation. The molecular interactions with these enzymes are supposed to hinder the DNA replications of these species (Bhatt, Stender, Joshi, Wu, & Katzenellenbogen, 2016). Therefore, the good interactions with the amino acid residues of these enzymes could be the antibacterial drug targets of synthesized materials.

The results of molecular docking analysis of MO NMs and standard drug (Chloramphenicol) against *S. aureus* (PDB: 2w9h) and *E. coli* (PDB: 6F86) have been presented in Table 13. CuO NPs has demonstrated binding interactions with amino acids of *S. aureus* gyrase (Figure 45) through hydrogen bond (Ser49), and π-Sigma/π-Alkyl (Leu20, Ile14, Val6, Val31, Leu54, Lys45, Leu28, Thr121), interactions with a binding affinity -15.16 kcal/mol and an inhibition constant (IC) of 7.77 pM. The binding interactions of CuO NPs against *E. coli* (Table 13 and Appendix 4) is through hydrogen bond (Asn46, Glu50) and π-Sigma/π-Alkyl (Gln72, Val167, Val71, Thr165, Ala47, Val43, Val120, Ile94, Arg76, Pro79) interactions with a binding affinity (-8.25 kcal/mol) and an inhibition constant (892.55 µM). ZnO NPs has strong interactions with amino acids of *S. aureus* gyrase (Table 13 and Figure 46) through hydrogen bond (Ser49), and π-Sigma/π-Alkyl (Leu20, Leu28, Lys45, Thr121, Val31, Leu54) binding affinity (-13.60 kcal/mol) and an inhibition constant (107.23 pM). Its binding interactions against *E. coli* (Table 13 and Appendix 5) is through hydrogen bond (Asn46, Glu50) and π-Sigma/π-Alkyl (Ile94, Val120, Arg76, Thr165, Ala47, Val71, Val167, Asn46, Val43, Pro79) with binding affinity (-8.47 kcal/mol) and an inhibition constant (0.61 µM). MgO NPs have interaction with amino acid residues of *S. aureus* gyrase (Table 13 and Figure 47) through hydrogen bond (Ser49) and π-Sigma/π-Alkyl (Leu20, Lys45, Val6, Phe92, Val31, Leu28) with binding affinity and inhibition constant of -12.63 kcal/mol and 548.19 pM respectively. It has demonstrated hydrogen bond (Asn46) and π-Sigma/π-Alkyl (Ile94, Pro79, Asp49, Glu50, Asp73, Val43, Thr165, Val71, and Val167) interactions against *E. coli* (Table 13 and Appendix 6). The results revealed that from monometallic MO NPs (CuO, ZnO and MgO NPs), CuO NPs showed relatively the highest binding energy and lower inhibition constants against *S. aureus* gyrase and *E. coli*. It could be due to the greater number of interactions with the amino acids in the binding pocket of the proteins of bacterial strains.

Table 13. Molecular docking scores and the corresponding prominent residual amino acid interactions of NPs and standard drugs against *S. aureus* (PDB: 2w9h), *E. coli* (PDB: 6F86) and estrogen receptor alpha (ERα; PDB: 5GS4).

Samples	Lowest binding E (kcal/mol)	Inhibition constant (K_i)	H-bonding	π-Sigma/π-Alkyl	van der Waals
S. aureus (PDB: 2w9h)					
CuO NPs	-12.16	7.77 pM	Ser49	Leu20, Ile14, Val6, Val31, Leu54, Lys45, Leu28, Thr121	
ZnO NPs	-11.60	107.23 pM	Ser49	Leu20, Leu28, Lys45, Thr121, Val31, Leu54	
MgO NPs	-10.63	54.19 pM	Ser49	Leu20, Lys45, Val6, Phe92, Val31, Leu28	
MZ NCs	-12.04	9.46 pM	Ser49	Leu54, Leu28, Leu20, Ala7, Val31, Leu5, Lys45,	
MC NCs	-14.02	52.74 pM	Ser49	Leu20, Ala7, Leu28, Lys45	Ile50, Phe92, Gly94
ZC NCs	-14.80	77 pM	Asn46, Glu50	Val43, Asp73, Met95, Val167, Ala47, Val71, Arg76, Ile78, Pro79, Glu50	Gly77, Ile94
ZMC NCs	-15.16	77.7 pM	Ser49	Leu28, Val31, Leu54, Phe92	Leu20, Ile50, Arg57, Asp27
Chloramphenicol	-11.16	56.7 pM	Leu20,Trp46, Gln95,Thr121	Leu20	Ser49
E. coli (PDB: 6F86)					
CuO NPs	-8.25	892.55 µM	Asn46, Glu50	Gln72, Val167, Val71, Thr165, Ala47, Val43, Val120, Ile94, Arg76, Pro79	
ZnO NPs	-8.47	10.61 µM	Asn46, Glu50	Ile94, Val120, Arg76, Thr165, Ala47, Val71, Val167, Asn46, Val43, Pro79	
MgO NPs	-6.58	14.93 µM	Asn46	Ile94, Pro79, Asp49, Glu50, Asp73, Val43, Thr165, Val71, Val167	
MZ NCs	-9.13	32.36 µM		Ala53, Ile94, Ala47, Val43, Thr165, Val167, Ile78	
MC NCs	-9.73	11.68 µM		Ile94, Ile78, Glu50, Asp49, Thr165,Ala47,	

				Val167, Val71, Val43	
ZC NCs	-9.02	11.32 µM	Gln19, Leu20	Phe92, His23, Leu28, Leu20, Ile50, Ile14, Phy92	
ZMC NCs	-11.94	37.42 µM	Arg76	Asp49, Ile94, Thr165, Val167	Asn46, Glu50, Asp73, Ile78
Chloramphenicol	-10.19	29.02 µM	Asp73, Asn46, Glu50	Glu50	Val43, Ala47, Pro79
Estrogen receptor alpha (ERα; PDB:5GS4)					
MZ NCs	-7.97	1.44 µM		Met396, Trp393, Glu323, Glu353, Leu387, Met357	Gly390
MC NCs	-7.84	1.78 µM	Arg357, Lys449, Glu390	His353, Glu323, Ala350, Leu391, Leu387	
ZC NCs	-8.50	1.59 µM	-	Glu-353, His-356, Leu-391, Trp-393	Arg363,Trp360, Met357, Lys449
ZMC NCs	-9.85	2.55 µM	Arg363, Lys449	Glu353, His356, Met357, Arg394	Ala322,Glu323, Trp360, Trp393
Doxorubicin	-7.54	2.99 µM	Glu353, Arg394, Trp393, Glu323	Met357, Trp360, Ile386, His356	Gly390,Leu387, Lys449

pM = picomolar; µM = micromolar

The binding affinities of bimetallic (MZ, MC and ZC) NCs and trimetallic ZMC NCs against amino acid residues of *S. aureus and E. coli* were computed as presented in Table 13. MZ NCs have revealed a total of 8 interactions with *S. aureus* gyrase: one hydrogen bonding with Ser49 and seven π-Sigma/π-Alkyl interactions with Leu54, Leu28, Leu20, Ala7, Val31, Leu5, Lys45 (Figure 48). Whereas, it has a total of seven interactions with *E. coli:* six π-Sigma/π-Alkyl interactions with Met396, Trp393, Glu323, Glu353, Leu387, Met357 and one van deer Waals interactions with Gly390 (Appendix 7). MC NCs has a total of seven interactions (Figure 49) with *S. aureus* gyrase: one hydrogen bonding with Ser49, four π-Sigma/π-Alkyl interactions with Leu20, Ala7, Leu28, Lys45 and three van deer Waals interactions with Ile50, Phe92, Gly94. It has also revealed nine (Ile94, Ile78, Glu50, Asp49, Thr165, Ala47, Val167, Val71, Val43) interactions with *E. coli* through π-Sigma/π-Alkyl interactions (Appendix 8). ZC NCs have revealed a total of fourteen interactions with amino acid residues of *S. aureus* gyrase as demonstrated in Figure 50. It has revealed two hydrogen bonding with Asn46, Glu50; ten π-Sigma/π-Alkyl interactions with Val43, Asp73, Met95, Val167, Ala47, Val71, Arg76, Ile78, Pro79, Glu50; and two van deer Waals interactions Gly77, Ile94. It also revealed nine interactions (Appendix 9) with amino acid residues of *E. coli:* two hydrogen bonding with Gln19, Leu20 and seven π-Sigma/π-Alkyl interactions with Phe92, His23, Leu28, Leu20, Ile50,

Ile14, and Phy92. As the resalts revealed all bimetallic (MZ, MC and ZC) NCs have the highest binding energy and lower inhibition constants than their monometallic counterparts in both bacterial targets. These findings also corroborated with the experimental results presented in Table 9.

Trimetallic ZMC NCs has demonstrated strong binding interaction with amino acids of *S. aureus* gyrase through hydrogen bond (Ser49), π-Sigma/π-Alkyl (Leu28, Val31, Leu54, and Phe92), and van der Waals (Leu20, Ile50, Arg57, and Asp27) interactions with a binding affinity -15.16 kcal/mol and an inhibition constant (IC) of 77.7 pM (Figure 51). It has also shown the binding interactions with *E. coli* (Appendix 10) through hydrogen bond (Arg76), π-Sigma/π-Alkyl (Asp49, Ile94, Thr165, and Val167), and van der Waals (Asn46, Glu50, Asp73, and Ile78) with a binding affinity and IC of -11.94 kcal/mol and an of 37.42 µM, respectively. Chloramphenicol (the standard drug) has revealed the interactions with *S. aureus* gyrase (Figure 52) through hydrogen bond (Trp121, Gln95, and Trp46), and van der Waals (Ile14, Gly93, Gly94, and Ser49) interactions with a respective binding affinity and an IC of -11.16 kcal/mol and 56.7 pM, respectively. It has also revealed the interaction of *E. coli* (Appendix 11) through hydrogen bond (Asp73, Asn46, and Glu50), π-Sigma/π-Alkyl (Val43), and van der Waals (Ile78, Arg76, and Trp165) with a binding affinity and an IC of -10.19 kcal/mol and 29.02 µM, respectively.

In general, the strong binding affinity of phytochemical mediated synthesized MO NMs with particular targets of *S. aureus* and *E. coli* have been observed and the resalts feasibly associated with experimental values; hence, the MO NMs can be possibly utilized as antibacterial agents.

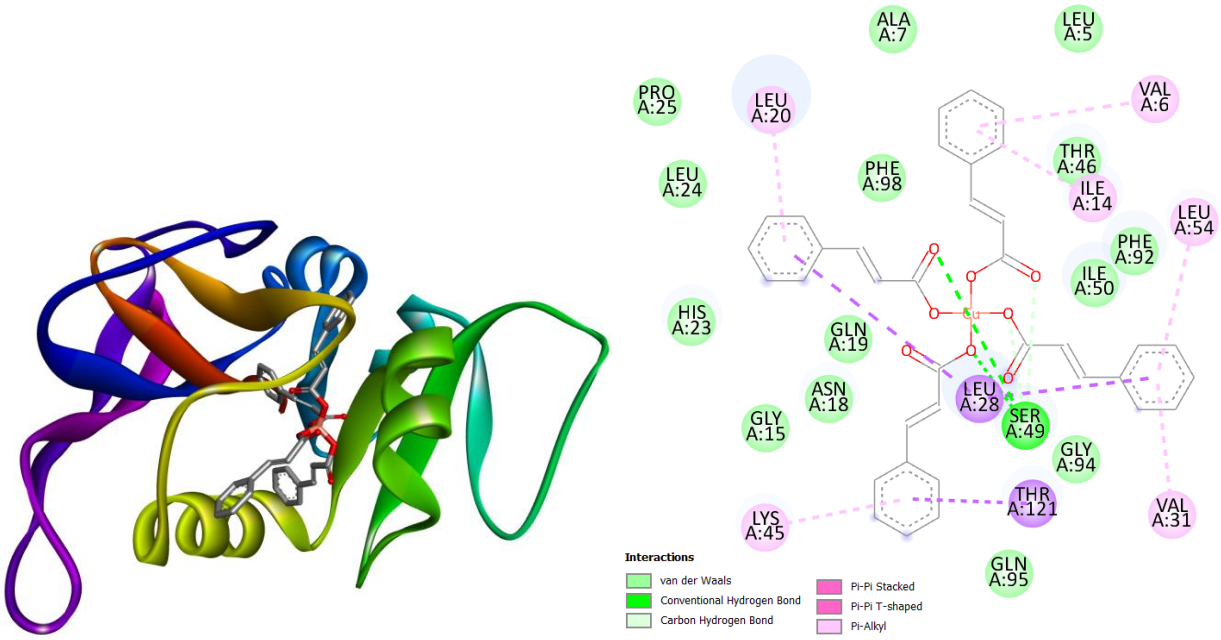

Figure 45. The binding interactions of CuO NPs against *S. aureus* (PDB: 2w9h)

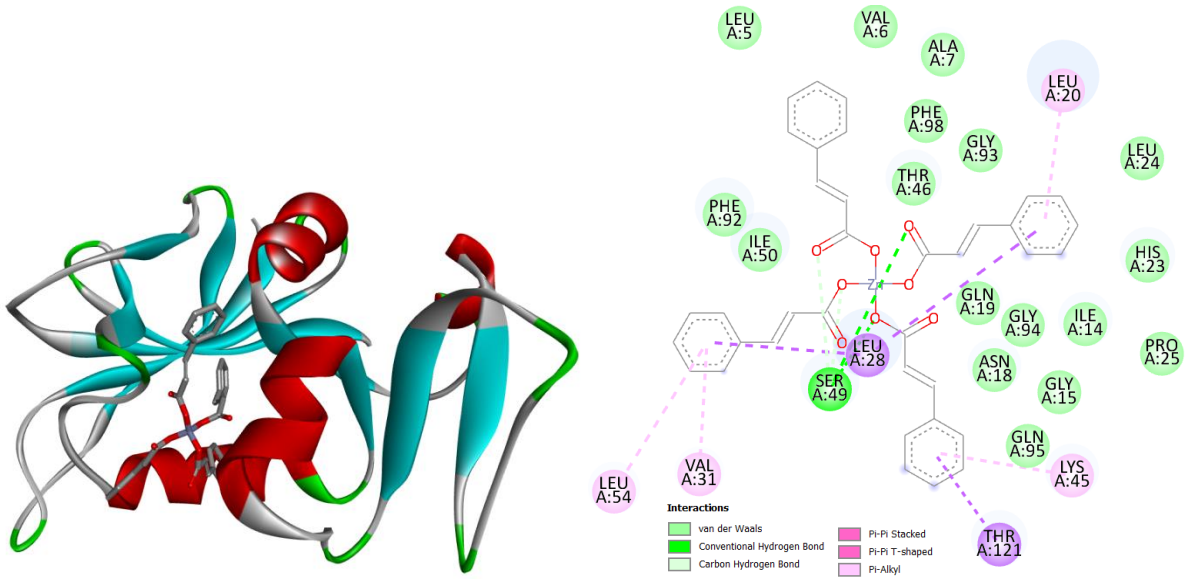

Figure 46. The binding interactions of ZnO NPs against *S. aureus* (PDB: 2w9h)

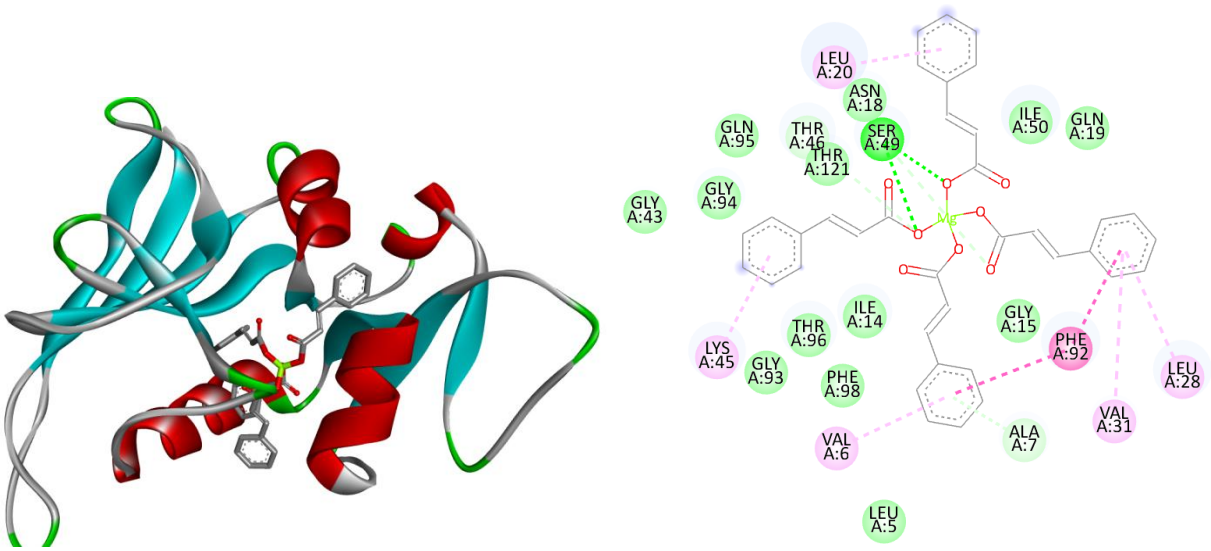

Figure 47. The binding interactions of MgO NPs against *S. aureus* (PDB: 2w9h)

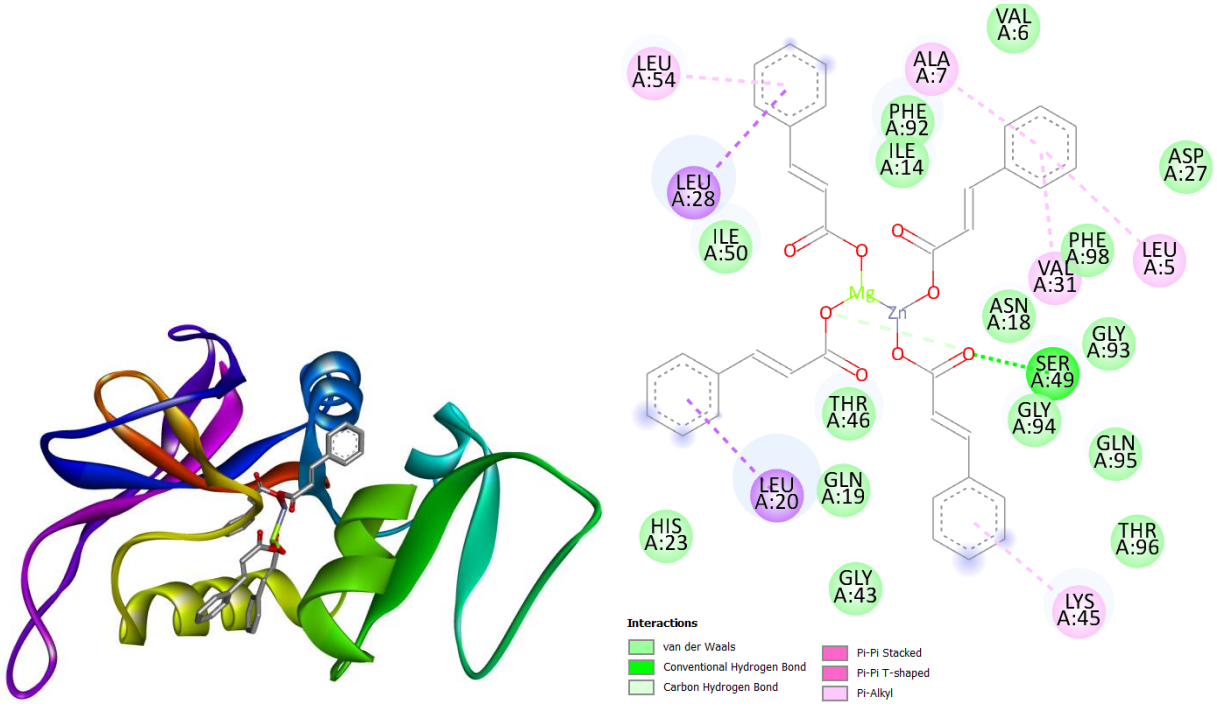

Figure 48. The binding interactions of MZ NCs against *S. aureus* (PDB: 2w9h)

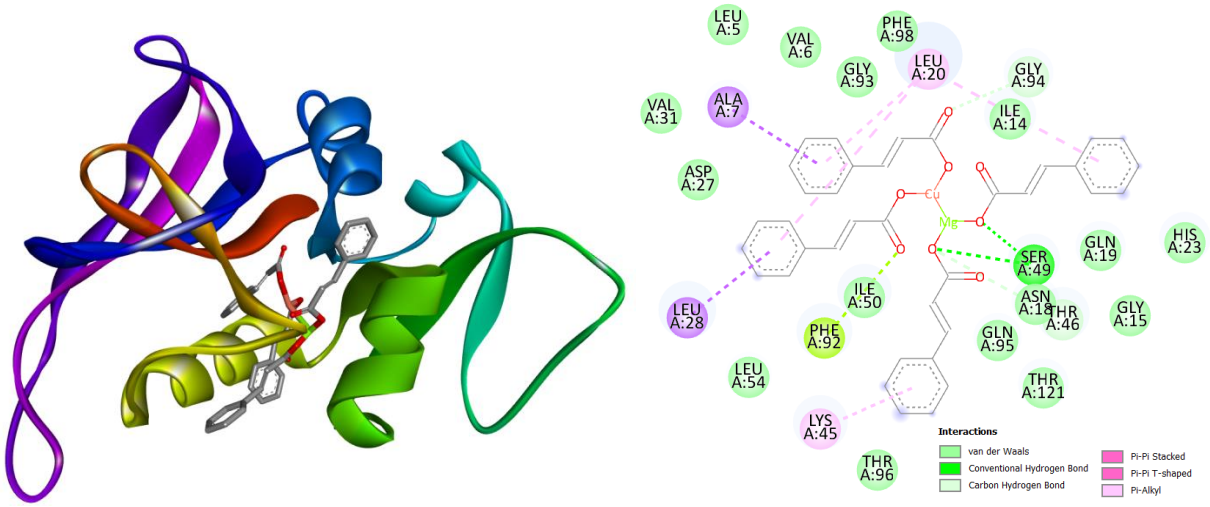

Figure 49. The binding interactions of MC NCs against *S. aureus* (PDB: 2w9h)

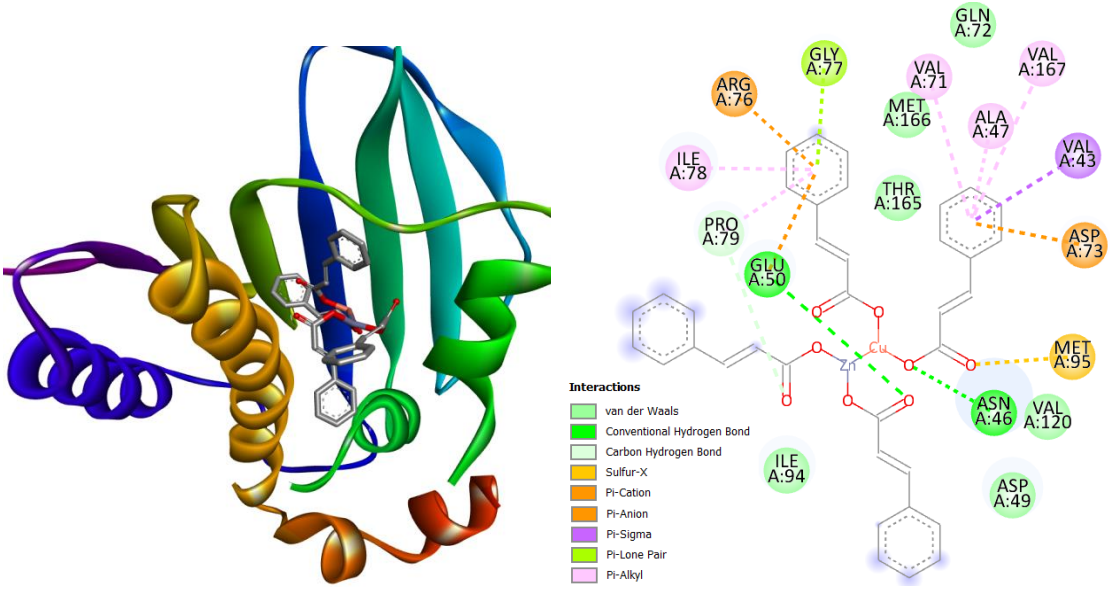

Figure 50. The binding interactions of ZC NCs against *S. aureus* (PDB: 2w9h)

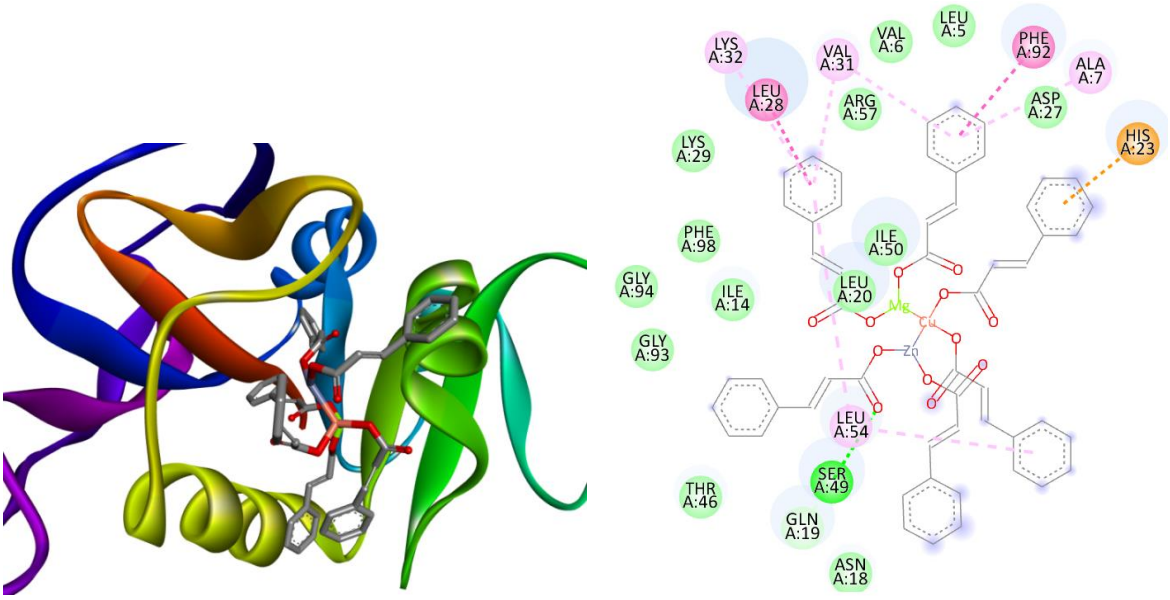

Figure 51. The binding interactions of ZMC NCs against S. *aureus* dihydrofolate reductase (PDB: 2w9h)

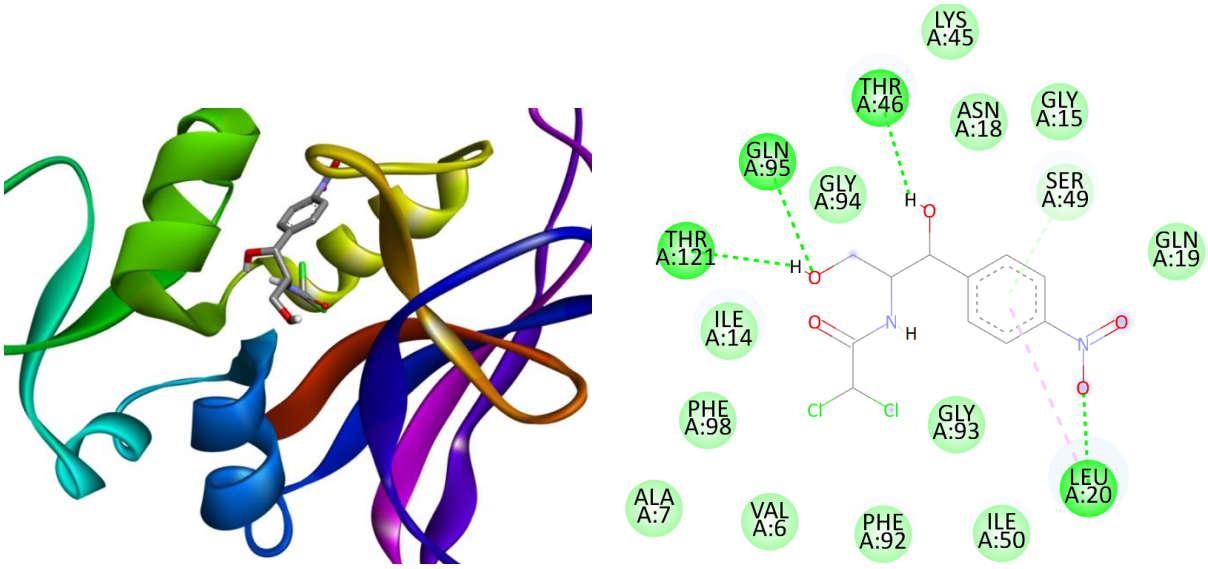

Figure 52. The binding interactions of chloramphenicol against *S. aureus* (PDB: 2w9h)

The molecular interactions of bio-prepared ZC, MC, and MZ, and ZMC NCs including the standard drug (doxorubicin) were investigated against estrogen receptor alpha (ERα; PDB: 5GS4) using AutoDock 4.2 (MGL tools 1.5.7) with a molecular docking database. Estrogen receptor (ERα) is the primary clinical biomarker used to subtype breast cancer (Backes et al., 2016). The estrogen receptor α (ERα) plays an important role in the development and

progression of hormonal-dependent type breast cancer (Vasiliou & Diamandis, 2019). MZ NCs have revealed hydrogen bonding with Ser49 and six π-Sigma/π-Alkyl interactions with Met396, Trp393, Glu323, Glu353, Leu387, Met357 and one van der Waals interactions with Gly390 of estrogen receptor alpha (ERα; PDB: 5GS4) (Appendix 12). Whereas, MC NCs has shown a total of eight interactions (Appendix 13) with estrogen receptor alpha (ERα; PDB: 5GS4): three hydrogen bonding with Arg357, Lys449 and Glu390, five π-Sigma/π-Alkyl interactions with His353, Glu323, Ala350, Leu391, Leu387. ZC NPs (Appendix 14) have revealed a total of eight interactions through van der Waals (Arg-363, Trp-360, Met-357, Lys- 449) and π-Sigma/π-Alkyl (Glu-353, His-356, Leu-391, Trp-393) interactions against estrogen receptor alpha (ERα; PDB: 5GS4). ZMC NPs in (Appendix 15) has revealed that two hydrogen bonding: Arg363, Lys449, four π-Sigma/π-Alkyl: Glu353, His356, Met357, and Arg394, four van der Waals (Ala322, Glu323, Trp360, and Trp393) interactions. Doxorubicin (Appendix 16) has shown H-bonding, π-Sigma/π-Alkyl, and van der Waals interactions within Glu-353, Arg-394, Trp-393, Glu-323, Met-357, Trp-360, Ile-386, His-356, Gly-390, Leu-387, and Lys-449 amino acid residues.

The resalts of tested MO NMs revealed that all MO NMs have strong interactions with active sites of amino acid residues of estrogen receptor alpha (ERα; PDB: 5GS4). Moreover, the binding affinities of biosynthesized MC, MZ, MC, ZC and ZMC NCs such as -7.97, -7.84, -8.50 and -9.85 kcal/mol respectively were higher than the standard drug doxorubicin, which was -7.54 kcal/mol. These strong binding with amino acids of estrogen receptors (ERα) are important to inhibit the proliferation rates of breast cancer cells (N. Kumar et al., 2021). Furthermore, the molecular docking interactions are also correlated with the experimental results presented in Table 12 and which confirming their anticancer efficacy in MCF-7 cell lines. The *in-vitro* and *in-sillico* analysis results of MO (MC, MZ, MC, ZC and ZMC) NMs showed their remarkeable anticancer efficacy against breast cancer ailments. Therfore, the biosynthesize (MC, MZ, MC, ZC and ZMC) NCs can also be designed as a possible remedy for breast cancer ailments.

5. CONCLUSIONS AND RECOMMENDATIONS

5.1 Conclusions

Currently, phytochemical mediated synthesized metal oxide nanomaterials (MO NMs) have played a substantial role in biological applications. In this study, constituent phytochemicals from *Artemisia abyssinica* leaf extract were employed as natural reducing and capping agents for the phytochemical mediated synthesis of novel monometallic (CuO, ZnO, and MgO), bimetallic (CuO-ZnO, CuO-MgO, ZnO-MgO) and trimetallic (CuO-ZnO-MgO) oxide NMs in a simple and eco-friendly way. The synthesis of possible nanoparticles in the reaction mixture was confirmed by the Surface Plasmon Resonance (SPR) peaks from UV-vis spectroscopy and their synthesized MO NMs band gaps revealed proper sizes and optical properties for biological activities. The presence of constituent functional groups from the extract of *Artemisia abyssinica*, which were responsible for reducing and capping of biosynthesized MO NMs, were confirmed by the FTIR and TGA/DTA analysis. The size, crystalline nature and morphology of phytochemical mediated MO NMs have been characterized by X-ray diffraction (XRD), scanning electron microscopy combined with energy dispersive analysis of X-rays (SEM-EDX), and transmission electron microscopy combined with selected area electron diffraction (TEM-SAED). The biological activity of phytochemical mediated MO NMs has been evaluated and revealed promising in *vitro* antioxidant, antibacterial and anticancer efficacies. All the synthesized MO NMs exhibited a promising antioxidant as evaluated in DPPH and FRAP assays. DPPH radical scavenging activities of monometallic CuO, ZnO, and MgO NPs were 88.81±0.02, 86.28±0.04 and 84.67±0.01 respectively with 5.75, 6.53, and 7.76 μg/mL respective IC50 values. Bimetallic ZC, MC and MZ NCs have revealed 95.71±0.00, 93.71±0.02 and 92.93±0.01 DPPH radical scavenging percentages at 200 μg/mL with IC50 values of 3.28, 4.80 and 5.26 μg/mL respectively. Trimetallic ZMC NCs have DPPH radical scavenging percentages of 98.41±0.01 with IC50 of 2.08 μg/mL at 200 μg/mL. The results revealed that antioxidant potency of trimetallic ZMC NPs > bimetallic (ZC, MC, MZ) NCs >> monometallic (CuO, ZnO, and MgO) NPs. Moreover, the phytochemical mediated MO NMs have exhibited the ferric ion reducing power (FRAP) with absorbance of 1.312±0.012-1.964±0.003 at 200 μg/mL. Antibacterial efficacy of phytochemical mediated MO NMs have been evaluated against human pathogenic gram-positive (*Staphylococcus aureus* and *Streptococcus pneumonia)* and gram-negative

(*Pseudomonas aeruginosa* and *Escherichia coli*) bacterial strains. All MO NMs have revealed a remarkable antibacterial activity against gram-positive and gram-negative bacterial strains. However, the highest and the lowest zone of inhibitions were revealed against *S.aures* (gram positive) and *Escherichia coli (*gram positive) bacterial species respectively. Antifungal evaluations showed that all the phytochemical mediated synthesized MO NMs are active against pathogenic (*Aspergillus flavus*, *Aspergillus niger* and Candida *albicans)* fungal strains. Anticancer activity results demonstrated that bi- and trimetallic ZC, MC, MZ and ZMC NMs showed promising cytotoxicity against MCF-7 cell lines with the reported IC50 values of 33.12, 35.24, 37.47 and 24.83 µg/mL respectively. Moreover, the *in silico* molecular docking results demonstrated that the phytochemical mediated MO NMs have strong affinity against S. *aureus* dihydrofolate reductase (PDB: 2w9h), *E. coli* DNA gyrase B (PDB: 6F86) and estrogen receptor alpha (ERα; PDB: 5GS4). In general, the phytochemical mediated MO NMs have a remarkable antioxidant, antibacterial, antifungal and anticancer efficacy and can be designed and developed as a therapeutic agent for these ailments further considering their *in vivo* analysis before clinical use.

5.2 Recommendations

This work reports an ecofriendly, cost-effective one-pot approach synthesized mono (CuO, ZnO, and MgO), bi (CuO-ZnO, CuO-MgO, ZnO-MgO) and trimetallic (CuO-ZnO-MgO) NMs from the leaf extract of *A. abyssinica* for the first time. Ultrapure, iso-morphological, and spherical NMs with average particle sizes below 16 nm were prepared and confirmed with UV-vis, FTIR, TGA, XRD, SEM, EDX, and TEM techniques. Overall, the single and mixed-phase phytochemeical mediated synthesized MO NMs have exhibited multifunctional biological activities. They have exhibited remarkable *in vitro* antioxidant potential as investigated through FRAP and DPPH assays. The phytochemeical mediated synthesized MO NMs have also revealed enhanced activity against various pathogenic bacterial and fungal strains. Moreover, the synthesized bi- (CuO-ZnO, CuO-MgO, and ZnO-MgO) and tri-metallic (CuO-ZnO-MgO) NMs have revealed a promising anticancer potency against MCF-7 cell lines. Further, the phytochemeical mediated synthesized MO NMs have also exhibited strong binding affinity against S. *aureus* dihydrofolate reductase (PDB: 2w9h), *E. coli* DNA gyrase B (PDB: 6F86) and estrogen receptor alpha (ERα; PDB: 5GS4) through *in-silico* molecular docking simulations. As

a result, the phytochemical mediated MO NMs can be used as potential bio safe antioxidant, antibacterial, antifungal and anticancer drug candidates, particularly for breast cancer ailments. However, the biological activities of the phytochemical mediated MO NMs in other microbial strains and cancer cells, *in-vivo* antimicrobial and anticancer activities on the same bacterial species and cancer cell line using animal models has to be conducted ensure wether they are effective in a living cell or not. Furthermore, we would like to recommend the utilization of these MO NMs for various applications such as photocatalysis, biosensor, and wastewater treatement due to their surface morphology, semiconductive nature.

6. REFERENCES

Abbas, S., Uzair, B., Sajjad, S., Leghari, S. A. K., Noor, S., Niazi, M. B. K., . . . Iqbal, H. (2022). Dual-functional green facile CuO/MgO nanosheets composite as an efficient antimicrobial agent and photocatalyst. *Arabian Journal for Science and Engineering, 47*(5), 5895-5909.

Abd El-Aziz, S. M., & Farahat, E. A. (2023). The Activity of Vossia cuspidata Polysaccharides-Derived Monometallic CuO, Ag, Au, and Trimetallic CuO-Ag-Au Nanoparticles Against Cancer, Inflammation, and Wound Healing. *Journal of Inorganic and Organometallic Polymers and Materials, 33*(3), 853-865.

Abdel-Fattah, W., & Ali, G. (2018). On the anti-cancer activities of silver nanoparticles. *J Appl Biotechnol Bioeng, 5*(1), 43-46.

Abdelghany, T. M., Al-Rajhi, A. M., Yahya, R., Bakri, M. M., Al Abboud, M. A., Yahya, R., . . . Salem, S. S. (2023). Phytofabrication of zinc oxide nanoparticles with advanced characterization and its antioxidant, anticancer, and antimicrobial activity against pathogenic microorganisms. *Biomass Conversion and Biorefinery, 13*(1), 417-430.

Abdullah, O. H., & Mohammed, A. M. (2021). Biosynthesis and characterization of MgO nanowires using Prosopis farcta and evaluation of their applications. *Inorganic Chemistry Communications, 125*, 108435.

Abid, S., Uzair, B., Niazi, M. B. K., Fasim, F., Bano, S. A., Jamil, N., . . . Sajjad, S. (2021). Bursting the virulence traits of MDR strain of Candida albicans using sodium alginate-based microspheres containing nystatin-loaded MgO/CuO nanocomposites. *International Journal of Nanomedicine, 16*, 1157.

Aboul-Soud, M. A., Siddique, R., Fozia, F., Ullah, A., Rashid, Y., Ahmad, I., . . . Mohany, M. (2023). Antiplatelet, cytotoxic activities and characterization of green-synthesized zinc oxide nanoparticles using aqueous extract of Nephrolepis exaltata. *Environmental Science and Pollution Research*, 1-11.

Achamo, T., Zereffa, E. A., Murthy, H. A., Ramachandran, V. P., & Balachandran, R. (2022). Phyto-mediated synthesis of copper oxide nanoparticles using Artemisia abyssinica leaf extract and its antioxidant, antimicrobial and DNA binding activities. *Green Chemistry Letters and Reviews, 15*(3), 598-614.

Adekoya, J. A., Dare, E. O., & Mesubi, M. A. (2014). Tunable morphological properties of silver enriched platinum allied nanoparticles and their catalysed reduction of p-nitrophenol. *Advances in Natural Sciences: Nanoscience and Nanotechnology, 5*(3), 035007.

Adeyemi, A. I., Vincent, O. I., & Olujenyo, O. M. (2018). Phytochemical screening and antifungal activity of Chromolaena odorata extracts against isolate of Phytophthora megakarya using agar-well diffusion method. *Asian Journal of Medical and Biological Research, 4*(1), 7-13.

Adeyemi, J. O., Onwudiwe, D. C., & Oyedeji, A. O. (2022). Biogenic synthesis of CuO, ZnO, and CuO–ZnO nanoparticles using leaf extracts of Dovyalis caffra and their biological properties. *Molecules, 27*(10), 3206.

Aghamohammad, S., & Rohani, M. (2023). Antibiotic resistance and the alternatives to conventional antibiotics: The role of probiotics and microbiota in combating antimicrobial resistance. *Microbiological Research, 267*, 127275.

Ahamad Khan, M., Lone, S. A., Shahid, M., Zeyad, M. T., Syed, A., Ehtram, A., . . . Danish, M. (2023). Phytogenically Synthesized Zinc Oxide Nanoparticles (ZnO-NPs) Potentially Inhibit the Bacterial Pathogens: In Vitro Studies. *Toxics, 11*(5), 452.

Ahamed, M., Lateef, R., Khan, M. M., Rajanahalli, P., & Akhtar, M. J. (2023). Biosynthesis, Characterization, and Augmented Anticancer Activity of ZrO2 Doped ZnO/rGO Nanocomposite. *Journal of Functional Biomaterials, 14*(1), 38.

Ahmad, N., Sharma, S., Alam, M. K., Singh, V., Shamsi, S., Mehta, B., & Fatma, A. (2010). Rapid synthesis of silver nanoparticles using dried medicinal plant of basil. *Colloids and Surfaces B: Biointerfaces, 81*(1), 81-86.

Ahmed, T., Noman, M., Luo, J., Muhammad, S., Shahid, M., Ali, M. A., . . . Li, B. (2021). Bioengineered chitosan-magnesium nanocomposite: A novel agricultural antimicrobial agent against Acidovorax oryzae and Rhizoctonia solani for sustainable rice production. *International Journal of Biological Macromolecules, 168*, 834-845.

Ajitha, B., Reddy, Y. A. K., Reddy, P. S., Jeon, H.-J., & Ahn, C. W. (2016). Role of capping agents in controlling silver nanoparticles size, antibacterial activity and potential application as optical hydrogen peroxide sensor. *RSC advances, 6*(42), 36171-36179.

Akbar, S., Tauseef, I., Subhan, F., Sultana, N., Khan, I., Ahmed, U., & Haleem, K. S. (2020). An overview of the plant-mediated synthesis of zinc oxide nanoparticles and their antimicrobial potential. *Inorganic and Nano-Metal Chemistry, 50*(4), 257-271.

Al-Asfar, A., Zaheer, Z., & Aazam, E. S. (2018). Eco-friendly green synthesis of Ag@ Fe bimetallic nanoparticles: Antioxidant, antimicrobial and photocatalytic degradation of bromothymol blue. *Journal of Photochemistry and Photobiology B: Biology, 185*, 143-152.

Al-Hammadi, A., Alnehia, A., Al-Sharabi, A., Alnahari, H., & Al-Odayni, A.-B. (2023). Synthesis of trimetallic oxide (Fe2O3–MgO–CuO) nanocomposites and evaluation of their structural and optical properties. *Scientific Reports, 13*(1), 12927.

Alhujaily, M., Albukhaty, S., Yusuf, M., Mohammed, M. K., Sulaiman, G. M., Al-Karagoly, H., . . . AlMalki, F. A. (2022). Recent advances in plant-mediated zinc oxide nanoparticles with their significant biomedical properties. *Bioengineering, 9*(10), 541.

Ali, R., Shanan, Z. J., Saleh, G. M., & Abass, Q. (2020). Green synthesis and the study of some physical properties of MgO nanoparticles and their antibacterial activity. *Iraqi Journal of Science*, 266-276.

Ali, S., Sharma, A. S., Ahmad, W., Zareef, M., Hassan, M. M., Viswadevarayalu, A., . . . Chen, Q. (2020). Noble Metals Based Bimetallic and Trimetallic Nanoparticles: Controlled Synthesis, Antimicrobial and Anticancer Applications. *Critical Reviews in Analytical Chemistry*, 1-28.

Ali, S., Sharma, A. S., Ahmad, W., Zareef, M., Hassan, M. M., Viswadevarayalu, A., . . . Chen, Q. (2021). Noble metals based bimetallic and trimetallic nanoparticles: controlled synthesis, antimicrobial and anticancer applications. *Critical reviews in analytical chemistry, 51*(5), 454-481.

Ali, S., Sudha, K. G., Thirumalaivasan, N., Ahamed, M., Pandiaraj, S., Rajeswari, V. D., . . . Govindasamy, R. (2023). Green Synthesis of Magnesium Oxide Nanoparticles by Using Abrus precatorius Bark Extract and Their Photocatalytic, Antioxidant, Antibacterial, and Cytotoxicity Activities. *Bioengineering, 10*(3), 302.

Alnahari, H., Al-Sharabi, A., Al-Hammadi, A., Al-Odayni, A.-B., & Alnehia, A. (2023). Synthesis of glycine-mediated CuO–Fe2O3–MgO nanocomposites: Structural, optical,

and antibacterial properties. *Composites and Advanced Materials, 32*, 26349833231176838.

Alnehia, A., Al-Sharabi, A., Al-Hammadi, A., Al-Odayni, A.-B., Alramadhan, S. A., & Alodeni, R. M. (2023). Phyto-mediated synthesis of silver-doped zinc oxide nanoparticles from Plectranthus barbatus leaf extract: optical, morphological, and antibacterial properties. *Biomass Conversion and Biorefinery*, 1-13.

Alsamhary, K., Al-Enazi, N. M., Alhomaidi, E., & Alwakeel, S. (2022). Spirulina platensis mediated biosynthesis of Cuo Nps and photocatalytic degradation of toxic azo dye Congo red and kinetic studies. *Environmental Research, 207*, 112172.

Altenhoff, M., Aßmann, S., Teige, C., Huber, F. J., & Will, S. (2020). An optimized evaluation strategy for a comprehensive morphological soot nanoparticle aggregate characterization by electron microscopy. *Journal of Aerosol Science, 139*, 105470.

Aman, M., Asfaw, Z., & Dalle, G. (2020). Medicinal Plants Used for Treating Human and Livestock Ailments in Tiyo District, Arsi Zone of Oromia, Ethiopia.

Amina, M., Al Musayeib, N. M., Alarfaj, N. A., El-Tohamy, M. F., Oraby, H. F., Al Hamoud, G. A., . . . Moubayed, N. M. (2020). Biogenic green synthesis of MgO nanoparticles using Saussurea costus biomasses for a comprehensive detection of their antimicrobial, cytotoxicity against MCF-7 breast cancer cells and photocatalysis potentials. *PLoS One, 15*(8), e0237567.

Ammulu, M. A., Viswanath, K. V., Giduturi, A. K., Vemuri, P. K., Mangamuri, U., & Poda, S. (2021). Phytoassisted synthesis of magnesium oxide nanoparticles from Pterocarpus marsupium rox. b heartwood extract and its biomedical applications. *Journal of Genetic Engineering and Biotechnology, 19*(1), 21.

Amor, I. B., Hemmami, H., Laouini, S. E., Temam, H. B., Zaoui, H., & Barhoum, A. (2023). Biosynthesis MgO and ZnO nanoparticles using chitosan extracted from Pimelia Payraudi Latreille for antibacterial applications. *World Journal of Microbiology and Biotechnology, 39*(1), 19.

Anand, U., Carpena, M., Kowalska-Góralska, M., Garcia-Perez, P., Sunita, K., Bontempi, E., . . . Simal-Gandara, J. (2022). Safer plant-based nanoparticles for combating antibiotic resistance in bacteria: A comprehensive review on its potential applications, recent advances, and future perspective. *Science of The Total Environment, 821*, 153472.

Ananda, A., Ramakrishnappa, T., Archana, S., Yadav, L. R., Shilpa, B., Nagaraju, G., & Jayanna, B. (2022). Green synthesis of MgO nanoparticles using Phyllanthus emblica for Evans blue degradation and antibacterial activity. *Materials Today: Proceedings, 49*, 801-810.

Anjum, S., Hashim, M., Malik, S. A., Khan, M., Lorenzo, J. M., Abbasi, B. H., & Hano, C. (2021). Recent advances in zinc oxide nanoparticles (ZnO NPs) for cancer diagnosis, target drug delivery, and treatment. *Cancers, 13*(18), 4570.

Annathurai, S., Chidambaram, S., Baskaran, B., & Prasanna Venkatesan, G. (2019). Green synthesis and electrical properties of p-CuO/n-ZnO heterojunction diodes. *Journal of Inorganic and Organometallic Polymers and Materials, 29*(2), 535-540.

Ansari, M. A., & Asiri, S. M. M. (2021). Green synthesis, antimicrobial, antibiofilm and antitumor activities of superparamagnetic γ-Fe2O3 NPs and their molecular docking study with cell wall mannoproteins and peptidoglycan. *International Journal of Biological Macromolecules, 171*, 44-58.

Anza, M., Endale, M., Cardona, L., Cortes, D., Eswaramoorthy, R., Cabedo, N., . . . Domingo-Ortí, I. (2021). Cytotoxicity, antimicrobial activity, molecular docking, drug likeness and DFT analysis of benzo [c] phenanthridine alkaloids from roots of Zanthoxylum chalybeum. *Biointerface Research in Applied Chemistry, 12*(2), 1569-1586.

Arsianti, A., Bahtiar, A., Wangsaputra, V. K., Azizah, N. N., Fachri, W., Nadapdap, L. D., . . . Kakiuchi, K. (2020). Phytochemical composition and evaluation of marine algal Sargassum polycystum for antioxidant activity and in vitro cytotoxicity on hela cells. *Pharmacognosy Journal, 12*(1).

Arumugam, M., Manikandan, D. B., Dhandapani, E., Sridhar, A., Balakrishnan, K., Markandan, M., & Ramasamy, T. (2021). Green synthesis of zinc oxide nanoparticles (ZnO NPs) using Syzygium cumini: Potential multifaceted applications on antioxidants, cytotoxic and as nanonutrient for the growth of Sesamum indicum. *Environmental Technology & Innovation, 23*, 101653.

Asfaw, N., & Demissew, S. (2015). Essential oil composition of four Artemisia Species from Ethiopia. *Bulletin of the Chemical Society of Ethiopia, 29*(1), 123-128.

Ashishie, P. B., Anyama, C. A., Ayi, A. A., Oseghale, C. O., Adesuji, E. T., & Labulo, A. H. (2018). Green synthesis of silver monometallic and copper-silver bimetallic nanoparticles

using Kigelia africana fruit extract and evaluation of their antimicrobial activities. *International Journal of Physical Sciences, 13*(3), 24-32.

Assis, L. M., Nedeljković, M., & Dessen, A. (2017). New strategies for targeting and treatment of multi-drug resistant Staphylococcus aureus. *Drug Resistance Updates, 31*, 1-14.

Athira, K., Gurrala, L., & Kumar, D. V. R. (2021). Biosurfactant-mediated biosynthesis of CuO nanoparticles and their antimicrobial activity. *Applied Nanoscience, 11*(4), 1447-1457.

Augustine, R., & Hasan, A. (2020). Emerging applications of biocompatible phytosynthesized metal/metal oxide nanoparticles in healthcare. *Journal of Drug Delivery Science and Technology, 56*, 101516.

Azizi, S., Mohamad, R., Bahadoran, A., Bayat, S., Rahim, R. A., Ariff, A., & Saad, W. Z. (2016). Effect of annealing temperature on antimicrobial and structural properties of bio-synthesized zinc oxide nanoparticles using flower extract of Anchusa italica. *Journal of Photochemistry and Photobiology B: Biology, 161*, 441-449.

Backes, F. J., Walker, C. J., Goodfellow, P. J., Hade, E. M., Agarwal, G., Mutch, D., . . . Suarez, A. A. (2016). Estrogen receptor-alpha as a predictive biomarker in endometrioid endometrial cancer. *Gynecologic oncology, 141*(2), 312-317.

Bahrami, H., & Tafrihi, M. (2023). Global trends of cancer: The role of diet, lifestyle, and environmental factors. *Cancer Innovation, 2*(4), 290-301.

Barui, A. K., Das, S., & Patra, C. R. (2019). Biomedical applications of green-synthesized metal nanoparticles using polysaccharides *Functional Polysaccharides for Biomedical Applications* (pp. 329-355): Elsevier

Basavegowda, N., & Baek, K.-H. (2021). Multimetallic nanoparticles as alternative antimicrobial agents: challenges and perspectives. *Molecules, 26*(4), 912.

Batool, S., Hasan, M., Dilshad, M., Zafar, A., Tariq, T., Shaheen, A., . . . Iqbal, F. (2022). Green synthesized ZnO-Fe2O3-Co3O4 nanocomposite for antioxidant, microbial disinfection and degradation of pollutants from wastewater. *Biochemical Systematics and Ecology, 105*, 104535.

Benzie, I. F., & Strain, J. J. (1996). The ferric reducing ability of plasma (FRAP) as a measure of "antioxidant power": the FRAP assay. *Analytical biochemistry, 239*(1), 70-76.

Bharathi, D., & Bhuvaneshwari, V. (2019). Synthesis of zinc oxide nanoparticles (ZnO NPs) using pure bioflavonoid rutin and their biomedical applications: antibacterial, antioxidant and cytotoxic activities. *Research on Chemical Intermediates, 45*, 2065-2078.

Bhatt, S., Stender, J., Joshi, S., Wu, G., & Katzenellenbogen, B. (2016). OCT-4: A novel estrogen receptor-α collaborator that promotes tamoxifen resistance in breast cancer cells. *Oncogene, 35*(44), 5722-5734.

Biswal, A. K., & Misra, P. K. (2020). Biosynthesis and characterization of silver nanoparticles for prospective application in food packaging and biomedical fields. *Materials Chemistry and Physics, 250*, 123014.

Bouafia, A., Laouini, S. E., Khelef, A., Tedjani, M. L., & Guemari, F. (2021). Effect of ferric chloride concentration on the type of magnetite (Fe3O4) nanoparticles biosynthesized by aqueous leaves extract of artemisia and assessment of their antioxidant activities. *Journal of Cluster Science, 32*(4), 1033-1041.

Bray, F., Ferlay, J., Soerjomataram, I., Siegel, R. L., Torre, L. A., & Jemal, A. (2018). Global cancer statistics 2018: GLOBOCAN estimates of incidence and mortality worldwide for 36 cancers in 185 countries. *CA: a cancer journal for clinicians, 68*(6), 394-424.

Cao, Y., Dhahad, H. A., El-Shorbagy, M., Alijani, H. Q., Zakeri, M., Heydari, A., . . . Naderifar, M. (2021). Green synthesis of bimetallic ZnO–CuO nanoparticles and their cytotoxicity properties. *Scientific Reports, 11*(1), 23479.

Cassini, A., Högberg, L. D., Plachouras, D., Quattrocchi, A., Hoxha, A., Simonsen, G. S., . . . Cecchini, M. (2019). Attributable deaths and disability-adjusted life-years caused by infections with antibiotic-resistant bacteria in the EU and the European Economic Area in 2015: a population-level modelling analysis. *The Lancet infectious diseases, 19*(1), 56-66.

Ceylan, A., Jastrzembski, K., & Shah, S. I. (2006). Enhanced solubility Ag-Cu nanoparticles and their thermal transport properties. *Metallurgical and Materials Transactions A, 37*(7), 2033-2038.

Chau, T. P., Veeraragavan, G. R., Narayanan, M., Chinnathambi, A., Alharbi, S. A., Subramani, B., . . . Pikulkaew, S. (2022). Green synthesis of Zirconium nanoparticles using Punica granatum (pomegranate) peel extract and their antimicrobial and antioxidant potency. *Environmental Research, 209*, 112771.

Chaudhary, A., Kumar, N., Kumar, R., & Salar, R. K. (2019). Antimicrobial activity of zinc oxide nanoparticles synthesized from Aloe vera peel extract. *SN Applied Sciences, 1*, 1-9.

Chavali, M. S., & Nikolova, M. P. (2019). Metal oxide nanoparticles and their applications in nanotechnology. *SN applied sciences, 1*(6), 607.

Chekole, G. (2017). Ethnobotanical study of medicinal plants used against human ailments in Gubalafto District, Northern Ethiopia. *Journal of ethnobiology and ethnomedicine, 13*(1), 55.

Cheviron, P., Gouanvé, F., & Espuche, E. (2014). Green synthesis of colloid silver nanoparticles and resulting biodegradable starch/silver nanocomposites. *Carbohydrate polymers, 108*, 291-298.

Chouke, P. B., Shrirame, T., Potbhare, A. K., Mondal, A., Chaudhary, A. R., Mondal, S., . . . Kuca, K. (2022). Bioinspired metal/metal oxide nanoparticles: A road map to potential applications. *Materials Today Advances, 16*, 100314.

Contera, S., Bernardino de la Serna, J., & Tetley, T. D. (2020). Biotechnology, nanotechnology and medicine (Vol. 4, pp. 551-554): Portland Press Ltd.

Cucci, M., Wooten, C., Fowler, M., Mallat, A., Hieb, N., & Mullen, C. (2020). Incidence and Risk Factors Associated with Multi-Drug–Resistant Pathogens in a Critically Ill Trauma Population: A Retrospective Cohort Study. *Surgical Infections, 21*(1), 15-22.

d'Avigdor, E., Wohlmuth, H., Asfaw, Z., & Awas, T. (2014). The current status of knowledge of herbal medicine and medicinal plants in Fiche, Ethiopia. *Journal of ethnobiology and ethnomedicine, 10*(1), 38.

Dabhane, H., Ghotekar, S., Zate, M., Kute, S., Jadhav, G., & Medhane, V. (2022). Green synthesis of MgO nanoparticles using aqueous leaf extract of Ajwain (Trachyspermum ammi) and evaluation of their catalytic and biological activities. *Inorganic Chemistry Communications, 138*, 109270.

Dangana, R. S., George, R. C., & Agboola, F. K. (2023). The biosynthesis of zinc oxide nanoparticles using aqueous leaf extracts of Cnidoscolus aconitifolius and their biological activities. *Green Chemistry Letters and Reviews, 16*(1), 2169591.

Dappula, S. S., Kandrakonda, Y. R., Shaik, J. B., Mothukuru, S. L., Lebaka, V. R., Mannarapu, M., & Amooru, G. D. (2023). Biosynthesis of zinc oxide nanoparticles using aqueous extract of Andrographis alata: Characterization, optimization and assessment of their antibacterial, antioxidant, antidiabetic and anti-Alzheimer's properties. *Journal of Molecular Structure, 1273*, 134264.

Dauthal, P., & Mukhopadhyay, M. (2016). Noble metal nanoparticles: plant-mediated synthesis, mechanistic aspects of synthesis, and applications. *Industrial & Engineering Chemistry Research, 55*(36), 9557-9577.

De, A., Das, R., Jain, P., & Kaur, H. (2022). Green chemistry-assisted synthesis of CuO nanoparticles: Reaction optimization, DNA cleavage, and DNA binding studies. *Materials Today: Proceedings, 49*, 3122-3125.

De La Cruz, G. G., Rodríguez-Fragoso, P., Reyes-Esparza, J., Rodríguez-López, A., Gómez-Cansino, R., & Rodriguez-Fragoso, L. (2018). Interaction of nanoparticles with blood components and associated pathophysiological effects. *Unraveling the Safety Profile of Nanoscale Particles and Materials-From Biomedical to Environmental Applications*.

de Martel, C., Georges, D., Bray, F., Ferlay, J., & Clifford, G. M. (2020). Global burden of cancer attributable to infections in 2018: a worldwide incidence analysis. *The Lancet Global Health, 8*(2), e180-e190.

De Silva, G. O., Abeysundara, A. T., & Aponso, M. M. W. (2017). Extraction methods, qualitative and quantitative techniques for screening of phytochemicals from plants. *American Journal of Essential Oils and Natural Products, 5*(2), 29-32.

Del Genio, V., Bellavita, R., Falanga, A., Hervé-Aubert, K., Chourpa, I., & Galdiero, S. (2022). Peptides to overcome the limitations of current anticancer and antimicrobial nanotherapies. *Pharmaceutics, 14*(6), 1235.

Deo, S., Sharma, J., & Kumar, S. (2022). GLOBOCAN 2020 report on global cancer burden: challenges and opportunities for surgical oncologists. *Annals of surgical oncology, 29*(11), 6497-6500.

Desalegn, T., Murthy, H., Ravikumar, C., & Nagaswarupa, H. (2021). Green synthesis of CuO nanostructures using Syzygium guineense (Willd.) DC plant leaf extract and their applications. *Journal of Nanostructures, 11*(1), 81-94.

Dey, A. (2018). Semiconductor metal oxide gas sensors: A review. *Materials science and Engineering: B, 229*, 206-217.

Dey, A., Manna, S., Chattopadhyay, S., Mondal, D., Chattopadhyay, D., Raj, A., . . . Roy, S. (2019). Azadirachta indica leaves mediated green synthesized copper oxide nanoparticles induce apoptosis through activation of TNF-α and caspases signaling pathway against cancer cells. *Journal of Saudi Chemical Society, 23*(2), 222-238.

Djamila, B., Eddine, L. S., Abderrhmane, B., Nassiba, A., & Barhoum, A. (2022). In vitro antioxidant activities of copper mixed oxide (CuO/Cu2O) nanoparticles produced from the leaves of Phoenix dactylifera L. *Biomass Conversion and Biorefinery*, 1-14.

Dobrucka, R. (2018). Antioxidant and catalytic activity of biosynthesized CuO nanoparticles using extract of Galeopsidis herba. *Journal of Inorganic and Organometallic Polymers and Materials, 28*, 812-819.

Dobrucka, R., Kaczmarek, M., Łagiedo, M., Kielan, A., & Dlugaszewska, J. (2019). Evaluation of biologically synthesized Au-CuO and CuO-ZnO nanoparticles against glioma cells and microorganisms. *Saudi Pharmaceutical Journal, 27*(3), 373-383.

Dolati, M., Tafvizi, F., Salehipour, M., Komeili Movahed, T., & Jafari, P. (2023). Biogenic copper oxide nanoparticles from Bacillus coagulans induced reactive oxygen species generation and apoptotic and anti-metastatic activities in breast cancer cells. *Scientific Reports, 13*(1), 3256.

Doman, K. M., Gharieb, M. M., Abd El-Monem, A. M., & Morsi, H. H. (2023). Synthesis of silver and copper nanoparticle using Spirulina platensis and evaluation of their anticancer activity. *International Journal of Environmental Health Research*, 1-13.

Dowlath, M. J. H., Musthafa, S. A., Khalith, S. M., Varjani, S., Karuppannan, S. K., Ramanujam, G. M., . . . Chang, S. W. (2021). Comparison of characteristics and biocompatibility of green synthesized iron oxide nanoparticles with chemical synthesized nanoparticles. *Environmental Research, 201*, 111585.

Dubey, A. K., Kumar Gupta, V., Kujawska, M., Orive, G., Kim, N.-Y., Li, C.-z., . . . Kaushik, A. (2022). Exploring nano-enabled CRISPR-Cas-powered strategies for efficient diagnostics and treatment of infectious diseases. *Journal of Nanostructure in Chemistry, 12*(5), 833-864.

Dudonne, S., Vitrac, X., Coutiere, P., Woillez, M., & Mérillon, J.-M. (2009). Comparative study of antioxidant properties and total phenolic content of 30 plant extracts of industrial interest using DPPH, ABTS, FRAP, SOD, and ORAC assays. *Journal of agricultural and food chemistry, 57*(5), 1768-1774.

Efati, Z., Shahangian, S. S., Darroudi, M., Amiri, H., Hashemy, S. I., & Aghamaali, M. R. (2023). Green chemistry synthesized zinc oxide nanoparticles in Lepidium sativum L. seed extract and evaluation of their anticancer activity in human colorectal cancer cells. *Ceramics International*.

El-Saadony, M. T., El-Hack, A., Mohamed, E., Taha, A. E., Fouda, M. M., Ajarem, J. S., . . . Elshaer, N. (2020). Ecofriendly synthesis and insecticidal application of copper nanoparticles against the storage pest Tribolium castaneum. *Nanomaterials, 10*(3), 587.

El Shafey, A. M. (2020). Green synthesis of metal and metal oxide nanoparticles from plant leaf extracts and their applications: A review. *Green Processing and Synthesis, 9*(1), 304-339.

Elemike, E. E., Onwudiwe, D. C., & Singh, M. (2020). Eco-friendly synthesis of copper oxide, zinc oxide and copper oxide–zinc oxide nanocomposites, and their anticancer applications. *Journal of Inorganic and Organometallic Polymers and Materials, 30*, 400-409.

Elsayed, A. M., Sherif, N. M., Hassan, N. S., Althobaiti, F., Hanafy, N. A., & Sahyon, H. A. (2021). Novel quercetin encapsulated chitosan functionalized copper oxide nanoparticles as anti-breast cancer agent via regulating p53 in rat model. *International Journal of Biological Macromolecules, 185*, 134-152.

Erol, I., Hazman, Ö., Özkan, M., Uygur, I., Khamidov, G., & Gerengi, H. (2023). Synthesis of novel PVA-PFPAMA nanocomposites by the hydrothermal method: Evaluation of thermal, antimicrobial, and anticarcinogenic properties. *Progress in Organic Coatings, 185*, 107889.

Estevez, M. B., Mitchell, S. G., Faccio, R., & Alborés, S. (2020). Biogenic silver nanoparticles: understanding the antimicrobial mechanism using Confocal Raman Microscopy. *Materials Research Express, 6*(12), 1250f1255.

Faisal, S., Jan, H., Shah, S. A., Shah, S., Khan, A., Akbar, M. T., . . . Akhtar, N. (2021). Green synthesis of zinc oxide (ZnO) nanoparticles using aqueous fruit extracts of Myristica

fragrans: their characterizations and biological and environmental applications. *ACS omega*, *6*(14), 9709-9722.

Fathy, R. M., & Mahfouz, A. Y. (2021). Eco-friendly graphene oxide-based magnesium oxide nanocomposite synthesis using fungal fermented by-products and gamma rays for outstanding antimicrobial, antioxidant, and anticancer activities. *Journal of Nanostructure in Chemistry*, *11*, 301-321.

Fauzia, V., Irmavianti, D., Roza, L., Hafizah, M. A. E., Imawan, C., & Umar, A. A. (2019). Bimetallic AuAg sharp-branch mesoflowers as catalyst for hydrogenation of acetone. *Materials Chemistry and Physics*, *225*, 443-450.

Fayaz, A. M., Balaji, K., Kalaichelvan, P., & Venkatesan, R. (2009). Fungal based synthesis of silver nanoparticles—an effect of temperature on the size of particles. *Colloids and Surfaces B: Biointerfaces*, *74*(1), 123-126.

Ferlay, J., Colombet, M., Soerjomataram, I., Mathers, C., Parkin, D., Piñeros, M., . . . Bray, F. (2019). Estimating the global cancer incidence and mortality in 2018: GLOBOCAN sources and methods. *International journal of cancer*, *144*(8), 1941-1953.

Filippi, A., Liu, F., Wilson, J., Lelieveld, S., Korschelt, K., Wang, T., . . . Tremel, W. (2019). Antioxidant activity of cerium dioxide nanoparticles and nanorods in scavenging hydroxyl radicals. *RSC advances*, *9*(20), 11077-11081.

Fouda, A., Eid, A. M., Abdel-Rahman, M. A., El-Belely, E. F., Awad, M. A., Hassan, S. E.-D., . . . Hamza, M. F. (2022). Enhanced antimicrobial, cytotoxicity, larvicidal, and repellence activities of brown algae, Cystoseira crinita-mediated green synthesis of magnesium oxide nanoparticles. *Frontiers in Bioengineering and Biotechnology*, *10*, 849921.

Gaber, S. E., Hashem, A. H., El-Sayyad, G. S., & Attia, M. S. (2023). Antifungal activity of myco-synthesized bimetallic ZnO-CuO nanoparticles against fungal plant pathogen Fusarium oxysporum. *Biomass Conversion and Biorefinery*, 1-15.

Gao, Y., Arokia Vijaya Anand, M., Ramachandran, V., Karthikkumar, V., Shalini, V., Vijayalakshmi, S., & Ernest, D. (2019). Biofabrication of zinc oxide nanoparticles from Aspergillus niger, their antioxidant, antimicrobial and anticancer activity. *Journal of Cluster Science*, *30*(4), 937-946.

Ge, X., Cao, Z., & Chu, L. (2022). The antioxidant effect of the metal and metal-oxide nanoparticles. *Antioxidants*, *11*(4), 791.

Gebre, S. H. (2023). Bio-inspired synthesis of metal and metal oxide nanoparticles: the key role of phytochemicals. *Journal of Cluster Science*, *34*(2), 665-704.

Ghaffar, S., Abbas, A., Naeem-ul-Hassan, M., Assad, N., Sher, M., Ullah, S., . . . Al Bratty, M. (2023). Improved Photocatalytic and Antioxidant Activity of Olive Fruit Extract-Mediated ZnO Nanoparticles. *Antioxidants*, *12*(6), 1201.

Ghahremani, M., Sharifi, Y., & Haghi Ghahremanloi Olia, A. (2020). The effect of Silver nanoparticles on biofilm production of vancomycin resistant Staphylococcus aureus. *Journal of Research in Applied and Basic Medical Sciences, 6*(2), 72-78.

Ghasemi, M., Turnbull, T., Sebastian, S., & Kempson, I. (2021). The MTT assay: utility, limitations, pitfalls, and interpretation in bulk and single-cell analysis. *International journal of molecular sciences, 22*(23), 12827.

Ginting, B., Maulana, I., & Karnila, I. (2020). Biosynthesis copper nanoparticles using Blumea balsamifera leaf extracts: characterization of its antioxidant and cytotoxicity activities. *Surfaces and Interfaces, 21*, 100799.

Gmeiner, W. H., & Ghosh, S. (2014). Nanotechnology for cancer treatment. *Nanotechnology reviews*, *3*(2), 111-122.

Goldstein, J. I., Newbury, D. E., Michael, J. R., Ritchie, N. W., Scott, J. H. J., Joy, D. C., . . . Ritchie, N. W. (2018). SEM image interpretation. *Scanning Electron Microscopy and X-Ray Microanalysis*, 111-121.

Gopal, J., Chun, S., Anthonydhason, V., Jung, S., Mwang'ombe, B. N., Muthu, M., & Sivanesan, I. (2018). Assays evaluating antimicrobial activity of nanoparticles: a myth buster. *Journal of Cluster Science*, *29*, 207-213.

Gupta, M. N., Khare, S. K., & Sinha, R. (2021). *Interfaces Between Nanomaterials and Microbes*: CRC Press.

Habibullah, G., Viktorova, J., & Ruml, T. (2021). C urrent Strategies for Noble Metal Nanoparticle Synthesis. *Nanoscale Research Letters, 16*(1), 1-12.

Hadi, A. J., Nayef, U. M., Mutlak, F. A.-H., & Jabir, M. S. (2023). Laser-ablated zinc oxide nanoparticles and evaluation of their antibacterial and anticancer activity against an ovarian cancer cell line: in vitro study. *Plasmonics*, 1-11.

Haq, S., Rashid, M., Menaa, F., Shahzad, N., Shahzad, M. I., Alfaifi, S. Y., . . . Tayeb, R. A. (2023). Antibacterial and antioxidant screening applications of reduced-graphene oxide modified ternary SnO2-NiO-CuO nanocomposites. *Arabian Journal of Chemistry, 16*(8), 104917.

Hasan, M., Ullah, I., Zulfiqar, H., Naeem, K., Iqbal, A., Gul, H., . . . Mahmood, N. (2018). Biological entities as chemical reactors for synthesis of nanomaterials: Progress, challenges and future perspective. *Materials Today Chemistry, 8*, 13-28.

Hashem, A. H., & El-Sayyad, G. S. (2023). Antimicrobial and anticancer activities of biosynthesized bimetallic silver-zinc oxide nanoparticles (Ag-ZnO NPs) using pomegranate peel extract. *Biomass Conversion and Biorefinery*, 1-13.

Hirphaye, B. Y., Bonka, N. B., Tura, A. M., & Fanta, G. M. (2023). Biosynthesis of magnesium oxide nanoparticles using Hagenia abyssinica female flower aqueous extract for characterization and antibacterial activity. *Applied Water Science, 13*(9), 175.

Huang, D., Ou, B., & Prior, R. L. (2005). The chemistry behind antioxidant capacity assays. *Journal of agricultural and food chemistry, 53*(6), 1841-1856.

Huang, J., Li, Q., Sun, D., Lu, Y., Su, Y., Yang, X., . . . He, N. (2007). Biosynthesis of silver and gold nanoparticles by novel sundried Cinnamomum camphora leaf. *Nanotechnology, 18*(10), 105104.

Hussein, S., Mahmoud, A. M., Elgebaly, H. A., Hendawy, O. M., Hassanein, E. H., Moustafa, S., . . . Nassar, A. M. (2022). Green Synthesis of Trimetallic Nanocomposite (Ru/Ag/Pd)-Np and Its In Vitro Antimicrobial and Anticancer Activities. *Journal of Chemistry*.

Ikuta, K. S., Swetschinski, L. R., Aguilar, G. R., Sharara, F., Mestrovic, T., Gray, A. P., . . . Hayoon, A. G. (2022). Global mortality associated with 33 bacterial pathogens in 2019: a systematic analysis for the Global Burden of Disease Study 2019. *The Lancet, 400*(10369), 2221-2248.

Ioset, J.-R., Brun, R., Wenzler, T., Kaiser, M., & Yardley, V. (2009). Drug screening for kinetoplastids diseases. *A training manual for screening in neglected diseases*.

Ishaque, M. Z., Zaman, Y., Arif, A., Siddique, A. B., Shahzad, M., Ali, D., . . . Faizan, M. (2023). Fabrication of ternary metal oxide (ZnO: NiO: CuO) nanocomposite heterojunctions for enhanced photocatalytic and antibacterial applications. *RSC advances, 13*(44), 30838-30854.

Jaffri, S. B., & Ahmad, K. S. (2018). Phytofunctionalized silver nanoparticles: green biomaterial for biomedical and environmental applications. *Reviews in Inorganic Chemistry*, *38*(3), 127-149.

Jamdagni, P., Khatri, P., & Rana, J. (2018). Green synthesis of zinc oxide nanoparticles using flower extract of Nyctanthes arbor-tristis and their antifungal activity. *Journal of King Saud University-Science*, *30*(2), 168-175.

Jiang, S., Lin, K., & Cai, M. (2020). ZnO nanomaterials: current advancements in antibacterial mechanisms and applications. *Frontiers in Chemistry, 8*, 580.

Jiao, A., Dong, X., Zhang, H., Xu, L., Tian, Y., Liu, X., & Chen, M. (2019). Construction of pure worm-like AuAg nanochains for ultrasensitive SERS detection of pesticide residues on apple surfaces. *Spectrochimica Acta Part A: Molecular and Biomolecular Spectroscopy*, *209*, 241-247.

Joghee, S., Ganeshan, P., Vincent, A., & Hong, S. I. (2019). Ecofriendly biosynthesis of zinc oxide and magnesium oxide particles from medicinal plant Pisonia grandis R. Br. leaf extract and their antimicrobial activity. *BioNanoScience*, *9*, 141-154.

Jomova, K., Raptova, R., Alomar, S. Y., Alwasel, S. H., Nepovimova, E., Kuca, K., & Valko, M. (2023). Reactive oxygen species, toxicity, oxidative stress, and antioxidants: Chronic diseases and aging. *Archives of toxicology, 97*(10), 2499-2574.

Joshi, A., Sharma, A., Bachheti, R. K., Husen, A., & Mishra, V. K. (2019). Plant-mediated synthesis of copper oxide nanoparticles and their biological applications. *Nanomaterials and Plant Potential*, 221-237.

Kanagamani, K., Muthukrishnan, P., Saravanakumar, K., Shankar, K., & Kathiresan, A. (2019). Photocatalytic degradation of environmental perilous gentian violet dye using leucaena-mediated zinc oxide nanoparticle and its anticancer activity. *Rare metals*, *38*, 277-286.

Kannan, K., Radhika, D., Sadasivuni, K. K., Reddy, K. R., & Raghu, A. V. (2020). Nanostructured metal oxides and its hybrids for photocatalytic and biomedical applications. *Advances in Colloid and Interface Science, 281*, 102178.

Karthik, K., Dhanuskodi, S., Gobinath, C., Prabukumar, S., & Sivaramakrishnan, S. (2018). Multifunctional properties of microwave assisted CdO–NiO–ZnO mixed metal oxide nanocomposite: enhanced photocatalytic and antibacterial activities. *Journal of Materials Science: Materials in Electronics, 29*, 5459-5471.

Karthik, K., Dhanuskodi, S., Kumar, S. P., Gobinath, C., & Sivaramakrishnan, S. (2017). Microwave assisted green synthesis of MgO nanorods and their antibacterial and anti-breast cancer activities. *Materials Letters, 206*, 217-220.

Karthik, S., Siva, P., Balu, K. S., Suriyaprabha, R., Rajendran, V., & Maaza, M. (2017). Acalypha indica–mediated green synthesis of ZnO nanostructures under differential thermal treatment: Effect on textile coating, hydrophobicity, UV resistance, and antibacterial activity. *Advanced Powder Technology, 28*(12), 3184-3194.

Karthikeyan, M., Ahamed, A. J., Karthikeyan, C., & Kumar, P. V. (2019). Enhancement of antibacterial and anticancer properties of pure and REM doped ZnO nanoparticles synthesized using Gymnema sylvestre leaves extract. *SN Applied Sciences, 1*(4), 355.

Karunakaran, G., Jagathambal, M., Kumar, G. S., & Kolesnikov, E. (2020). Hylotelephium telephium flower extract-mediated biosynthesis of CuO and ZnO nanoparticles with promising antioxidant and antibacterial properties for healthcare applications. *Jom, 72*(3), 1264-1272.

Khalil, A. T., Ayaz, M., Ovais, M., Wadood, A., Ali, M., Shinwari, Z. K., & Maaza, M. (2018). In vitro cholinesterase enzymes inhibitory potential and in silico molecular docking studies of biogenic metal oxides nanoparticles. *Inorganic and Nano-Metal Chemistry, 48*(9), 441-448.

Khan, M. I., Akhtar, M. N., Ashraf, N., Najeeb, J., Munir, H., Awan, T. I., . . . Kabli, M. R. (2020a). Green synthesis of magnesium oxide nanoparticles using Dalbergia sissoo extract for photocatalytic activity and antibacterial efficacy. *Applied Nanoscience, 10*(7), 2351-2364.

Khan, M. I., Akhtar, M. N., Ashraf, N., Najeeb, J., Munir, H., Awan, T. I., . . . Kabli, M. R. (2020b). Green synthesis of magnesium oxide nanoparticles using Dalbergia sissoo extract for photocatalytic activity and antibacterial efficacy. *Applied Nanoscience, 10*, 2351-2364.

Khan, S. U., Ahemad, N., Chuah, L.-H., Naidu, R., & Htar, T. T. (2020). Illustrated step by step protocol to perform molecular docking: Human estrogen receptor complex with 4-hydroxytamoxifen as a case study. *Progress in Drug Discovery & Biomedical Science, 3*(1).

Khani, R., Roostaei, B., Bagherzade, G., & Moudi, M. (2018). Green synthesis of copper nanoparticles by fruit extract of Ziziphus spina-christi (L.) Willd.: application for adsorption of triphenylmethane dye and antibacterial assay. *Journal of Molecular Liquids, 255*, 541-549.

Khonkarn, R., Okonogi, S., Ampasavate, C., & Anuchapreeda, S. (2010). Investigation of fruit peel extracts as sources for compounds with antioxidant and antiproliferative activities against human cell lines. *Food and Chemical Toxicology, 48*(8-9), 2122-2129.

Kim, J. A., Åberg, C., Salvati, A., & Dawson, K. A. (2012). Role of cell cycle on the cellular uptake and dilution of nanoparticles in a cell population. *Nature nanotechnology, 7*(1), 62-68.

Kojom, L. P., & Singh, V. (2021). A review on emerging infectious diseases prioritized under the 2018 WHO research and development blueprint: lessons from the Indian context. *Vector-Borne and Zoonotic Diseases, 21*(3), 149-159.

Koltover, V. (2010). Antioxidant biomedicine: from free radical chemistry to systems biology mechanisms. *Russian Chemical Bulletin, 59*(1), 37-42.

Krishnamoorthy, N., Sivasankarapillai, V. S., Natarajan, V. K., Eldesoky, G. E., Wabaidur, S. M., Eswaran, M., & Dhanusuraman, R. (2023). Biocidal activity of ZnO NPs against pathogens and antioxidant activity-a greener approach by Citrus hystrix leaf extract as bio-reductant. *Biochemical Engineering Journal, 192*, 108818.

Król, A., Railean-Plugaru, V., Pomastowski, P., & Buszewski, B. (2019). Phytochemical investigation of Medicago sativa L. extract and its potential as a safe source for the synthesis of ZnO nanoparticles: The proposed mechanism of formation and antimicrobial activity. *Phytochemistry Letters, 31*, 170-180.

Kumar, N., Gulati, H. K., Sharma, A., Heer, S., Jassal, A. K., Arora, L., . . . Kaur, A. (2021). Most recent strategies targeting estrogen receptor alpha for the treatment of breast cancer. *Molecular Diversity, 25*, 603-624.

Kumar, R., Sharma, S., & Devi, L. (2018). Investigation of total phenolic, flavonoid contents and antioxidant activity from extracts of Azadirachta indica of Bundelkhand Region. *Int. J. Life. Sci. Scienti. Res. eISSN, 2455*(1716), 1716.

Kumar, S. A., Jarvin, M., Inbanathan, S., Umar, A., Lalla, N., Dzade, N. Y., . . . Baskoutas, S. (2022). Facile green synthesis of magnesium oxide nanoparticles using tea (Camellia

sinensis) extract for efficient photocatalytic degradation of methylene blue dye. *Environmental Technology & Innovation, 28*, 102746.

Kumaravel, J., Lalitha, K., Arunthirumeni, M., & Shivakumar, M. S. (2021). Mycosynthesis of bimetallic zinc oxide and titanium dioxide nanoparticles for control of Spodoptera frugiperda. *Pesticide Biochemistry and Physiology, 178*, 104910.

Küünal, S., Rauwel, P., & Rauwel, E. (2018). Plant extract mediated synthesis of nanoparticles *Emerging applications of nanoparticles and architecture nanostructures* (pp. 411-446): Elsevier

Letchumanan, D., Sok, S. P., Ibrahim, S., Nagoor, N. H., & Arshad, N. M. (2021). Plant-based biosynthesis of copper/copper oxide nanoparticles: an update on their applications in biomedicine, mechanisms, and toxicity. *Biomolecules, 11*(4), 564.

Letha, N., Ganesan, K., Nair, S. K. P., & Gani, S. (2016). Studies on phytochemical screening and in vitro antioxidant activity of Ethiopian indigenous medicinal Plants, Artemisia abyssinica Sch. Bip. ex A. *Rich. World J. Pharm. Res, 5*, 1048-1058.

Li, M., Liu, Y., Gong, Y., Yan, X., Wang, L., Zheng, W., . . . Zhao, Y. (2023). Recent advances in nanoantibiotics against multidrug-resistant bacteria. *Nanoscale Advances*.

Li, Q., Duan, M., Liu, L., Chen, X., Fu, Y., Li, J., . . . McClements, D. J. (2021). Impact of polyphenol interactions with titanium dioxide nanoparticles on their bioavailability and antioxidant activity. *Journal of Agricultural and Food Chemistry, 69*(33), 9661-9670.

Li, X., Feng, Y., Li, H., & Zhang, Q. (2022). Effect of anionic groups on the antibacterial activity of magnesium oxide nanoparticles. *Colloids and Surfaces A: Physicochemical and Engineering Aspects, 635*, 127978.

Logeswari, P., Dineshkumar, V., Usha, P., & Kumar, S. (2012). Proximate analysis of Sida rhombifolia L. root and its effect on cadmium chloride induced alterations in body weight of Wistar rats. *Int J Pharma Bio Sci, 2*, 303-309.

Lucky, S. S., Idris, N. M., Huang, K., Kim, J., Li, Z., Thong, P. S. P., . . . Zhang, Y. (2016). In vivo biocompatibility, biodistribution and therapeutic efficiency of titania coated upconversion nanoparticles for photodynamic therapy of solid oral cancers. *Theranostics, 6*(11), 1844.

Lv, Q., Zhang, B., Xing, X., Zhao, Y., Cai, R., Wang, W., & Gu, Q. (2018). Biosynthesis of copper nanoparticles using Shewanella loihica PV-4 with antibacterial activity: Novel approach and mechanisms investigation. *Journal of hazardous materials, 347,* 141-149.

MacNair, C. R., Rutherford, S. T., & Tan, M.-W. (2024). Alternative therapeutic strategies to treat antibiotic-resistant pathogens. *Nature Reviews Microbiology, 22*(5), 262-275.

Madhyastha, H., Madhyastha, R., Nakajima, Y., Daima, H., Navya, P., & Maruyama, M. (2019). An opinion on nanomedicine and toxico-cellular crosstalk: considerations and caveats. *Materials Today: Proceedings, 10*, 100-105.

Maheo, A. R., Vithiya B, S. M., Arul Prasad T, A., Mangesh, V., Perumal, T., Al-Qahtani, W. H., & Govindasamy, M. (2023). Cytotoxic, Antidiabetic, and Antioxidant Study of Biogenically Improvised Elsholtzia blanda and Chitosan-Assisted Zinc Oxide Nanoparticles. *ACS omega, 8*(12), 10954-10967.

Mahmood, R. I., Kadhim, A. A., Ibraheem, S., Albukhaty, S., Mohammed-Salih, H. S., Abbas, R. H., . . . AlMalki, F. A. (2022). Biosynthesis of copper oxide nanoparticles mediated Annona muricata as cytotoxic and apoptosis inducer factor in breast cancer cell lines. *Scientific Reports, 12*(1), 16165.

Majeed, M., Hakeem, K. R., & Rehman, R. U. (2022). Synergistic effect of plant extract coupled silver nanoparticles in various therapeutic applications-present insights and bottlenecks. *Chemosphere, 288*, 132527.

Majeed, S., Danish, M., Ismail, M. H. B., Ansari, M. T., & Ibrahim, M. N. M. (2019). Anticancer and apoptotic activity of biologically synthesized zinc oxide nanoparticles against human colon cancer HCT-116 cell line-in vitro study. *Sustainable Chemistry and Pharmacy, 14*, 100179.

Majhi, J. K., & Kuiri, P. K. (2021). Large spectral shift of plasmon resonances in Au–Cu alloy nanoparticles through anisotropy and interaction. *Bulletin of Materials Science, 44*(1), 18.

Makarov, V., Love, A., Sinitsyna, O., Makarova, S., Yaminsky, I., Taliansky, M., & Kalinina, N. (2014). “Green” nanotechnologies: synthesis of metal nanoparticles using plants. *Acta Naturae (англоязычная версия), 6*(1 (20)).

Makvandi, P., Wang, C. y., Zare, E. N., Borzacchiello, A., Niu, L. n., & Tay, F. R. (2020). Metal-based nanomaterials in biomedical applications: antimicrobial activity and cytotoxicity aspects. *Advanced Functional Materials*, *30*(22), 1910021.

Malapermal, V., Mbatha, J. N., Gengan, R. M., & Anand, K. (2015). Biosynthesis of bimetallic Au-Ag nanoparticles using Ocimum basilicum (L.) with antidiabetic and antimicrobial properties. *Advanced materials letters (Online)*.

Mandal, A. K., Katuwal, S., Tettey, F., Gupta, A., Bhattarai, S., Jaisi, S., . . . Parajuli, N. (2022). Current research on zinc oxide nanoparticles: synthesis, characterization, and biomedical applications. *Nanomaterials, 12*(17), 3066.

Mao, X., Gu, C., Chen, D., Yu, B., & He, J. (2017). Oxidative stress-induced diseases and tea polyphenols. *Oncotarget, 8*(46), 81649.

Marslin, G., Siram, K., Maqbool, Q., Selvakesavan, R. K., Kruszka, D., Kachlicki, P., & Franklin, G. (2018). Secondary metabolites in the green synthesis of metallic nanoparticles. *Materials, 11*(6), 940.

Meer, B., Andleeb, A., Iqbal, J., Ashraf, H., Meer, K., Ali, J. S., . . . Khan, T. (2022). Bio-Assisted Synthesis and Characterization of Zinc Oxide Nanoparticles from Lepidium Sativum and Their Potent Antioxidant, Antibacterial and Anticancer Activities. *Biomolecules, 12*(6), 855.

Mohamed, H., Thema, T., & Dhlamini, M. (2021). Green synthesis of CuO nanoparticles via Hyphaene thebaica extract and their optical properties. *Materials Today: Proceedings, 36*, 591-594.

Mohamed, N., Hessen, O. E., & Mohammed, H. S. (2021). Thermal stability, paramagnetic properties, morphology and antioxidant activity of iron oxide nanoparticles synthesized by chemical and green methods. *Inorganic Chemistry Communications, 128*, 108572.

Mohammad, B. R., Algburi, A., & Alzubaidy, Z. (2020). Antibacterial Activity of CuO and MgO nanoparticles in combination with levofloxacin against multidrug resistant escherichia coli causing urinary tract infections. *Journal of Research in Ecology, 8*(1), 2654-2663.

Mohammad, M. S., & Shyam, P. (2023). Structural Analysis of Biogenic Copper Oxide Nanoparticles, and their Bio-Activity Assessment. *BioNanoScience*, 1-11.

Mohammadi, F. M., & Ghasemi, N. (2018). Influence of temperature and concentration on biosynthesis and characterization of zinc oxide nanoparticles using cherry extract. *Journal of Nanostructure in Chemistry, 8*, 93-102.

Morris, G. M., Huey, R., Lindstrom, W., Sanner, M. F., Belew, R. K., Goodsell, D. S., & Olson, A. J. (2009). AutoDock4 and AutoDockTools4: Automated docking with selective receptor flexibility. *Journal of computational chemistry, 30*(16), 2785-2791.

Mousa, A. B., Moawad, R., Abdallah, Y., Abdel-Rasheed, M., & Zaher, A. M. A. (2023). Zinc Oxide Nanoparticles Promise Anticancer and Antibacterial Activity in Ovarian Cancer. *Pharmaceutical Research*, 1-10.

Mthana, M. S., Mthiyane, D. M., Onwudiwe, D. C., & Singh, M. (2022). Biosynthesis of ZnO nanoparticles using capsicum Chinense fruit extract and their in vitro cytotoxicity and antioxidant assay. *Applied Sciences, 12*(9), 4451.

Munawar, T., Iqbal, F., Yasmeen, S., Mahmood, K., & Hussain, A. (2020). Multi metal oxide NiO-CdO-ZnO nanocomposite–synthesis, structural, optical, electrical properties and enhanced sunlight driven photocatalytic activity. *Ceramics International, 46*(2), 2421-2437.

Munawar, T., Mukhtar, F., Yasmeen, S., Naveed-ur-Rehman, M., Nadeem, M. S., Riaz, M., . . . Iqbal, F. (2021). Sunlight-induced photocatalytic degradation of various dyes and bacterial inactivation using CuO–MgO–ZnO nanocomposite. *Environmental Science and Pollution Research, 28*, 42243-42260.

Munawar, T., Yasmeen, S., Hasan, M., Mahmood, K., Hussain, A., Ali, A., . . . Iqbal, F. (2020). Novel tri-phase heterostructured ZnO–Yb2O3–Pr2O3 nanocomposite; structural, optical, photocatalytic and antibacterial studies. *Ceramics International, 46*(8), 11101-11114.

Munguti, L., & Dejene, F. (2021). Effects of Zn: Ti molar ratios on the morphological, optical and photocatalytic properties of ZnO-TiO2 nanocomposites for application in dye removal. *Materials Science in Semiconductor Processing, 128*, 105786.

Murali, M., Kalegowda, N., Gowtham, H. G., Ansari, M. A., Alomary, M. N., Alghamdi, S., . . . Aiyaz, M. (2021). Plant-Mediated Zinc Oxide Nanoparticles: Advances in the New Millennium towards Understanding Their Therapeutic Role in Biomedical Applications. *Pharmaceutics, 13*(10), 1662.

Murray, C. J., Ikuta, K. S., Sharara, F., Swetschinski, L., Aguilar, G. R., Gray, A., . . . Wool, E. (2022). Global burden of bacterial antimicrobial resistance in 2019: a systematic analysis. *The Lancet, 399*(10325), 629-655.

Murthy, H., Desalegn, T., Kassa, M., Abebe, B., & Assefa, T. (2020). Synthesis of green copper nanoparticles using medicinal plant hagenia abyssinica (Brace) JF. Gmel. leaf extract: Antimicrobial properties. *Journal of nanomaterials, 2020*.

Murthy, S., Effiong, P., & Fei, C. C. (2020). Metal oxide nanoparticles in biomedical applications *Metal oxide powder technologies* (pp. 233-251): Elsevier

Mustapha, S., Ndamitso, M., Abdulkareem, A., Tijani, J., Shuaib, D., Mohammed, A., & Sumaila, A. (2019). Comparative study of crystallite size using Williamson-Hall and Debye-Scherrer plots for ZnO nanoparticles. *Advances in Natural Sciences: Nanoscience and Nanotechnology, 10*(4), 045013.

Muthuvel, A., Jothibas, M., & Manoharan, C. (2020). Effect of chemically synthesis compared to biosynthesized ZnO-NPs using Solanum nigrum leaf extract and their photocatalytic, antibacterial and in-vitro antioxidant activity. *Journal of Environmental Chemical Engineering, 8*(2), 103705.

Nagajyothi, P., Muthuraman, P., Sreekanth, T., Kim, D. H., & Shim, J. (2017). Green synthesis: in-vitro anticancer activity of copper oxide nanoparticles against human cervical carcinoma cells. *Arabian journal of chemistry, 10*(2), 215-225.

Naika, H. R., Lingaraju, K., Manjunath, K., Kumar, D., Nagaraju, G., Suresh, D., & Nagabhushana, H. (2015). Green synthesis of CuO nanoparticles using Gloriosa superba L. extract and their antibacterial activity. *Journal of Taibah University for Science, 9*(1), 7-12.

Narendhran, S., & Sivaraj, R. (2016). Biogenic ZnO nanoparticles synthesized using L. aculeata leaf extract and their antifungal activity against plant fungal pathogens. *Bulletin of Materials Science, 39*, 1-5.

Naseem, T., & Durrani, T. (2021). The role of some important metal oxide nanoparticles for wastewater and antibacterial applications: A review. *Environmental Chemistry and Ecotoxicology, 3*, 59-75.

Naser, S. S., Ghosh, B., Simnani, F. Z., Singh, D., Choudhury, A., Nandi, A., . . . Suar, M. (2023). Emerging Trends in the Application of Green Synthesized Biocompatible ZnO Nanoparticles for Translational Paradigm in Cancer Therapy. *Journal of Nanotheranostics, 4*(3), 248-279.

Nasrollahzadeh, M., Sajjadi, M., Iravani, S., & Varma, R. S. (2020). Trimetallic nanoparticles: Greener synthesis and their applications. *Nanomaterials, 10*(9), 1784.

Negrescu, A. M., Killian, M. S., Raghu, S. N., Schmuki, P., Mazare, A., & Cimpean, A. (2022). Metal Oxide Nanoparticles: Review of Synthesis, Characterization and Biological Effects. *Journal of Functional Biomaterials, 13*(4), 274.

Ngom, I., Ngom, B., Sackey, J., & Khamlich, S. (2021). Biosynthesis of zinc oxide nanoparticles using extracts of Moringa Oleifera: Structural & optical properties. *Materials Today: Proceedings, 36*, 526-533.

Nieto-Maldonado, A., Bustos-Guadarrama, S., Espinoza-Gomez, H., Flores-López, L. Z., Ramirez-Acosta, K., Alonso-Nuñez, G., & Cadena-Nava, R. D. (2022). Green synthesis of copper nanoparticles using different plant extracts and their antibacterial activity. *Journal of Environmental Chemical Engineering*, 107130.

Nikam, A., Prasad, B., & Kulkarni, A. (2018). Wet chemical synthesis of metal oxide nanoparticles: a review. *CrystEngComm, 20*(35), 5091-5107.

Nikolova, M. P., & Chavali, M. S. (2020). Metal oxide nanoparticles as biomedical materials. *Biomimetics, 5*(2), 27.

Noori, A. J., & Kareem, F. A. (2019). The effect of magnesium oxide nanoparticles on the antibacterial and antibiofilm properties of glass-ionomer cement. *Heliyon, 5*(10), e02568.

Nyabadza, A., McCarthy, É., Makhesana, M., Heidarinassab, S., Plouze, A., Vazquez, M., & Brabazon, D. (2023). A review of physical, chemical and biological synthesis methods of bimetallic nanoparticles and applications in sensing, water treatment, biomedicine, catalysis and hydrogen storage. *Advances in Colloid and Interface Science*, 103010.

Ogunyemi, S. O., Zhang, M., Abdallah, Y., Ahmed, T., Qiu, W., Ali, M. A., . . . Li, B. (2020). The bio-synthesis of three metal oxide nanoparticles (ZnO, MnO2, and MgO) and their antibacterial activity against the bacterial leaf blight pathogen. *Frontiers in Microbiology, 11*, 588326.

Oloya, B., Namukobe, J., Ssengooba, W., Afayoa, M., & Byamukama, R. (2022). Phytochemical screening, antimycobacterial activity and acute toxicity of crude extracts of selected medicinal plant species used locally in the treatment of tuberculosis in Uganda. *Tropical medicine and health, 50*(1), 1-13.

Organization, W. H. (2020). First meeting of the WHO antifungal expert group on identifying priority fungal pathogens: meeting report.

Orshiso, T. A., Zereffa, E. A., Murthy, H. A., Demissie, T. B., Pardeshi, O., Avhad, L. S., & Ghotekar, S. (2023). Biosynthesis of Artemisia abyssinica Leaf Extract-Mediated Bimetallic ZnO–CuO Nanoparticles: Antioxidant, Anticancer, and Molecular Docking Studies. *ACS Omega*.

Ovais, M., Khalil, A. T., Islam, N. U., Ahmad, I., Ayaz, M., Saravanan, M., . . . Mukherjee, S. (2018). Role of plant phytochemicals and microbial enzymes in biosynthesis of metallic nanoparticles. *Applied microbiology and biotechnology, 102*(16), 6799-6814.

Palma, E., Tilocca, B., & Roncada, P. (2020). Antimicrobial resistance in veterinary medicine: an overview. *International Journal of Molecular Sciences, 21*(6), 1914.

Panchal, P., Paul, D. R., Sharma, A., Hooda, D., Yadav, R., Meena, P., & Nehra, S. (2019). Phytoextract mediated ZnO/MgO nanocomposites for photocatalytic and antibacterial activities. *Journal of Photochemistry and Photobiology A: Chemistry, 385*, 112049.

Panchal, P., Sharma, R., Reddy, A. S., Nehra, K., Sharma, A., & Nehra, S. (2023). Eco-friendly synthesis of Ag-doped ZnO/MgO as a potential photocatalyst for antimicrobial and dye degradation applications. *Coordination Chemistry Reviews, 493*, 215283.

Peluso, P., & Chankvetadze, B. (2023). Recent developments in molecular modeling tools and applications related to pharmaceutical and biomedical research. *Journal of Pharmaceutical and Biomedical Analysis*, 115836.

Periakaruppan, R., Ariuthayan, B., Vanathi, P., Selvaraj, K. S. V., Al-Dayan, N., Dhanasekaran, S., & Parthiban, A. (2023). Fabrication of Allium cepa–assisted magnesium oxide nanoparticles with antibacterial and antioxidant properties. *Biomass Conversion and Biorefinery*, 1-8.

Pillai, A. M., Sivasankarapillai, V. S., Rahdar, A., Joseph, J., Sadeghfar, F., Rajesh, K., & Kyzas, G. Z. (2020). Green synthesis and characterization of zinc oxide nanoparticles with antibacterial and antifungal activity. *Journal of Molecular Structure, 1211*, 128107.

Pisoschi, A. M., & Negulescu, G. P. (2011). Methods for total antioxidant activity determination: a review. *Biochem Anal Biochem, 1*(1), 106.

Poonguzhali, R. V., Srimathi, M., Kumar, E. R., Arunadevi, N., Elansary, H. O., Abdelbacki, A. A., & Abdelmohsen, S. A. (2022). Citrus limon assisted green synthesis of MgO nanoparticles: Evaluation of phase, functional groups, surface morphology, thermal stability and colloidal stability. *Ceramics International, 48*(19), 27774-27778.

PP, V. (2020). In vitro biocompatibility and antimicrobial activities of zinc oxide nanoparticles (ZnO NPs) prepared by chemical and green synthetic route—a comparative study. *BioNanoScience, 10*(1), 112-121.

Pugazhendhi, A., Prabhu, R., Muruganantham, K., Shanmuganathan, R., & Natarajan, S. (2019). Anticancer, antimicrobial and photocatalytic activities of green synthesized magnesium oxide nanoparticles (MgONPs) using aqueous extract of Sargassum wightii. *Journal of Photochemistry and Photobiology B: Biology, 190*, 86-97.

Rafie, M., & Meshkini, A. (2021). Tailoring the proliferation of fibroblast cells by multiresponsive and thermosensitive stem cells composite F127 hydrogel containing folic acid. MgO: ZnO/chitosan hybrid microparticles for skin regeneration. *European Journal of Pharmaceutical Sciences, 167*, 106031.

Raj Preeth, D., Shairam, M., Suganya, N., Hootan, R., Kartik, R., Pierre, K., . . . Rajalakshmi, S. (2019). Green synthesis of copper oxide nanoparticles using sinapic acid: an underpinning step towards antiangiogenic therapy for breast cancer. *JBIC Journal of Biological Inorganic Chemistry, 24*(5), 633-645.

Rajagopal, G., Nivetha, A., Sundar, M., Panneerselvam, T., Murugesan, S., Parasuraman, P., . . . Kunjiappan, S. (2021). Mixed phytochemicals mediated synthesis of copper nanoparticles for anticancer and larvicidal applications. *Heliyon, 7*(6), e07360.

Rajeshkumar, S., Kumar, S. V., Ramaiah, A., Agarwal, H., Lakshmi, T., & Roopan, S. M. (2018). Biosynthesis of zinc oxide nanoparticles usingMangifera indica leaves and evaluation of their antioxidant and cytotoxic properties in lung cancer (A549) cells. *Enzyme and microbial technology, 117*, 91-95.

Ramanathan, S., Gopinath, S. C., Arshad, M. M., Poopalan, P., & Perumal, V. (2021). Nanoparticle synthetic methods: Strength and limitations *Nanoparticles in Analytical and Medical Devices* (pp. 31-43): Elsevier

Rana, A., Pathak, S., Lim, D.-K., Kim, S.-K., Srivastava, R., Sharma, S. N., & Verma, R. (2023). Recent advancements in plant-and microbe-mediated synthesis of metal and metal oxide nanomaterials and their emerging antimicrobial applications. *ACS Applied Nano Materials, 6*(10), 8106-8134.

Rani, N., Rawat, K., Saini, M., Yadav, S., Shrivastava, A., Saini, K., & Maity, D. (2022). Azadirachta indica leaf extract mediated biosynthesized rod-shaped zinc oxide nanoparticles for in vitro lung cancer treatment. *Materials Science and Engineering: B, 284*, 115851.

Raut, S. K., & Khullar, M. (2023). Oxidative stress in metabolic diseases: Current scenario and therapeutic relevance. *Molecular and cellular biochemistry, 478*(1), 185-196.

Ravichandran, S., Radhakrishnan, J., Sengodan, P., Rajendran, R., Ramalingam, R., & Arunachalam, K. D. (2022). Bio synthesis of Zinc oxide nanoparticles using Clerodendrum phlomidis extract for antibacterial, anticancer, antioxidant and photocatalytic studies. *Journal of Materials Science: Materials in Electronics, 33*(14), 11455-11466.

Rehana, D., Mahendiran, D., Kumar, R. S., & Rahiman, A. K. (2017). Evaluation of antioxidant and anticancer activity of copper oxide nanoparticles synthesized using medicinally important plant extracts. *Biomedicine & Pharmacotherapy, 89*, 1067-1077.

Ribeiro, A. B., Chisté, R. C., Freitas, M., da Silva, A. F., Visentainer, J. V., & Fernandes, E. (2014). Psidium cattleianum fruit extracts are efficient in vitro scavengers of physiologically relevant reactive oxygen and nitrogen species. *Food chemistry, 165*, 140-148.

Ringwal, S., Bartwal, A. S., & Sati, S. C. (2022). Determination of antioxidant and catalytic activity of bio-synthesized Ag-MgO nanocomposite from peels extract of Citrus aurantium in the rapid treatment of wastewater management. *Inorganic Chemistry Communications, 140*, 109385.

Rodríguez-Félix, F., Graciano-Verdugo, A. Z., Moreno-Vásquez, M. J., Lagarda-Díaz, I., Barreras-Urbina, C. G., Armenta-Villegas, L., . . . Tapia-Hernández, J. A. (2022). Trends in Sustainable Green Synthesis of Silver Nanoparticles Using Agri-Food Waste Extracts and Their Applications in Health. *Journal of Nanomaterials, 2022*.

Rodríguez-Proenza, C. A., Palomares-Báez, J. P., Chávez-Rojo, M. A., García-Ruiz, A. F., Azanza-Ricardo, C. L., Santoveña-Uribe, A., . . . Esparza, R. (2018). Atomic surface segregation and structural characterization of PdPt bimetallic nanoparticles. *Materials, 11*(10), 1882.

Ruggeri, F. S., Šneideris, T., Vendruscolo, M., & Knowles, T. P. (2019). Atomic force microscopy for single molecule characterisation of protein aggregation. *Archives of biochemistry and biophysics, 664*, 134-148.

Ryu, S., Park, S., Lee, H. Y., Lee, H., Cho, C.-W., & Baek, J.-S. (2021). Biodegradable nanoparticles-loaded plga microcapsule for the enhanced encapsulation efficiency and controlled release of hydrophilic drug. *International Journal of Molecular Sciences, 22*(6), 2792.

Sabeena, G., Rajaduraipandian, S., Pushpalakshmi, E., Alhadlaq, H. A., Mohan, R., Annadurai, G., & Ahamed, M. (2022). Green and chemical synthesis of CuO nanoparticles: A comparative study for several in vitro bioactivities and in vivo toxicity in zebrafish embryos. *Journal of King Saud University-Science, 34*(5), 102092.

Sakthivel, C., Nivetha, A., & Prabha, I. (2022). Evaluation on synthesis and catalytic properties of ZnO enriched MgO nanomaterials using Limonia Acidissima as effective green substrate. *Arabian Journal for Science and Engineering*, 1-11.

Salem, N. M., & Awwad, A. M. (2022). Green synthesis and characterization of ZnO nanoparticles using Solanum rantonnetii leaves aqueous extract and antifungal activity evaluation. *Chem. Int, 8*(1), 12-17.

Salmaso, V., & Jacobson, K. A. (2020). In silico drug design for purinergic GPCRs: overview on molecular dynamics applied to adenosine and P2Y receptors. *Biomolecules, 10*(6), 812.

Samari, F., Baluchi, L., Salehipoor, H., & Yousefinejad, S. (2019). Controllable phyto-synthesis of cupric oxide nanoparticles by aqueous extract of Capparis spinosa (caper) leaves and application in iron sensing. *Microchemical Journal, 150*, 104158.

Sandhir, R., Yadav, A., Sunkaria, A., & Singhal, N. (2015). Nano-antioxidants: an emerging strategy for intervention against neurodegenerative conditions. *Neurochemistry international, 89*, 209-226.

Santhosh, P., Mukhtar, L., Kamaraj, M., Nithya, T., Ganesh, M., Aswathy, K., . . . Lopes, B. S. (2023). Phytomediated synthesis of copper oxide nanoparticles from floating fern

Salvinia cucullata Roxb. and their antibacterial, antioxidant, and anticancer potential. *Biomass Conversion and Biorefinery*, 1-15.

Sapsford, K. E., Algar, W. R., Berti, L., Gemmill, K. B., Casey, B. J., Oh, E., . . . Medintz, I. L. (2013). Functionalizing nanoparticles with biological molecules: developing chemistries that facilitate nanotechnology. *Chemical reviews, 113*(3), 1904-2074.

Sarkar, J., Chakraborty, N., Chatterjee, A., Bhattacharjee, A., Dasgupta, D., & Acharya, K. (2020). Green synthesized copper oxide nanoparticles ameliorate defence and antioxidant enzymes in Lens culinaris. *Nanomaterials, 10*(2), 312.

Sarwar, N., Humayoun, U. B., Kumar, M., Zaidi, S. F. A., Yoo, J. H., Ali, N., . . . Yoon, D. H. (2021). Citric acid mediated green synthesis of copper nanoparticles using cinnamon bark extract and its multifaceted applications. *Journal of Cleaner Production, 292*, 125974.

Sathiyavimal, S., Durán-Lara, E. F., Vasantharaj, S., Saravanan, M., Sabour, A., Alshiekheid, M., . . . Pugazhendhi, A. (2022). Green synthesis of copper oxide nanoparticles using Abutilon indicum leaves extract and their evaluation of antibacterial, anticancer in human A549 lung and MDA-MB-231 breast cancer cells. *Food and Chemical Toxicology, 168*, 113330.

Sathiyavimal, S., Vasantharaj, S., Kaliannan, T., Garalleh, H. A., Garaleh, M., Brindhadevi, K., . . . Pugazhendhi, A. (2023). Bio-functionalized copper oxide/chitosan nanocomposite using Sida cordifolia and their efficient properties of antibacterial, anticancer activity against on breast and lung cancer cell lines. *Environmental Research, 218*, 114986.

Sathiyavimal, S., Vasantharaj, S., Veeramani, V., Saravanan, M., Rajalakshmi, G., Kaliannan, T., . . . Pugazhendhi, A. (2021). Green chemistry route of biosynthesized copper oxide nanoparticles using Psidium guajava leaf extract and their antibacterial activity and effective removal of industrial dyes. *Journal of Environmental Chemical Engineering, 9*(2), 105033.

Saw, W. S., Ujihara, M., Chong, W. Y., Voon, S. H., Imae, T., Kiew, L. V., . . . Chung, L. Y. (2018). Size-dependent effect of cystine/citric acid-capped confeito-like gold nanoparticles on cellular uptake and photothermal cancer therapy. *Colloids and Surfaces B: Biointerfaces, 161*, 365-374.

Shah, M., Fawcett, D., Sharma, S., Tripathy, S. K., & Poinern, G. E. J. (2015). Green synthesis of metallic nanoparticles via biological entities. *Materials, 8*(11), 7278-7308.

Shahriary, S., Tafvizi, F., Khodarahmi, P., & Shaabanzadeh, M. (2022). Phyto-mediated synthesis of CuO nanoparticles using aqueous leaf extract of Artemisia deserti and their anticancer effects on A2780-CP cisplatin-resistant ovarian cancer cells. *Biomass Conversion and Biorefinery*, 1-17.

Shaikh, J. R., & Patil, M. (2020). Qualitative tests for preliminary phytochemical screening: An overview. *International Journal of Chemical Studies*, *8*(2), 603-608.

Shalaby, E. A., Shanab, S. M., El-Raheem, W. M. A., & Hanafy, E. A. (2022). Biological activities and antioxidant potential of different biosynthesized nanoparticles of Moringa oleifera. *Scientific reports*, *12*(1), 18400.

Shang, L., Nienhaus, K., & Nienhaus, G. U. (2014). Engineered nanoparticles interacting with cells: size matters. *Journal of nanobiotechnology*, *12*(1), 5.

Shankar, S. S., Ahmad, A., Pasricha, R., & Sastry, M. (2003). Bioreduction of chloroaurate ions by geranium leaves and its endophytic fungus yields gold nanoparticles of different shapes. *Journal of Materials Chemistry*, *13*(7), 1822-1826.

Sharma, A., Goyal, A. K., & Rath, G. (2018). Recent advances in metal nanoparticles in cancer therapy. *Journal of drug targeting*, *26*(8), 617-632.

Sharma, H., Mishra, P. K., Talegaonkar, S., & Vaidya, B. (2015). Metal nanoparticles: a theranostic nanotool against cancer. *Drug discovery today*, *20*(9), 1143-1151.

Sharma, S., & Kumar, K. (2021). Aloe-vera leaf extract as a green agent for the synthesis of CuO nanoparticles inactivating bacterial pathogens and dye. *Journal of Dispersion Science and Technology*, *42*(13), 1950-1962.

Shukla, A. K., & Iravani, S. (2017). Metallic nanoparticles: green synthesis and spectroscopic characterization. *Environmental Chemistry Letters*, *15*(2), 223-231.

Siddiqui, H., Parra, M. R., & Haque, F. Z. (2018). Optimization of process parameters and its effect on structure and morphology of CuO nanoparticle synthesized via the sol− gel technique. *Journal of Sol-Gel Science and Technology*, *87*, 125-135.

Siegel, R. L., Miller, K. D., & Jemal, A. (2019). Cancer statistics, 2019. *CA: a cancer journal for clinicians*, *69*(1), 7-34.

Singh, A., Gaud, B., & Jaybhaye, S. (2020). Optimization of synthesis parameters of silver nanoparticles and its antimicrobial activity. *Materials Science for Energy Technologies*, *3*, 232-236.

Singh, A., & Kaushik, M. (2019). Physicochemical investigations of zinc oxide nanoparticles synthesized from Azadirachta Indica (Neem) leaf extract and their interaction with Calf-Thymus DNA. *Results in Physics, 13*, 102168.

Singh, A. K., Talat, M., Singh, D., & Srivastava, O. (2010). Biosynthesis of gold and silver nanoparticles by natural precursor clove and their functionalization with amine group. *Journal of Nanoparticle Research, 12*(5), 1667-1675.

Singh, J., Kumar, V., Kim, K.-H., & Rawat, M. (2019). Biogenic synthesis of copper oxide nanoparticles using plant extract and its prodigious potential for photocatalytic degradation of dyes. *Environmental research, 177*, 108569.

Singh, R., & Nalwa, H. S. (2011). Medical applications of nanoparticles in biological imaging, cell labeling, antimicrobial agents, and anticancer nanodrugs. *Journal of biomedical nanotechnology, 7*(4), 489-503.

Sirivibulkovit, K., Nouanthavong, S., & Sameenoi, Y. (2018). based DPPH assay for antioxidant activity analysis. *Analytical sciences, 34*(7), 795-800.

Soleimani-Amiri, S., Hossaini, Z., & Azizi, Z. (2023). Synthesis and Investigation of Biological Activity of New Oxazinoazepines: Application of Fe3O4/CuO/ZnO@ MWCNT Magnetic Nanocomposite in Reduction of 4-Nitrophenol in Water. *Polycyclic Aromatic Compounds, 43*(4), 2938-2959.

Sonbol, H., AlYahya, S., Ameen, F., Alsamhary, K., Alwakeel, S., Al-Otaibi, S., & Korany, S. (2021). Bioinspired synthesize of CuO nanoparticles using Cylindrospermum stagnale for antibacterial, anticancer and larvicidal applications. *Applied Nanoscience*, 1-11.

Srinoi, P., Chen, Y.-T., Vittur, V., Marquez, M. D., & Lee, T. R. (2018). Bimetallic nanoparticles: enhanced magnetic and optical properties for emerging biological applications. *Applied Sciences, 8*(7), 1106.

Stanić, V., & Tanasković, S. B. (2020). Antibacterial activity of metal oxide nanoparticles *Nanotoxicity* (pp. 241-274): Elsevier

Stark, W. J. (2011). Nanoparticles in biological systems. *Angewandte Chemie International Edition, 50*(6), 1242-1258.

Subbaiya, R., & Selvam, M. M. (2015). Green synthesis of copper nanoparticles from Hibicus Rosasinensis and their antimicrobial, antioxidant activities. *Research Journal of Pharmaceutical Biological and Chemical Sciences, 6*(2), 1183-1190.

Sukri, S. N. A. M., Shameli, K., Wong, M. M.-T., Teow, S.-Y., Chew, J., & Ismail, N. A. (2019). Cytotoxicity and antibacterial activities of plant-mediated synthesized zinc oxide (ZnO) nanoparticles using Punica granatum (pomegranate) fruit peels extract. *Journal of Molecular Structure, 1189*, 57-65.

Sukumar, S., Rudrasenan, A., & Padmanabhan Nambiar, D. (2020). Green-synthesized rice-shaped copper oxide nanoparticles using Caesalpinia bonducella seed extract and their applications. *ACS omega, 5*(2), 1040-1051.

Sung, H., Ferlay, J., Siegel, R. L., Laversanne, M., Soerjomataram, I., Jemal, A., & Bray, F. (2021). Global cancer statistics 2020: GLOBOCAN estimates of incidence and mortality worldwide for 36 cancers in 185 countries. *CA: a cancer journal for clinicians, 71*(3), 209-249.

Suresh, P., Doss, A., Praveen Pole, R., & Devika, M. (2023). Green synthesis, characterization and antioxidant activity of bimetallic (Ag-ZnO) nanoparticles using Capparis zeylanica leaf extract. *Biomass Conversion and Biorefinery*, 1-9.

Sutradhar, K. B., & Amin, M. (2014). Nanotechnology in cancer drug delivery and selective targeting. *International Scholarly Research Notices, 2014*.

Tabrez, S., Khan, A. U., Hoque, M., Suhail, M., Khan, M. I., & Zughaibi, T. A. (2022a). Biosynthesis of ZnO NPs from pumpkin seeds' extract and elucidation of its anticancer potential against breast cancer. *Nanotechnology Reviews, 11*(1), 2714-2725.

Tabrez, S., Khan, A. U., Hoque, M., Suhail, M., Khan, M. I., & Zughaibi, T. A. (2022b). Investigating the anticancer efficacy of biogenic synthesized MgONPs: An in vitro analysis. *Frontiers in Chemistry, 10*, 970193.

Thakur, S., & Bharti, S. (2023). The Synergy of Nanoparticles and Metal-Organic Frameworks in Antimicrobial Applications: a Critical Review. *Journal of Environmental Chemical Engineering*, 111458.

Thamer, N., Muftin, N., & Al-Rubae, S. (2018). Optimization properties and characterization of green synthesis of copper oxide nanoparticles using aqueous extract of Cordia myxa L. leaves. *Asian J. Chem, 30*(7), 1559-1563.

Thandapani, G., Arthi, K., Pazhanisamy, P., John, J. J., Vinothini, C., Rekha, V., . . . Sekar, V. (2023). Green synthesis of copper oxide nanoparticles using Spinacia oleracea leaf extract and evaluation of biological applications: Antioxidant, antibacterial, larvicidal and biosafety assay. *Materials Today Communications*, *34*, 105248.

Toy, R., Hayden, E., Shoup, C., Baskaran, H., & Karathanasis, E. (2011). The effects of particle size, density and shape on margination of nanoparticles in microcirculation. *Nanotechnology, 22*(11), 115101.

Umaralikhan, L., & Jamal Mohamed Jaffar, M. (2018). Green synthesis of MgO nanoparticles and it antibacterial activity. *Iranian Journal of Science and Technology, Transactions A: Science, 42*(2), 477-485.

Uwizeyimana, J. D., Kim, D., Lee, H., Byun, J.-H., & Yong, D. (2020). Determination of colistin resistance by simple disk diffusion test using modified Mueller-Hinton agar. *Annals of laboratory medicine, 40*(4), 306-311.

Varshney, S., Nigam, A., Singh, A., Samanta, S. K., Mishra, N., & Tewari, R. (2022). Antibacterial, structural, and mechanical properties of MgO/ZnO nanocomposites and its HA-based bio-ceramics; synthesized via physio-chemical route for biomedical applications. *Materials Technology*, *37*(13), 2503-2516.

Vasiliou, S. K., & Diamandis, E. P. (2019). Androgen receptor: a promising therapeutic target in breast cancer. *Critical reviews in clinical laboratory sciences, 56*(3), 200-223.

Velsankar, K., Aravinth, K., Cláudia, P.-S. A., Wang, Y., Ameen, F., & Sudhahar, S. (2023). Bio-derived synthesis of MgO nanoparticles and their anticancer and hemolytic bioactivities. *Biocatalysis and Agricultural Biotechnology, 53*, 102870.

Velsankar, K., Venkatesan, A., Muthumari, P., Suganya, S., Mohandoss, S., & Sudhahar, S. (2022). Green inspired synthesis of ZnO nanoparticles and its characterizations with biofilm, antioxidant, anti-inflammatory, and anti-diabetic activities. *Journal of Molecular Structure, 1255*, 132420.

Vidhya, E., Vijayakumar, S., Prathipkumar, S., & Praseetha, P. (2020). Green way biosynthesis: Characterization, antimicrobial and anticancer activity of ZnO nanoparticles. *Gene Reports, 20*, 100688.

Vijayakumar, S., Chen, J., Sánchez, Z. I. G., Tungare, K., Bhori, M., Durán-Lara, E. F., & Anbu, P. (2023). Moringa oleifera gum capped MgO nanoparticles: Synthesis, characterization,

cyto-and ecotoxicity assessment. *International Journal of Biological Macromolecules, 233*, 123514.

Vijayakumar, S., Punitha, V., & Parameswari, N. (2022). Phytonanosynthesis of MgO nanoparticles: green synthesis, characterization and antimicrobial evaluation. *Arabian Journal for Science and Engineering, 47*(6), 6729-6734.

Vijayaraghavan, K., & Ashokkumar, T. (2017). Plant-mediated biosynthesis of metallic nanoparticles: a review of literature, factors affecting synthesis, characterization techniques and applications. *Journal of environmental chemical engineering, 5*(5), 4866-4883.

Vindhya, P., & Kavitha, V. (2023). Effect of cobalt doping on antimicrobial, antioxidant and photocatalytic activities of CuO nanoparticles. *Materials Science and Engineering: B, 289*, 116258.

Vinothkanna, A., Mathivanan, K., Ananth, S., Ma, Y., & Sekar, S. (2023). Biosynthesis of copper oxide nanoparticles using Rubia cordifolia bark extract: characterization, antibacterial, antioxidant, larvicidal and photocatalytic activities. *Environmental Science and Pollution Research, 30*(15), 42563-42574.

Vinu, D., Govindaraju, K., Vasantharaja, R., Amreen Nisa, S., Kannan, M., & Vijai Anand, K. (2021). Biogenic zinc oxide, copper oxide and selenium nanoparticles: preparation, characterization and their anti-bacterial activity against Vibrio parahaemolyticus. *Journal of Nanostructure in Chemistry, 11*(2), 271-286.

Waghchaure, R. H., & Adole, V. A. (2023). Biosynthesis of metal and metal oxide nanoparticles using various parts of plants for antibacterial, antifungal and anticancer activity: A review. *Journal of the Indian Chemical Society*, 100987.

Wahid, F., Khan, T., Shehzad, A., Ul-Islam, M., & Kim, Y. (2014). Interaction of nanomaterials with cells and their medical applications. *Journal of nanoscience and nanotechnology, 14*(1), 744-754.

Wan, R., Mo, Y., Feng, L., Chien, S., Tollerud, D. J., & Zhang, Q. (2012). DNA damage caused by metal nanoparticles: involvement of oxidative stress and activation of ATM. *Chemical research in toxicology, 25*(7), 1402-1411.

Wong, C. W., Chan, Y. S., Jeevanandam, J., Pal, K., Bechelany, M., Abd Elkodous, M., & El-Sayyad, G. S. (2020). Response surface methodology optimization of mono-dispersed

MgO nanoparticles fabricated by ultrasonic-assisted sol–gel method for outstanding antimicrobial and antibiofilm activities. *Journal of Cluster Science, 31*(2), 367-389.

Wu, S., Powers, S., Zhu, W., & Hannun, Y. A. (2016). Substantial contribution of extrinsic risk factors to cancer development. *Nature, 529*(7584), 43-47.

Yadav, N., Jaiswal, A. K., Dey, K. K., Yadav, V. B., Nath, G., Srivastava, A. K., & Yadav, R. R. (2018). Trimetallic Au/Pt/Ag based nanofluid for enhanced antibacterial response. *Materials Chemistry and Physics, 218*, 10-17.

Yadav, S., & Maurya, P. K. (2021). Biomedical applications of metal oxide nanoparticles in aging and age-associated diseases. *3 Biotech, 11*(7), 338.

Yaqub, A., Malkani, N., Shabbir, A., Ditta, S. A., Tanvir, F., Ali, S., . . . Ullah, R. (2020). Novel biosynthesis of copper nanoparticles using Zingiber and Allium sp. with synergic effect of doxycycline for anticancer and bactericidal activity. *Current Microbiology, 77*(9), 2287-2299.

Younas, M., Zubair, M., Rizwan, M., Khan, M. A., Hussaini, K. M., Mumtaz, R., . . . Ali, S. (2023). Synthesis and characterization of cerium, silver and copper oxide nanoparticles and their anticancer potential of hepatocellular carcinoma HepG2 cancer cells. *Journal of Molecular Structure, 1288*, 135756.

Zain, M., Yasmeen, H., Yadav, S. S., Amir, S., Bilal, M., Shahid, A., & Khurshid, M. (2022). Applications of nanotechnology in biological systems and medicine *Nanotechnology for hematology, blood transfusion, and artificial blood* (pp. 215-235): Elsevier

Zambonino, M. C., Quizhpe, E. M., Mouheb, L., Rahman, A., Agathos, S. N., & Dahoumane, S. A. (2023). Biogenic selenium nanoparticles in biomedical sciences: properties, current trends, novel opportunities and emerging challenges in theranostic nanomedicine. *Nanomaterials, 13*(3), 424.

Zayed, M. F., Mahfoze, R. A., El-kousy, S. M., & Al-Ashkar, E. A. (2020). In-vitro antioxidant and antimicrobial activities of metal nanoparticles biosynthesized using optimized Pimpinella anisum extract. *Colloids and Surfaces A: Physicochemical and Engineering Aspects, 585*, 124167.

Zewde, D., & Geremew, B. (2022). Biosynthesis of ZnO nanoparticles using Hagenia abyssinica leaf extracts; their photocatalytic and antibacterial activities. *Environmental Pollutants and Bioavailability, 34*(1), 224-235.

Zhang, J., Hu, K., Di, L., Wang, P., Liu, Z., Zhang, J., . . . Chen, T. (2021). Traditional herbal medicine and nanomedicine: Converging disciplines to improve therapeutic efficacy and human health. *Advanced Drug Delivery Reviews, 178*, 113964.

Zhang, R., Yu, J., Guo, X., Li, W., Xing, Y., & Wang, Y. (2021). Monascus pigment-mediated green synthesis of silver nanoparticles: Catalytic, antioxidant, and antibacterial activity. *Applied Organometallic Chemistry, 35*(3), e6120.

Zhao, X., Jia, Y., Dong, R., Deng, J., Tang, H., Hu, F., . . . Jiang, X. (2020). Bimetallic Nanoparticles against Multi-Drug Resistant Bacteria. *Chemical Communications*.

Zughaibi, T. A., Mirza, A. A., Suhail, M., Jabir, N. R., Zaidi, S. K., Wasi, S., . . . Tabrez, S. (2022). Evaluation of anticancer potential of biogenic copper oxide nanoparticles (CuO NPs) against breast cancer. *Journal of Nanomaterials, 2022*.

Appendixes

Appendix 1. Tripilicate absorbances of extract, NPs and ascorbic acid agains DPPH free radicals

Samples	Con (µg/mL)	Abs 1	Abs2	Abs3	Average	% Scavegning
Blank	-	0.530	0.531	0.53505	0.53505	
AA	12.5	0.194	0.192	0.190	0.192	63.91±0.03
	25	0.156	0.154	0.154	0.155	70.83±0.00
	50	0.118	0.114	0.110	0.114	78.51±0.06
	100	0.063	0.066	0.068	0.066	87.58±0.01
	200	0.029	0.029	0.028	0.029	94.56±0.02
Extract	12.5	0.320	0.318	0.316	0.318	39.88±0.04
	25	0.283	0.282	0.284	0.283	46.66±0.01
	50	0.245	0.247	0.246	0.246	53.49±0.02
	100	0.220	0.218	0.219	0.219	58.75±0.01
	200	0.183	0.184	0.187	0.185	65.02±0.02
CuO NPs	12.5	0.216	0.217	0.214	0.219	58.67±0.00
	25	0.184	0.177	0.182	0.181	65.86±0.02
	50	0.143	0.136	0.144	0.141	73.32±0.01
	100	0.097	0.098	0.099	0.098	81.26±0.03
	200	0.062	0.060	0.056	0.059	88.81±0.02
MgO NPs	12.5	0.329	0.232	0.241	0.234	55.76±0.00
	25	0.203	0.202	0.204	0.203	61.72±0.03
	50	0.169	0.167	0.165	0.167	68.55±0.02
	100	0.129	0.131	0.130	0.130	75.49±0.04
	200	0.081	0.083	0.077	0.081	84.67±0.01
ZnO NPs	12.5	0.227	0.225	0.223	0.225	57.48±0.04
	25	0.194	0.190	0.198	0.194	63.37±0.02
	50	0.150	0.149	0.154	0.151	71.46±0.03
	100	0.113	0.107	0.111	0.110	79.22±0.00

	200	0.076	0.070	0.072	0.073	86.28±0.04
ZC NCs	12.5	0.194	0.188	0.190	0.191	63.91±0.03
	25	0.154	0.154	0.154	0.154	70.83±0.00
	50	0.117	0.115	0.111	0.114	78.51±0.06
	100	0.069	0.063	0.067	0.066	87.58±0.01
	200	0.032	0.029	0.027	0.029	94.56±0.11
MC NCs	12.5	0.197	0.198	0.199	0.198	62.72±0.04
	25	0.166	0.168	0.164	0.166	68.59±0.02
	50	0.123	0.123	0.124	0.123	76.83±0.01
	100	0.077	0.077	0.083	0.079	84.99±0.03
	200	0.033	0.033	0.033	0.033	93.71±0.02
MZ NCs	12.5	0.200	0.206	0.203	0.203	61.77±0.03
	25	0.165	0.166	0.167	0.166	68.59±0.01
	50	0.125	0.125	0.119	0.123	76.47±0.04
	100	0.086	0.085	0.087	0.086	83.68±0.06
	200	0.037	0.037	0.036	0.037	92.93±0.01
ZMC NCs	12.5	0.169	0.169	0.166	0.168	68.37±0.11
	25	0.124	0.124	0.123	0.124	76.57±0.01
	50	0.083	0.087	0.084	0.085	83.88±0.06
	100	0.045	0.046	0.047	0.046	91.27±0.02
	200	0.011	0.013	0.018	0.014	97.41±0.01

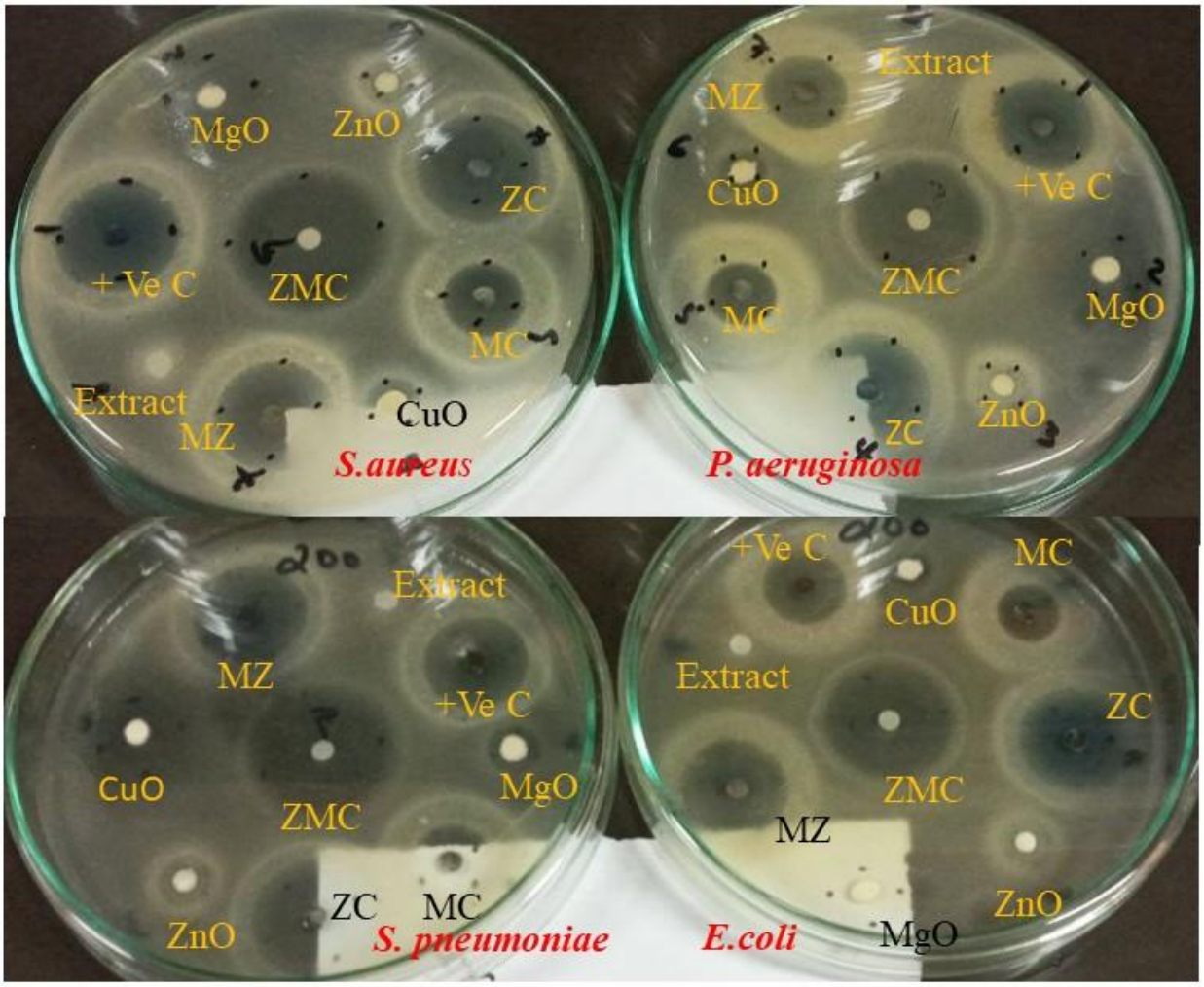

Appendix 2. Sample disc diffusion for antibacterial activity of extract, chlorophenicol (Positive control) and biosynthesized MO NMs.

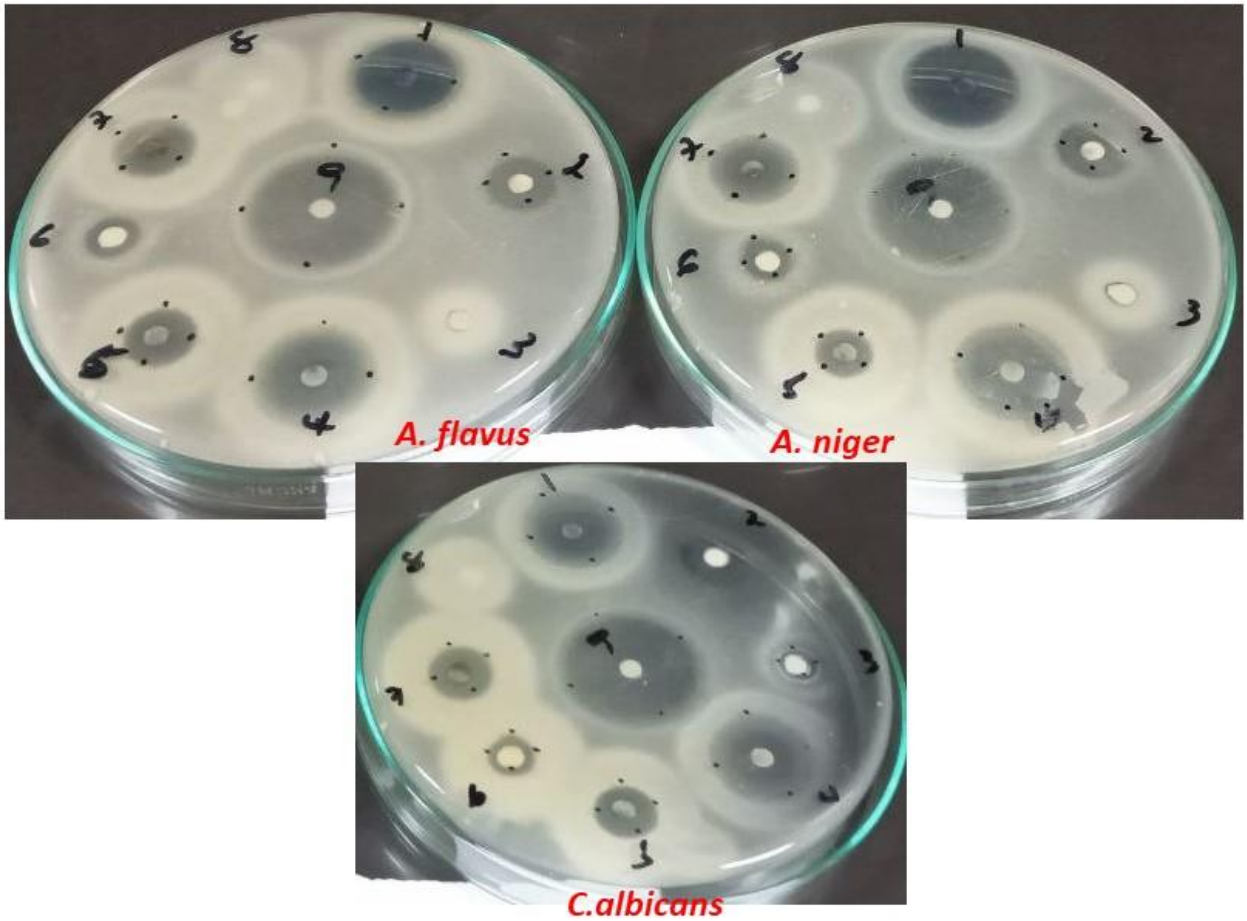

Appendix 3. Sample disc diffusion for antifungal activity of extract, chlorophenicol (Positive control) and biosynthesized nanoparticles (8, 1, 2, 3, 4, 5, 6, 7, and 9 are Extract, Fluconazole, MgO, ZnO, ZC, MC, CuO, and ZMC NMs respectively).

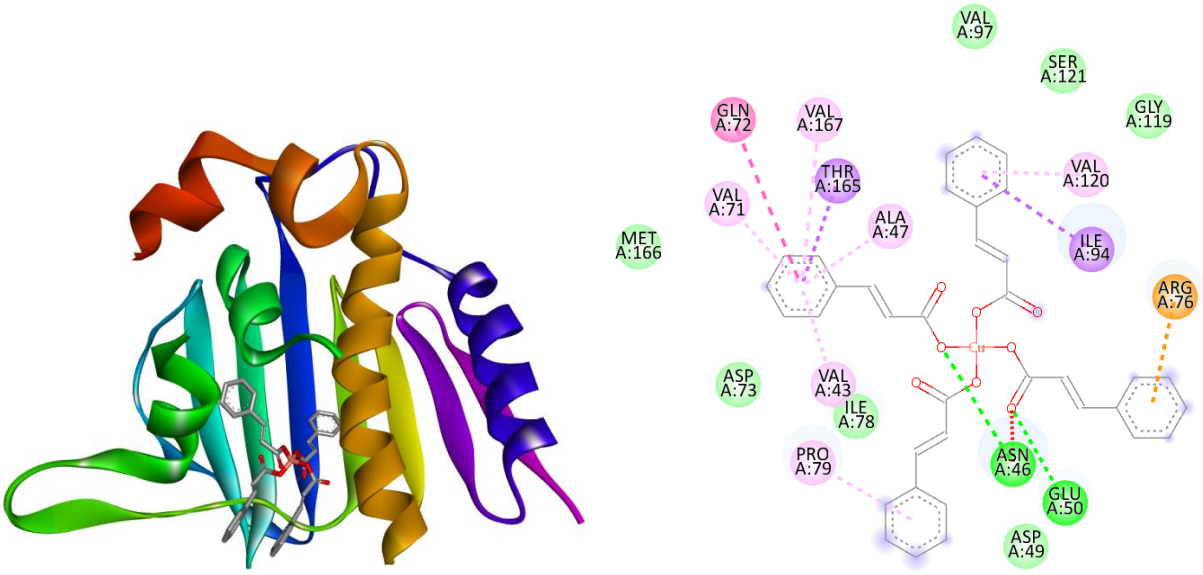

Appendix 4. The binding interactions of CuO NPs against *E. coli* (PDB: 6F86)

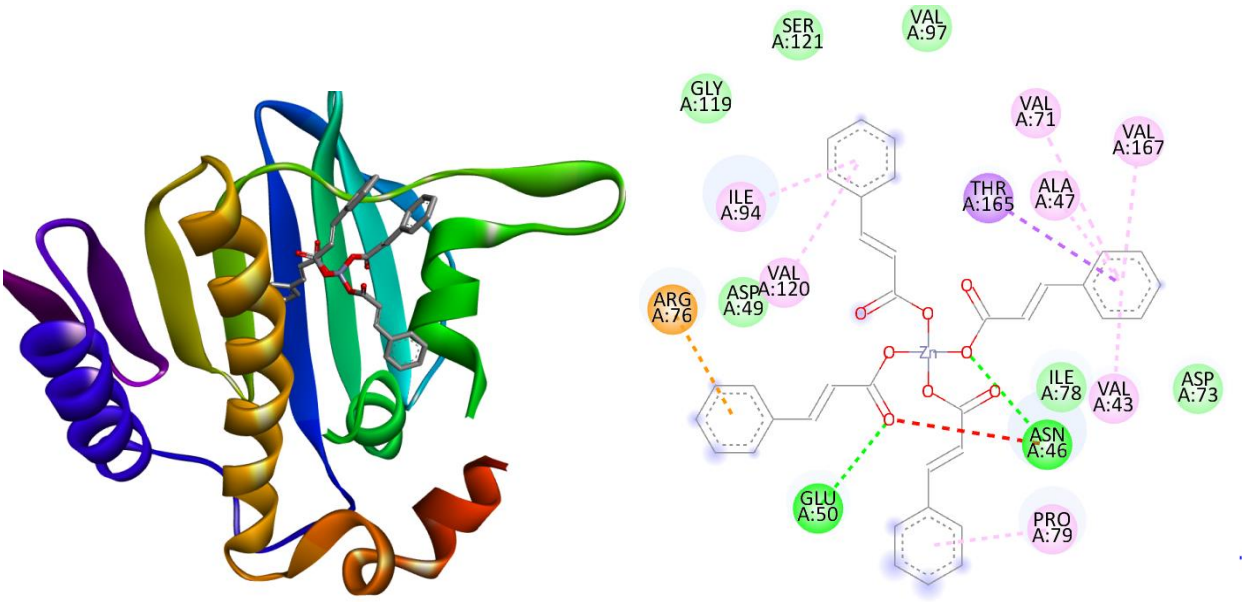

Appendix 5. The binding interactions of ZnO NPs against *E. coli* (PDB: 6F86

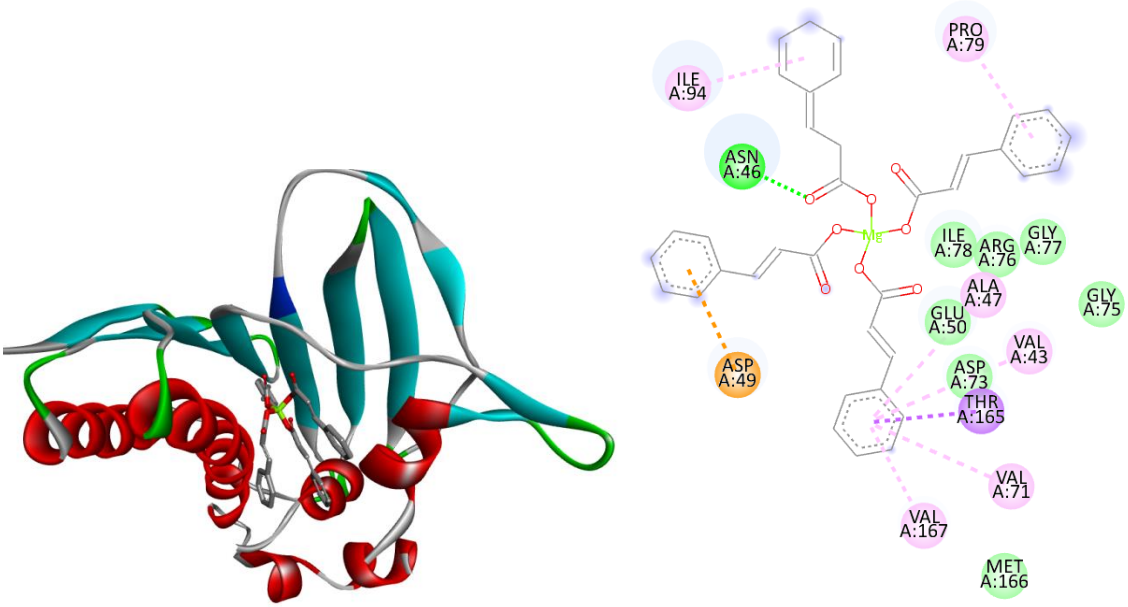

Appendix 6. The binding interactions of MgO NPs against *E. coli* (PDB: 6F86)

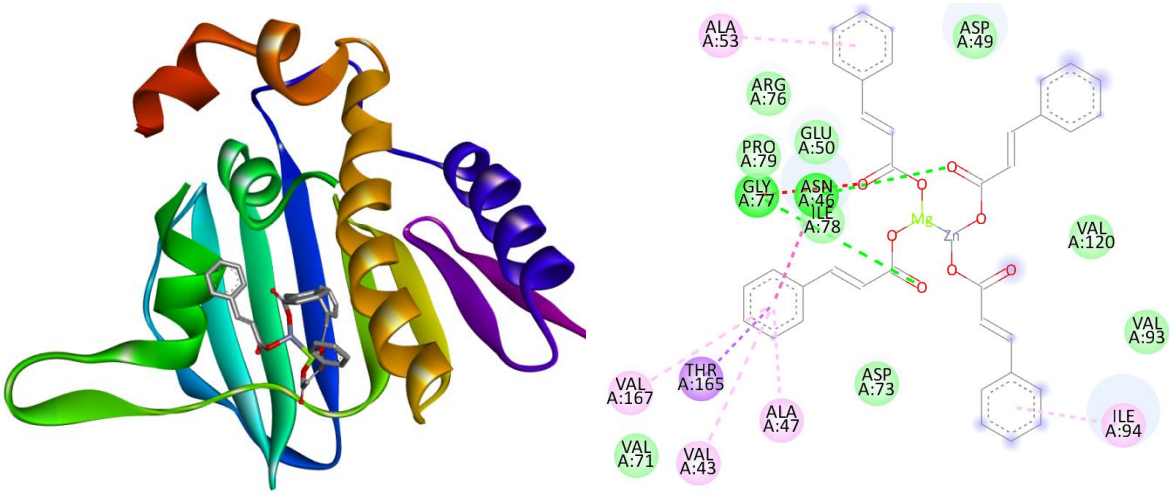

Appendix 7. The binding interactions of MZ NCs against *E. coli* (PDB: 6F86)

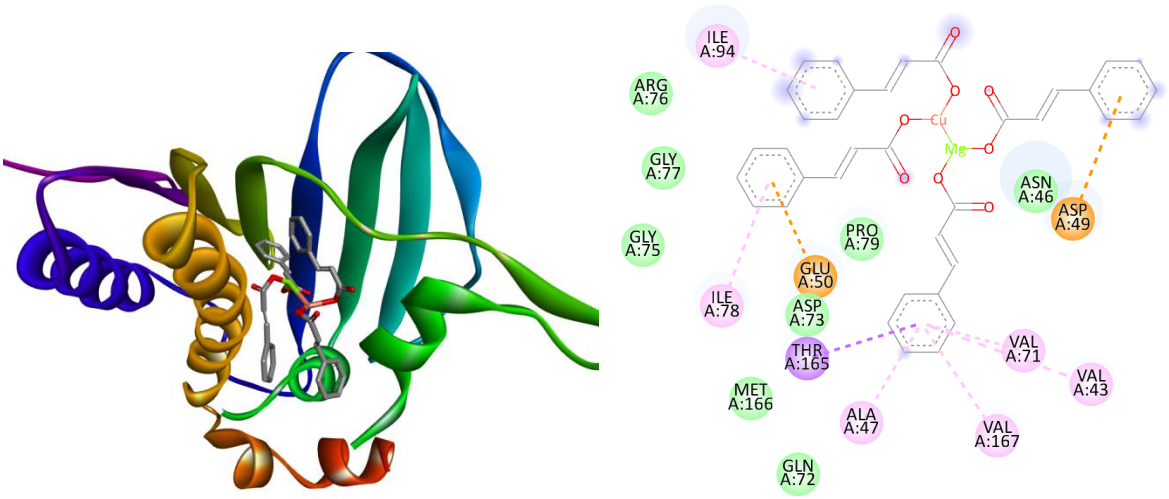

Appendix 8. The binding interactions of MC NCs against *E. coli* (PDB: 6F86)

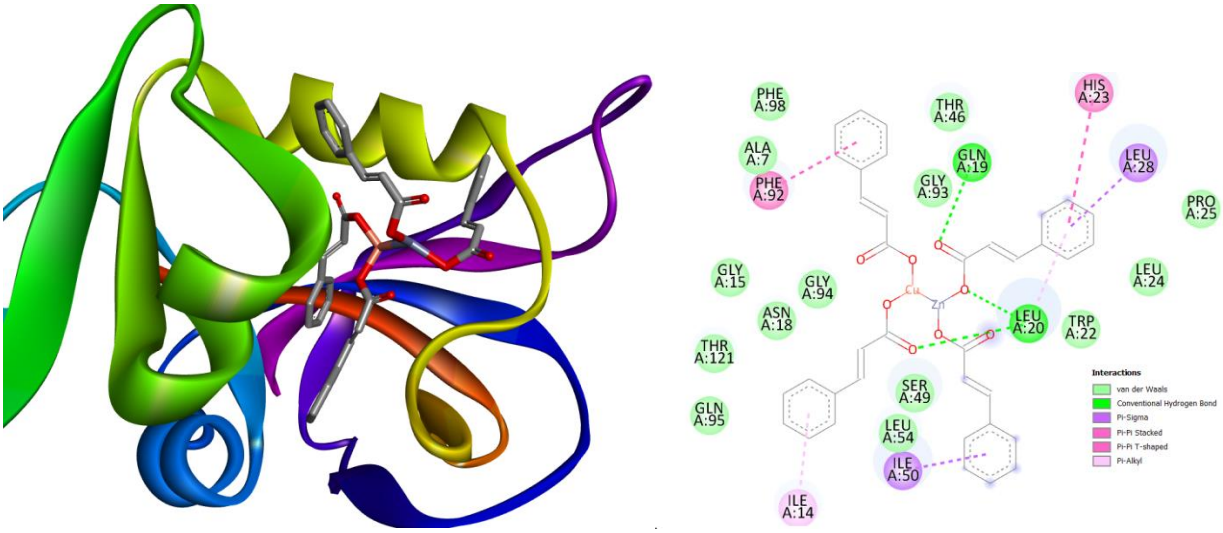

Appendix 9. The binding interactions of ZC NCs against *E. coli* (PDB: 6F86)

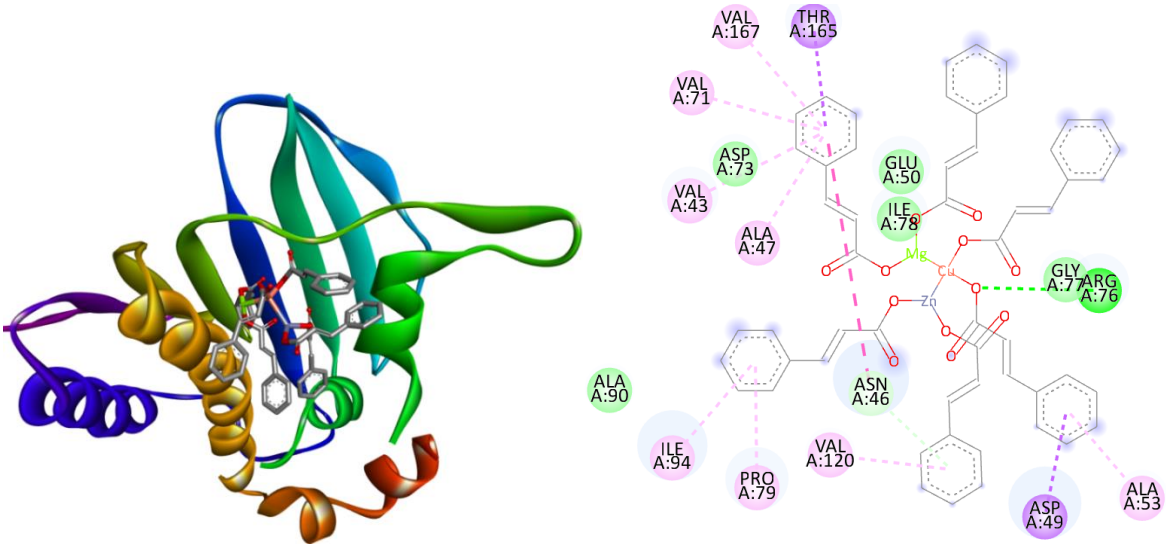

Appendix 10. The binding interactions of ZMC NCs against *E. coli* DNA gyrase B (PDB: 6F86)

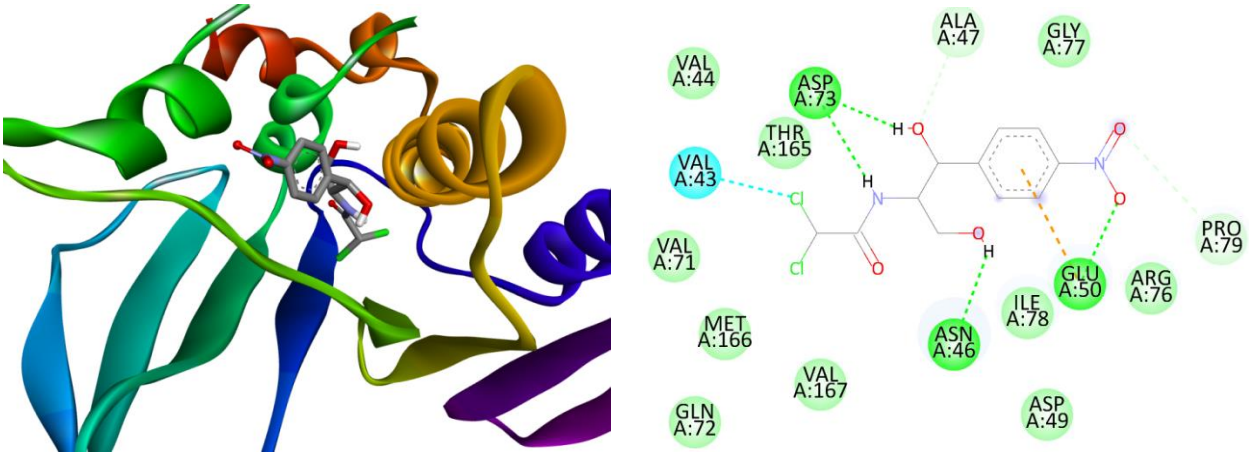

Appendix 11. The binding interactions of chloramphenicol against *E. coli* (PDB: 6F86)

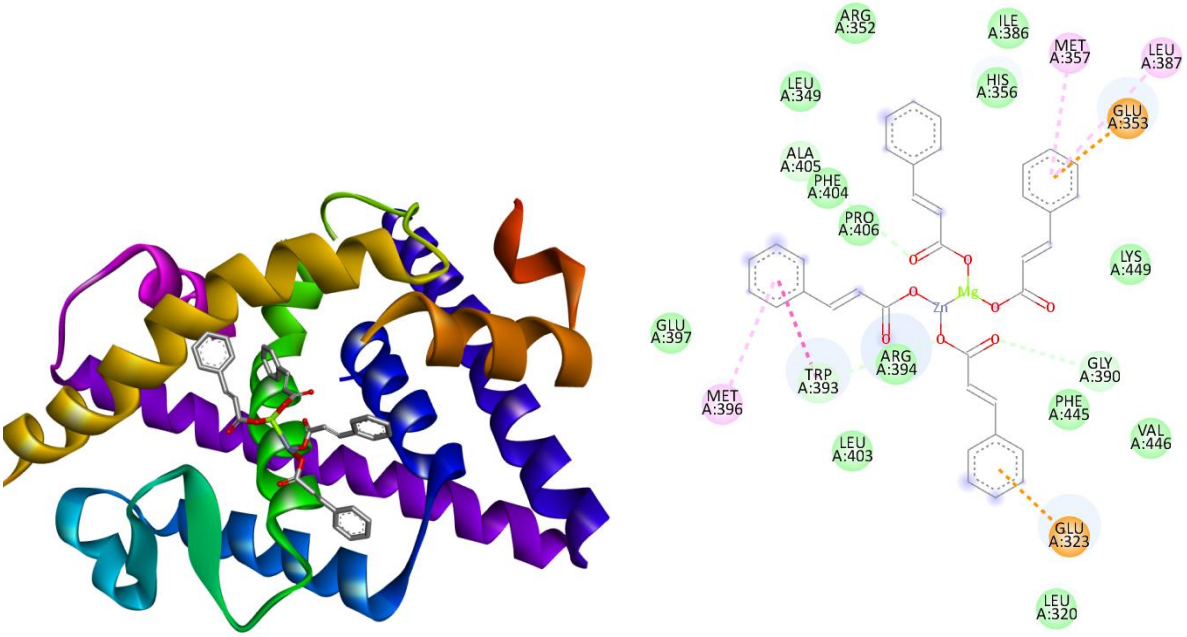

Appendix 12. The binding interactions of MZ NCs against estrogen receptor alpha (ERα; PDB: 5GS4)

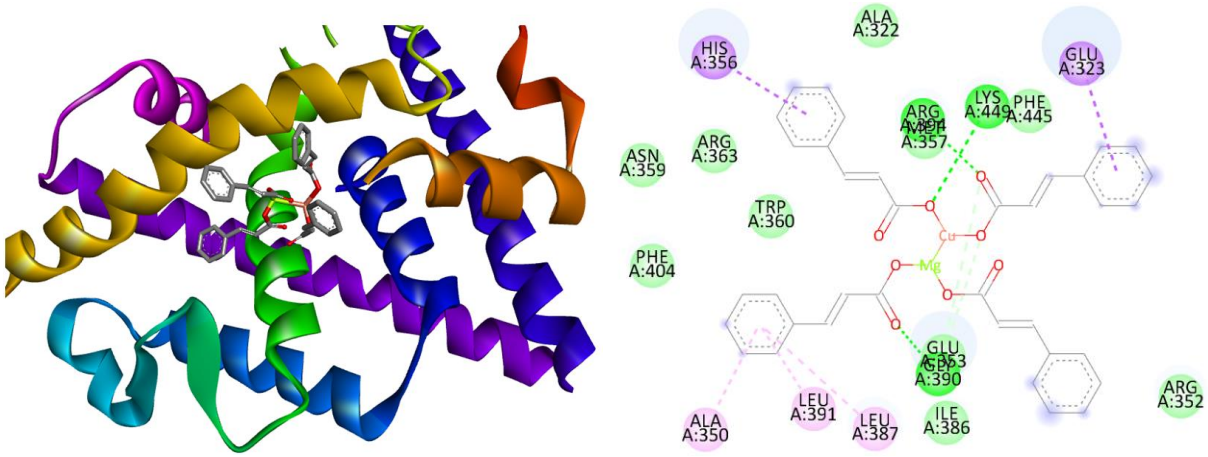

Appendix 13. The binding interactions of MC NCs against estrogen receptor alpha (ERα; PDB: 5GS4)

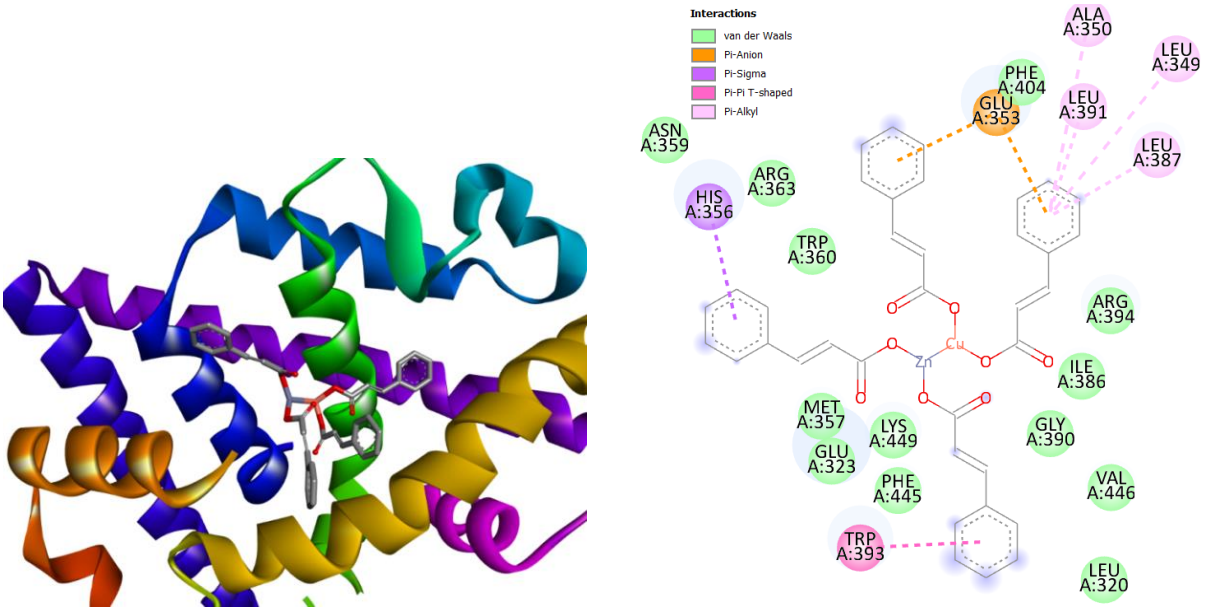

Appendix 14**.** The binding interactions of ZC NCs against estrogen receptor alpha (ERα; PDB: 5GS4)

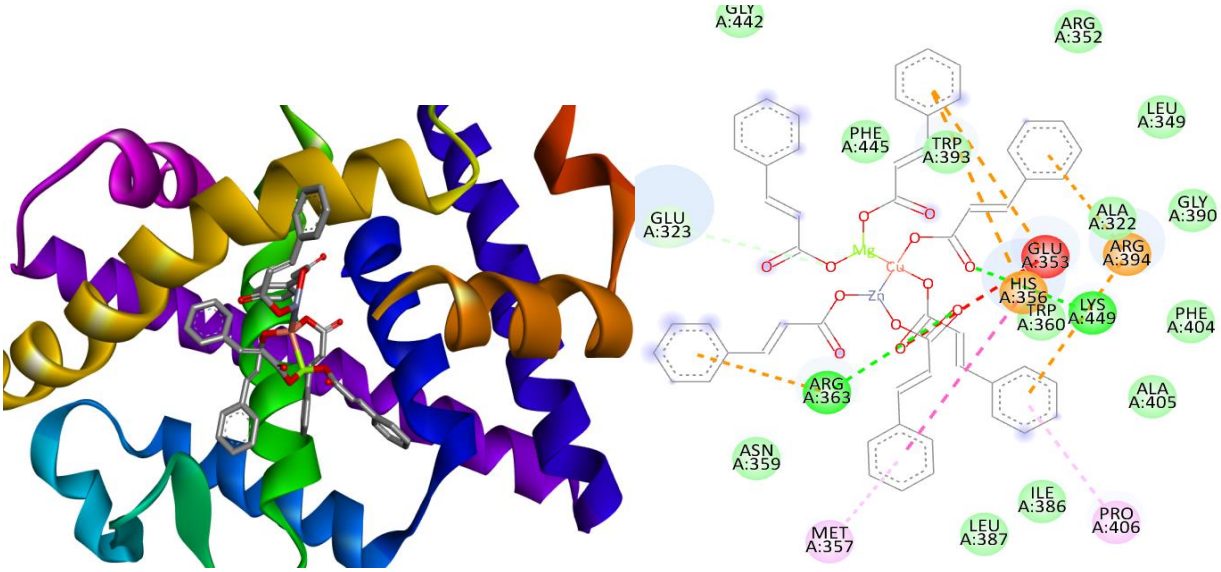

Appendix 15. The binding interactions of ZMC NCs against estrogen receptor alpha (ERα; PDB: 5GS4)

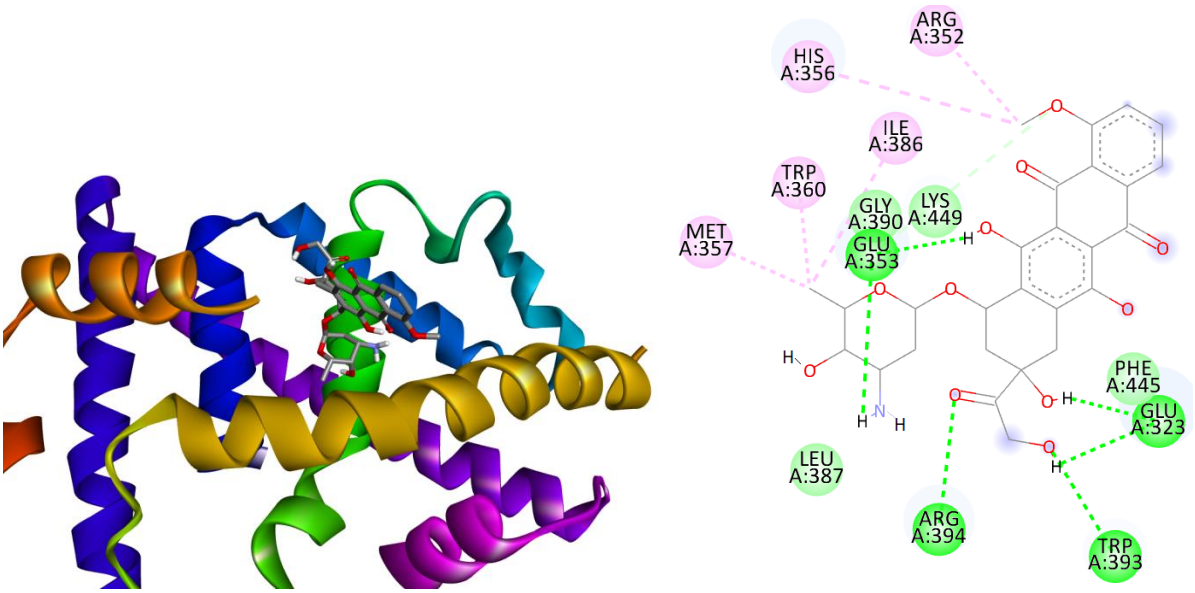

Appendix 16. The binding interactions of doxorubicin against estrogen receptor alpha (ERα; PDB: 5GS4)

List of Publications Releated to this Work

1. **Temesgen Achamo**, Enyew Amare Zereffa, H. C. Ananda Murthy, Venkatesha Perumal Ramachandran & Ruthramurthy Balachandran (2022). Phyto-mediated synthesis of copper oxide nanoparticles using *Artemisia abyssinica* leaf extract and its antioxidant, antimicrobial and DNA binding activities, *Green Chemistry Letters and Reviews*, 15:3, 598-614, **Teylor and Francis:** DOI: 10.1080/17518253.2022.2121620.
2. **Orshiso, T. A**., Zereffa, E. A., Murthy, H. A., Demissie, T. B., Pardeshi, O., Avhad, L. S., & Ghotekar, S. (2023). Biosynthesis of Artemisia abyssinica Leaf Extract-Mediated Bimetallic ZnO–CuO Nanoparticles: Antioxidant, Anticancer, and Molecular Docking Studies. *ACS Omega*, 8, 44, 41039–41053: https://doi.org/10.1021/acsomega.3c01814
3. **Orshiso, T.A**., Zereffa, E.A., Murthy, H.C.A. *et al.* One-Pot Biopreparation of Trimetallic ZnO–MgO–CuO Nanoparticles: Enhanced Cytotoxicity, Antibacterial Activities and Molecular Docking Studies. *Chemistry Africa* (2024), Springer Nature. https://doi.org/10.1007/s42250-023-00830-0.
4. **Temesgen Achamo,** H. C. Ananda Murthy, Enyew Amare Zereffa, Venkatesha Perumal Ramachandran. Emerging Trends in Metal-based Anticancer Agents: Drug Design to Clinical Trials and their Mechanism of Action. *ChemistrySelect,* **Wiely,** https://doi.org/10.1002/slct.202302113.
5. **Temesgen Achamo**, Enyew Amare Zereffa, H. C. Ananda Murthy, T.Naveen kumar, C. R. Ravikumar. Biosynthesis of bimetallic MgO-ZnO nanoparticles from leaf extract of *Artemisia abyssinica* plant and their enhanced *in vitro* antimicrobial and antioxidant activities. *Inorganic and Nanometal Cheistry*, **Teylor and Francis** (Under review)
6. **Temesgen Achamo Orshiso**, Enyew Amare Zereffa, H. C. Ananda Murthy. Phytochemical Mediated MgO-based Mono and Bimetallic Oxide Nanomaterials: Cytotoxicity, Antioxidant, Antifungal and Molecular Docking Studies. *Inorganic Chemistry Communication*, **Elsevier** (Under review).